Characterization of Concrete Materials Using Non-Destructive Wave-Propagation Testing Techniques

Saber Taghavipour

M.Sc. Structural Engineering

A thesis submitted in fulfillment of the

requirements for the degree of

Doctor of Philosophy

Centre for Infrastructure Engineering

School of Computing, Engineering and Mathematics

Western Sydney University, Australia

2017

Acknowledgments

This thesis would not have been possible without the guidance and the help of individuals who in one way or another contributed and extended their valuable assistance in the preparation and completion of my study. I would like to express my sincere gratitude to my advisor, Associate Professor Sergiy Kharkivskiy, who unfortunately passed away a few weeks before the final thesis submission. This thesis would not have been possible without his advice and guidance. May his soul rest in peace. I would also grateful to Professor Bijan Samali, Dr. Won Hee Kang and Dr. Olivia Mirza for their support and advices. The present thesis would not have been possible without their technical insight.

I would like to thank all the academic, administrative and technical staff in the Centre for Infrastructure Engineering at Western Sydney University. Special thanks go to the technical staff, Dr. Mithra Fernando, Mr David Batten, Mr Robert Marshall, Mr Murray Bolden, Mr Ali Gharizadeh, Mr Ranjith Ratnayake and, Mr Nathan McKinlay, for their assistance and technical support in the experimental programme and software support.

I would like to extend my gratitude to my friends and colleagues, who have offered fruitful suggestions and support during this work: Dr. Ali Jamshidi, Dr. Amir Azad, Dr. Rui Li, Dr. Mahdi Moosazadeh, Mr Mohsen Mousavi and Mr Naser Mehrafshan for their encouragement and friendship.

I finally would like to show my deepest gratefulness to my family, my father Ali, my mother Jila, my brother Saied and my sister Farnaz. They witnessed my happiness and my struggle through the years. It was them who have always shown their confidence on me. I thank them for bearing my absence for the many years while I was pursuing my PhD. I would like to dedicate this thesis to them.

Statement of Authentication

The work presented in this thesis is, to the best of my knowledge and belief, original except as acknowledged in the text. I hereby declare that I have not submitted this material, either in full or in part, for a degree at this or any other institution.

Saber Taghavipour
……………………………………………

30 October 2017
……………………………………………

Table of contacts

Table of contacts i

List of figures v

List of tables xii

List of abbreviations xiii

Abstract xv

Chapter 1 : Introduction 1

1.1 Overview 1

1.2 Research Objectives 2

1.3 Publications 3

1.4 Thesis Outlines 4

Chapter 2 : Literature Review 7

2.1 Introduction 7

2.2 Concrete materials and structures 7

2.2.1 Characterisation of concrete structures (property, damages, etc.) 12

2.2.2 Concrete structure crack classifications 18

2.2.3 Sensory techniques for concrete assessment 26

2.3 Concrete structure health monitoring using piezoceramic transducers 31

2.3.1 Detection and monitoring of cracks in concrete structures 38

2.4 Smart aggregates material, setup, and arrangement 43

2.5 Summary 49

Chapter 3 : Smart Aggregate Based Nondestructive Testing Systems 51

3.1 Introduction 51

3.2 Measurement and data processing.. 51

3.2.1 Data analysis approach.. 55

3.2.2 Measurement error analysis 57

3.3 Specimens and arrangement of SAs 60

3.3.1 Embedded SA transducers 61

3.3.2 Embedded and mounted SAs 65

3.3.3 Mounted SAs... 68

3.4 Boundary condition effect on wave propagation in specimen 71

3.5 Summary 73

Chapter 4 : Early-Age Concrete Hydration Characterization Using Embedded Smart Aggregates 76

4.1 Introduction 76

4.2 Concrete mixture and relevant general tests... 77

4.2.1 Concrete mix design.. 77

4.2.2 Slump test... 79

4.2.3 Determination of compressive strength 81

4.3 SA arrangement, testing with water and concrete specimens preparation 83

4.3.1 SA arrangement and testing with water 83

4.3.2 Concrete specimens preparation 86

4.4 Results and discussions 88

4.4.1 Hydration process monitoring.. 88

4.4.2 Effect of change of distances between transducers on early-age concrete hydration monitoring.. 102

4.5 Summary 104

Chapter 5 : Detection and Monitoring of Crack in Concrete Beams under Bending Using Mounted Smart Aggregates 106

5.1 Introduction 106

5.2 Concrete beam preparation and loading setup 107

5.3 Sensor arrangement and setup.. 112

5.4 Results and discussions 114

5.5 Summary 139

Chapter 6 : Detection and Monitoring of Crack on RC Beams under 4-point Bending Load Using Mounted Smart Aggregates... 141

6.1 Introduction 141

6.2 Reinforced concrete beams and loading setup 141

6.3 Sensor arrangement and setup.. 146

6.4 Results and discussions 149

6.4.1 Signal processing data analysis.. 149

6.4.2 Verification of signal processing data... 177

6.5 Summary 187

Chapter 7 : Detection and Monitoring of Crack on RC Composite Slab under Cyclic Load Using Mounted Smart Aggregates 189

7.1 Introduction 189

7.2 Specimen preparation and loading setup 190

7.3 Sensor arrangement and measurement setup 195

7.4 Results and discussion 197

7.4.1 Signal processing data analysis 198

7.4.1 Verification of signal processing data 205

7.5 Summary 208

Chapter 8 : Conclusion and Future Work 210

8.1 Conclusion 210

8.2 Future work 212

References 214

Appendix A 223

Appendix B 226

List of figures

Figure 2-1: Crack classification chart a) before and b) after concrete hardening (Gilbert and Ranzi, 2010)........ 21

Figure 2-2: Structural cracks in a reinforced concrete beam and tension members (Gilbert and Ranzi, 2010)........ 24

Figure 2-3: Flexural cracks at overload in a RC beam with ductile reinforcement (Gilbert and Ranzi, 2010)........ 25

Figure 2-4: Piezoelectric coupling coefficients (Gu, 2007)........ 33

Figure 2-5: Schematic of stress wave propagate through cracks a) stress wave propagating parallel to the crack and b) stress wave propagating perpendicular to the crack (Feng et al., 2015)........ 43

Figure 2-6: A Smart Aggregate with a connector and its structure (Feng et al., 2015)........ 44

Figure 2-7: Sensor arrangement for a) three-points bending test, one emitter (actuator) and one receiver and b) pull-out test, two receivers and one emitter (Dumoulin et al., 2014)........ 46

Figure 2-8: Notch added to bottom of beam to ensure the crack initiation started from the notch (Dumoulin et al., 2015)........ 47

Figure 2-9: Schematic of embedded Smart Aggregate and mounted piezoceramic patches for a) RC beam and b) concrete-encased composite structure (Zhao et al., 2016, Liang et al., 2016)........ 48

Figure 3-1: Fabricated SA with cable and BNC connector........ 52

Figure 3-2: SA-based measurement system........ 53

Figure 3-3: A view of multi-channel program on LabVIEW software...................... 54

Figure 3-4: View of LabVIEW software with a run on TDMS file........................... 55

Figure 3-5: Frequency-domain received signal 56

Figure 3-6: Schematic of the embedded SAs setup and its received signal in time-domain for a) material characterisation and b) detection and evaluation of defect ... 62

Figure 3-7: Picture showing calibration of SAs using the proposed SA-loaded approach 63

Figure 3-8: Schematic position of specimens and embedded SAs 64

Figure 3-9: Specimen of (a) schematic with a gird and measurement points and (b) picture of the specimen tested by an external SA with a load............................. 66

Figure 3-10: Variation of peak of PSD for different points on surface of specimen. 67

Figure 3-11: Concrete specimens with mounted SAs... 69

Figure 3-12: Concrete specimen with crack and SAs 70

Figure 3-13: Schematic of SAs location on surface of concrete specimen................ 70

Figure 3-14: Specimen with (a) polywood sheet and (b) metal plate. 72

Figure 4-1: Slump test (a) equipment and (b) measurement approach used in this investigation. 81

Figure 4-2: Cylindrical specimens made for 7- and 28-day compressive strength test. 82

Figure 4-3: Compressive strength hydraulic machine testing cylindrical concrete specimen: (a) before and (b) after test... 83

Figure 4-4: SAs position inside the mould with different level of water.................. 84

Figure 4-5: Results of SAs with different level of water for (a) time-domain and (b) frequency-domain... 85

Figure 4-6: Concrete moulds with SAs: (a) before and (b) after casting.................. 87

Figure 4-7: Received time-domain signals from the embedded sensor every 5 hours after casting for SC2 specimen with 50 mm distance. 90

Figure 4-8: Power Spectral Density (PSD) of from the embedded sensor every 5 hours after casting for SC2 specimen with 50 mm distance. 92

Figure 4-9: Resonant frequencies of all specimens versus hours for (a) 50 mm, (b) 100 mm and (c) 150 mm distance. 94

Figure 4-10: Peak of PSDs of received signal at the distances of a) 50 mm b) 100 mm and c) 150 mm during first 20 hours. 95

Figure 4-11: Peak of PSDs of received signal versus times at the distances of a) 50 mm b) 100 mm and c) 150 mm during first 8 days... 96

Figure 4-12: Total power received of received signal at the distances of a) 50 mm b) 100 mm and c) 150 mm during first 20 hours. 99

Figure 4-13: Total power received of received signal at the distances of a) 50 mm b) 100 mm and c) 150 mm during first 8 days...................................... 100

Figure 4-14: Peak of PSDs of received signal versus times for a) 0.45 b) 0.50 and c) 0.55 w/c ratio in first 20 hours. 103

Figure 5-1: a) Slump test before casting and b) concrete cylinders after casting 108

Figure 5-2: Concrete beam casting and preparation 109

Figure 5-3: Instron universal test machine. 110

Figure 5-4: Software setup for Instron machine 111

Figure 5-5: Locations of a through crack, an actuator, and sensors at the specimen under a 3-point bending test 112

Figure 5-6: Schematic of SA transducers mounted on the concrete beam under test 113

Figure 5-7: Strain gauge location at the bottom of a concrete beam 114

Figure 5-8: Cylindrical concrete specimen: (a) before and (b) after the test 115

Figure 5-9: Average compressive strengths of the concrete cylinder specimens recorded 7, 14, 28, 56 and 92 days after casting 116

Figure 5-10: Time-domain signals received by the tension sensor (S_T) every 5 minutes after loading commenced 118

Figure 5-11: Power spectral density (PSD) for the tension sensor (S_T) every 5 minutes after loading commenced 121

Figure 5-12: Peak of PSD for (a) S_T sensor at the tension side and (b) S_C sensor at the compression side of concrete beam SB22 123

Figure 5-13: Total received power for (a) S_T sensor at the tension side and (b) S_C sensor at the compression side of concrete beam SB22 124

Figure 5-14: Peak of PSD for (a) S_T sensor at the tension side and (b) S_C sensor at the compression side of concrete beam SB16 125

Figure 5-15: Total received power for (a) S_T sensor at the tension side and (b) S_C sensor at the compression side of concrete beam SB16 126

Figure 5-16: Peak of PSD for (a) S_T sensor at the tension side and (b) S_C sensor at the compression side of concrete beam SB03 127

Figure 5-17: Total received power for (a) S_T sensor at the tension side and (b) S_C sensor at the compression side of concrete beam SB03 128

Figure 5-18: a) Peak of PSD results obtained from ten concrete beams after normalization and b) their standard deviation 130

Figure 5-19: a) Total received power results obtained from 10 concrete beams after normalisation and b) their standard deviation 131

Figure 5-20: Results for (a) loading history recorded by a load cell and (b) a strain gauge result at mid-span of concrete beam SB22 133

Figure 5-21: Results for (a) loading history recorded by a load cell and (b) a strain gauge result at mid-span of concrete beam SB16 134

Figure 5-22: Results for (a) loading history recorded by a load cell and (b) a strain gauge result at mid-span of concrete beam SB03 135

Figure 5-23: The damage index values for concrete beam a) SB22, b) SB16 and c) SB03 139

Figure 6-1: Schematic of rebar arrangement cross-sectional view 143

Figure 6-2: RC beams specimens (a) before and (b) after casting 144

Figure 6-3: 4-Point test frame used in this study 145

Figure 6-4: Rubber sheets used to prevent vibration 146

Figure 6-5: Schematic of SA transducers on the specimen under test 147

Figure 6-6: Strain gauges and LVDT location at the bottom of specimen 148

Figure 6-7: Power spectral density (PSD) for the sensor (S_T), measured every 5 minutes, after loading commenced, for the duration of 60 minutes........................ 153

Figure 6-8: Power spectral density (PSD) for the sensor (S_C) measured every 5 minutes, after commencing loading, for the duration of 60 minutes 158

Figure 6-9: Different stage of loading which caused a) tension cracks and b) tension and compression cracks.. 160

Figure 6-10: Peak of PSD vs time for (a) S_T sensor at the tension side and (b) S_C sensor at the compression side of RC beam LB01 161

Figure 6-11: Total received power vs time for (a) S_T sensor at the tension side and (b) S_C sensor at the compression side of RC beam LB01 162

Figure 6-12: Peak of PSD vs time for (a) S_T sensor at the tension side and (b) S_C sensor at the compression side of RC beam LB02 163

Figure 6-13: Total received power vs time for (a) S_T sensor at the tension side and (b) S_C sensor at the compression side of RC beam LB02 164

Figure 6-14: Peak of PSD vs time for (a) S_T sensor at the tension side and (b) S_C sensor at the compression side of RC beam LB03 165

Figure 6-15: Total received power vs time for (a) S_T sensor at the tension side and (b) S_C sensor at the compression side of RC beam LB03 166

Figure 6-16: Peak of PSD vs time for (a) S_T sensor at the tension side and (b) S_C sensor at the compression side of RC beam LB04 167

Figure 6-17: Total received power vs time for (a) S_T sensor at the tension side and (b) S_C sensor at the compression side of RC beam LB04 168

Figure 6-18: Peak of PSD results obtained from four RC beams after a) normalisation and b) standard deviation 171

Figure 6-19: Total received power results obtained from four RC beams after a) normalisation and b) standard deviation 172

Figure 6-20: Damage index value for RC beam specimens a) LB01, b) LB02, c) LB03 and d) LB04 176

Figure 6-21: The loading history recorded by load cell for specimens a) LB01, b) LB02, c) LB03 and d) LB04 180

Figure 6-22: Results of LVTD installed at the bottom of specimens a) LB01, b) LB02, c) LB03 and d) LB04 183

Figure 6-23: Results of five strain gauges attached at the bottom of RC beam specimens a) LB01, b) LB02, c) LB03 and d) LB04 185

Figure 6-24: The location of cracks and bonded strain gauges in bottom of RC beam 187

Figure 7-1: Configuration of the specimen (units: mm) (Li et al., 2017) 192

Figure 7-2: Details of the steel tube (units: mm) (Li et al., 2017) 193

Figure 7-3: Schematic of test setup (units: mm) 194

Figure 7-4: Cyclic loading protocol 195

Figure 7-5: Schematic of the specimen, measurement setup, and its output signal in time-domain 197

Figure 7-6: Top view of RC slab with SAs and demountable mechanical strain gauge 197

Figure 7-7: Power spectral density (PSD) for sensor 1 measured every 30 minutes after loading commenced 200

Figure 7-8: Cracking area when the RC slab is under (a) tension and (b) compression 202

Figure 7-9: Peak of PSD vs time for (a) sensor 1 and (b) sensor 2 203

Figure 7-10: Total received power vs time for (a) sensor 1 and (b) sensor 2 204

Figure 7-11: Setup of instrumentation LVDTs, LPs and inclinometers (units: mm) (Li et al., 2017). 206

Figure 7-12: M-θ Hysteretic curves of specimen (Li et al., 2017) 206

Figure 7-13: Displacement monitoring results using demountable mechanical strain gauge 208

List of tables

Table 2-1: The elastic modulus for in-situ concrete, Ec 15

Table 2-2: Increase in elastic modulus with age of concrete $t - Ec\ t/Ec(28)$ 16

Table 3-1: Results of calibration of SAs using the constant load 63

Table 3-2: Measurement results of specimens with gap 65

Table 3-3: Results of specimens with external SA 67

Table 3-4: Results of specimens with gap 69

Table 3-5: Results of specimens with and without crack 71

Table 3-6: Results for specimens with 50-mm distance between SAs 72

Table 3-7: Results of specimens with 100-mm distance between SAs 73

Table 3-8: Results of specimens with 150-mm distance between SAs 73

Table 4-1: Material Properties used in concrete mixture 78

Table 4-2: Concrete mixing design for 1m^3 79

Table 4-3: Characterisation of SAs inside the water at 50 mm distance 85

Table 4-4: Characterisation of SAs inside the water at 100 mm distances 86

Table 4-5: Characterisation of SAs inside the water at 150 mm distances 86

Table 4-6: The results of slump test 88

Table 4-7: Compressive strength test results 102

Table 5-1: Properties of materials used in concrete mixture 107

Table 5-2: Material compressive strength test results 115

Table 5-3: Damage index values vs. time for concrete beam SB22, SB16, and SB03 137

Table 6-1: Longitudinal Rebar Arrangement 143

Table 6-2: Damage index values calculated at different time of loading 174

List of abbreviations

AC	Actuator
ADS	Active Sensing Diagnostic
AE	Acoustic Emission
AFC	Active Fibre Composite
APA	Amplified Piezoelectric Actuators
BNC	Bayonet Neill-Concelman
CFST	Concrete-Filled Steel Tubular
CJP	Complete Joint Penetration
DAQ	Data Acquisition
DSP	Digital Signal Processing
EMI	Electromechanical Impedance
HDT	Horizontal Differential Transducers
LP	Liner Potentiometer
LVTD	Linear Variable Differential Transformer
MLA	Multi-Layer Piezoelectric Actuators
NDE	Non-Destructive Evaluation

NDT	Non-Destructive Testing
PC	Personal Computer
PSD	Power Spectrum Density
PZT	Lead Zirconate Titanate
RBS	Reduced Beam Section
RC	Reinforced Concrete
RMSD	Root-Mean-Square Deviation
SA	Smart Aggregate
SD	Standard Deviation
SE	Sensor
TDMS	Technical Data Management Streaming
UPV	Ultrasonic Pulse Velocity
UT	Ultrasonic Testing
VDT	Vertical Differential Transducers

Abstract

Non-destructive testing (NDT) of concrete members has been widely used for characterisation of material and assessment of functional structures without impairing their functions and performances. This thesis focuses on addressing critical challenges related to the practical implementation of NDT techniques based on wave-propagation approaches for characterisation of concrete members used in civil infrastructures. Specially, this research aims to achieve three interdependent objectives related to developing NDT techniques with piezoceramic-based transducers: monitoring of very early-age concrete hydration process, detection, and monitoring of cracking in concrete members of different complexity under loading. The concept of piezoceramic-based Smart Aggregate (SA) transducers is central to this research. Embedded SA transducers with an active sensing method have shown great potential for characterisation of construction materials such as concrete and concrete-steel composites. Based on the developed SA based approaches, an active-sensing approach with appropriate arrangement of SAs in and on concrete members, and analysis of the received signal using the power spectral density, total received power and damage indexes is developed and applied in this thesis. To confirm its applicability for characterisation of very early-age concrete, a systematic investigation is performed into concrete specimens with different values of water-to-cement ratio due to slightly different initial water amounts, and different separation distances between the embedded SAs. For the detection and monitoring of cracking in concrete members under loading the mounted SA based approach is proposed and applied. It is shown that NDT systems, based on this approach, provide detection and monitoring of cracking in a variety of concrete members under loading, including

relatively simple concrete beams and reinforced concrete beams under bending, and reinforced concrete slab as a part of a complex composite member under cyclic loading. Comparisons are provided between the proposed system and conventional load cell and strain gauge systems with each tested member.

Chapter 1 : Introduction

1.1 Overview

Defects and damage can be present or introduced inside materials or functional structures during fabrication and/or service due to various effects including loading and environmental exposure. Non-destructive testing (NDT) methods have been widely used to detect, evaluate and monitor these defects and damages without impairing function and performance of the materials and structures.

During hydration process in concrete, in the presence of water, various compounds in cement particles would hydrate to form new compounds which build up the infrastructure of hardened cement paste in concrete. The hardening process of concrete or other cement-based materials is considered to be the most critical time period during the life of a structure. It is important to have reliable information about the early age properties of the materials. In addition to cracks, many factors, such as earthquakes, climatic, chemical, or accidental, will cause damage of hardened concrete. It is imperative to quickly assess the severity of the damage and health status of a structure, especially for an infrastructure, in real time or near-real time after such an event to provide vital information for decision-makers. It is desirable to have a reliable NDT system to perform damage and defect detection, and health monitoring of materials and structures.

With the rapid development of modern data processing methods and improvement on signal analysis technique, piezoelectric-based transducers had become a weak link of the NDT technique chain. Most of the transducer utilised is designed as outside-mounted components attached on the surface of concrete materials. The compatibility between the piezoelectric sensor and concrete material turn out to be a critical issue in NDT technique. A good compatibility on acoustic properties and mechanical properties can ensure the accurate and reliable monitoring results. Li et al (2002) developed a brand new embedded Smart Aggregate (SA) piezoelectric composite that owns an acoustic impedance value quite close to that of the concrete matrix, which ensures a minimum signal distortion and maximum signal energy transmission efficiency. Based on SA piezoelectric composite, assorted new monitoring systems need to be designed and developed to match the characteristic of introduced composite. New systems shall be geared to the needs of practical testing instead of merely laboratory usage. Apart from monitoring system design, various suitable evaluation methods may be continually proposed to comprehensively study the fracture process and the hydration process of early-age and hardened concrete.

1.2 Research Objectives

The main aim of this research is to address critical challenges related to the practical implementation of NDT techniques based on a SA active sensing approach for characterization of concrete members used in civil infrastructures. The objectives of this research are as follows:

1. To develop NDT techniques with piezoceramic-based SA transducers for characterisation of concrete members at different stages of their life. It should use stress wave propagation characteristics, appropriate arrangement of SAs in and on concrete members, and analysis of the received signal using the power spectral density, total received power and damage indexes.

2. To perform a systematic investigation into early-age and hardened concrete specimens with different values of water-to-cement ratio due to slightly different initial water amounts, and different separation distances between the embedded SAs.
3. To develop and apply a mounted SA based approach for detection and monitoring of cracking in concrete members under loading using propagation characteristics of stress waves in the members.
4. To perform an experimental investigation into concrete and reinforced concrete beams under bending for detection and monitoring of cracks in these beams using the proposed system with mounted SA based approach and conventional load cell and strain gauge measurement systems.
5. To monitor the development of cracking in a concrete-steel composite structure with connectors and reinforced concrete slab under cyclic loading using the proposed system with mounted SA based approach and conventional load cell and strain gauge measurement systems.

1.3 Publications

1. TAGHAVIPOUR, S., CHUNG, K., KHARKOVSKY, S., KONG, Q. & SONG, G. "Characterization of cement concrete specimens during hydration process with piezoelectric-based smart aggregates". *Proceedings of the 11th European Conference on Non-Destructive Testing (ECNDT 2014)*, 6 pages, October 6-10, 2014, Prague, Czech Republic, 2014.

2. TAGHAVIPOUR, S., KHARKOVSKY, S., KANG, W-H., SAMALI, B. & MIRZA, O. 2017 "Detection and monitoring of flexural cracks in reinforced concrete

beams using mounted Smart Aggregate transducers," *Smart Materials and Structures,* 26**,** 104009.

3. NOORI HOSHYAR, A., KHARKOVSKY, S., TAGHAVIPOUR, S. & SAMALI, B. "Structural damage detection of concrete based on the autoregressive all-pole model parameters and artificial intelligence techniques". *The 5th International Conference on Civil and Environmental Engineering (I2C2E)*, Auckland, New Zealand.

4. TAGHAVIPOUR, S., KHARKOVSKY, S., KANG, W-H., SAMALI, B. & MIRZA, O. "Detection and monitoring of crack in concrete beams under bending using mounted smart aggregates," *Smart Materials and Structures* (under review).

5. TAGHAVIPOUR, S., KHARKOVSKY, S., KANG, W-H., SAMALI, B., LI, R. & MIRZA, O. "Detection and monitoring of crack on RC composite slab under cyclic load using mounted smart aggregates," *Smart Materials and Structures* (under review).

1.4 Thesis Outlines

The other chapters are as follows:

Chapter 2 provides literature review of state-of-the-art in characterization of concrete materials and members at different stages of their life. It also emphasizes challenges which are still existed in this area. Background of sensory techniques with piezoelectric-based SA transducers is also provided.

Chapter 3 presents developing NDT techniques with piezoceramic-based transducers. Based on the developed SA based approaches, an active-sensing approach with appropriate arrangement of SAs in and on concrete members, and analysis of the received signal using the power spectral density, total received power and damage indexes is developed in this chapter. Three arrangements of SA are applied for detection of cracks in concrete specimens and mapping of stress wave field distribution in the surface of concrete.

Chapter 4 presents an early-age concrete characterization using embedded SAs. Concrete specimens are tested with different values of w/c ratio and separation distances during first 8 days. The emphasis is made on the received signal in very early aged concrete using its power spectral density (PSD) and total received power.

Chapter 5 presents the detection and monitoring of crack on concrete beams under bending load using the proposed mounted SA based approach. Concrete beam preparation, loading setup and sensor arrangement used in this experimental study is described. The received signal characteristics are monitoring during loading and the detection of cracks is performed using PSD, total received power and damage index as well as loading history and the results of measurement by strain gauges.

Chapter 6 presents detection and monitoring of crack in large-scale reinforced concrete (RC) beams under bending load using the proposed mounted SA based approach, load cell and strain gauges. In this case these measurements techniques allow monitoring of cracks development and the advantages of the proposed approach are highlighted.

Chapter 7 presents detection and monitoring of crack in a relatively complex concrete-steel composite under cyclic loading. Experiments are performed on the composite member under cyclic load with SAs mounted on its RC slab to detect load-induced cracks. The measurements with a mechanical strain gauge are also conducted.

Chapter 8 provides concluding remarks of the thesis and some suggestions for future works.

Chapter 2 : Literature Review

2.1 Introduction

Concrete is one of the most widely used construction materials in infrastructure all over the world. Evaluation of concrete quality is a crucial task for engineers, as possible disastrous failure or malfunction of civil infrastructure can lead to human fatalities, as well as high financial costs. The field of structural health monitoring has been pursuing new-sensing technologies for monitoring short and long-term performance, and assessing the health condition of critical infrastructure systems.

This chapter consists of three main sections. The first section provides the general description of concrete materials and structures, including their characterisation based on the Australian standard. Different types of cracks are introduced, that occur in concrete materials and structures before and after hardening. The background of sensory techniques for concrete assessment is also presented. The second section provides a background of concrete structure health monitoring, using piezoceramic transducers, including early age characterisation and detection and monitoring of cracks. The final section presents the latest experimental investigations of piezoceramic transducers (smart aggregates) on concrete materials and structures.

2.2 Concrete materials and structures

Concrete is used in nearly every type of construction. Traditionally, concrete was primarily composed of cement, water, and aggregates (including both coarse and fine aggregates). Although aggregates make up the bulk of the mix, it is the hardened cement paste that binds the aggregates together and contributes to the strength of concrete, with the aggregates serving largely as low-cost fillers (though their strength is also important). Concrete is not a homogeneous material, and its strength and structural properties may vary greatly depending upon its ingredients and the method in which it is manufactured. However, concrete is normally treated in design as a homogeneous material. Steel reinforcements are often included to increase the tensile strength of concrete; such concrete is called reinforced cement concrete (RCC) or simply, reinforced concrete (RC).

RC has been used in a variety of applications, such as buildings, bridges, roads and pavements, dams, retaining walls, tunnels, arches, domes, shells, tanks, pipes, chimneys, cooling towers, and poles, because of the following advantages (Williams, 2003):

Moulds to any shape: It can be poured and moulded into any shape varying from simple slabs, beams, and columns to complicated shells and domes, by using formwork.

Availability of materials: The materials required for concrete (sand, gravel, and water) are often locally available and are relatively inexpensive. Only small amounts of cement (about 14% by weight) and reinforcing steel (about 2–4% by volume) are required for the production of RC, which may have to be shipped from other parts of the country.

Water and fire resistance: RC offers great resistance to fire and water. A concrete member, with sufficient cover, can have a rating of one to three hours of fire resistance without any special fire proofing material.

Good rigidity: RC members are very rigid due to their increased stiffness and mass.

Compressive strength: Concrete has considerable compressive strength compared to most other materials.

Economical: It is economical, especially for footings, basement walls, and slabs.

Low-skilled labour: A comparatively lower grade of skilled labour is required for the fabrication, erection, and construction of concrete structures.

In order to use concrete efficiently, the designer should also know the weakness of the material. The disadvantages of concrete include the following:

Low tensile strength: Concrete has a very low tensile strength, which is about one-tenth of its compressive strength, and hence cracks when subjected to tensile stresses. Reinforcements are, therefore, often provided in the tension zones to carry tensile forces and to limit crack widths. If proper care is not taken in the design and detailing, and also during construction, wide cracks may occur, which will subsequently lead to the corrosion of reinforcement bars and even failure of structures.

Time-dependent volume changes: Concrete that undergoes drying shrinkage, if restrained, will result in cracking or defection. Moreover, defections will tend to increase with time, due to creep of the concrete under sustained loads (the defection may possibly double, especially in cantilevers).

Variable properties: The properties of concrete may widely vary due to variation in its proportioning, mixing, and curing. Water plays an important role in the workability, strength, and durability of concrete, and could change the concrete properties significantly. Since cast in situ concrete is site-controlled, its quality may not be uniform when compared to materials such as structural steel and laminated wood, which are produced in the factory.

The art of structural design is manifested in the selection of the most suitable structural system for a given structure. The arrangement of beams and columns to support the vertical (gravity) loads, and the selection of a suitable structural system to resist the horizontal (lateral) loads, pose a great challenge to structural engineers, as these factors determine the economy and functional suitability of the building (Subramanian, 2014, Williams, 2003, Whittle, 2012).

An RC structure consists of different structural elements, and may also contain non-structural elements, such as partitions and false ceilings. The function of any structure is to resist the applied loads (e.g. gravitational, dead and imposed loads, lateral, wind, and earthquake) effectively and to transmit the resulting forces to the supporting ground without differential settlement. At the same time, the structure should satisfy adequate safety (strength, stability, and structural integrity), adequate serviceability (stiffness, durability, etc.), economy (cost of construction and maintenance), durability, aesthetics, environment friendliness, functional requirements, and adequate ductility (Subramanian, 2014).

Safety requirements are paramount to any structure and require that the collapse of the structure (partial or total) is acceptably low, not only under the normal expected loads (service loads), but also under less-frequent loads (such as earthquakes or extreme wind) and accidental loads (blast, impact, etc.). The collapse of a structure due to various possibilities should be prevented, such as exceeding the load-bearing capacity, overturning, sliding, buckling, and fatigue fracture. Another related aspect of safety is structural integrity and stability. Concrete structures can be considered as braced frames, with bracing in the form of shear walls, stairwells, or elevator shafts that are considerably stiffer than columns. The structure, as a whole, should be stable under all conditions. Even if a portion of the structure is affected or collapses, the remaining parts of the structure should be able to redistribute the loads.

In most developed countries, approximately 40–50% of construction industry expenditure is spent on repair, maintenance, and remediation of existing structures. The growing number of deteriorating concrete structures not only affects the productivity of the society, but also has a great impact on our resources, environment, and human safety. It has now been realised that the reason for the deterioration of concrete structures is the emphasis placed on mechanical properties and structural capacity, while construction quality and life cycle management has been neglected (ACI201.2R-08, 2008). Strength and durability are known as two separate aspects of RC structures; neither guarantees the other.

Serviceability requirements are related to the utility of the structure, and mean that the structure should satisfactorily perform under service loads, without discomfort to the user, due to excessive defection, cracking, vibration etc. Serviceability is measured by considering the scale of defection, cracking, and vibration of structures, as well as considering durability (amounts of surface deterioration of concrete and corrosion of reinforced steel) (Ebrahimpour and Sack, 2005, Pozos-Estrada et al., 2010).

There has been a continuous increase in the strength of concrete over the last hundred years; much of the increase has developed since 1980. Around the 1980s, the value of blended cements and the use of admixtures were realised. Modern concretes have become complex, with almost infinite variations available to meet a multitude of requirements. The knowledge bank of how to change the properties of concrete and reinforcement is developing rapidly. Furthermore, the concrete safety factor has increased during the 20th century (Bungey et al., 2006, Bentz et al., 2006).

For many structural elements, the serviceability limit state is becoming more critical than the ultimate limit state, due to the increase in concrete strength and reduction in overall factor of safety.

2.2.1 Characterisation of concrete structures (property, damages, etc.)

To adequately predict deflections and crack widths in designs for serviceability, methods of analysis are required that realistically account for cracking and time-dependent deformations caused by creep and shrinkage of the concrete and so too are appropriate material modelling rules. The properties and deformation characteristics of concrete that are most often required in serviceability calculations are the tensile strength, elastic modulus, creep coefficient and shrinkage strain. The elastic modulus is needed in the analysis of structures to estimate the stiffness of each member and to determine the internal actions; it is also required to estimate the instantaneous deformations caused by internal actions and the stresses induced by imposed deformations. The tensile strength of concrete is required to determine the extent of cracking due to both applied load and applied deformation. The creep coefficient associated with a particular time period and a particular loading regime is needed to estimate the time-dependent deformation of the structure, and the magnitude and rate of shrinkage strain is required to predict the development of load-independent deformations over time and the onset of time-dependent cracking (Gilbert and Ranzi, 2010, Plevris and Triantafillou, 1994, Zhou, 1992).

The strength of concrete is usually specified in terms of the lower characteristic compressive cylinder (or cube) strength at 28 days ($f_c^{'}$). This is the value of compressive strength exceeded by 95% of all standard cylinders or cubes tested 28 days after being cured under standard laboratory conditions. The mean compressive strength of the sample cylinders or cubes at 28 days (f_{cm}) is about 25% higher than the characteristic strength when $f_c^{'} = 20\ MPa$, reducing to about 10% higher than the characteristic strength when $f_c^{'} = 100\ MPa$. The in-situ strength of concrete (i.e. the strength of the concrete in the structure on site) is often taken to be about 90% of the cylinder strength (AS3600, 2009).

The tensile strength, f_{ct}, is defined here as the maximum stress that the concrete can withstand when subjected to uniaxial tension. Direct uniaxial tensile tests are difficult to perform and tensile strength is usually measured from either flexural tests on prisms or indirect splitting tests on cylinders. In flexure, the apparent tensile stress at the extreme tensile fibre of the critical cross-section under the peak load is calculated assuming linear elastic behaviour, and taken to be the flexural tensile strength (or modulus of rupture), $f_{ct.f}$. The flexural tensile strength $f_{ct.f}$ is significantly higher than f_{ct} due to the strain gradient and the post-peak unloading portion of the stress-strain curve for concrete in tension. Typically, f_{ct} is about 50-60% of $f_{ct.f}$. The indirect tensile strength, measured from a split cylinder test, is also higher than f_{ct} (usually by about 10%) due to the confining effect of the bearing plate in the standard test. For design purposes, the lower characteristic flexural tensile strength, $f'_{ct.f}$, and the lower characteristic uniaxial tensile stress, f'_{ct}, may be taken as:

$$f'_{ct.f} = 0.6\sqrt{f'_c} \quad (2\text{-}1)$$

and

$$f'_{ct} = 0.36\sqrt{f'_c} \quad (2\text{-}2)$$

The mean and upper characteristic values may be estimated by multiplying the lower characteristic values by 1.4 and 1.8, respectively (AS3600, 2009). In serviceability calculations, mean values of tensile strength should be used, rather than characteristic values in most situations.

The value of the elastic modulus, E_c, increases with time as the concrete gains strength and stiffness. It is common practice to assume that E_c is constant with time, and equal to its value calculated at the time of first loading. A numerical estimate of the in-situ elastic modulus may be made from the following formulas, for stress levels less than about 0.4 f_{cm} for normal strength concrete ($f'_c \leq 50\ MPa$) and about $0.6f_{cm}$ for high strength concrete ($50 < f'_c \leq 100\ MPa$), and for stresses applied over a relatively short period (say up to 5 minutes):

For $f_{cmi} \leq 40\ MPa$:

$$E_c = \rho^{1.5} 0.043\sqrt{f_{cmi}} \text{ (in MPa)} \quad (2\text{-}3)$$

For $40 < f_{cmi} \leq 100\ MPa$:

$$E_c = \rho^{1.5}\left[0.024\sqrt{f_{cmi}} + 0.12\right] \text{ (in MPa)} \quad (2\text{-}4)$$

where ρ is the density of the concrete in kg/m^3 (not less than 2400 kg/m^3 for normal weight concrete), and f_{cmi} is the mean in-situ compressive strength in MPa at the time of first loading. Equation 2-3 was originally proposed by Pauw (Adrian). Values for E_c obtained using equation 2-3 and 2-4 for in-situ normal weight concrete ($\rho = 2400kg/m^3$) aged 28 days for different values of $f_c^{'}$ are given in Table 2-1. The mean in-situ strength compressive strength, f_{cmi}, in Table 2.1 is taken to be 90% of the standard mean cylinder strength, and for 100 MPa concrete is actually smaller than the characteristic cylinder strength, $f_c^{'}$.

Table 2-1: The elastic modulus for in-situ concrete, E_c

$\boldsymbol{f_c^{'}}$ **(MPa)**	20	25	32	40	50	65	80	100
$\boldsymbol{f_{cmi}}$ **(MPa)**	22.5	27.9	35.4	43.7	53.7	68.2	81.9	99.0
$\boldsymbol{E_c}$ **(MPa)**	24,000	26,700	30,100	32,750	34,800	37,400	39,650	42,200

For stresses applied over a longer time period, significant increases in deformation occur due to the rapid early development of creep. Yet in a broad sense, loads of one day duration is usually considered to be short-term and the effects of creep are often ignored, which may lead to significant error. If the short-term deformation after 1 day of loading is required, it is suggested that E_c be reduced by about 20% to account for early creep (Gilbert, 1988). Equation 2-5 provides an estimate of the variations of the elastic modulus with time (du béton, 1993):

$$E_c\,(t) = \left(e^{s\left(1-\sqrt{\frac{28}{t}}\right)}\right)^{0.5} E_c(28) \tag{2-5}$$

where the coefficient s is taken as 0.38 for ordinary portland cement, and 0.25 for high early strength cement, and $E_c(28)$ is the 28-day value of the elastic modulus. Eurocode 2 adopts an exponent of 0.3 in equation 2-5 (instead of 0.5) (Institution and Standardization, 2004). Typical variations in E_c with time t are shown in Table 2.2.

Table 2-2: Increase in elastic modulus with age of concrete $t - (E_c\ (t)/E_c(28))$

Cement type	Age of concrete in days (t)					
	3	7	28	90	360	30,000
Ordinary Portland Cement	0.68	0.83	1.0	1.09	1.15	1.20
High Early Strength Cement	0.77	0.88	1.0	1.06	1.09	1.13

Other factors which are considered for concrete serviceability calculations are creep and shrinkage. These limits of concrete depend on the number of factors, including the ambient humidity, the dimensions of the element, the composition, and the age of the concrete at the time of loading.

The creep coefficient at time, t, associated with a constant stress first applied at age, τ, was defined as the ratio of the creep strain at time, t, to the (initial) elastic strain and given the symbol, $\varphi(t, \tau)$. The most accurate way of determining the final creep coefficient is by testing or using results obtained from measurements on similar local concretes. However, testing is often not a practical option for the structural designer. In the absence of long-term test results, the final creep coefficient may be determined by extrapolation from short-term test results, where creep is measured over a relatively short period (28 days) in specimens subjected to constant stress. Various mathematical expressions for the shape of the creep coefficient versus time curve are available, from which long-term values may be predicted from the short-term measurements (Gilbert, 1988, Gilbert and Ranzi, 2010). The longer the period of measurement was, the more accurate the long-term predictions. If testing is not an option, numerous analytical methods are available for predicting the creep coefficient. These predictive methods vary in complexity. Some methods are simple and easy to use and provide a quick and approximate estimate of $\varphi(t,\tau)$; such a method is included in the Australian Standard AS3600-2009 (AS3600, 2009). Some other methods are more complicated and attempt to account for the many parameters that affect the magnitude and rate of development of creep. Unfortunately, an increase in complexity does not necessarily result in an increase in accuracy, and predictions made by some of the more well-known methods differ widely (ACI209, 2008, Bažant and Li, 2008, Bazant and Baweja, 2000).

To estimate the magnitude of shrinkage strain in normal and high strength concrete, a model proposed by Gilbert (Gilbert and Ranzi, 2010) has been presented, and is included in the Australian Standard AS3600-2009. Many other approaches are available in the following literature: (Rebibou et al., 2003, Weiss et al., 1998, Goto, 1971, Beeby, 1978, Husain and Ferguson, 1968, ACi, 2001). The model divides the total shrinkage strain, ε_{sh}, into two components: endogenous shrinkage, ε_{she}, and drying shrinkage, ε_{shd}, as given in equation 2-6.

$$\varepsilon_{sh} = \varepsilon_{she} + \varepsilon_{shd} \tag{2-6}$$

Endogenous shrinkage is taken to be the sum of chemical (or autogenous) shrinkage and thermal shrinkage, and is assumed to develop relatively rapidly and to increase with concrete strength. Drying shrinkage develops more slowly and decreases with concrete strength.

2.2.2 Concrete structure crack classifications

Cracking in reinforced concrete structures is common and normal. In many members, it is inevitable. Cracks occur wherever and whenever the tensile stress in the concrete reaches the tensile strength of the concrete. If care is not taken during construction, cracking can occur in the wet concrete before the concrete sets, due to plastic shrinkage or plastic settlement. After the concrete sets and hardens, tensile stress at any location in the structure may be caused by many different factors, including the applied loads and restraint to deformations caused by early-age heat of hydration, autogenous shrinkage, drying shrinkage, temperature changes, settlement of the supports.

Cracks caused predominantly by the internal actions resulting from applied loads are often termed structural cracks, which include direct tension cracks, bending or flexural cracks, shear cracks, torsion cracks, and bursting cracks. Cracks caused by restraint to load independent deformation are often termed intrinsic cracks, which include deformations due to early-age cooling, shrinkage or ambient temperature changes. Often cracks are initiated by a combination of causes. For example, the bending moment at which cracking occurs in a beam or slab may be significantly reduced if tensile stresses, caused by restraint to early-age temperature contractions and shrinkage acting in the same direction, have developed in the member before loading. Although the shrinkage-induced tensile stresses may not be sufficient to initiate cracking in an unloaded member, they may initiate cracking in the weeks and months after first loading in a lightly loaded member. Shrinkage deformation may also cause significant increases in crack widths with time in a previously cracked member. Defects or cracks that occur when the concrete is in the plastic state may also provide the initiation point for longer term drying shrinkage cracking. The combination of many factors can make the prediction and diagnosis of cracking difficult.

Many of the factors and concrete properties that influence cracking are highly variable, and significantly more variable than those that influence the strength of a reinforced concrete member, and even more variable than those affecting load-induced stresses and strains under typical in-service conditions. The early-age properties of concrete also depend on the temperature and weather conditions at the time the concrete is placed. These factors may not be known at the time the structure is designed, but they may significantly affect the on-set and extent of early-age cracking.

Cracks formed by tensile stresses over the entire cross-section of a member, due to axial tensile forces and/or restrained shrinkage, are direct tension cracks that penetrate completely through a member, although the cracks do taper to the reinforcement. Where bending causes a triangular tensile stress distribution over part of the cross-section, flexural cracks occur at the tensile face when the extreme fibre tensile stress reaches the tensile strength of the concrete. Flexural cracks propagate from the extreme tensile fibre through the tensile zone, and are arrested at or near the neutral axis. Shear and torsion cause inclined or diagonal cracking in the web of a beam. Inclined cracks, caused by shear, penetrate through the web, and torsion cracks tend to spiral around the member. The width of each of these crack types tends to increase with time due to the gradual development of shrinkage.

Many variables influence the width and spacing of both structural and intrinsic cracks, including the degree of restraint to thermal and shrinkage deformations (both internal and external restraint), the magnitude and rate of development of the tensile strength of concrete, the magnitude and duration of the loads, the quantity, orientation and distribution of the reinforcement crossing the crack, the cover to the reinforcement, the slip between the reinforcement and the concrete in the vicinity of the crack (which depends on the bond characteristics of the reinforcement), the deformational properties of the concrete (including its tensile creep and shrinkage characteristics), and the size of the member. Considerable variations exist in the crack width from crack to crack and the spacing between adjacent cracks, largely because of random variations in the properties of concrete.

The various types of cracks that commonly occur in concrete structures are classified in Figure 2-1, where cracking in the plastic concrete in the first few hours after casting, and before the concrete sets, is distinguished from cracking in the hardened concrete.

Cracks in the plastic concrete are classified as either plastic shrinkage cracks, plastic settlement cracks, or formwork or sub-grade movement cracks. These cracks cannot be controlled by reinforcement or the provision of movement joints, but they can be prevented from occurring if appropriate construction practices are adopted.

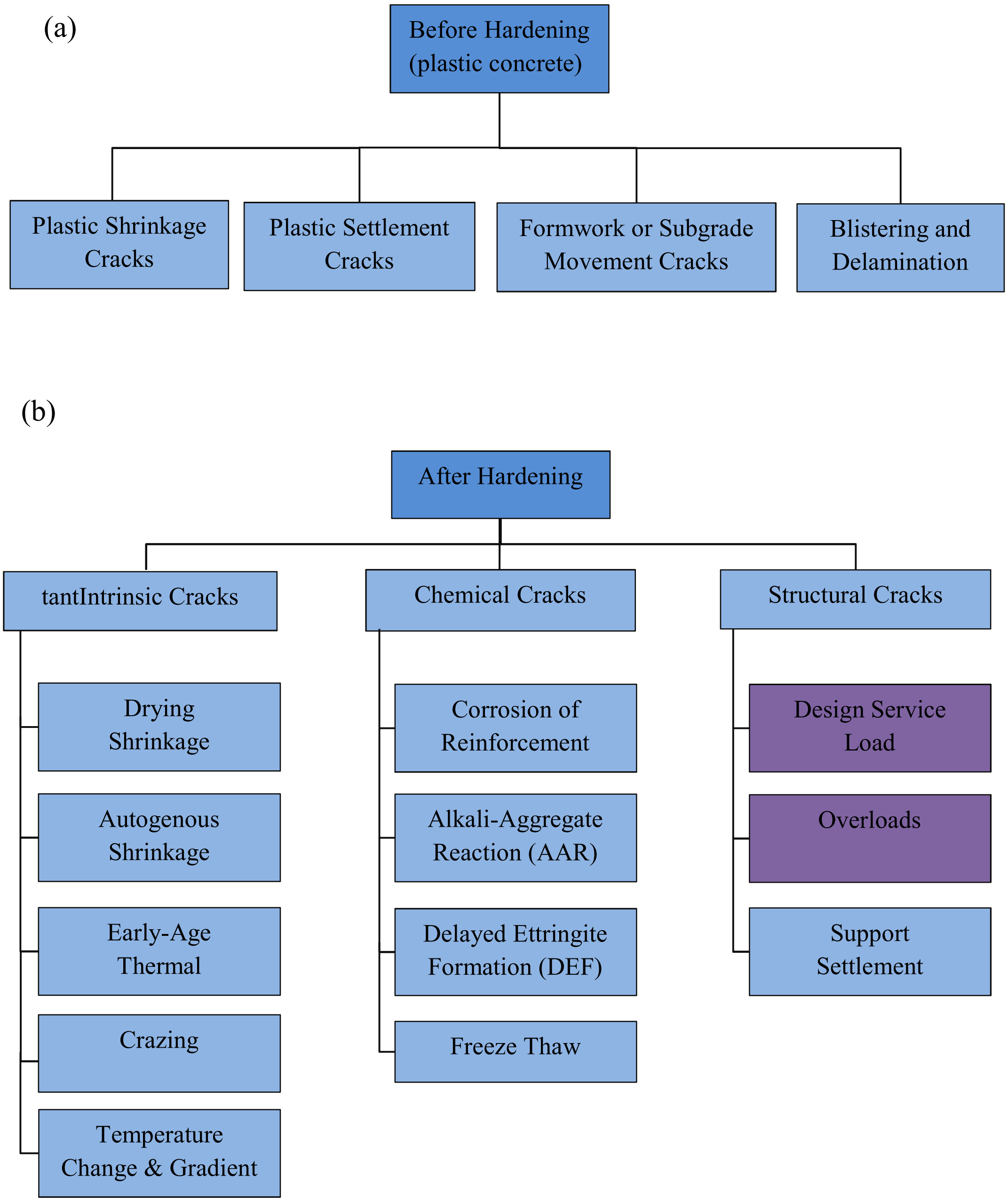

Figure 2-1: Crack classification chart (a) before and (b) after concrete hardening (Gilbert and Ranzi, 2010)

In Figure 2-1 cracks in the hardened concrete are classified as intrinsic, chemical, or structural cracks.

Early-age cooling and subsequent shrinkage of concrete are perhaps the most common causes of cracking in concrete structures. Early thermal cracking is more likely in larger elements where the temperature differentials are large. Thermal effects can aggravate and extend plastic shrinkage and plastic settlement cracking, although this is not usually a significant problem in thin slabs or floors. Crazing is also the result of relatively high surface tensile stresses in immature concrete caused by a very early shrinkage differential through the thickness of a member (Collins and Sanjayan, 2000).

The most common causes of chemical cracking in RC structures are cracks due to corrosion of the reinforcement. Some concretes are prone to cracking caused by a reaction in the presence of water between the alkali in the cement (sodium and potassium) and elements in the aggregate, which is known as alkali-aggregate reaction (Cabrera, 1996). Cracks caused by delayed ettringite formation are the late formation of ettringite and associated expansion that has been observed after heat curing of concrete at too high a temperature (Taylor et al., 2001).

The structural crack is another type of crack which is investigated in this dissertation. When concrete structures are subjected to the applied service loads, cracking may occur. Cracks caused by bending in reinforced concrete beams and slabs (flexural cracks) occur at the tensile face when the extreme fibre tensile stress reaches the tensile strength of the concrete (Torres et al., 2004, Borosnyói and Balázs, 2005, Wolanski, 2004, Padmarajaiah and Ramaswamy, 2002, Hamrat et al., 2016). Flexural cracks propagate from the extreme tensile fibre through the tensile zone and are arrested at or near the neutral axis (as shown in Figure 2-2a). Flexural cracks increase in width as the distance from the tensile reinforcement increases and taper to zero width near the neutral axis. A linear relationship is generally assumed to exist between the crack width at the side or soffit of a member and the distance from the bar. In general, the spacing between flexural cracks is in the range 0.5 to 1.5 times the depth of the member. The spacing of flexural cracks in a one-way slab specimen can be seen in Figure 2-2c. By contrast, direct tension cracks in a tension member are more parallel-sided and extend completely through the member. Direct tension cracks in a reinforced concrete member can be seen in the specimens shown in Figure 2-2d.

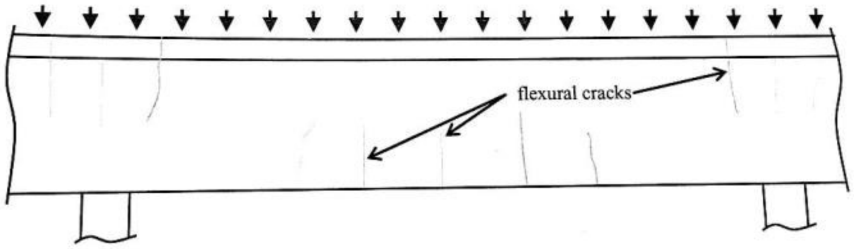

b) Typical structural cracks at service load in RC beam

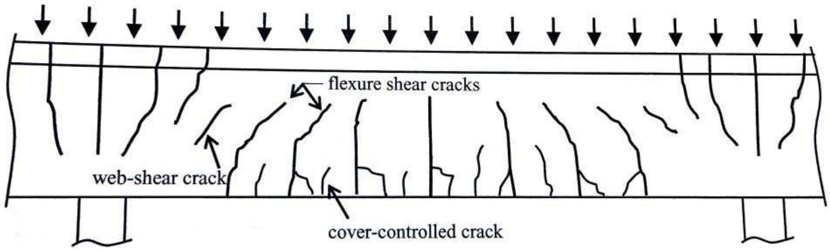

a) Typical flexural and shear cracks at overloads in RC beam

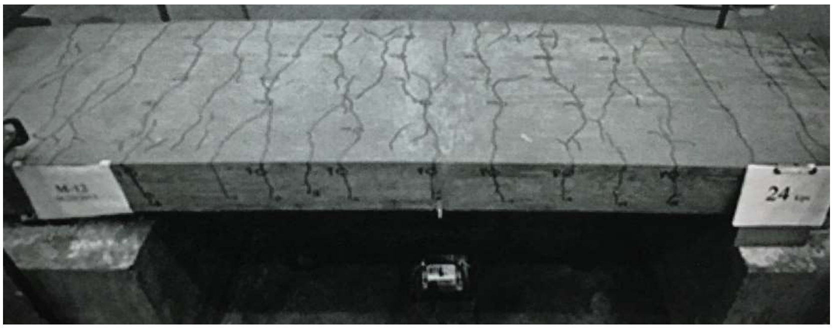

c) Flexural cracks in a one-way slab specimen

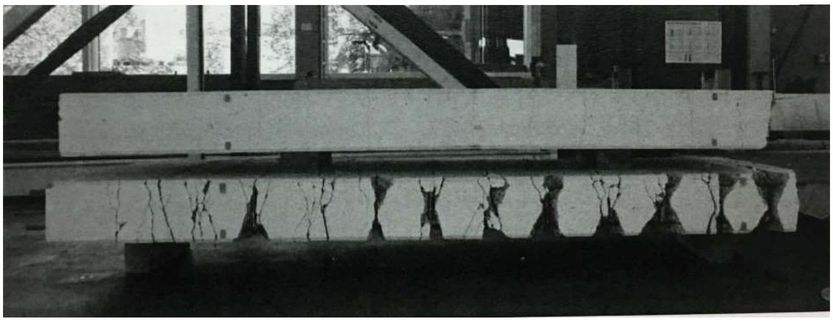

d) Direct tension cracks in a RC tension member

Figure 2-2: Structural cracks in a reinforced concrete beam and tension members

(Gilbert and Ranzi, 2010)

The level of tensile stress that exists in concrete, due to restraint to early cooling and shrinkage, directly influences the load at which flexural cracks and/or direct tension cracks first occur. In addition, the width of a structural crack at any time after loading depends on the level of shrinkage, as well as the level of the service loading.

As the applied loads are increased above the service load levels, into the overload region, the extent of cracking increases, and the steel crossing cracks that exist may yield and extend and widen (as shown in Figure 2-3). In the shear span of beams, flexural cracks may become inclined, forming flexure-shear cracks, and cracks known as web-shear cracks may form within the web of members (see Figure 2-2b) (Kim and White, 1999). Additional cracking, sometimes called cover-controlled cracking, occurs in the tension zone in the cover regions around the tensile reinforcement (see Figure 2-2b) (Castel and François, 2011). In members subjected to torsion, inclined cracks may spiral around the beam.

Figure 2-3: Flexural cracks at overload in a RC beam with ductile reinforcement (Gilbert and Ranzi, 2010)

Controlling cracking in concrete structures is a serviceability requirement. At the point of overload, the main design concerns are strength and ductility, and the control of cracking is not required. The wide cracks at overload provide warning of overload and structural distress. These wide cracks are associated with large deformations that are a necessary requirement for ductility. The bottom specimen, shown in Figure 2-2d, is a tension member containing ductile reinforcement. The member continued to carry the peak load after a large elongation, as is evidenced by the wide cracks, and in spite of obvious signs of distress. By contrast, the upper specimen in Figure 2-2d contained low ductility reinforcement and failed suddenly, due to the fracture of the bars, while the crack width remained relatively fine and the specimen showed no obvious sign of distress.

2.2.3 Sensory techniques for concrete assessment

To ensure structural integrity, and hence maintain safety, in- service health and usage monitoring techniques are employed in many engineering areas. Structural health is directly related to structural performance and in this respect, it is one of the major parameters with regard to safety of operations. Real-time structural health monitoring and controlling systems can provide instantaneous information on a condition of a specified structure. This will result in a significant increase of safety margins and reductions in maintenance cost (Chang, 1998, Sohn et al., 2003, Park et al., 2007).

In concrete structures, a destructive evaluation method is generally used, in which concrete cylinders are crushed to directly obtain concrete information. This method is straightforward and reliable. However, this method is not suitable or convenient to monitor in situ, large-scale reinforced concrete structures (Shiotani and Aggelis, 2009, Song et al., 2008). Therefore, non-destructive evaluation (NDE) has been effectively used to monitor and evaluate material or functional structures without impairing function and performance. Common NDE methods basically include: visual inspection, magnetic particle testing, radiographic method, ultrasonic testing (UT), acoustic emission method, liquid penetrant testing, eddy current testing. These methods assigned to passive sensor diagnostics (PSD) or active sensing diagnostic (ADS) (Wang et al., 2001). In ADS, an ultrasonic signal is generated by a pulsar and detected by a receiver. Hence, through continuously tracking the evolution of detected ultrasound signals, information on the status of the material or structure can be obtained. While for PSD, ultrasonic signal or acoustic emission is generated by the rapid release of energy from a localised source within a material or structure. The released energy propagates in the form of transient elastic waves and can be detected by a piezoelectric transducer. The output of the transducer is further processed by suitable electronic equipment and interpreted into valuable information about the source causing the energy release.

Ultrasonic (sound having a frequency above 20,000 Hertz) testing has attracted great attention due to its features, including low cost, high accuracy, less harmfulness to human life, and environmental friendliness. Normally, the UT method can be subdivided into ADS and PSD. As a possible means of non-destructive evaluation method, UT has been studied by Mason, McSkimin and Shockley in a quantitative manner (Mason et al., 1948). UT techniques have been extensively studied in materials engineered during the 1950s (Krautkrämer and Krautkrämer, 1977). UT-based evaluation methods have been widely used for characterisation of concrete materials since the 1990s (Ohtsu et al., 1991). Theoretical investigation, based on analogy of seismology, was introduced to reflect local behaviour of concrete micro-cracks (Lu, 2010). A series of automatic monitoring systems and evaluation software were designed to carry the task (Grosse, 2002, Reinhardt and Grosse, 2004). Carpinteri et al (2007) studied the feasibility of the application of AE in monitoring concrete structures. Zhu et al (2013) studied the feasibility of piezoelectric actuators/sensors for the detection of delamination between steel bars and concrete using an embedded sensor.

However, with the swift development of modern data processing devices and improvement on signal analysis technique, the piezoelectric transducer has become a weak link of the UT technique chain. Most of the transducers were designed as outside components attached on the surface of concrete materials. The compatibility between the piezoelectric sensor and concrete material turn out to be a critical issue in UT technique. A good compatibility on acoustic properties and mechanical properties can ensure accurate and reliable monitoring results. Yet, there exist relatively large differences on stiffness and the acoustic impedance between concrete and traditional piezoelectric ceramic sensors.

A brand new cement-based piezoelectric composite has been developed that owned an acoustic impedance value quite close to that of the concrete matrix, which ensured a minimum signal distortion and maximum signal energy transmission efficiency (Li et al., 2002). Based on cement-based piezoelectric composite, assorted new monitoring systems need to be designed and developed to match the characteristic of introduced composite. New systems shall be geared to the needs of practical testing instead of mere laboratory usage. Apart from monitoring system design, various suitable evaluation methods may be continually proposed to comprehensively study: the fracture process or the hydration process of concrete material and structures, to properly reveal the micro-crack behaviour of concrete during fracture process, microstructure development of early-age concrete during hydration (Liu et al., 2011). Hydration heat-based monitoring and ultrasonic-based monitoring methods are major categories that are well-known for non-destructive early-age performance monitoring of concrete (Song et al., 2008).

The hydration heat-based monitoring method was considered by Ayotte et al. (Ayotte et al., 1997) by monitoring the heat generated during the hydration process. The heat can be continuously monitored by a thermocouple or fibre optical sensors, especially fibre Bragg grating sensors (Chen and Ansari, 1999, Lu and Xie, 2006, Ren et al., 2006, Zhang et al., 2006, Zou et al., 2012, André et al., 2012). However, fibre optical sensors are fragile and expensive, and offer only local measurements, which limit their application.

The ultrasonic-based monitoring method is the velocity of an ultrasonic wave that is thoroughly related to the inner physical properties of the medium. Thus, early-age concrete strength can be monitored by observing the propagation velocity of ultrasonic waves (Krauss and Hariri, 2001, Demirboğa et al., 2004, Voigt et al., 2005a). The disadvantage of this method is its high cost and bulky equipment.

Kong et al. (2013) investigated the three states of very-early age concrete hydration based on classification of the received electrical signal using a piezoelectric sensor. Specifically, the amplitude and frequency response were of interest. Both the swept sine wave and the constant frequency sine wave excitation methods presented the same conclusion on the three concrete states during the hydration, which enhances the reliability of the piezoelectric sensor and active-sensing approach for very early-age concrete hydration monitoring. On other hand, the detection of local damage, such as cracks in early-age concrete, requires higher frequencies for which piezoelectric-based transducers are ideal candidates because of their small size, low cost, and large bandwidth (Dumoulin et al., 2014).

In the field of damage detection using ultrasonic transducers, two major trends coexist. Acoustic emission testing is one of the most widely used techniques, which consists of recording acoustic events generated by the appearance of cracks using a large network of sensors. The technique allows us to localise the source of each event, either by comparing the time of arrival of the acoustic wave on the different sensors or by correlating the acoustic events with the crack mode (Grosse and Ohtsu, 2008, Ohtsu et al., 1991, Aggelis, 2011, Behnia et al., 2014). The second trend is based on active ultrasonic systems. In such systems, the acoustic waves are generated by the monitoring system itself. The wavelengths corresponding to the frequency bands used for active sensing are much smaller than the ones used in monitoring systems based on ambient low-frequency vibrations. Consequently, there is a stronger interaction with local defects, as cracks enable their detection (Planès and Larose, 2013). The methods have been first developed and intensively used in aeronautics for metallic and composite materials. During the last twenty years, a few research teams have started to apply these techniques to concrete structures using either surface-mounted or embedded transducers (Bungey et al., 2006). The latter has several advantages, which are the added flexibility in the choice of their position and better integration in the overall design of the structure (Dumoulin et al., 2014).

From the literature reviewed, the piezoelectric shows a particularly good capacity to satisfy exigent applications, due to unique mechanical strength, wide frequency response range, and favourable cost.

2.3 Concrete structure health monitoring using piezoceramic transducers

The direct piezoelectric effect was discovered in 1880 by the Jacques and Pierre Curie brothers. They found that when a mechanical stress was applied on crystals such as tourmaline, topaz, quartz, Rochelle salt and cane sugar, electrical charges appeared, and the charges were proportional to the stress. And soon after, the converse piezoelectric effect was discussed by Lippmann (Lippmann, 1987). The discovery of piezoelectricity generated significant interest within the European scientific community. The first application for piezoelectric materials appeared during World War I. Langevin and his co-workers in France used the effect of converse and direct piezoelectric effect to the emission and detection of underwater sound waves. Nicholson (1918) and Cady (1919) invented a piezoelectric resonator based on property observation of piezocrystals driven at frequencies close to their mechanical resonances. Many classic piezoelectric, applications such as microphones and accelerometers, were introduced and commercialised in this period.

Study of piezoelectric materials received a great deal of attention during and after World War II. Shubnikov predicted that piezoelectric properties would be discovered in amorphous and polycrystalline materials. Countries such as Japan and the former Soviet Union did a significant amount of work aiming at very high dielectric constants for construction of capacitors. Piezoelectric ceramic materials were discovered in this period; Piezoelectric ceramic is a mass of perovskite manmade crystals which exhibits strong piezoelectric properties. These discoveries inspired a great deal of research on properties of ceramic ferroelectrics and their application in a wide range of ultrasonic devices and systems. In the early 1950s, solid solution of lead zirconate titanate (PZT) was introduced by Jaffe et al. which have very strong piezoelectric properties (Jaffe et al., 1971). In recent years, there has been a tremendous amount of research on piezoelectric ceramic composites and piezoelectric polymers. Pioneer work on piezoelectric composite at Pennsylvania State University was done by Rittenmyer et al. (1982), Safari et al. (1998), and Bhalla et al. (1985). Piezoelectric composite combines the function of piezoelectricity and the advantage of appended materials. The introduction of piezoelectric composite significantly widened the field of application, especially in medical imaging, generator, transmitters and detector of surface acoustic waves.

Piezoelectricity is a property of certain classes of crystalline materials. When mechanical pressure is applied to the sample made of these materials, a charge will be induced on the electrode surface of the sample. The charges are linearly proportional to the magnitude of the applied pressure within a certain range. Conversely, when a voltage is applied to one sample of these materials, the sample changes its shape. From an energy-exchange-viewpoint, piezoelectricity is the property to convert mechanical energy into electric energy and vice versa. Sensing of piezoelectric materials is the application of mechanical energy converting into electrical energy, while actuating is the implementation of electrical energy converting into mechanical energy (Lu et al., 2013, Lu, 2010). An important group of piezoelectric polycrystalline ceramics is ferroelectric materials with the perovskite crystal structure, such as barium titanate and PZT. Ferroelectric ceramics become piezoelectric when poled. PZT and their modifications are solid solutions of lead titanate and lead zirconate.

The ability of a piezoeletric material to transform electrical energy to mechanical energy, and vice versa, is measured by piezoelectric coefficient. This transformation of energy between mechanical and electrical domains is employed in both piezoelectric sensors and actuators (see Figure 2-4).

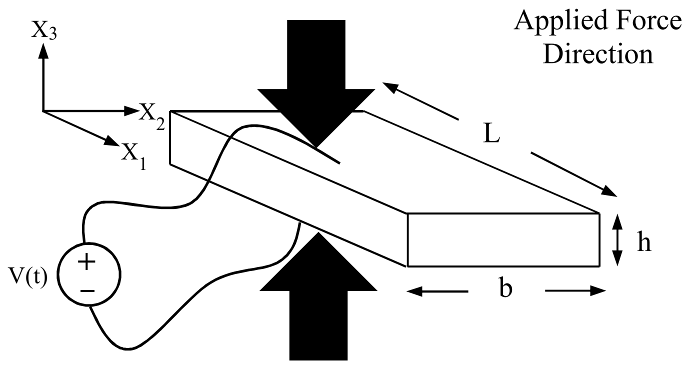

Figure 2-4: Piezoelectric coupling coefficients (Gu, 2007)

Piezoceramics have been known as a simple, low-cost, lightweight, and easy-to-implement material for passive and active control of structural vibration. Because of the piezoelectric nature of the material, it can transform mechanical vibration energy of the structure to electrical energy or vice versa. Piezoceramics are available in various forms such as stack actuators, patch actuators, flexible patch actuators, macro-fibre composite actuators developed at the NASA Langley Research Centre (Wilkie et al., 2000), and active fibre composite actuators developed at the Continuum Control Corporation. Bent et al. (2000) presented Active Fibre Composite (AFC) actuators that are comprised of piezoelectric fibres, polymer matrix, and electrodes. PZT fibres are uni-directionally aligned in order to sense and actuate in-plane stresses and strains for structural actuation applications. Horner (2001) developed a new packaging technique for piezoceramic wafers in which the encapsulation of the piezoceramic incorporates the electrical leads. Their technique for an encapsulation produces a hermetically sealed package that is also flexible and can be surface mounted or embedded into composites.

Stacking type actuators are commonly used piezoceramics in civil applications, and they are also known as multi-layered actuators. Multi-Layer Piezoelectric Actuators (MLAs) offer many advantages, such as high energy density, compared to other active materials, and consequently they are increasingly used in various smart actuator applications (Bouchilloux et al., 2004). Typically, a 100 mm length, with a cross-sectional area of 1 cm^2, provides a free stroke of 100 μm and a blocked force of about 3 kN. These MLAs do have some disadvantages because of the low tensile strength. This is a source of failure in bending conditions, in vibration environments, and in dynamic applications where high transient stresses are present.

Recently, Cedrat Technologies (Bouchilloux et al., 2004) introduced mechanically Amplified Piezoelectric Actuators (APAs) to overcome the tensile stress limitation of MLAs, by applying a compressive prestress on the ceramic, which, additionally, enhances the piezoelectric deformation. The APA actuator form shows significant improvement in terms of output energy per actuator mass or per actuator volume.

PZT is a piezoceramic material that has the property of generating a certain voltage when a strain is applied on the material, and conversely, in a large frequency range. This kind of material is therefore suitable to generate or measure mechanical waves. In the field of design of embedded piezoelectric-based transducers, one can report two main different approaches. The first approach uses thin PZT patches cast in small mortar pieces with multiple coating layers. The design of these transducers is based on those initially produced at the University of Houston (Song et al., 2008).

Most of these transducers have been designed for compression waves (P-Waves), for damage detection (Dumoulin et al., 2015), and monitoring of early age properties of concrete (Gu et al., 2006, Dumoulin et al., 2012). Such embedded transducers have also been developed to simultaneously measure the P-Wave and S-wave velocities (Li et al., 2009). Piezoelectric-based transducers can also be composed of composite piezoelectric material where the piezoelectric material is embedded in a matrix of cement (Newnham et al., 1980). The piezoelectric material can be in the form of either particles of piezoelectric material (0–3 composite), multiple PZT plates (2–2 composite), or PZT rods (1–3 composite) (Li et al., 2002, Dong and Li, 2005, Cheng et al., 2010). These type of transducers have been used to assess the hydration properties of concrete (Qin and Li, 2008), acoustic emission detection (Qin et al., 2009), and damage monitoring (Lu et al., 2011). They offer a better impedance matching, but are more difficult to manufacture.

In the presence hydration properties of concrete, various compounds in cement particles hydrate to form new compounds, which are the infrastructure of hardened cement paste in concrete. C3S (Tricalcium silicate) and C2S (Dicalcium silicate) in cement hydrates to form the most important strength contributor, calcium silicate hydrate, which is well-known for its amorphous character; their reaction also produces calcium hydroxide with a distinctive hexagonal tabular morphology. C3A, sulfate, and water reacts to form a hexagonal crystal named calcium sulfoaluminates and normally, they are observed to be long slender needles. Pores are the major component of hydrated concrete. According to the size of the pores, they can be classified as a capillary pore, gel pore, and entrapped isolated air pore. The hydration compounds and the pore’s structures make up the fundamental microstructure of hydrated concrete. Since the microstructure of concrete determines the mechanical behaviour, a great effort has been made to study and evaluate the process and mechanism of microstructure development during concrete hydration (Lu et al., 2013).

Various methods have been developed to monitor and characterise the hydration of cementitious materials (Qin and Li, 2008, Dumoulin et al., 2012, Lu et al., 2013, Xiao and Li, 2008, Xiao, 2007, Ni et al., 2012). Temperature measurement is a traditional and common method to monitor early-age concrete hydration (Azenha et al., 2011, Mikulić et al., 2013, Norris et al., 2008). Branco et al. present a numerical method dealing with the environmental interaction and concreting phases to measure the temperature and stress characterisation during the first days after casting (Branco et al., 1992). Sayers and Dahlin (1993) discussed the possibility of continuous measurement of velocity and amplitude of ultrasonic compressional waves to reflect the evolution of cement paste microstructure development. Based on their results, the microstructure development of cement paste was treated as a process from a viscous suspension of irregularly shaped cement particles into a porous elastic solid with non-vanishing bulk and shear moduli. Inspired by this idea, Grosse (2002) and Song et al. (2008) made and improved a series of ultrasound testing devices aimed at characterising the hydration and deterioration process of cement-based materials. Ye et al. (2004) studied the development of microstructure in cement-based materials by means of HYMOSTRUC model simulation and ultrasonic pulse velocity measurement. They explained and clearly identified the microstructure development and percolation time point of cement paste. A non-contact resistivity method was introduced by Li et al. (2003) to evaluate the hydration process of early-age concrete. It was found that non-contact resistivity measurement was especially suitable for detailed monitoring of concrete at a very early-age, since it was quite sensitive to the ionic concentrations and mobility in the liquid and pore solution, and various distinct hydration stages were identified (Xiao and Li, 2008).

Recently, an electromechanical impedance (EMI) based method has been used for concrete characterisation and damage detection (Divsholi and Yang, 2012, Park et al., 2003, Yang et al., 2008). It was found that the impedance of Portland cement paste is sensitively related to the paste hydration process (Yang et al., 2010). To indicate the characteristics of early hydration concrete, Yang et al. employed the measured admittance of a reusable PZT sensor and the root mean square deviation (RMSM) method (Yang et al., 2010).

Lu et al. (2013) studied hydration processes of early-age concrete using two non-destructive monitoring systems: embedded active acoustic and non-contact complex resistivity. They found that the hydration stages could be distinguished according to the characteristics of acquired parameters, and the maturity of the concrete. Furthermore, they found that the non-contact complex resistivity measurement turned out to be capable of detecting the variation of the liquid phase morphology and pore structure.

Wave-propagation-based concrete hydration monitoring, including ultrasonic wave measurement, has also been studied to reflect the change of concrete properties (Abo-Qudais, 2005, Keating et al., 1989, Voigt et al., 2005a, Voigt et al., 2005b, Desmet et al., 2011). Both the electrical resistivity and ultrasonic techniques have been applied for cement-based materials hydration monitoring during the first seven days and four stages of the concrete hydration (Zhang et al., 2009). SAs were proposed by Song et al (Song et al., 2005, Song et al., 2008) as multi-functional sensors and an active-sensing approach, using a couple of SAs for concrete characterisation and structure health monitoring (Yang et al., 2010, Song et al., 2008, Gu et al., 2006, Kong et al., 2013, Chung et al., 2014). It is shown that the SAs can be embedded at the desired position in a concrete structure before casting, to perform early-age concrete compressive strength determination and hydration characterisation monitoring (Chung et al., 2014, Gu et al., 2006, Kong et al., 2013, Dumoulin et al., 2012).

Recently, piezoceramic based smart aggregates were used by Kong et al. (2013) to monitor very early-age concrete (0-20 hour) hydration characterisation. The electrical signal transferred from the Smart Aggregate sensor was recorded during the test. As the concrete hydration reaction was occurring, the characteristic of the electrical signal continuously changed. These results were based on investigation of the three states (fluid, transition, and hardened state) of very early-age concrete hydration based on the classification of the received electrical signal. Specifically, the amplitude and frequency response of the electrical signal were of main interest. Both the swept sine wave and the constant frequency sine wave excitation methods presented the same conclusion on the three concrete states during the hydration, which enhanced the reliability of the active-sensing approach for very early-age concrete hydration monitoring.

2.3.1 Detection and monitoring of cracks in concrete structures

The piezoelectric material will generate an electric charge when it is subjected to a stress or strain (the direct piezoelectric effect); the piezoelectric material will also produce a stress or strain when an electric field is applied to a piezoelectric material in its poled direction (the converse piezoelectric effect). Due to this special piezoelectric property, piezoelectric material can be utilized as both an actuator and a sensor. This property enables the multi-functionality of the piezoelectric materials.

A concrete structure can be subjected to several factors that may damage it and potentially lead it to be turned out of service, or in the most dramatic cases, to the complete failure. These factors are either climatic, chemical, or accidental. To ensure the safety of a structure, it is important to evaluate its state regularly. Visual inspections and destructive tests were, until recently, the only ways to assess the state of the structure. Such inspections require specific equipment and manpower. They are consequently very costly and only a few numbers of tests can be carried out. Furthermore, visual inspection can only identify macroscopic damage at accessible locations. As an alternative, several non-destructive testing (NDT) techniques have been developed during the last thirty years (McCann and Forde, 2001, Malhotra and Carino, 2003). The recent developments in the field of NDT have led to the possibility of automated tests, which greatly improves their repeatability and efficiency (Maierhofer, 2010).

Damage detection and failure analysis of concrete structures have been studied for many years (Otani and Sozen, 1972, Abrams, 1979, Saiidi and Sozen, 1981, Kreger and Sozen, 1983, Park et al., 1985, Hassan and Sozen, 1997, Wang and Wen, 2000, Nojavan and Yuan, 2006). Various sensors and methods have been developed for damage detection and health monitoring. Fiber optical sensors (FOS), especially Fiber Bragg Grating (FBG) sensors, are now used for the health monitoring of various RC structures (Zhang et al., 2006, Ren et al., 2006, Lu and

Xie, 2006, Chen and Ansari, 1999). However, FOSs offers only local measurements, limiting their applications. These methods are more suitable to detecting large-scale effects than local damage (Deraemaeker and Worden, 2012). The detection of local damage requires higher frequencies, for which piezoelectric PZT transducers are ideal candidates because of their small size, low cost, and large bandwidth.

In the field of damage detection using ultrasonic transducers, two major trends coexist. Acoustic emission testing is one of the most widely used techniques. It consists of recording acoustic events generated by the appearance of cracks using a large network of sensors. The technique allows us to localise the source of each event by comparing the time of arrival of the acoustic wave on the different sensors or by correlating the acoustic events with the crack mode (Ohtsu, 1996, Gooch, 2011, Aggelis, 2011, Behnia et al., 2014). The second trend consists of using active ultrasonic systems. In such systems, the acoustic waves are generated by the monitoring system itself. The wavelengths corresponding to the frequency bands used for active sensing are much smaller than the ones used in monitoring systems based on ambient low-frequency vibrations. Consequently, there is a stronger interaction with local defects, as cracks enable their detection (Planès and Larose, 2013). The methods were first developed and intensively used in aeronautics for metallic and composite materials. During the last twenty years, a few research teams have started to apply these techniques to concrete structures using surface-mounted or embedded transducers (Naik et al., 2004, Bungey et al., 2006). The latter has several advantages, which are the added flexibility in the choice of their position and better integration in the overall design of the structure. Within this framework, the concept of smart aggregates have been developed by researchers at the University of

Houston (Song et al., 2007, Song et al., 2005, Song et al., 2008, Song et al., 2006, Gu et al., 2006).

In the field of active sensing using piezoelectric-based transducers, several authors have used impedance curves to assess the strength and damage state of concrete. The impedance curve is measured using a single PZT transducer, which is very attractive from a practical point of view. Experiments show that this technique is sensitive to damage in very local areas around the transducers (Park et al., 2006, Tawie and Lee, 2010). Other techniques are based on a pitch catch configuration and require at least two transducers (one emitter and one receiver). The methods differ mainly in the choice of the signal generated at the emitter side (Dumoulin et al., 2014).

Harmonic signals can be used to reveal nonlinearities due to damage, which generate harmonics of the fundamental frequency (Shah et al., 2009, Shah and Ribakov, 2010). A second type of excitation is the chirp signal, which allows more energy to be sent into the system and therefore enhances the signal-to-noise ratio of the measurements. This type of excitation signals has been recently used for damage detection in concrete (Song et al., 2007, Liao et al., 2011). The main idea of this technique is to measure the evolution of the energy contained in the wave as a function of the evolution of cracking, using a wavelet packet decomposition of the signal. This technique has been shown to be sensitive to significant damage.

Finally, pulse excitation is traditionally used in commercial systems designed to estimate the quality of the concrete based on the ultrasonic pulse velocity (UPV). This system consists of external probes that need to be placed on two opposite faces of the concrete specimen, using an adequate coupling agent. In practice, for real structures, this limits the application to through thickness propagation, or repeated wave reflections, which makes the interpretation difficult. It is also often impractical due to limited accessibility when in service. Coupling such systems to embedded piezoelectric-based transducers can overcome most of these difficulties.

More complex analysis of the wave amplitude generated by pulse excitation can be carried out, such as backscattered waves amplitude analysis. In this method, the response signal attenuation form (decreasing exponential) is used as a damage indicator (Chaix et al., 2003). The backscattered waves result from numerous interactions, such as voids, cracks, or microcracks in the concrete structure. Each contains information over the state of the material. Indeed, in multiple scattering media, the wave path can be compared to the Brownian random behaviour of a particle (Pacheco and Snieder, 2005). Thus, one can describe the average intensity of the wave in time and space using the diffusion equation (Tourin et al., 2000). Several authors have studied the impact of damage on diffusivity of concrete (Deroo et al., 2010, Quiviger et al., 2012). Recently, some authors have used the so-called coda-wave interferometry method (Planès and Larose, 2013, Snieder, 2006) to study the influence of stress on the wave velocity (Zhang et al., 2012, Larose and Hall, 2009), as well as the evolution of the acoustoelastic parameters of concrete with the appearance of damage (Schurr et al., 2011, Shokouhi et al., 2010). This method is based on the principle that the received signal in multiple scattering media is the superposition of the same wave packets with random amplitudes and delays. The 'damaged signal' is therefore a stretched copy of the original signal.

(a) (b)

Figure 2-5: Schematic of stress wave propagation inside the specimen (a) stress wave propagating parallel to the crack and (b) stress wave propagating perpendicular to the crack (Feng et al., 2015)

2.4 Smart aggregates material, setup, and arrangement

An emerging field of study has arisen, in which smart material and structure technology has been applied in civil infrastructures. These applications include condition/health monitoring, damage assessment, structural control, structural repair and maintenance, integrity assessment, and more recently, asset management, preservation, and operation of civil infrastructures. The potential benefits of this technology include improved infrastructure reliability and longevity, enhanced structural performance and durability, improved safety against natural hazards and vibrations, and a reduction in life-cycle costs in operating and managing civil infrastructures (Han et al., 2015).

Piezoelectricity includes the direct piezoelectric effect and the converse piezoelectric effect. The direct piezoelectric effect is when an electric charge is generated in a piezoelectric material subjected to either stress or strain. The converse piezoelectric effect is the reverse process. Stress or strain is produced due to the applied electric field. The lead zirconate titanate (PZT) is one of the most common piezoelectric materials successfully used as smart materials (Song et al., 2008).

Since the fragile PZT has a lot of limitations in field applications, a Smart Aggregate is fabricated by sandwiching the waterproofed PZT with protection materials, as shown in Figure 2-6 (Hou et al 2012). The diameter and the height of the Smart Aggregate are 25 mm and 20 mm, respectively. The dimension of the PZT patch is 15mm×15mm square.

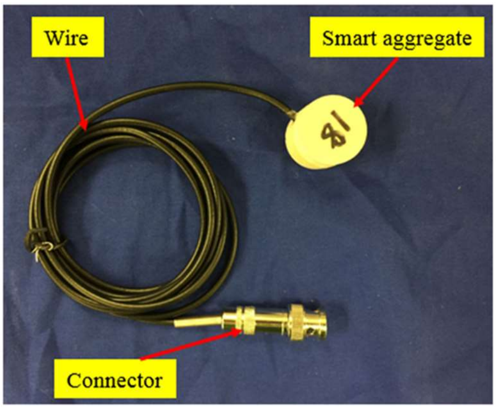

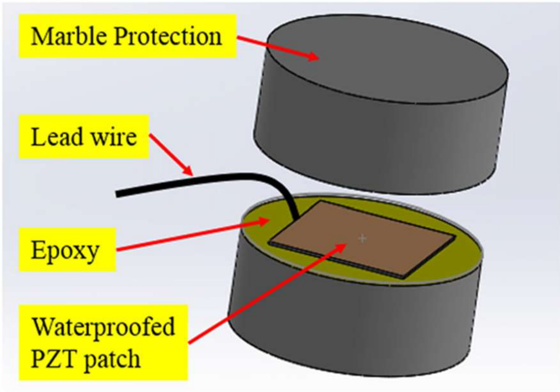

(a) (b)

Figure 2-6: A Smart Aggregate with (a) connector and (b) its structure (Feng et al., 2015)

Smart Aggregate can be utilised as both the actuator and the sensor, based on the piezoelectricity. The active sensing approach using smart aggregates is illustrated by two smart aggregates which are used as an actuator and a sensor, respectively. The guided wave is applied to the Smart Aggregate and generates a stress wave. The spectrum of excitation frequencies starts from a very low frequency and increased to a high frequency (e.g., 100 Hz to 150 kHz). Smart aggregates have been used in concrete structural health monitoring research, including crack detection of the concrete shear wall, crack detection of reinforced concrete column, early age concrete hydration monitoring, and active de-bonding monitoring of a concrete-filled steel tube (Song et al., 2008, Yan et al., 2009, Liao et al., 2011, Xu et al., 2013, Zou et al., 2015, Feng et al., 2015, Zhang et al., 2016, Su et al., 2016, Feng et al., 2016).

The previous investigation’s results show that the detection area was concentrated between the actuator and sensor (Song et al., 2008, Kong et al., 2013). Therefore, the detection covered area by transducers was very critical in the arrangement of the sensors, and proved to be a challenge to the researchers.

An experimental study was done by Kong et al. (2013) in which they investigated using a Smart Aggregate for early-age concrete monitoring, as requested by Texas Department of Transportation. The two smart aggregates were fixed to rebars prior to concrete casting. In this concrete specimen, the distance between the two rebars, which were used to install the two SAs, was 50.8 mm. since the Smart Aggregate diameter was 25 mm, so there was a very small distance between the actuator and sensor. Dumoulin et al. (2012) also organised a series of experimental investigations for early-age concrete health monitoring using different distances (6 and 10 cm). Their results aligned with the results obtained on the same concrete using a commercial system for 6 cm, while not receiving any signal for the distance of 10 cm’s. And hence, as mentioned previously, the covered area by transducers was very important for researchers and much of the investigations to achieve highest covered area were unsuccessful. Some researchers suggested using more than one couple (actuator and sensor) in the critical zone of structure to avoid this problem (Dumoulin et al., 2014, Feng et al., 2015).

The Belgian company MS3 takes an interest in evaluating the quality of concrete around the anchorage system of highway security barriers after substantial shocks. The failure mechanism can be viewed as a combination of bending and the failure of the anchorages. Accordingly, the company organised the laboratory monitoring tests using smart aggregates for a three-point bending test and several pull-out tests (Dumoulin et al., 2014). They used the general sensor arrangement (one actuator and one sensor) for the three-points bending test, while adding additional sensors in a pull-out test improved their accuracy of detection (Figure 2-7). In our research, we took the advantages of this sensor arrangement and introduced a new setup for concrete early-age hydration monitoring (Chapter 4) with two different distances (50 and 100 mm).

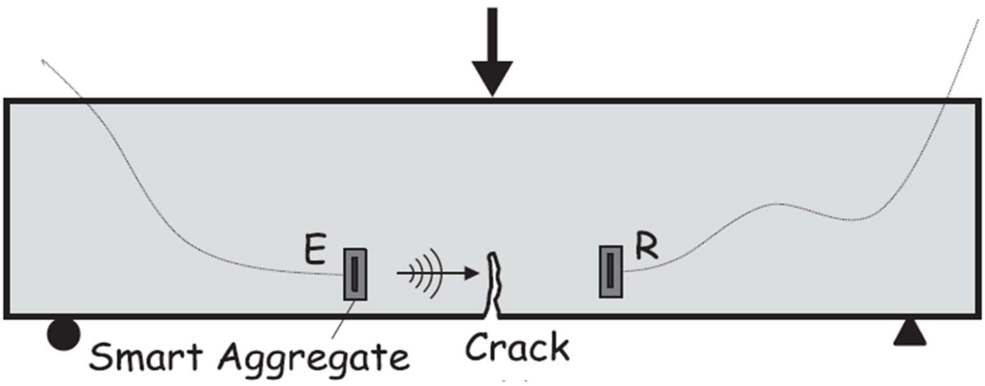

(a) Three-points bending test

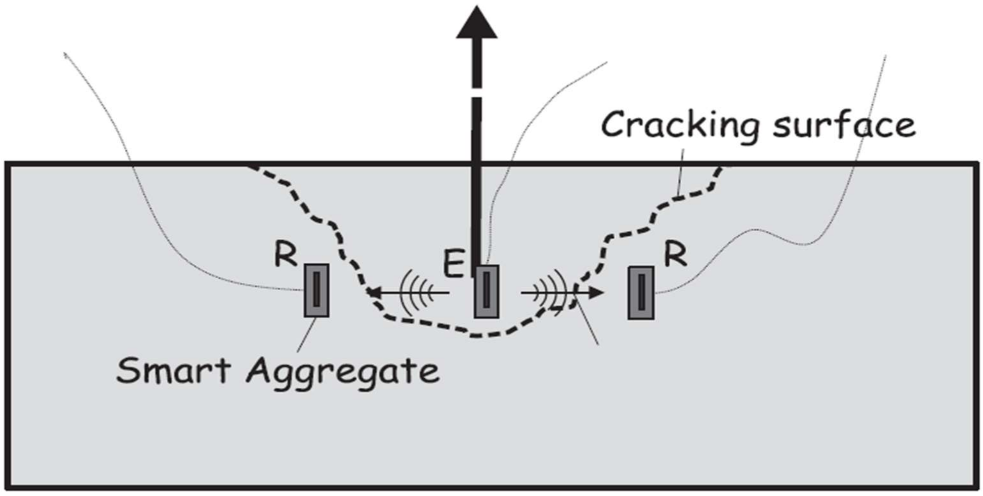

(b) Pull-out test

Figure 2-7: Sensor arrangement for (a) three-points bending test, one emitter (actuator) and one receiver and (b) pull-out test, two receivers and one emitter (Dumoulin et al., 2014)

Recent investigations made some changes and improvements to the general sensor arrangement to ensure clarity of detection and evaluation of damages in concrete. The improvement would be a series of changes in sensor arrangement in terms of number and location or measurement setup.

In the experimental investigation by Dumoulin et al. (2015) for crack detection on an RC beam, they added a notch in the bottom of the beam to locally reduce the strength of the beam and create stress-concentrations (Figure 2-8); cracks were not always initiated exactly at the centre of the beam due to the heterogeneity of concrete. This pre-cracking (notch) ensured the crack initiation was at the right place. This method is not applicable for real structures and only can be used for laboratory investigation.

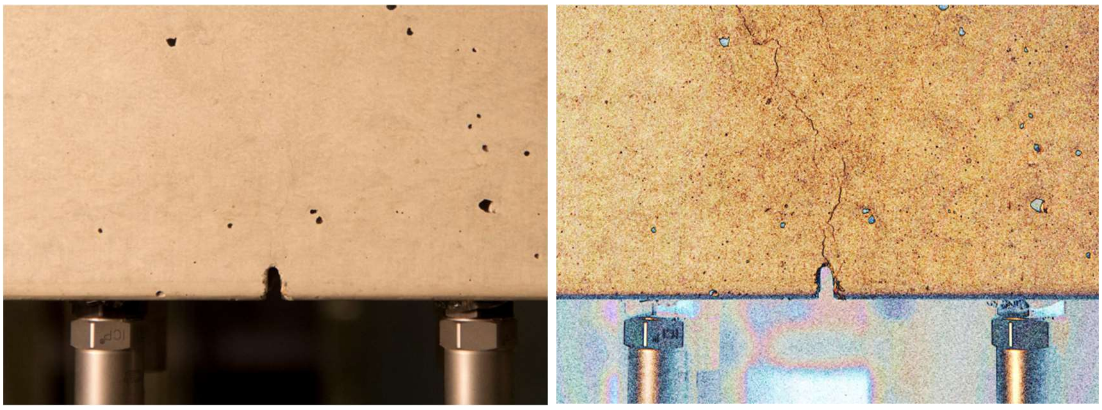

a) Before test b) After test

Figure 2-8: Notch added to bottom of beam to ensure the crack initiation started from the notch (Dumoulin et al., 2015)

Another setup has been used by Zhao et al. (2016) for health monitoring of RC beams using the combination of an embedded Smart Aggregate and surface mounted piezoceramic patches. A three-point bending test was conducted to induce damage in the concrete beam. The Smart Aggregate was embedded in a concrete beam as an actuator (or transmitter), and piezoceramic patches were attached on the surface of the concrete beam as sensors (Figure 2-9a).

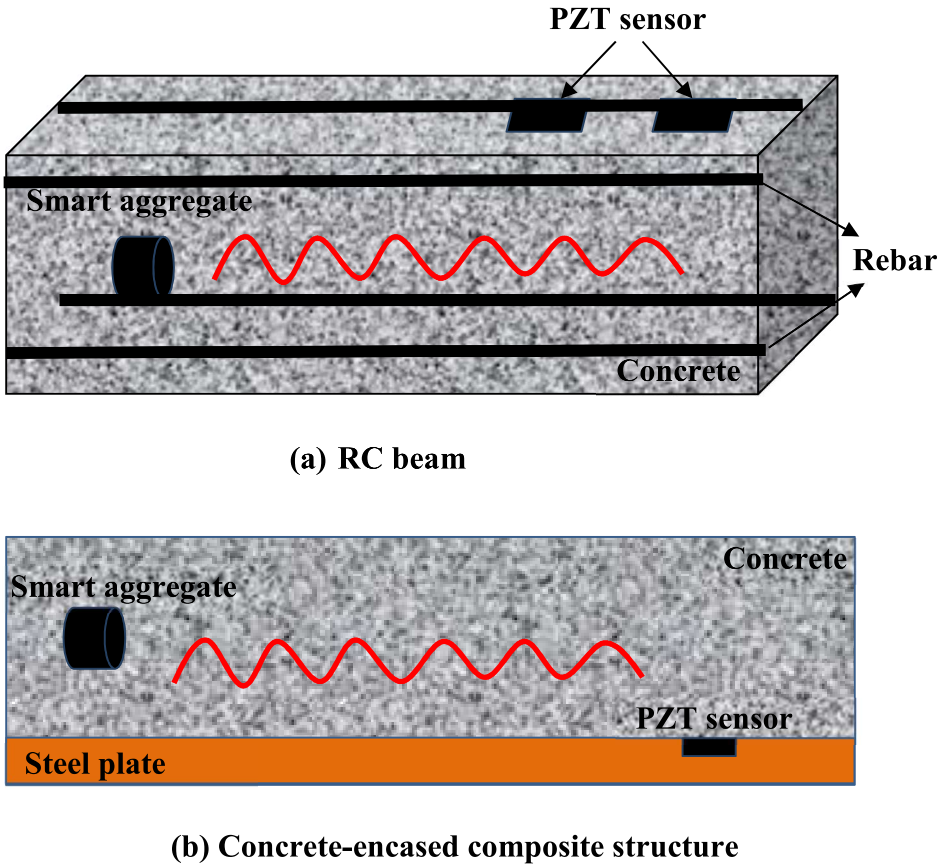

Figure 2-9: Schematic of embedded Smart Aggregate and mounted piezoceramic patches for (a) RC beam and (b) concrete-encased composite structure (Zhao et al., 2016, Liang et al., 2016)

A similar method was also proposed by Zeng et al. (2015) and Liang et al. (2016) for bond slip detection of concrete-encased composite structure. An active sensing approach has been to provide monitoring and early warning of the development of bond slip in the concrete-encased composite structure. The setup was based on a Smart Aggregate embedded in the concrete which acted as an actuator and generated desired shear stress waves. Distributed piezoceramic transducers installed in the cavities of steel plates acted as sensors and detected the wave response from the shear mode Smart Aggregate (Figure 2-9b). The disadvantage of the above investigations is the proposed setup is not applicable for existing structures due to the necessity of having at least one embedded actuator.

2.5 Summary

This literature review shows wave-propagation testing has provided an innovative approach for the characterisation of early-age concrete and the detection of cracks in concrete structures. Previous investigations show applications of SA techniques are promising, with the advantages of structural simplicity, low cost, quick response, and high reliability.

However, several issues are still remaining and leave challenging tasks to explore. The concrete hydration characterisation, using embedded SAs, has not received enough attention in previous investigations. It is well known that the early-age concrete hydration is a very significant part of the entire concrete hydration which can affect the final compressive strength. In this study, the active-sensing approach using SAs concentrated on early-age concrete hydration characterisation, with different water to cement ratio.

This literature review shows that remaining challenges face researchers in the area of localisation of sensors in concrete structures for detection and monitoring of cracks. The transducers arrangement, using SAs mounted on the surface of concrete, has not been reported. The performance of the crack initiation and propagation approach monitoring, using SAs for slap under cycling loading, has also not been investigated.

Chapter 3 : Smart Aggregate Based Nondestructive Testing Systems

3.1 Introduction

Non-destructive testing of concrete material and structures has been used for material characterisation, and detection and evaluation of defects such as voids, damages and corrosion of rebars. There are several NDT techniques which have own advantages and limitations. An embedded SA based approach/arrangement has demonstrated a great potential for the structural health monitoring of concrete material and structures. Another SA based approach uses SAs transducers embedded in and mounted on concrete based members. As mentioned, embedded SAs must be implemented in new concrete structures during their fabrication. This is one of the limitations of these two approaches. In this chapter a mounted SA based approach is proposed.

Second section of this chapter introduces the measurement and data processing techniques for these SA based approaches. They include measurement of wave propagation characteristic, data analysis and measurement error analysis. To compare the three SA based approaches they are presented and applied for characterisation of concrete specimens in the third section.

3.2 Measurement and data processing

In this study, the second generation of SAs were used and designed by sandwiching a waterproofed PZT patch with lead wires between two mating marble blocks to protect the fragile piezoelectric patch. The size of the PZT patch is 15 mm × 15 mm, and the thickness is 0.3 mm. The diameter of the SA is 25 mm and the height is 20 mm (Song et al., 2008). In order to connect to instruments, a Bayonet Neill–Concelman (BNC) connector is used as shown in Figure 3-1.

Figure 3-1: Fabricated SA with cable and BNC connector

Throughout this study, the active sensing approach was employed for all experiments, which is based on the measurement of propagation of characterises of stress waves in concrete. The SA-based measurement setup is shown in Figure 3-2. It includes a data acquisition (DAQ) board connected to a PC and SA transducers. An SA actuator generates a guided stress wave in a specimen, which is partially received by SA sensors. The received wave signals are recorded by the DAQ board connected with the PC and the developed LabVIEW software.

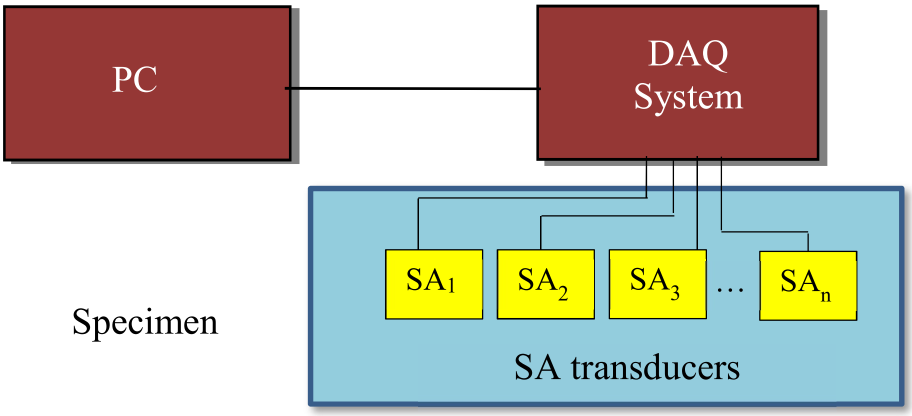

Figure 3-2: SA-based measurement system

The LabVIEW software is used to generate a swept sine wave as an excitation wave and to process the signals received by the SA sensors. The frequency range varies from 100Hz — 150kHz, and the signal swept period and the amplitude of the sine waves are set to be 1 s and 10 V, respectively. The primary program used to input the guide wave setup and to record received signal was single-channel program with the capability to connect two transducers (one actuator and one sensor) (Kong et al., 2013). The program was upgraded to multi-channel one to connect more transducers (i.e. sensors) in one system for more accurate and wide monitoring. The number of transducers used in a system highly depends on the DAQ card's power to generate stress waves. Figure 3-3 shows the multi-channel program setup window six sensors.

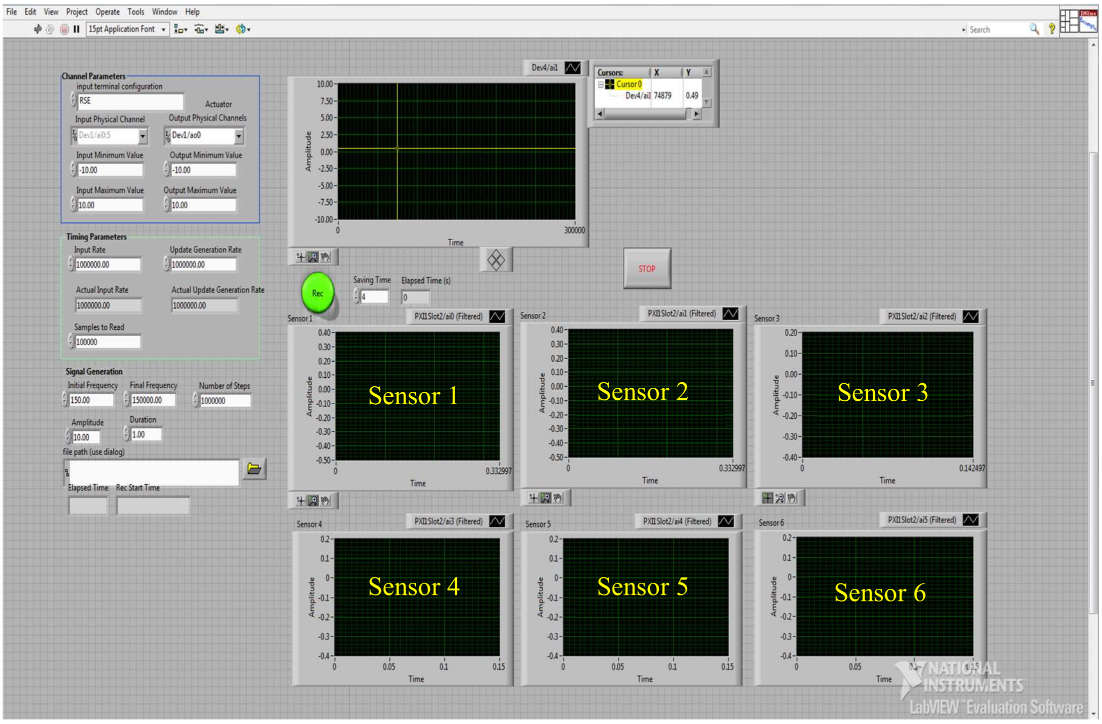

Figure 3-3: A view of multi-channel program on LabVIEW software

The received signals are saved in Technical Data Management Streaming (TDMS) format by LabVIEW software. The LabVIEW software is capable of reading the TDSM format and plotting the received signal in both time-domain and frequency-domain. Figure 3-4 shows the program window with the received and plotted signals of time domain and frequency domain.

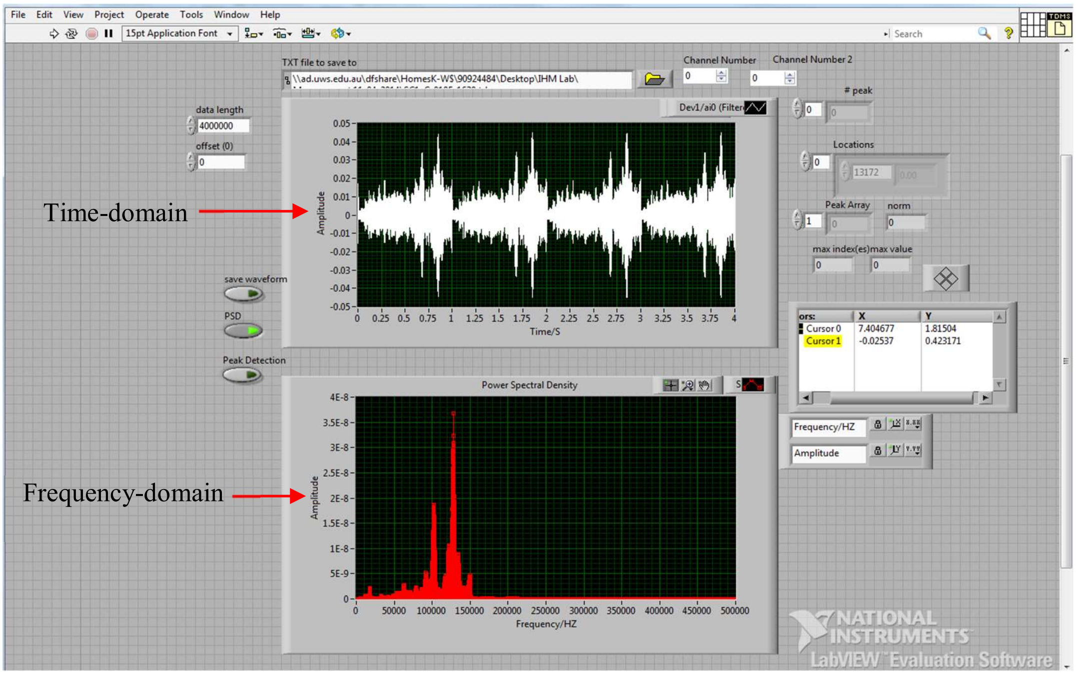

Figure 3-4: View of LabVIEW software with a run on TDMS file

3.2.1 Data analysis approach

Signal processing is one of the very important aspects of concrete health monitoring. There are various kinds of signal-processing approaches, such as Fourier transform, Hilbert–Huang transform, and wavelet analysis, among others. The wavelet analysis approach is a useful signal-processing tool and successfully applied by researchers for structural health monitoring and can be viewed as an extension of the traditional Fourier transform. One major advantage of the wavelet analysis is the ability to perform local analysis (Gu, 2007).

In this study, power spectral density (PSD) is calculated using four periods of swept sine-wave in order to obtain better accuracy. PSD describes the distribution of the power contained in a received signal over a certain frequency range. In addition, in this study the maximum of PSD (peak of PSD) and corresponding resonant frequency was used for comparison purpose when material properties changed as shown in Figure 3-5.

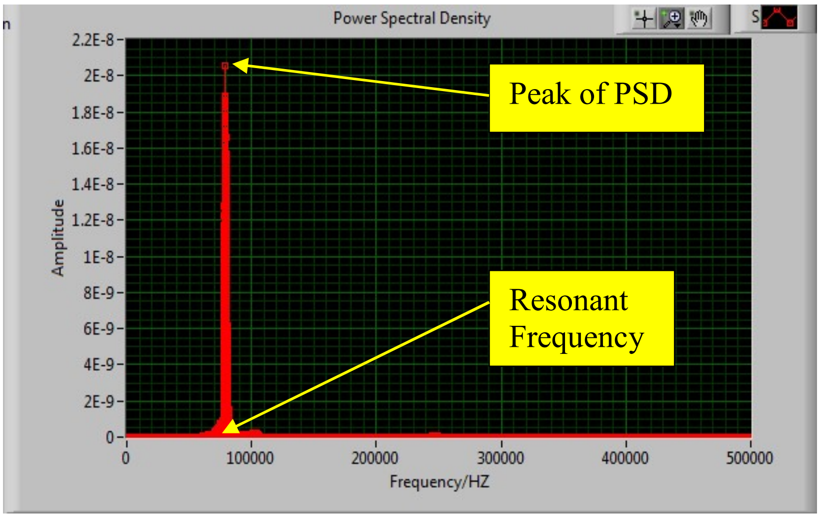

Figure 3-5: Frequency-domain received signal

If the peak PSD is not outstanding, rather a number of frequencies share the received power. Therefore, in this study the total received power is introduced as an alternative method for analysis and comparison. The following formula presents the total received power calculated in the frequency range of 50Hz to 150kHz, as given by Equation 3-1 (Chung et al., 2014):

$$P_T = \sum_{i=50}^{150k} PSD(f_i) \times f_i \tag{3-1}$$

where i represent the frequency number.

In order to evaluate damage in concrete-based structures, various kinds of damage indices have been developed in recent years. Root-mean-square deviation (RMSD) is a suitable damage index to compare the difference between the signatures of the healthy state and the damaged state (Soh et al., 2000). In this thesis, a damage index is formulated by calculating the RMSD between the energy vectors of the healthy state and the damage state.

The energy vector for the healthy data is E_h (where h is healthy stage or zero time index). The energy vector for the healthy data is E_h (where E is total received energy by sensor and h is healthy stage or zero time index). The energy vector E_i for the damage status at time index i is defined as E_i. The damage index at time index i and frequency band index j are defined as (Moslehy et al., 2010);

$$I = \sqrt{\frac{\sum_{j=1}^{n}\left(E_{i,j}-E_{h,j}\right)^2}{\sum_{j=1}^{n}E_{h,j}^2}} \tag{3-2}$$

The proposed damage index represents the transmission energy loss caused by structural damage. When the damage index is close to 0, it means the structure is in a healthy state. When the damage index is greater than a certain threshold, it means damage has appeared. In this case, the greater the index, is the more serious the damage. When the damage index is very close to 1, it means the concrete structure is near failure.

3.2.2 Measurement error analysis

Measurement error analysis is very important for characterisation of concrete specimen. Measurement errors may be classified as either random or systematic, depending on how the measurement was obtained, as an instrument could cause a random error in one situation and a systematic error in another (Taylor, 1997).

Random errors are statistical fluctuations (in either direction) in measured data due to the precision limitations of measurement devices. Random errors can be evaluated through statistical analysis and can be reduced by averaging over a large number of observations (Taylor, 1997). Systematic errors are reproducible inaccuracies that are consistently in the same direction. These errors are difficult to detect and cannot be analysed statistically. If a systematic error is identified when calibrating against a standard, applying a correction or correction factor to compensate for the effect can reduce the bias. Unlike random errors, systematic errors cannot be detected or reduced by increasing the number of observations. The easiest estimate of the systematic error is the average, or mean, of *N* independent measurements (x_1, x_2,…, x_N):

$$(Average)\bar{x} = \frac{x_1+x_2+\cdots+x_N}{N} \tag{3-3}$$

This average is the best available estimate of the results, but it is certainly not exact unless there are infinite measurements. Standard deviation is the most common way to characterize the spread of a data set. The standard deviation is always slightly greater than the average or average deviation, and is used because of its association with the normal distribution that is frequently encountered in statistical analyses. So we can write out the formula for the standard deviation as the following equation (Taylor, 1997):

$$SD = \sqrt{\frac{(\delta x_1^2+\delta x_2^2+\cdots+\delta x_N^2}{(N-1)}} = \sqrt{\frac{\sum \delta x_i^2}{(N-1)}} \tag{3-4}$$

where the *N* measurements be called $x_1, x_2, \ldots, x_N$ and each deviation is given by $\delta x_i = x_i - \bar{x}$, for i = 1, 2, ..., *N*.

The "*N*-1" term in the above equation represents the degrees of freedom. Loosely interpreted, the term "degrees of freedom" indicates how much freedom or independence there is within a group of numbers. The degrees of freedom have been limited by 1 and only N-1 degrees of freedom remain. In the standard deviation formula, the degrees of freedom are N minus 1 because the mean of the data has already been calculated (which imposes one condition or restriction on the data set).

Another statistical term that is related to the distribution is the variance, which is the standard deviation squared (variance = SD^2). The standard deviation may be either positive or negative in value because it is calculated as a square root, which can be either positive or negative. By squaring the standard deviation, the problem of signs is eliminated. One common application of the variance is its use in the F-test (variance analysing test) to compare the variance of two methods and determine whether there is a statistically significant difference in the imprecision between the methods.

In this study, the standard deviation is selected because it is expressed in the same concentration units as the data. Using the standard deviation, it is possible to predict the range of control values that should be observed if the method remains stable.

Designing a sensory system requires careful consideration of the limitations imposed by the construction, operating conditions, and medium. Some of the factors influencing the accuracy of the system are intrinsic to a specific design. Several researchers have examined the mechanisms that cause errors in ultrasonic ranging, and the principal mechanisms are included of variations in boundary conditions, sensors misalignment, time accuracy of electronic signals for wave generation and signal processing, and signal detection. The above variations in boundary conditions have been considered mostly in composite structures due to concrete abutment with steel.

Johnson and Truman (2004) utilized a damage detection procedure using unconstrained, nonlinear optimization. The method detected damage in two dimensional beam-element frame models through the use of sequential quadratic programming. An objective function was created by again using the error in the measured displacements of the actual structure and that of a mathematical model of the structure.

Hajela and Soeiro (1990) used a static based identification method that used the output error approach. Again, an optimization routine was used to minimize the error between measured displacements of a structure and calculated analytical displacements, the difference of this method lied in the loading procedure. When loads are applied to a structure the various displacements at each degree of freedom can be of different magnitudes. As a result, elements will experience different levels of stress. To avoid this complication, Hajela and Soeiro (1990) performed the output error method using an equal stress loading condition. The equal stress loading condition is calculated by first applying a unit load at each degree of freedom and observing the resulting stress in each member.

3.3 Specimens and arrangement of SAs

Two arrangements of SAs transducers have been used for detection of defects or monitoring of material characterisation. These arrangements are as follows:

1. Embedded SA transducers;
2. Embedded SA and mounted SA transducers.

In this study, the following new arrangement has been proposed and applied for detection and monitoring of cracks on concrete and reinforced concrete specimens under loading:

- Mounted SA transducers (actuator and sensors).

For all these arrangements calibration and/or selection of SA transducers are required. A novel method of calibration will be presented in the next sub-section.

3.3.1 Embedded SA transducers

The SA embedded transducers can be used for both detection of defects or monitoring of material characterisation. In the SAs-based active sensing system, one SA is used as an actuator to generate certain excitation waves; the other SAs are used as sensors to detect the response. For material characterisation and detection of defect such as crack two similar setups are used as shown on Figure 3-6a, and Figure 3-6b, respectively. Each setup includes a specimen with two embedded SAs at the distance (*d*), a personal computer (PC) and a DAQ card. The energy of the propagation waves is attenuated due to the existence of defect/crack. The drop value of the transmission energy is correlated with the severe degree of defect/crack inside the specimen.

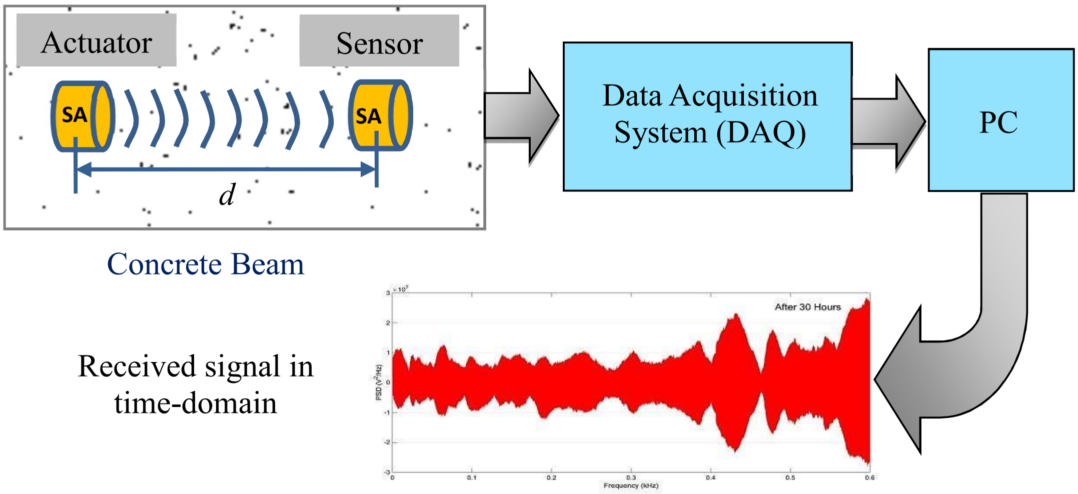

(a)

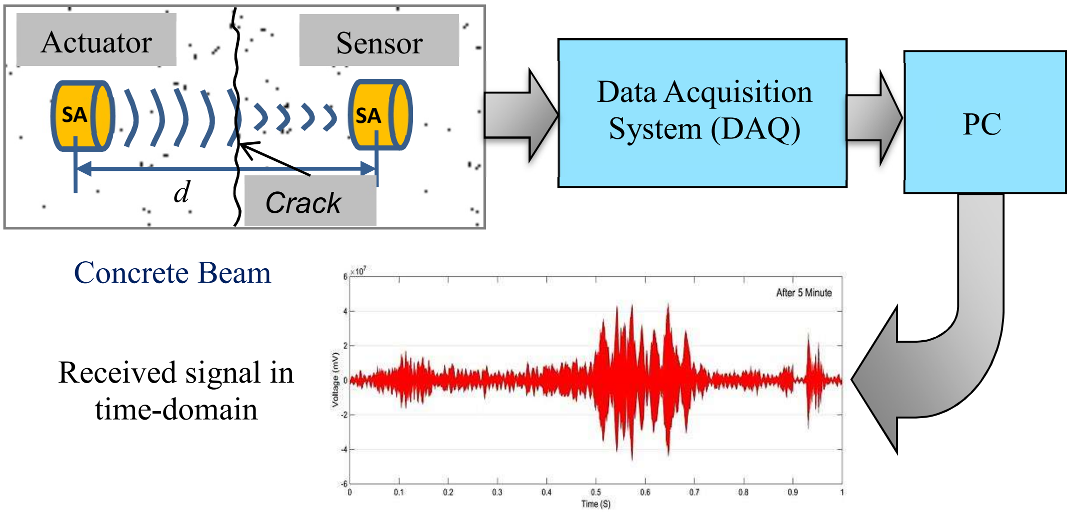

(b)

Figure 3-6: Schematic of the embedded SAs setup and its received signal in time-domain for a) material characterisation and b) detection and evaluation of defect

In this study, the SA-loaded method is proposed and applied for calibration or selection of SAs (Figure 3-7). Criterion for this calibration/selection method is the highest amplitude of received signal in time domain for each couple of transducers.

The frequency, signal swept period and amplitude of the sine waves were set to be 70 kHz, 1 s and of 10 V, respectively.

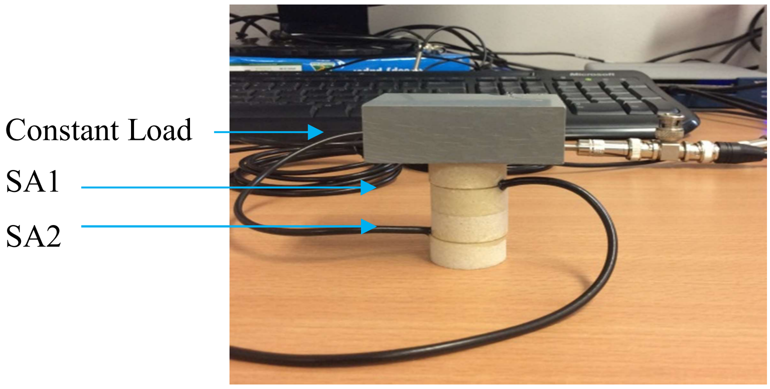

Figure 3-7: Picture showing calibration of SAs using the proposed SA-loaded approach

Fifteen SAs were selected for this study using the proposed approach. The SAs were tested by bonding each surface and the results recorded for each couple. Then from the recorded results SAs were selected based on highest and similar amplitude. Table 3-1 shows the SAs which selected using this approach. It can be seen from Table 3-1 that the maximum amplitude variation is from 0.4 to 0.46.

Table 3-1: Results of calibration of SAs using the constant load

Sensor Number	Max Received Amplitude	Actuator Number	Max Received Amplitude	Sensor Number
34	0.46	43	0.4	35
48	0.42	36	0.4	26
38	0.42	42	0.45	47
40	0.45	37	-	-
44	0.42	33	-	-
39	0.41	25	-	-

In order to investigate the performance of embedded SAs for the detection of cracks, two concrete specimens were attached from the side. The surface of each specimen was carefully polished before each test to achieve maximum bonding. Three SAs were used in this investigation, one as a sensor and two as both the sensor and actuator. Figure 3-8 shows a schematic view of specimens with embedded SAs. When two specimens were connected from the small side, there was no gap and the signal was saved in time-domain. In the next step, a small gap was created between specimens using a sheet of paper to simulate the cracks on concrete. The LabVIEW program for frequency range, signal swept period and amplitude of the sine waves were set to be 150 Hz -150 kHz, 1 s and of 10 V, respectively.

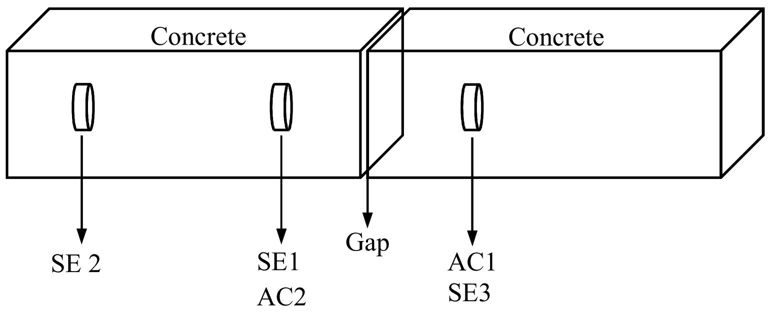

Figure 3-8: Schematic position of specimens and embedded SAs

The results show the signal, which propagated from one specimen, partially was received on the other specimen successfully. Total received power, peak of PSD, and peak of amplitude of the recorded signal are presented on Table 3-2. Table 3-2 shows that energy of the propagation waves attenuated due to the existence of a gap. The reduction in value of total received power, peak of PSD, and peak of amplitude confirms this observation. For example, total received power value between actuator 1 and sensor 1 from 0.38 dBm dropped to 0.249 dBm when a gap occurred.

Table 3-2: Measurement results of specimens with gap

Specimens	Total Received Power (dBm)	Δ	Peak of PSD (nV^2/Hz)	Δ	Max of Amplitude	Δ
AC1-SE1	0.38	-0.131	0.473	-0.269	0.006	-0.002
AC1-SE1+Gap	0.249		0.204		0.004	
AC1-SE2	0.192	-0.022	0.108	-0.026	0.0035	-0.003
AC1-SE2+Gap	0.17		0.082		0.0032	
AC2-SE1	0.158	-0.044	0.075	-0.025	0.0038	-0.002
AC1-SE1+Gap	0.114		0.050		0.0036	

3.3.2 Embedded and mounted SAs

Sensory systems with an embedded SA actuator and mounted SA sensors can be used for detecting of defects in concrete materials and mapping of stress wave intensity distribution in concrete specimens. This system is very sensitive to the location of sensors at the surface of specimens, and hence the use of sensors in the right location is important. To investigate the impact of the location of SA sensors, the specimen with an embedded SA actuator and loaded external SA sensor was prepared and used. The measurements were conducted at each point shown in Figure 3-9.

The results of these measurements are presented in Table 3-3. The LabVIEW program for frequency range, signal swept period and amplitude of the sine waves were set to 150 Hz -150 kHz, 1 s and of 10 V, respectively.

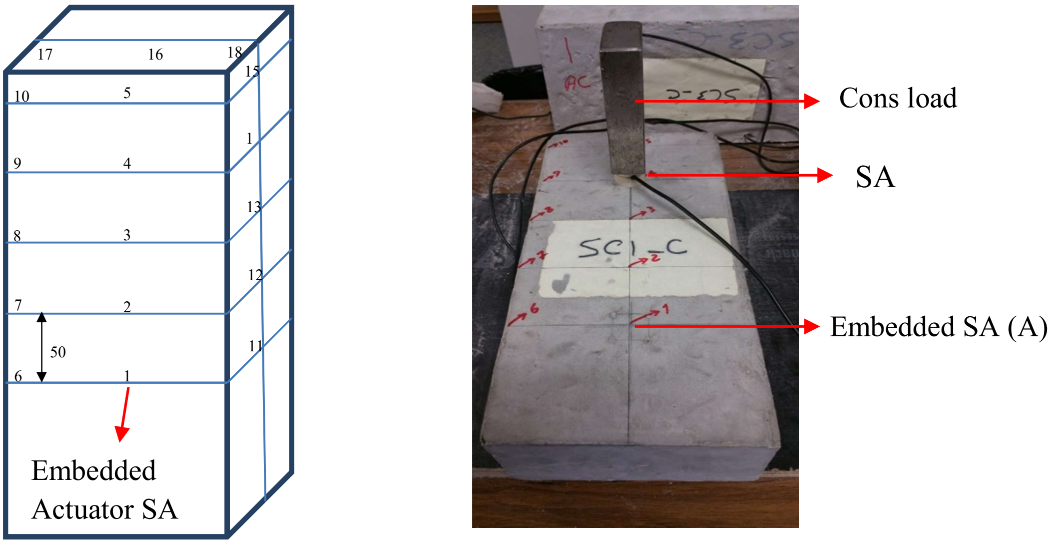

(a) (b)

Figure 3-9: concrete specimen with nominates locations for measurement shown in (a) schematic plan view and (b) during measurement

The results listed in the table reveal that when a sensor is in same cross section with an embedded actuator the received signals significantly increase. For example, the peak of PSD value received by the sensor in point 1 is 6.3 nV^2/Hz, while in point 2 is 0.72 nV^2/Hz. For better comparison, the results are plotted and shown in Figure 3-10. Similar observations can be drawn from the figure, such as the number 1 and 6 which are in same cross section where the actuator received the highest signal. The signal in other coordination also received some variation. In conclusion, although this system transmitted signal was successful received by the external SA, the variation of the received signal is an issue for detection and evaluation of defects.

Table 3-3: Results of specimens with external SA

Recorded number	Specimen	Peak of PSD (nV^2/Hz)	Peak of Amplitude
1	SC2C	6.3	0.034
2	SC2C	0.72	0.007
3	SC2C	0.86	0.008
4	SC2C	0.66	0.007
5	SC2C	0.51	0.006
6	SC2C	5.11	0.018
7	SC2C	0.49	0.006
8	SC2C	1.59	0.011
9	SC2C	0.39	0.005
10	SC2C	0.86	0.007
11	SC2C	1.30	0.01
12	SC2C	2.22	0.011
13	SC2C	0.77	0.008
14	SC2C	3.21	0.014
15	SC2C	0.74	0.007
16	SC2C	0.42	0.006
17	SC2C	0.27	0.004
18	SC2C	0.92	0.008

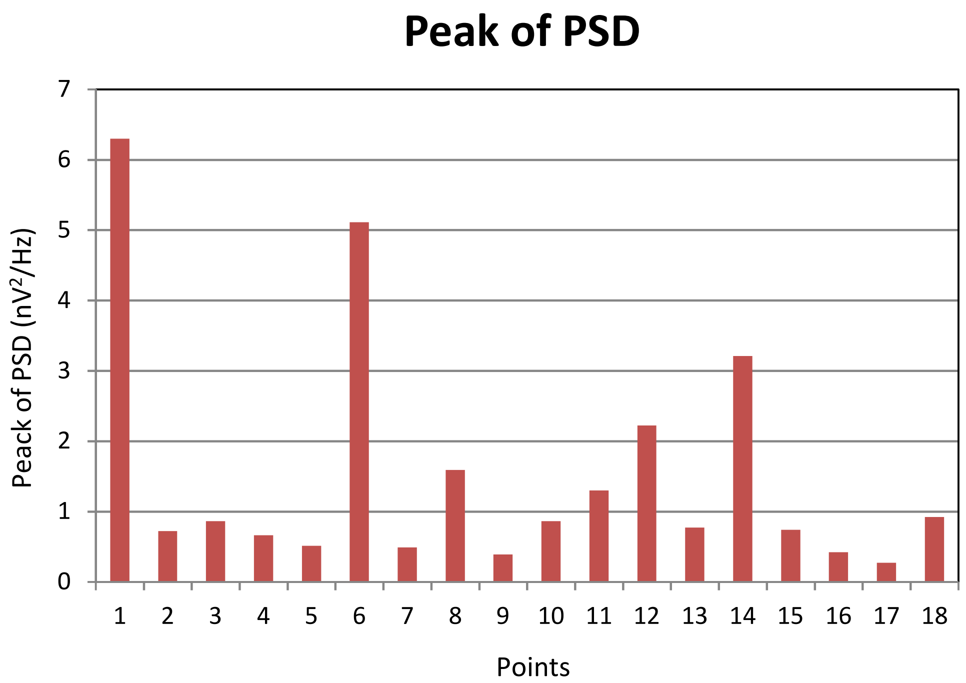

Figure 3-10: Variation of peak of PSD for different points on surface of specimen

3.3.3 Mounted SAs

As mentioned, in the study the mounted SA arrangement has been proposed using mounted transducers. To demonstrate feasibility of this approach, the preliminary investigation into detection of gap and crack in concrete material was performed. The investigation process was consisting of two parts: 1) detection of gap and 2) detection of crack in concrete. The application of this arrangement was verified with concrete specimen similar to one used in previous investigation.

The small gap between two concrete specimens can mimic a crack with a wide width. In order to detect the gap between two concrete specimens using the external SAs, firstly SAs were tested on one specimen without any gap with different distances. Following this, the selected couple of SAs were tested on two specimens with the gap (Figure 3-11). The SAs distances were set to be 20 mm and 40 mm and the results in time-domain and frequency-domain have been recorded and presented on Table 3-4. Both concrete specimens were casted from a concrete mix at same time. The surface of each specimen carefully polished before test to achieve to maximum connection between the specimens. LabVIEW program for frequency range, signal swept period and amplitude of the sine waves, was set to be 150 Hz - 150 kHz, 1 s and of 10 V, respectively.

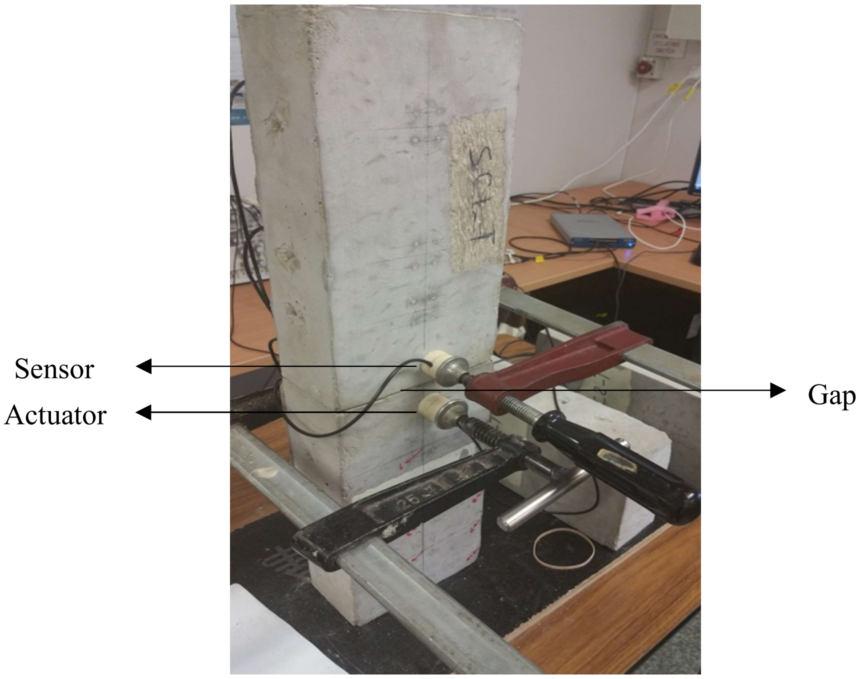

Figure 3-11: Concrete specimens with mounted SAs

Table 3-4 shows the results of this experiment. The main observation which can be making from Table 3-4 is that the gap was successfully detected by mounted SAs due to reduction the value of total received power, peak of PSD and peak of amplitude.

Table 3-4: Results for specimens with gap

Specimen	Total received power (dBm)	Peak of PSD (nV^2/Hz)	Peak of Amplitude
AC-SE-20mm	1.25	1.35	0.0112
AC-SE-20mm-Gap	0.44	0.60	0.0075
AC-SE-40mm	0.81	0.70	0.009
AC-SE-40mm-Gap	0.29	0.25	0.0062

For detection of crack using mounted SAs, a concrete specimen with a natural tiny crack was used (Figure 3-12). Firstly, SAs were mounted on the parts of concrete without a crack, which were healthy concrete. Secondly, the SAs were mounted on the cracked area and the received signal in time domain and frequency domain were recorded. Figure 3-13 shows a schematic view of specimen with location of mounted SAs. LabVIEW program for frequency range, signal swept period and amplitude of the sine waves were set to be 150 Hz -150 kHz, 1 s and of 10 V, respectively. Table 3-5 presents the calculations of the received signal peak of amplitude, peak of PSD, and total received power.

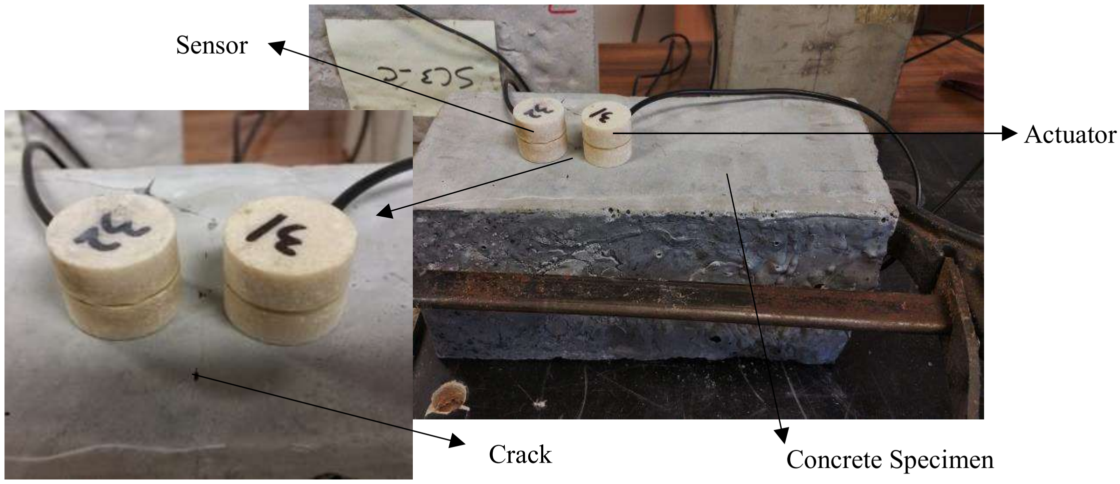

Figure 3-12: Concrete specimen with crack and SAs

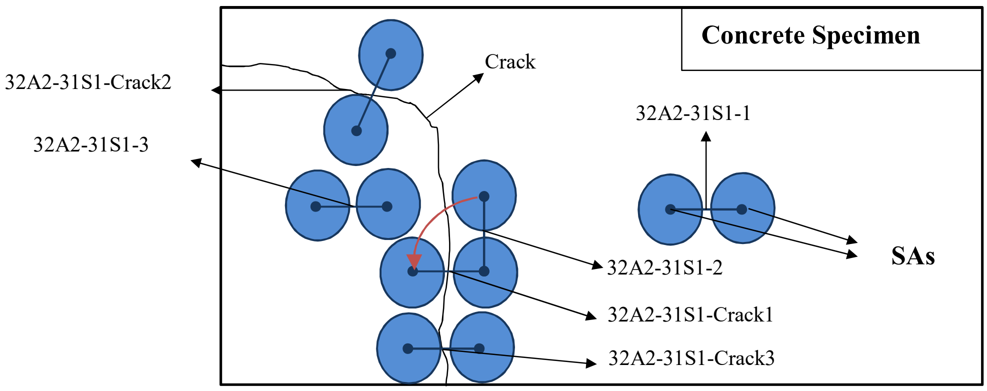

Figure 3-13: Schematic of SAs location on surface of concrete specimen

Table 3-5 shows that three recorded signals in healthy area shows their values of peak of amplitude, peak of PSD and total received power were very similar. This means the field distribution of mounted SAs received the same signal, contrary to the previous section in which the received signal varied.

A comparison between the results of the recorded signal in healthy and cracked areas of concrete shows the significantly decreased received signal in the cracked area, due to the crack. Therefore, the mounted SAs successfully detected cracks in concrete specimen.

Table 3-5: Results for specimens with and without crack

Specimen	Total received power (dBm)	Peak of PSD (nV^2/Hz)	Peak of Amplitude
32A2-31S1-1	1.32	3	0.013
32A2-31S1-2	1.57	3.8	0.015
32A2-31S1-3	1.48	3.21	0.017
32A2-31S1-Crack1	0.083	0.18	0.005
32A2-31S1-Crack2	0.061	0.13	0.003
32A2-31S1-Crack3	0.073	0.12	0.006

3.4 Boundary condition effect on wave propagation in specimen

There is an increasing demand in composite structures in many applications. Composite concrete-steel structures have been widely used. It is expected that when using mounted SA transducers and active sensing approach, steel material on concrete boundary can affect the wave propagation inside the concrete. Therefore, in this section the effect of steel plate on the propagation of stress wave in a concrete specimen is investigated.

Nine concrete specimens with three set of embedded SAs (50, 100 and 150 mm distances) have been used in this investigation. For comparison, specimens were tested using a plywood sheet and then a steel plate (Figure 3-14). LabVIEW program for frequency range, signal swept period and amplitude of the sine waves were set to be 150 Hz -150 kHz, 1 s and of 10 V, respectively.

Figure 3-14: Specimen with (a) plywood sheet and (b) metal plate

The SAs (i.e., SA actuator and SA sensor) were embedded in each specimen at the separation distance of 50, 100 and 150 mm. Therefore, the results of boundary condition were investigated in three groups. The first group included the results for the specimens with 50 mm distances between SAs, and the second and third group are including the results for the specimens with 100 and 150 mm distances, respectively (Table 3-6 to Table 3-8).

Table 3-6: Results for specimens with 50-mm distance between SAs

Specimen	Total received power (dBm)	Δ	Peak of PSD (nv^2/Hz)	Δ	Peak of Amplitude
SC1- Wood	88.13	+0.32	42.5	+0.5	0.052
SC1-Metal	88.45		43		0.055
SC2- Wood	143.96	+0.41	88.1	+3.4	0.076
SC2- Metal	144.37		91.5		0.078
SC3- Wood	79.87	+0.06	38.3	+1.4	0.048
SC3- Metal	79.93		39.7		0.053

Table 3-7: Results for specimens with 100-mm distance between SAs

Specimen	Total received power (dBm)	Δ	Peak of PSD (nv^2/Hz)	Δ	Peak of Amplitude
SC1- Wood	74.84	+0.02	43.1	+2	0.05
SC1- Metal	74.86		45.1		0.05
SC2- Wood	109.04	+1.36	46.5	+0.7	0.052
SC2- Metal	110.4		47.2		0.054
SC3- Wood	48.61	+0.02	32	+0.5	0.04
SC3- Metal	48.63		32.5		0.042

Table 3-8: Results for specimens with 150-mm distance between SAs

Specimen	Total received power (dBm)	Δ	Peak of PSD (nv^2/Hz)	Δ	Peak of Amplitude
SC1-Wood	61.72	+0.43	24	+0.01	0.038
SC1- Metal	62.15		24.1		0.038
SC2- Wood	53.39	+1.2	27.6	+2.9	0.04
SC2- Metal	54.59		30.5		0.042
SC3- Wood	26.86	+0.31	13.9	+1.3	0.03
SC3- Metal	27.17		15.2		0.031

The results show that the presence of steel plate slightly increases the total received power, peak of PSD, and peak of amplitude in concrete specimens compared to the influence of the plywood sheet. This increase is more obvious when there is a 150-mm distance between SAs which can be correlated to increasing the length of interaction between stress waves in concrete with a steel boundary. This effect should be considered when plan and set experiments based on propagation stress waves in concrete specimens and structures.

3.5 Summary

This chapter introduced the SA based systems with three SA arrangement approaches along with the active sensing method for experimental investigation of concrete members. It is shown that the received signals in time-domain and frequency-domain do not solely provide adequate information about a status of concrete member with respect to quality of concrete and integrity of the member. Therefore, power spectral density (PSD), total received power, and damage indexes were presented as useful data analysis tools for health monitoring of concrete members.

Systematic experimental investigation into capability of the SA based arrangements was performed and the following concluding remarks can be made:

1. It is shown that embedded SAs are able to provide the detection of gap in concrete based specimens. However, they could apply for detection and evaluation of crack in new structures while it is not applicable for existing structure. In addition, location of the embedded SAs cannot be changed. On the other hand, it is well known that they are very sensitive to changes of concrete and can be used for its characterisation. This advantage will be used in Chapter 4 for characterisation of early-age concrete.

2. A combination of embedded and mounted SA transducers can overcome some limitations of the embedded SA transducers. The investigation with an embedded SA actuator and mounted SA sensor performed in this this chapter showed that ability of this arrangement to change location of the mounted SA sensor on the surface of concrete specimen provided opportunity to measure stress wave field distribution and to optimize the location of SA sensor.

3. The proposed mounted SA based approach has demonstrated ability to detect cracks in concrete members. In this case location of any SA transducers on the surface of concrete members can be changed and optimized. This approach will be applied for detection and monitoring of cracks in concrete and reinforced concrete beams under loading.

Preliminary investigation into the effect of boundary condition on the received signal in concrete specimen has also been performed. It was shown that the presence of a steel plate as a part of concrete-steel composite slightly increase the total received power, peak of PSD and peak of amplitude of the received signal.

Chapter 4 : Early-Age Concrete Hydration Characterization Using Embedded Smart Aggregates

4.1 Introduction

One of the major variables influencing the performance of cementitious materials is their water-to-cement ratio (w/c). The w/c directly controls the volume of water available for hydration per unit volume of cement and establishes the initial spacing between cement particles. It also influences a wide variety of early-age concrete properties such as setting time, semi-adiabatic temperature rise, and autogenous shrinkage (Gu, 2007). The latter two variables can potentially be major contributors to early-age cracking of cement-based materials (Gilbert and Ranzi, 2010). The predesigned w/c ratio generally can be affected by natural aggregates saturation ratio, weather condition or transportation. It is very common that the w/c ratio and consequently slump test results in the field are slightly different than theoretical design requirements. Therefore, the determination of initial w/c ratio is one of the challenging tasks and non-destructive methods with high accuracy are desired for this purpose (Kong et al., 2013).

Previous investigations showed a successful application of SA transducers for early-age concrete health monitoring (Dumoulin et al., 2012, Kong et al., 2013). However, feasibility of determination of the initial w/c ratio by these transducers has not been investigated yet. In this study, the hydration process of concrete specimens with different w/c ratios are investigated using embedded SAs. The transmission properties of stress wave are analysed and experimental compressive strength test is conducted for verification. As mentioned in Chapter 2, the area of sensing covered by transducers was a challenge in application of embedded SA transducers and a potential of its increasing is investigated in this chapter through experimental test.

In this chapter, embedded SAs are used as actuator and sensors for the very early-age (0-20 hours) and early-age (0-8 days) concrete hydration characterisation. The second section describes the concrete mixture design, slump and compressive strength test procedure and results. The third section presents the transducers arrangements in moulds, their testing in water and the preparation of concrete specimens with the SAs. The forth section presents the results and discussion of measurement of concrete specimens with three values of w/c ratio and three distances between embedded SA transducers.

4.2 Concrete mixture and relevant general tests

4.2.1 Concrete mix design

In this investigation, several specimens have been prepared and the results for three batches of cement concrete fabrication are presented. Mixture was designed with w/c = 0.5 using the method recommended by ACI Committee 211 (ACI, 1991) for specimen SC2 referred to as a standard-based mix design. Other two concrete mixtures were prepared by simply reducing and increasing amount of water in weight to obtain w/c ratios of 0.45 and 0.55, and specimens SC1 and SC3, respectively, were made.

Locally available natural river gravel (coarse aggregate), natural river sand (fine aggregate), Australian Portland cement type GB and tap water were used in preparing the concrete mixture. The materials were tested to determine the physical properties required for mixture proportioning of concrete (Table 4-1).

Table 4-1: Material Properties used in concrete mixture

Materials	Property
Portland cement type GB	Specific gravity: 3.15
Natural river sand (Fine aggregate)	Specific gravity: 2.55 Size: 0.15 to 4.75 mm
Natural river gravel (Coarse aggregate)	Specific gravity: 2.60 Density: 1600 $\frac{kg}{m^3}$ Maximum size: 20 mm
Tap water	Density: 998 ~ 1000 kg/m3

In this research concrete mixing was designed based on the given w/c ratio. To prepare mixture for conventional concrete specimen the total weight per volume (U) can be defined as (ACI, 1991):

$$U = FA + CA + W + C \tag{4-1}$$

where FA, CA, W and C are the weight of fine aggregate, coarse aggregate, water and cement, respectively.

The total weight per volume of fresh concrete (U_f) was obtained from:

$$U_f = 10G_a(100 - A) + C\left(1 - \frac{G_a}{G_c}\right) - \mathrm{W}(G_a - 1) \tag{4-2}$$

$$G_a = 1/2(G_{CA} + G_{FA}) \tag{4-3}$$

where G_a is the weighted average specific gravity of combined fine and coarse aggregate and G_c and A are the specific gravity of cement and percentage of air content, respectively.

Amount of water, coarse aggregate, fine aggregate and cement for 1m^3 were calculated and the results are shown in Table 4-2.

From Table 4.1 the specific gravity of sand, gravel and cement are 2.55, 2.60 and 3.15, respectively. Then the weighted average specific gravity (G_a) can be calculated from Equation 4-3 as follows;

$$G_a = \frac{1}{2(2.60+2.55)} = 2.575$$

Table 4-2: Concrete mixing design for 1m^3

Mixture	w/c	Cement (kg)	Water (kg)	Sand (kg)	Gravel (kg)
SC1-1	0.45	410	184.5	644.7	992
SC2-1	0.5	410	205	644.7	992
SC3-1	0.55	410	225.5	644.7	992

The constituent materials were batched by weight and mixed in a drum-type-mixer for about six minutes. The batch volume was calculated taking the quantity of fresh concrete at least 20% more than the required in order to compensate the loss during mixing, sampling and testing of slump.

4.2.2 Slump test

The consistency and uniformity of fresh concrete are described by the term "slump." The slump of a given sample of ready-mixed concrete is measured in inches or millimetre and is determined by means of the universally accepted testing procedure described by ASTM designation C-143 (C143, 2004). A slump test is used to determine the correct hydration of a batch of concrete and directly depends on its w/c ratio.

Slump tests were performed by placing the fresh concrete into a metal mould in the shape of a cone. This slump cone was 203 mm in diameter at the bottom, 102 mm in diameter at the top, 305 mm in height, and open at both ends. The mould provided with foot pieces and handles, and tests were performed on a flat, rigid, nonabsorbent surface (Figure 4-1a). The tamping rod was used to consolidate the sample a round. The cone held firmly in place during filling by the operator standing on the two-foot pieces. By using a small shovel or scoop the cone filled 1/3 full by volume with fresh concrete and rod 25 times with the tamping rod. Distribute rodding strokes evenly over the entire cross section of the concrete. Each stroke penetrates the entire depth of this first layer. Immediately the cone filled another 1/3 by volume (to about half the height) and again rod 25 times. The rod to passes through this second layer of concrete and penetrates about 13 mm into the underlying layer. Finally, the cone filled to overflowing and again rod 25 times following the previous procedure. Strike off excess concrete from the top of the cone by means of a screeding motion of the tamping rod. After cleaning the overflow away from the base of the mould, removed the mould by raising it carefully in a vertical direction. The removal process performed in 5 ± 2 seconds. Finally, determine the slump of the concrete by simply placing the tamping rod horizontally across the inverted mould so the rod extends over the slumped concrete, immediately measured the distance from the bottom of the rod to the original centre of the top of the specimen (Figure 4-1b).

(a) (b)

Figure 4-1: Slump test (a) equipment and (b) measurement approach used in this investigation

4.2.3 Determination of compressive strength

Concrete mixture must be designed to provide a wide range of mechanical and durability properties to meet the design requirements of a structure. The compressive strength of concrete is the most common performance used by the engineer in designing building and other structures. In this investigation, the compressive strength is determined by breaking cylindrical concrete specimens in a compression testing machine and calculated from the failure load divided by the cross-sectional area resisting the load, and reported in units of a pound-force per square inch (Psi) or Mega Pascals (MPa).

The cylinders were tested using the procedure described for standard-cured specimens in ASTM C 31 (Standard, 2003). A test result is the average of measurement three standard-cured strength specimens made from same concrete mixture and tested at the same age. In this research strength requirements for concrete were at the age of 7 and 28 days. Each cylindrical specimen has dimensions of 150×300 mm or 100×200 mm when specified. Recording the mass of the specimen before capping provides useful information in case of disputes. To provide a uniform load distribution when testing, the cylinder under test was capped with sulphur mortar (ASTM, 2009).

Figure 4-2 shows photos of number cylindrical (C) concrete specimens made for 7th and 28th day compressive strength test. They have diameter of 100 mm and height of 200 mm.

Figure 4-2: Cylindrical specimens made for 7- and 28-day compressive strength test

The cylinder diameter measured in two locations at right angles to each other at mid-height of the specimen and averaged to calculate the cross-sectional area. The cylinder under test was centred in the compression testing machine under uniaxial compression and loaded to complete failure (Figure 4-3). The loading rate on a hydraulic machine was maintained in a range of 20 to 50 psi/s (0.15 to 0.35 MPa/s) during the latter half of the loading phase. The concrete strength was calculated by dividing the maximum load at failure by the average cross-sectional area. Three cylinders were tasted for each w/c ratio at same age and the average strength was reported as a test result.

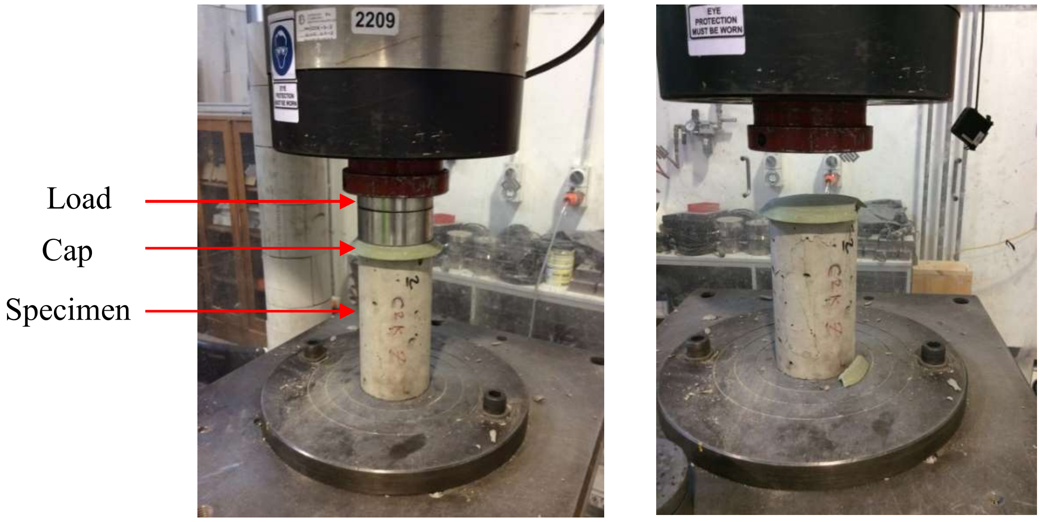

(a) (b)

Figure 4-3: Compressive strength hydraulic machine testing cylindrical concrete specimen: (a) before and (b) after test

4.3 SA arrangement, testing with water and concrete specimens preparation

4.3.1 SA arrangement and testing with water

Wooden moulds (300×150×75 mm) have been chosen and SAs fixed in entire position. Fresh concrete properties change with time. Hardening of concrete can be an issue if recalibration required. So, in this study water used as best homogenous material for characterisation of SAs signal before concrete casting.

For characterisation of SAs signal inside the specimen, the amount of water inside the moulds can be affected the transmission propagation of received signal. Figure 4-4 shows the mould fill in different levels of water and the signal recorded in time-domain and frequency-domain for comparison (Figure 4-5). Frequency range, signal swept period and amplitude of the sine waves were set to be 150 Hz -150 kHz, 1 s and of 10 V, respectively.

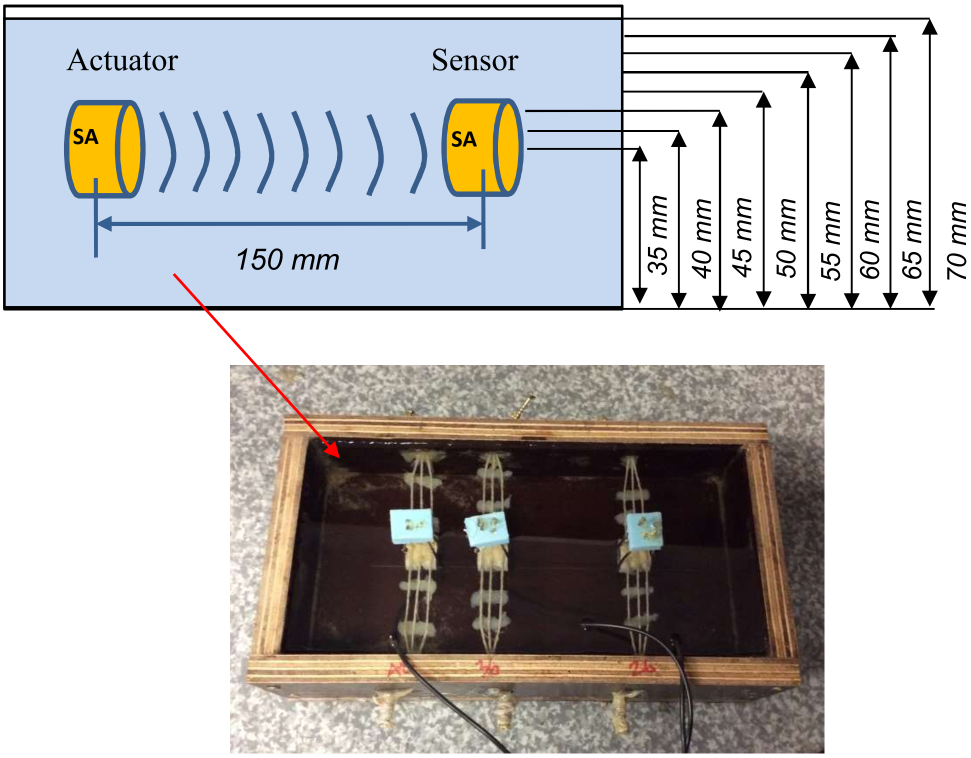

Figure 4-4: SAs position inside the mould with different levels of water

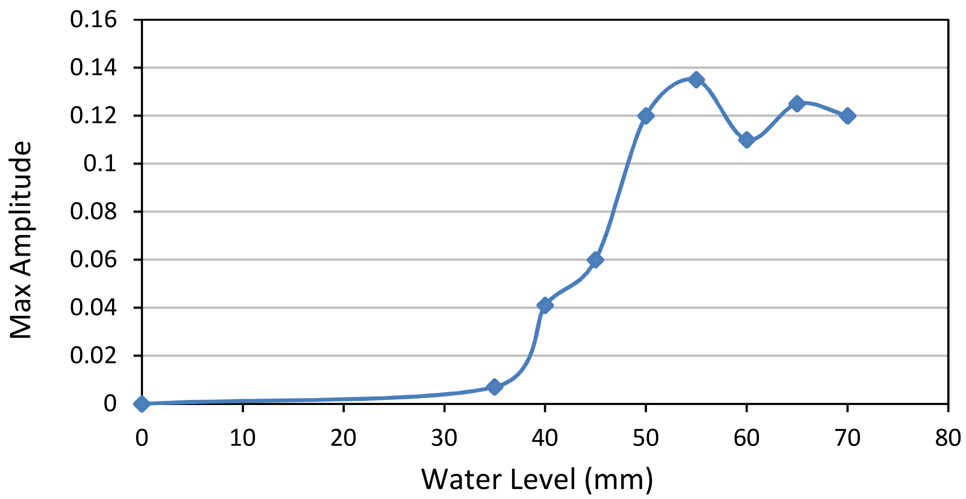

(a)

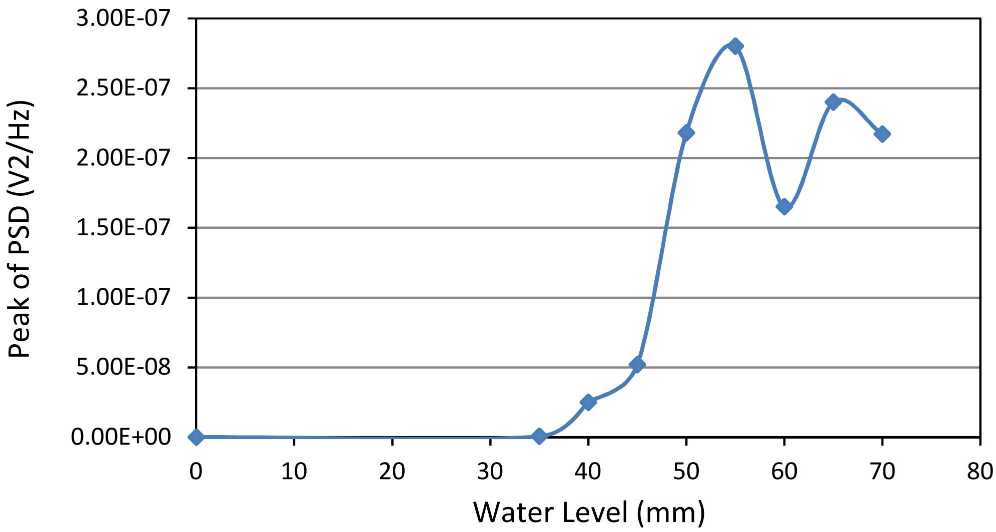

(b)

Figure 4-5: Results of SAs with different levels of water for (a) time-domain and (b) frequency-domain

The results show that the signal from the actuator successfully received by the sensor and it can be presented in both time-domain and frequency-domain. The results also show that the received signal significantly increased when the mould fill more than 45 mm in height, i.e. when water covered SAs. In addition, the highest amplitude and peak of PSD value have been received at 55 mm levels of water. Therefore, the calibrated SAs on free space are testing inside the mould filled with water at 55 mm in height. The results of this investigation are presented in Table 4-3 to Table 4-5.

Table 4-3: Characterisation of SAs inside the water at 50 mm distance

SA number	Distance (mm)	Total received power (dBm)	Peak of PSD (nv^2/Hz)	Peak of Amplitude
47-42A-38	50	12.455	9.28	0.07
26-36A-48	50	12.813	10.25	0.06
34-43A-35	50	11.25	8.86	0.054

Table 4-4: Characterisation of SAs inside the water at 100 mm distances

SA number	Distance (mm)	Total received power (dBm)	Peak of PSD (nv^2/Hz)	Peak of Amplitude
47-42A-38	100	4.368	2.12	0.011
26-36A-48	100	4.89	4.65	0.02
34-43A-35	100	4.569	3.6	0.012

Table 4-5: Characterisation of SAs inside the water at 150 mm distances

SA number	Distance (mm)	Total received power (dBm)	Peak of PSD (nv^2/Hz)	Peak of Amplitude
44-33A	150	3.183	1.22	0.015
40-37A	150	3.697	1.87	0.011
25-39A	150	3.375	2.8	0.0135

The results show that all the SAs received very similar signal in constant distances. The results also show that the highest signal received at the distance of 50 mm. Furthermore, the total received power results show less variation in different SAs arrangement rather than peak of PSD and peak of amplitude. Thus, testing SA arrangement in water confirms the free space calibration.

4.3.2 Concrete specimens preparation

Wooden cases were used as moulds to make specimens SC1, SC2 and SC3 with dimensions of 300×150×75 mm^3. In this study two specimens were taken from each batch of concrete with different SAs arrangement. Two or three SAs were embedded in each specimen at the separation distance of 150 mm, 50 mm and 100 mm, respectively (Figure 4-6a). After casting, the materials were vibrated for approximately 5 min. the moulds with a freshly cast concrete were covered with preservative plastic lids to provide a sound local moisture condition. The fresh concrete specimens were cured under laboratory condition with room temperature of 22 °C. Once all preliminary specimen treatments were finished (approximately 1 hour after casting), the piezoelectric monitoring system was activated right away to commence the measurement every one hour (Figure 4-6b).

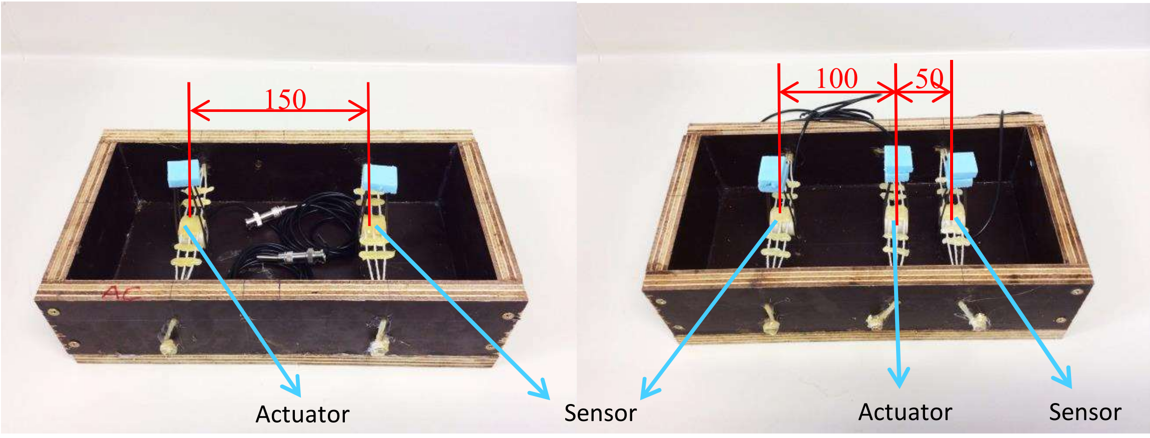

(a)

(b)

Figure 4-6: Concrete moulds with SAs: (a) before and (b) after casting

A LabVIEW program has been used to generate the swept sine-wave as the excitation wave and to provide signal processing of received signals. Frequency range, signal swept period and amplitude of the sine waves were set to be 150 Hz - 150 kHz, 1 s and of 10 V, respectively. The program recorded every hour after casting and saved the data in time-domain format.

4.4 Results and discussions

The results of monitoring of the concrete specimens with SAs were categorised in two main groups. The first group investigated the concrete very early-age (0-20 hours) and early-age (0-8 days) hydration characterisation with different w/c ratios, while the second group investigated effect of distance between embedded transducer on concrete early-age hydration monitoring.

4.4.1 Hydration process monitoring

In this research for verification purpose slump test were taken for SC1, SC2 and SC3 specimens from the start of the filling through the removal of the mould without interruption. The results illustrated at Table 4-6 and as expected, SC1 with lower w/c ratio and SC3 with higher w/c ratio show lower and higher slump value, respectively. The results also show that ratio value of the slump test result for (SC1/SC2) and (SC2/SC3) are 0.55 and 0.52, respectively.

Table 4-6: The results of slump test

Mixture	SC1	SC2	SC3
Water-to-cement ratio	0.45	0.5	0.55
Slump (mm)	55	100	190

The hydration process of the concrete had been monitored for 8 days. Utilizing the active-sensing approach, the sensor SA continuously received the propagated wave signal transmitted from the actuator SA. Figure 4-7 depicts the received time-domain signals from the sensor embedded in SC2 specimens with 50 mm distance every 5 hours after casting. Each plot corresponds to only one cycle of the detected signal, in the level of millivolts, from repeated swept sine wave. During first 5 hours, no received signal was detected for all specimens. After 5 hours, the figures show time-domain signals amplitudes in many different frequencies are growing with hydration time. From each plot, resonance peaks can be observed when hydration time increases. However, comparison between figures clearly shows changes of the received signal for each specimen, which can be correlated to changes of the specimens physical properties.

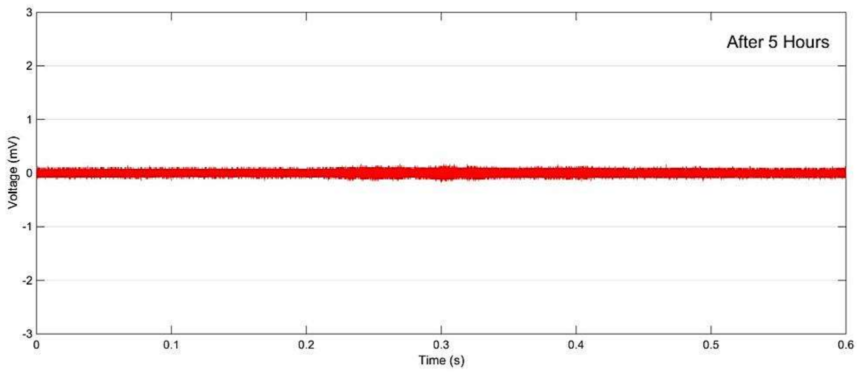

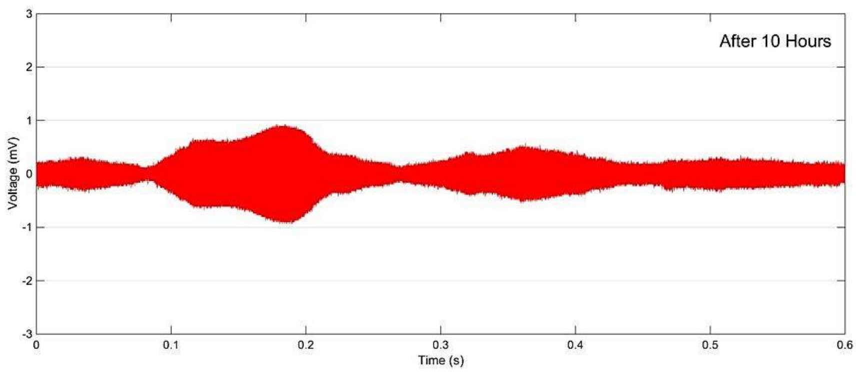

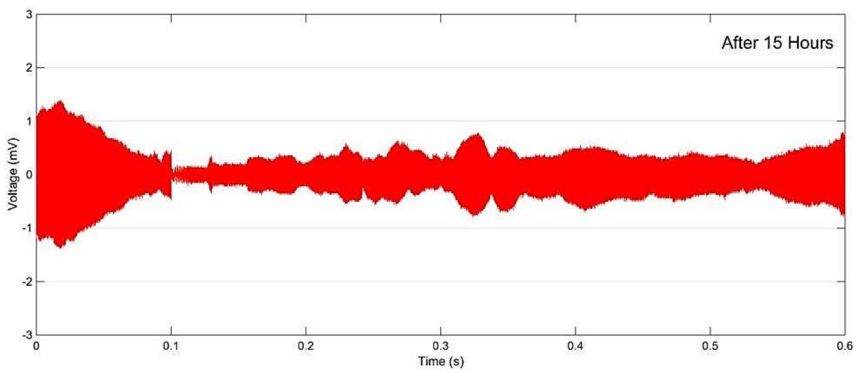

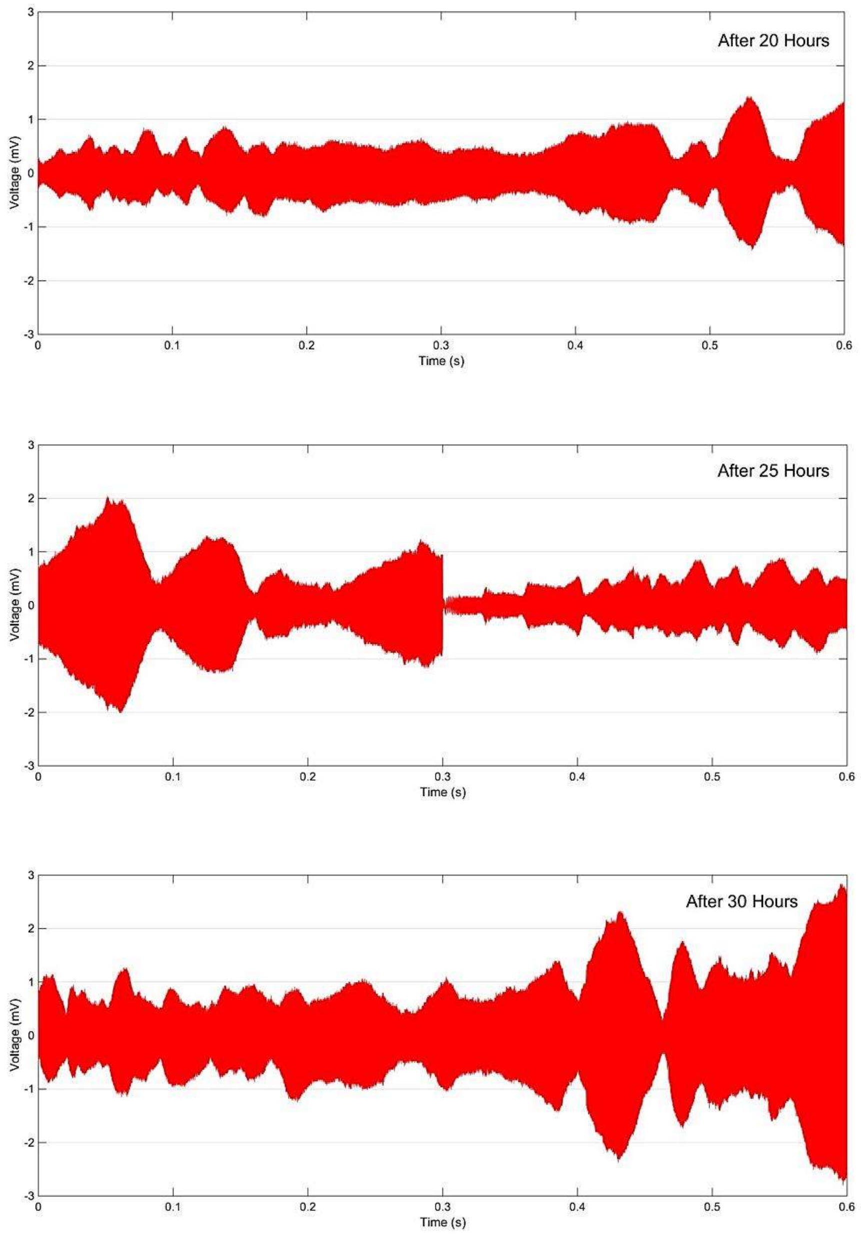

Figure 4-7: Received time-domain signals from the embedded sensor every 5 hours after casting for SC2 specimen with 50 mm distance

The results of time-domain received signal reveal that during concrete hydration the propagation properties of stress waves in concrete were changed. The results of this investigation confirm these changes and provide more information about monitoring of concrete hydration process using power spectral density (PSD).

Figure 4-8 shows the PSD plots (frequency-domain) for the corresponding time-domain signals shown in Figure 4-7. These frequency-domain power signals also display the maximum peak of PSD value for comparison. All PSDs are calculated using four periods of swept sine-wave in order to obtain a better accuracy.

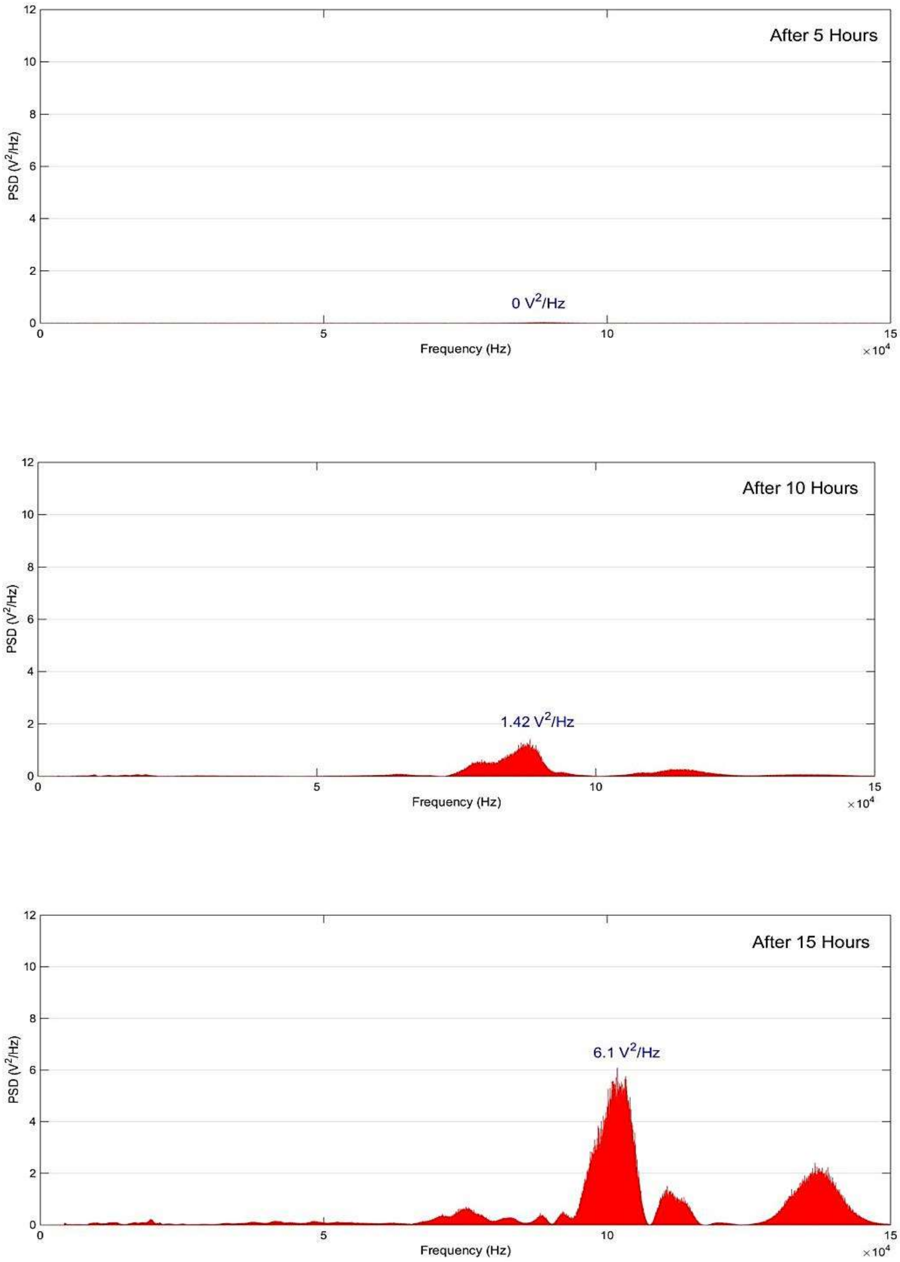

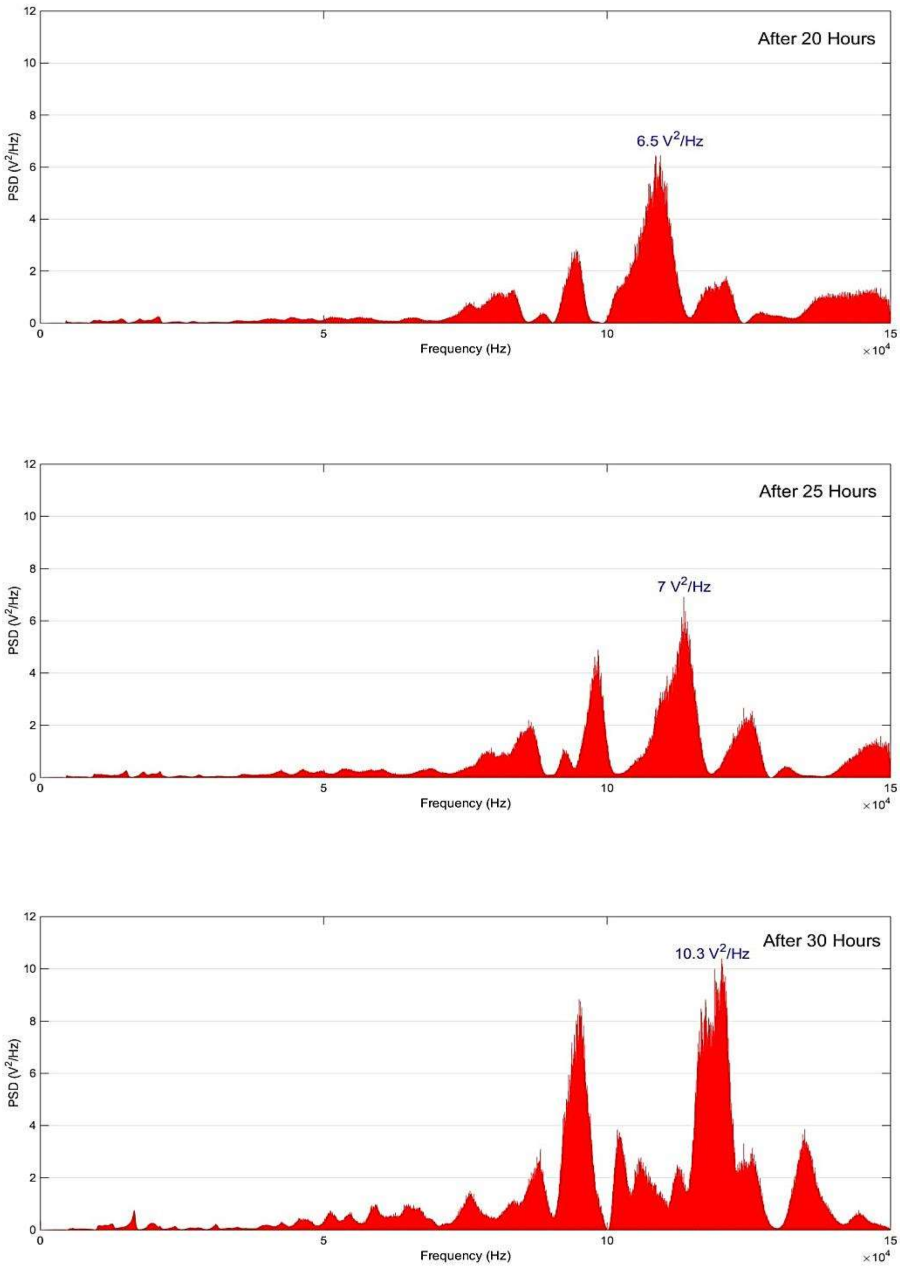

Figure 4-8: Power Spectral Density (PSD) of from the embedded sensor every 5 hours after casting for SC2 specimen with 50 mm distance

The test results in frequency-domain clearly show the changing in received signal versus concrete hydration. Furthermore, the maximum peak of PSD increases versus hydration process of concrete which means increases with concrete hardening process. The peak of PSD value after 5 hours is close to 1.42 V^2/Hz, while after 30 hours it is close to 10.3 V^2/Hz. Similar observations could be seen from other specimens during the hydration process (Figure 4-9).

Figure 4-8 also shows that the resonant frequency after 10 hours was close to 80 kHz while after 30 hours it increases to 120 kHz. To emphasise Figure 4-9 shows that the resonant frequency increases in first hours of measurement in all distances and then become more constant with small variations. This increase of the resonant frequency is probably caused by the increasing stiffness of the host structure.

The SC2 specimens with 0.5 w/c ratio show the highest resonant frequency in first hours while SC3 with 0.55 w/c ratio shows the lowest one. As Figure 4-9b shows for 100 mm distance; the highest resonate frequency received on the SC2 at the first hours, while the lowest resonate frequency in SC3. This observation is more obvious for 150 mm distance as shown in Figure 4-9c.

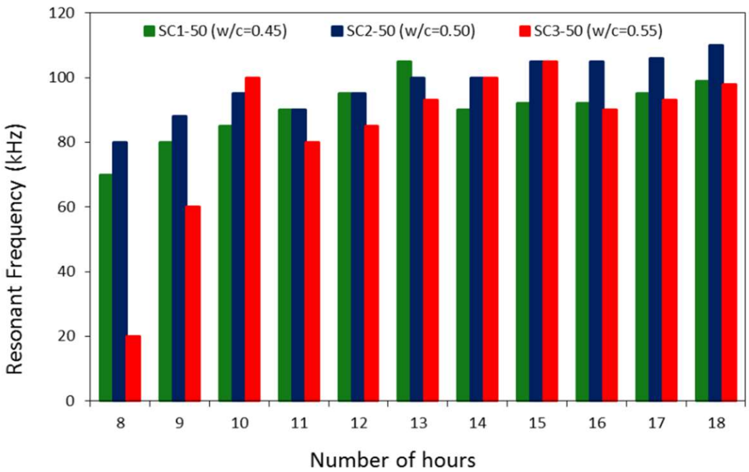

(a)

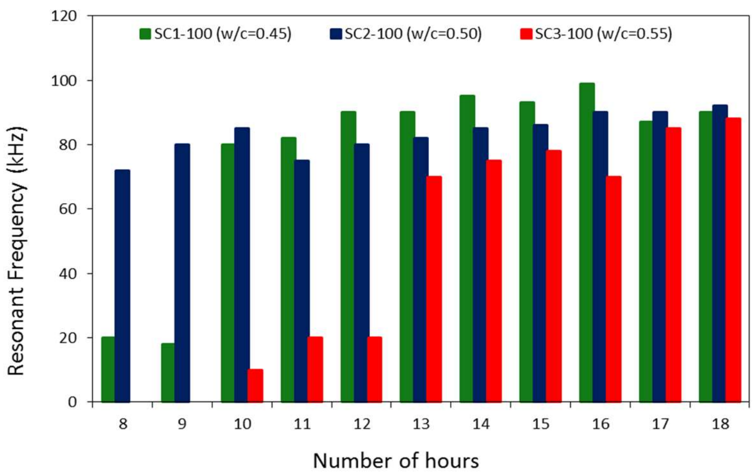

(b)

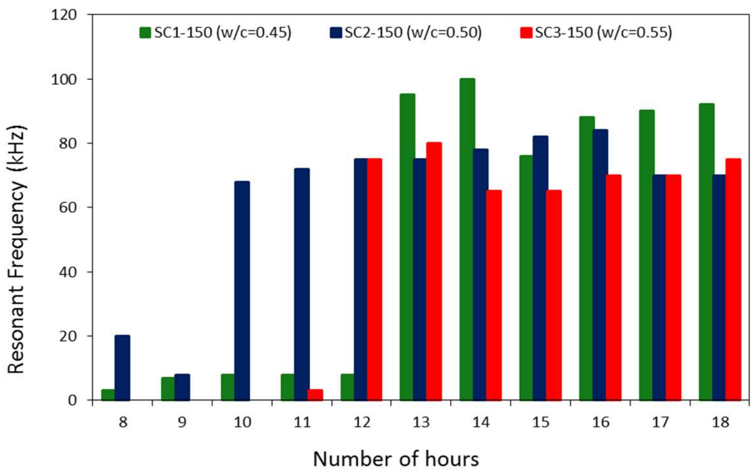

(c)

Figure 4-9: Resonant frequencies of all specimens versus hours for (a) 50 mm, (b) 100 mm and (c) 150 mm distance

For future investigation and analysis, the PSD results on LabVIEW program were exported to MATLAB program. The results of monitoring of the amplitude of peak of PSD were obtained using MATLAB code and shown in Figure 4-10 and Figure 4-11 for 50, 100 and 150 mm distance for very early-age and early-age concrete, respectively.

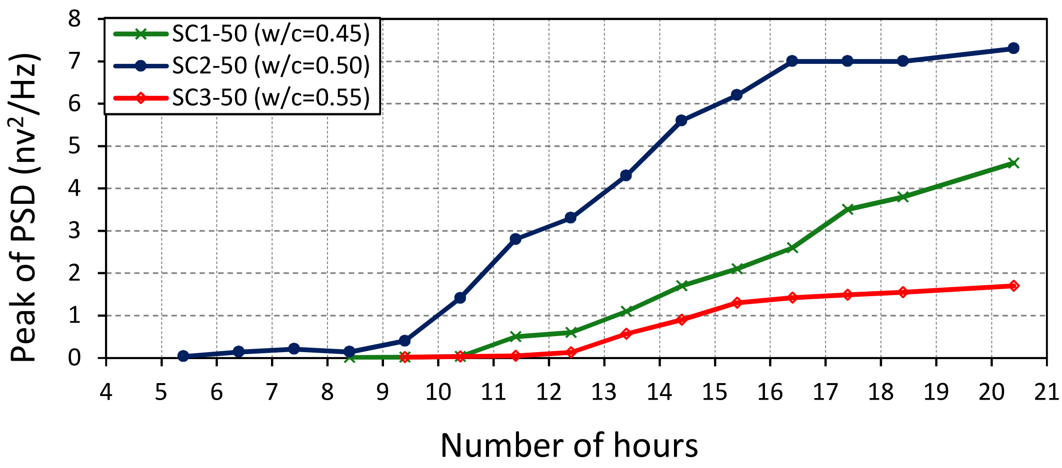

(a)

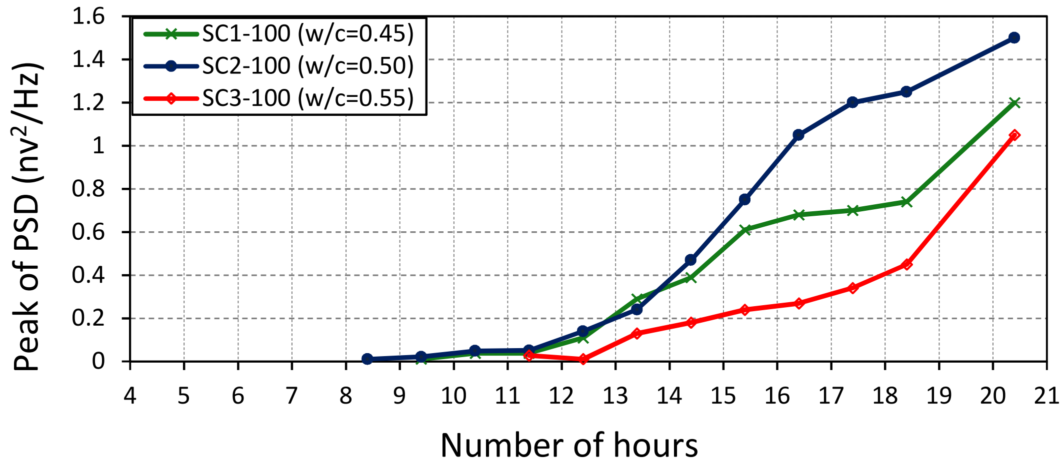

(b)

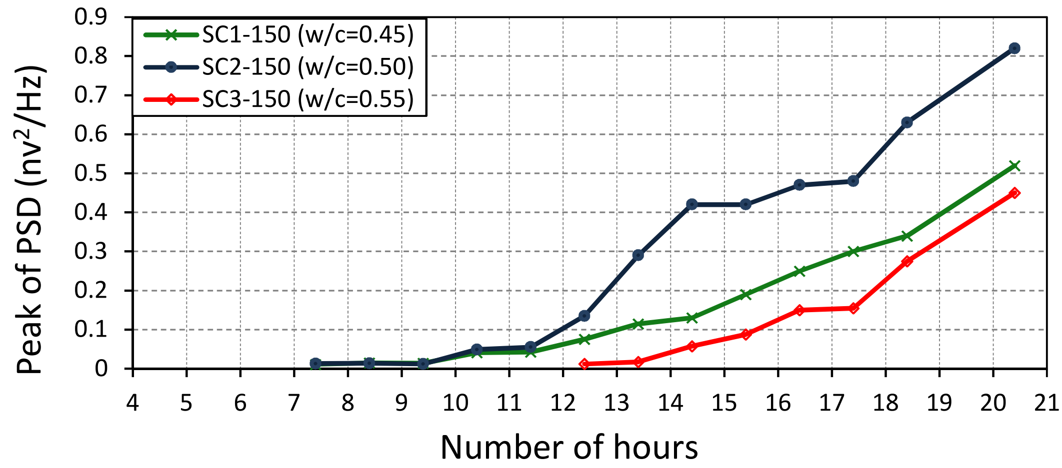

(c)

Figure 4-10: Peak of PSDs of received signal at the distances of a) 50 mm b) 100 mm and c) 150 mm during first 20 hours.

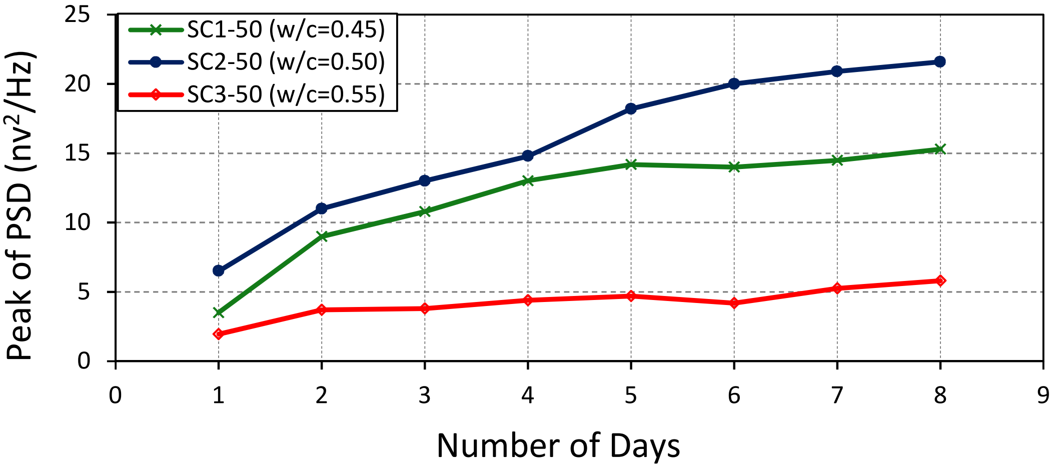

(a)

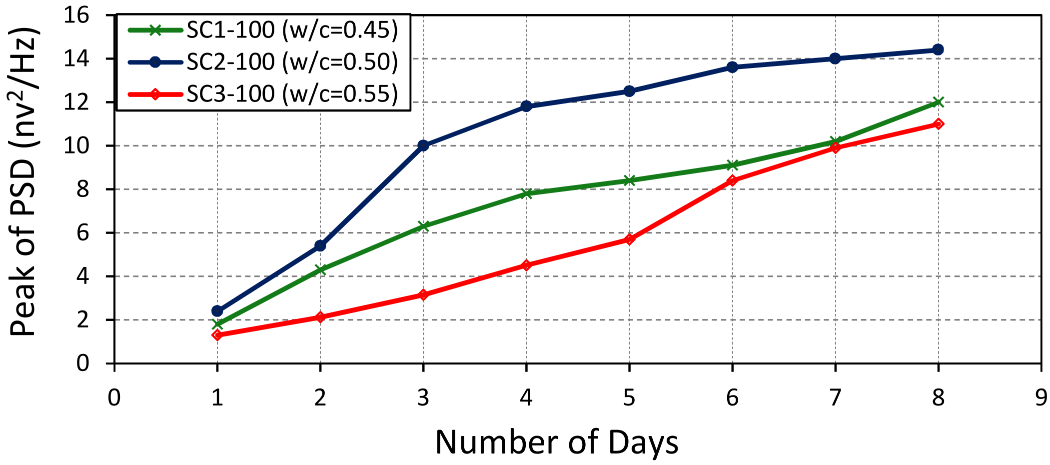

(b)

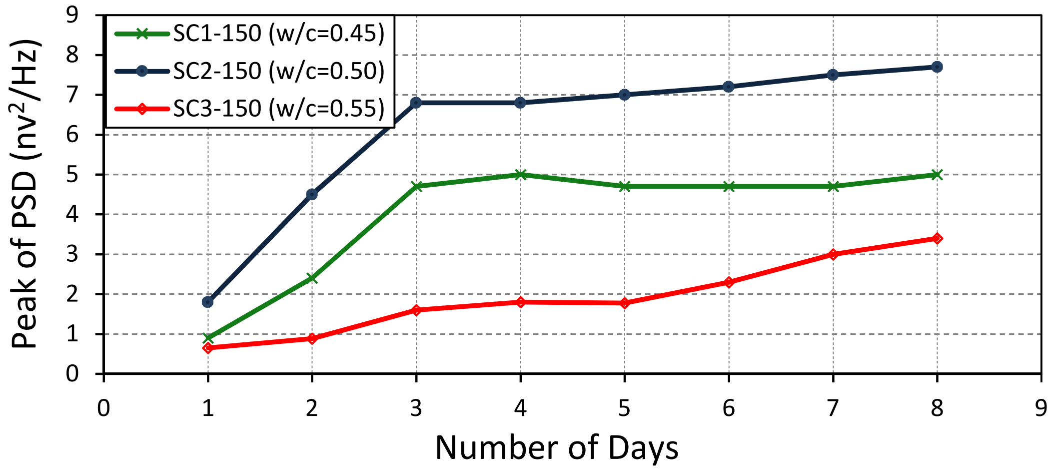

(c)

Figure 4-11: Peak of PSDs of received signal versus times at the distances of a) 50 mm b) 100 mm and c) 150 mm during first 8 days

Several observations can be made from above figures as follows:

The results very early age concrete plotted in Figure 4-10 show that the peak of PSD value significantly increases during concrete hydration process in first 20 hours. In Figure 4-10a the peak of PSD value for specimen SC2 after around 5.30 hours is close to 0.013 V^2/Hz, while after 20 hours it is close to 7.3 V^2/Hz. Same observation can be taken for other specimens with different distances between transducers.

As the Figure 4-10a results for 50 mm distance shows the first signal received by specimens SC1, SC2 and SC3 were at around 8.30, 5.30 and 9.30 hours after casting, respectively. These results in Figure 4-10b with 100 mm distance were at around 9.30, 8.30 and 11.30, respectively. While in Figure 4-10c for 150 mm distance was at round 7.30, 7.30 and 12.30, respectively. Therefore at all distances, the SC2 specimens received the first signal among others, which means it has faster hydration process which could lead to highest compressive strength.

A comparison between Figures 4-8 a, b and c shows that the amplitude of peak of PSD significantly decreases with increasing the distance between transducers. The maximum peak of PSD for specimen SC2 in Figure 4-10a is close to 7.3 V^2/Hz, while in Figure 4-10b and Figure 4-10c is close to 1.5 V^2/Hz and 0.82 V^2/Hz, respectively.

The results of early-age concrete plotted in Figure 4-11 show that the peak of PSD value increases during concrete hydration process after 1st day with less slope to very early-age concrete. The SC2 specimen with 0.5 w/c ratio still shows the highest peak of PSD to other specimens in all distances. For example, Figure 4-11a shows that the peak of PSD value for specimen SC2 is close to 21.6 V^2/Hz, while for SC1 and SC3 are close to 15.3 V^2/Hz and 5.8 V^2/Hz, respectively.

In summary, the specimens SC2 which represented the standard-based concrete with 0.5 w/c ratio shows highest peak of PSD value in all distances between transducers. In addition, the first signal received by SC2 specimens due to faster hydration process which could lead to highest compressive strength.

The previous investigations show that the peak PSD is not outstanding, rather a number of frequencies share the received power. Therefore, this has motivated us to use an alternative method of total received power introduced in chapter 3 to monitor and gauge the hydration process. Figure 4-12 to Figure 4-13 shows the calculated total power received by the sensor versus number of hours. As expected, the growth of total power of frequencies increased more linear and more obvious than the use of peak PSD.

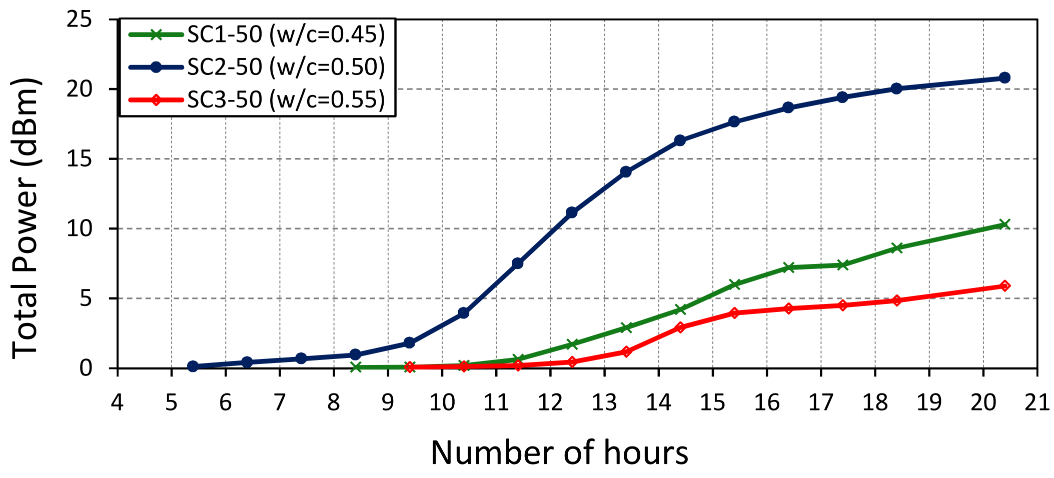

(a)

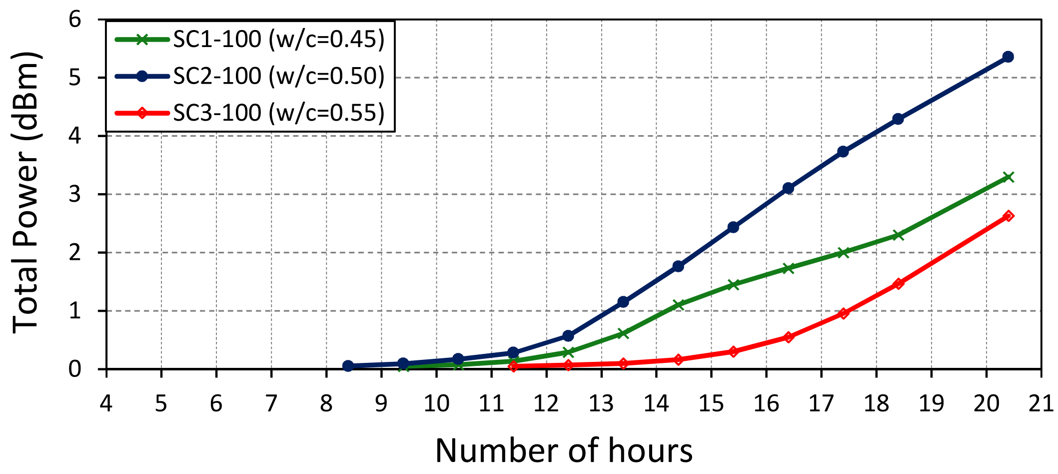

(b)

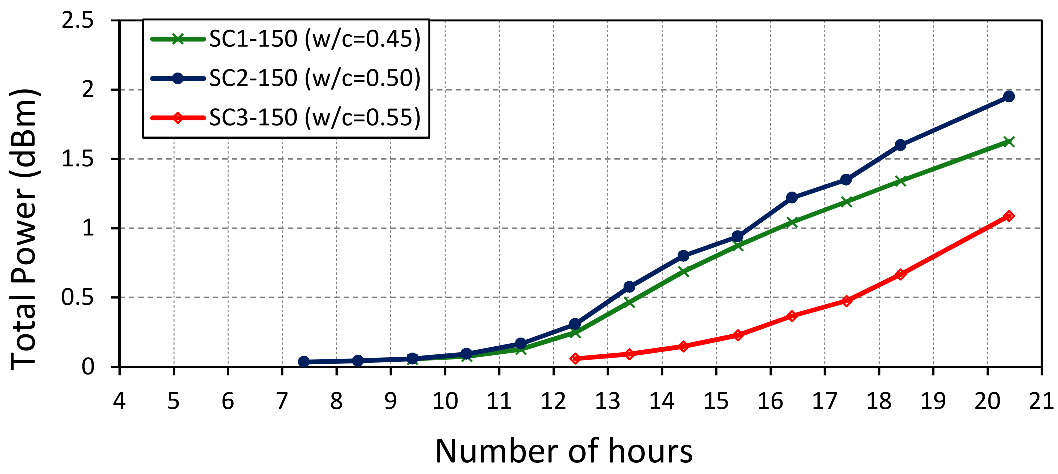

(c)

Figure 4-12: Total power received of received signal at the distances of a) 50 mm b) 100 mm and c) 150 mm during first 20 hours.

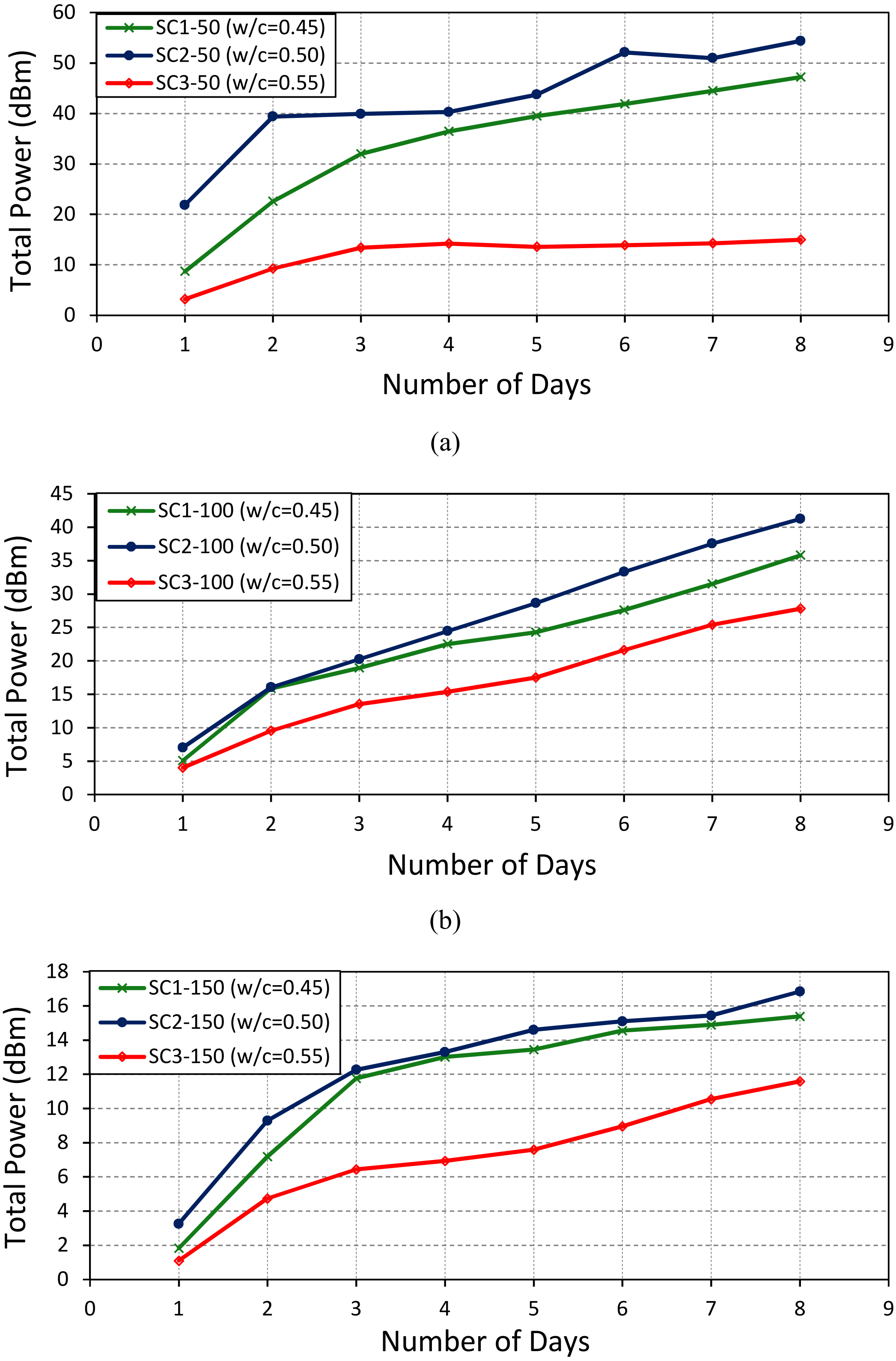

(a)

(b)

(c)

Figure 4-13: Total power received of received signal at the distances of a) 50 mm b) 100 mm and c) 150 mm during first 8 days

Several observations can be made from Figure 4-12 and Figure 4-13.

The results of very early-age concrete plotted in Figure 4-12 show that the total received power value significantly increases during concrete hydration process in first 20 hours. In Figure 4-12a the total received power value for specimen SC2 after around 5.30 hours is close to 0.119 dBm, while after 20 hours it is close to 20.79 dBm. Same observation can be taken for other specimens with different distances between transducer.

Similar to peak of PSD results for total received power results the SC2 specimens received the first signal due to faster hydration process which could lead to highest compressive strength.

A comparison between Figure 4-12a, b and c shows the peak of PSD significantly decreases with increasing the distance between transducers. The maximum total received power value for specimen SC2 in Figure 4-12a is close to 20.79 dBm, while in Figure 4-12a and Figure 4-12b is close to 5.35 dBm and 1.94 dBm, respectively.

The results of early-age concrete plotted in Figure 4-13 shows that the total received power value increases during concrete hydration process after 1st day with less slope to very early-age concrete. The SC2 specimen with 0.5 w/c ratio still shows the highest total received power to other specimens in all distances. For example, Figure 4-12a shows the total received power value for specimen SC2 is close to 54.37 dBm, while for SC1 and SC3 are close to 47.19 dBm and 14.97 dBm, respectively.

In summary, the specimens SC2 which represented the standard-based concrete with 0.5 w/c ratio shows highest total received power value in all distances between transducers. In addition, the first signal received by SC2 specimens due to faster hydration process which could lead to highest compressive strength. Therefore the results of compressive strength required for verification purpose.

Compressive strength tests were conducted at 7th and 28th days for each w/c ratio. The average values compressive strength test results are presented in Table 4.7.

Table 4-7: Compressive strength test results

Specimens	w/c	CS after7 Days (MPa)	CS after 28 Days (MPa)
SC1	0.45	18.90	29.20
SC2	0.50	20.60	32.45
SC3	0.55	13.67	22.37

As the results show the 28 days compressive strength for SC2 specimens meet the design requirement compressive strength which was 30 MPa. Furthermore as expected the highest compressive strength allocated to SC2 which was the main design concrete. SC1 specimens are in second rank while specimen SC3 has the lowest compressive strength value due to the highest w/c ratio. Therefore, the comparison between compressive strength results and signal processing results reveals that SC2 specimen with 0.5 w/c ratio shows highest received signal and compressive strength.

4.4.2 Effect of change of distances between transducers on early-age concrete hydration monitoring

This section investigated the properties of the received signal at different distances between the SA sensor and the SA actuator.

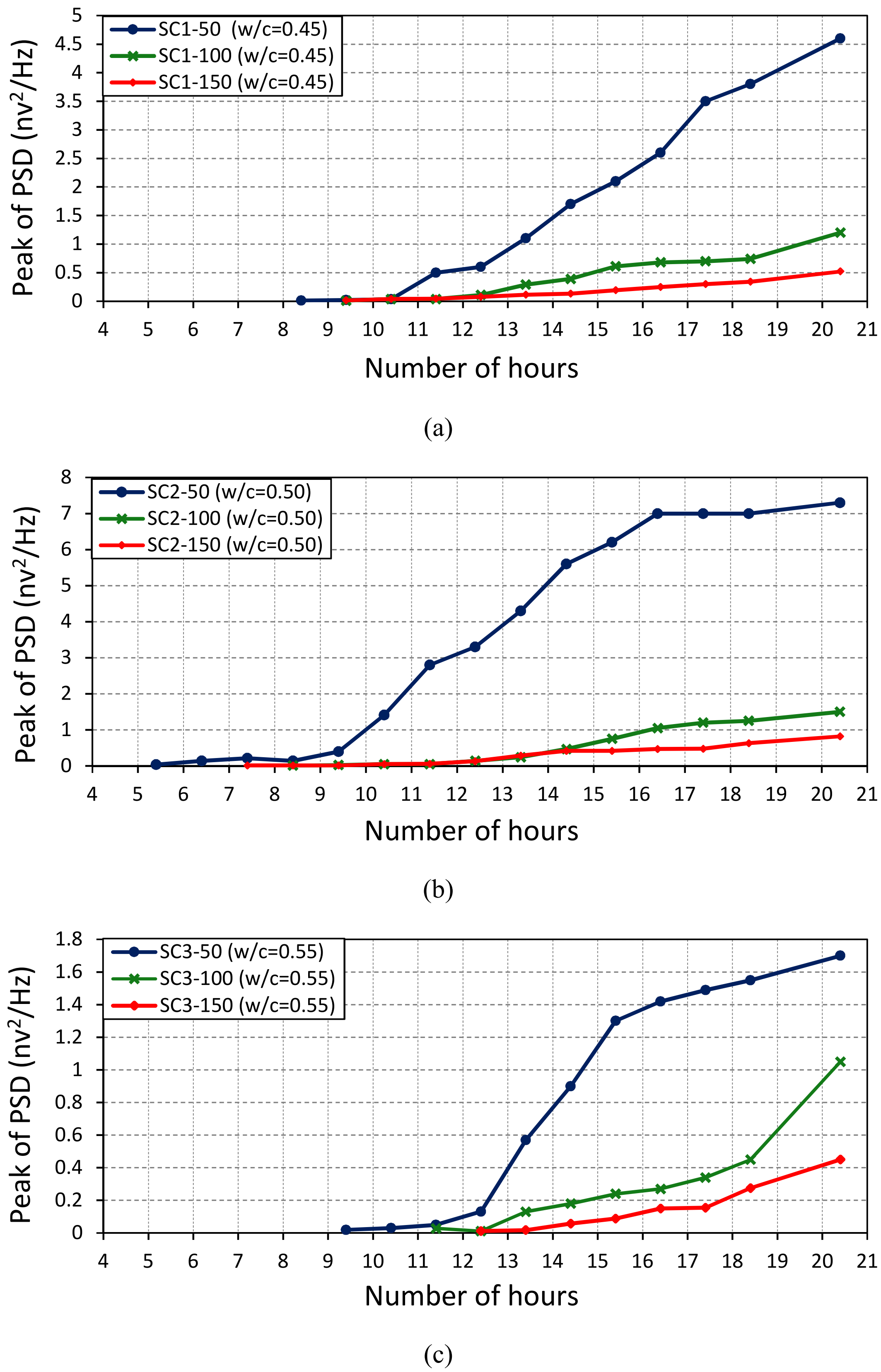

Figure 4-14: Peak of PSDs of received signal versus times for a) 0.45 b) 0.50 and c) 0.55 w/c ratio in first 20 hours

As the above figures shows the highest value of peak of PSD is for 50 mm distances between embedded SAs. Figure 4-14b shows for 0.5 w/c ratio the maximum peak of PSD value for SAs with 50 mm distance is close to 20.4 V^2/Hz, while for 100 mm and 150 mm distances are close to 1.5 V^2/Hz and 0.82 V^2/Hz, respectively. Furthermore the first signal received by embedded SAs with 50 mm distance, while the 100 mm and 150 mm received first signal few hours later. The results also show there is significant difference in value of peak of PSD for 50 mm distances in comparison to other distances, while the 100 mm and 150 mm shows very similar results with slightly difference. In summary, the 50 mm distances between embedded SAs shows better performance for monitoring early-age concrete hydration characterisation.

4.5 Summary

The main purpose of this chapter was hydration process monitoring in concrete specimens with different values of w/c ratio and distances between embedded SAs. Several moulds were prepared and in some of them two SAs were installed at the separation distance of 150 mm and in other moulds three SAs were installed at separation distances of 50, 100 and 150 mm. Preliminary measurements were conducted with water in these moulds with the SAs. The results of these measurements not only confirmed workability of the SAs active system but also demonstrated a measurable magnitude of the received signals and the influence of water level on the received signal.

For the preparation of concrete specimens three batches of cement concrete were prepared with values of w/c ratio of 0.45, 0.50 and 0.55. In this investigation very early-age (0-20 hours) and early-age (1-8 days) concrete hydration successfully monitored using proposed approach. For the first time indication of the received signal was observed in around 5.30 hours after casting for concrete with 0.5 w/c ratio and 50-mm distance between SAs.

Based on the experimental results, the following conclusion remarks can be drawn:

1. The investigation of SAs embedded in water showed that the received signal was measurable and its amplitude could be controlled by changing amount of water in moulds. In general, the preliminary measurement in water can be used for selection and calibration of SAs before concrete casting.

2. The result showed that SAs can be successfully applied for very early-age concrete hydration monitoring. The peak of PSD and total received power increased with the development of hydration process.

3. The results also showed that the changes of water amount (i.e., initial value of w/c ratio) in standard-based concrete mixtures decreased the received signal and compressive strength of concrete.

4. The received signal gradually decreased when the separation distance between SA actuator and sensor increased.

5. The proposed embedded SA based approach can be used for the determination of initial w/c ratio and compressive strength of concrete at its early-age stage.

Chapter 5 : Detection and Monitoring of Crack in Concrete Beams under Bending Using Mounted Smart Aggregates

5.1 Introduction

The previous chapter has demonstrated the capability of the use of embedded SA transducers to monitor concrete structures. As mentioned, embedded SAs must be implemented in new concrete structures during their fabrication. In addition, they are sensitive to changes of many parameters and it is difficult to distinguish their contributions to the changes of stress wave propagation characteristics. If we target the detection and monitoring of cracks in concrete members under loading, stress wave sensitivity to undesired changes of physical properties of concrete such as moisture and shrinkage may mask indication of cracks and/or their changes.

In this chapter, a mounted SA based active sensing approach is proposed and applied for detection and monitoring of cracks in unreinforced concrete beams under loading. This approach is different from mounted patch based techniques in terms of its relatively easy installation (even after a concrete casting) and the fact that there is no need for additional sensor protection. It is also expected that SA housing made of marble can provide better impedance matching with concrete than piezoelectric patches. In this study, the proposed technique is experimentally applied for concrete beam specimens, on which SAs are mounted, in order to monitor the status of the concrete beams under bending and to detect load-induced cracks.

This chapter has three main sections, with the first section presenting the experimental set up for testing concrete beams using three point bending tests. The second section provides details of sensor arrangement on concrete beams based on the approach presented in Chapter 3. The last section presents experimental results for the 10 concrete beams using recorded signals at both the time domain and the frequency domain, and data processing results including the PSD, total received power and their standard deviations. The correlation of these results with those obtained with load cell and strain gauges is analysed and discussed.

5.2 Concrete beam preparation and loading setup

To cast concrete beams, the mix proportion of the ready-mixed concrete was used. The design was based on the aggregates with the maximum size of 10 mm, a slump of 70 mm, 28 day-compressive strength of 40 MPa, and the water-to-cement ratio of 0.48. The Australian Portland cement type GB was used, and the concrete and sand conformed to AS3600 (2009). All the material properties used in this study are summarised in Table 5-1.

Table 5-1: Properties of materials used in concrete mixture

Materials	Properties	Values
Portland cement type GB	Specific gravity	3.15
Natural river sand (Fine aggregate)	Specific gravity	2.55
	Size	0.15 to 4.75 mm
Natural river gravel (Coarse aggregate)	Specific gravity	2.60
	Maximum size	10 mm
Tap water	Density	998 ─ 1000 kg/m^3

The slum test was taken before the concrete casting to check design requirement (Figure 5-1a). 20 standard cylinders were cast with the identical size of 102 mm x 203 mm (Figure 5-1b). The cylinders were cast and cured under the same environmental condition as that of the concrete beams, i.e. cured under moist burlap cover for 7 days and in an air-conditioned laboratory until the 3-point bending test was carried out. After 7, 14, 28, 56 and 92 days from the casting, the compressive strengths were measured for four specimens at each day.

a) A slump Test

b) Concrete Cylinders

Figure 5-1: a) Slump test before casting and b) concrete cylinders after casting

Figure 5-2: Concrete beam casting and preparation

Ten concrete beams with the nominally identical size of 400 mm × 100 mm × 100 mm were tested. The moulds were fabricated using plywood. The specimens were vibrated after casting and surface finishing was done by hand floating (Figure 5-2). The specimens were tested in the test frame shown in Figure 5-3. The Instron universal test machine, with a loading capacity of 200 kN was used, was installed in the Structural Laboratory at the Western Sydney University, Australia. The machine had high bandwidth DSP (Digital Signal Processing) based electronics and Bluehill modular applications software. The machine was equipped with loading cell to monitor real-time, and loaded onto a concrete beam specimen with software designed to record load change.

Figure 5-3: Instron universal test machine

The machine software was set up based on specimen dimensions, material properties, test type, and loading input as shown in Figure 5-4. The loading cell was initialised to zero force before the start of loading, after confirming that there was no pressure on a specimen. The displacement movement was set to be 0.01 mm/min to ensure generally accurate monitoring of the specimens cracking.

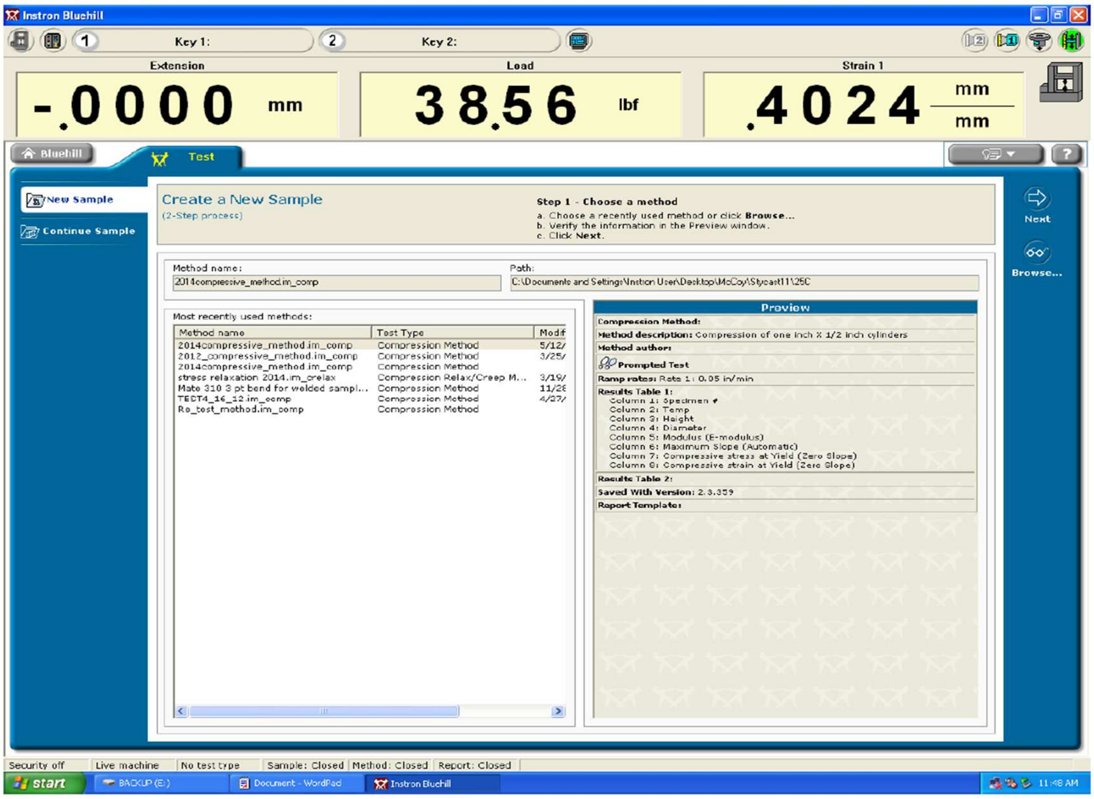

Figure 5-4: Software setup for Instron machine

A three point bending test was conducted, with the specimens placed on top of two pedestals, while a loading pin at the top of the specimens applied force to the specimens. The load was increased until the failure occurred at the mid-span of the specimens. Due to the very slow load increase, each test took almost one hour.

The concrete beams in this study were not reinforced, and thus only one thorough crack appeared in mid-spam of each beam, as shown in Figure 5-5. Immediately after the cracking, the concrete beam lost its resistance, and this was shown in the loading history as a sudden decrease of loading.

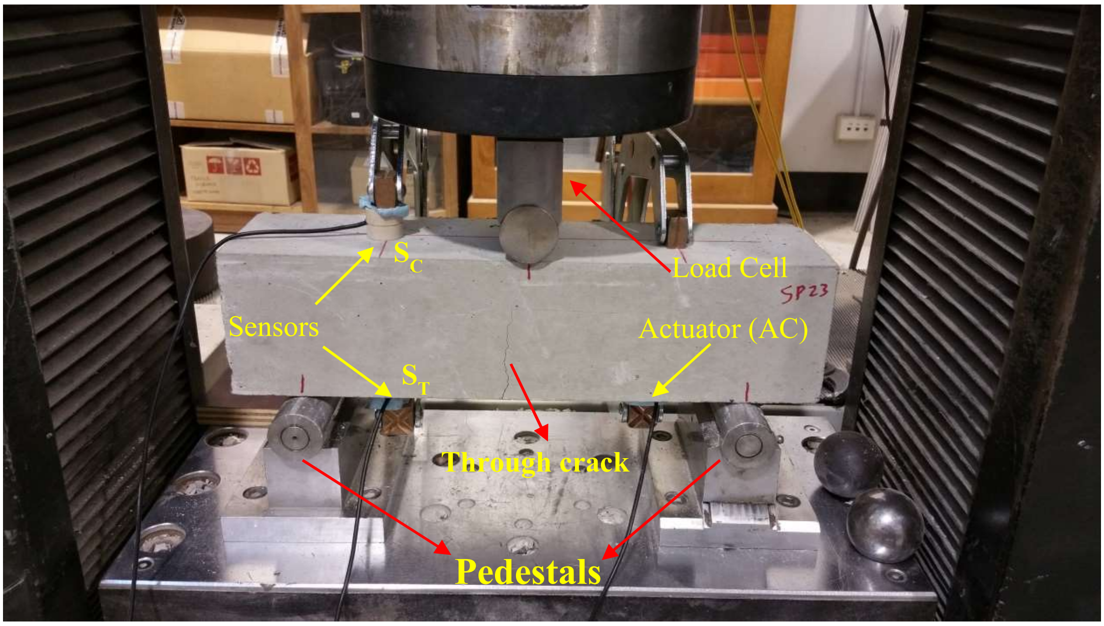

Figure 5-5: Locations of a through crack, an actuator, and sensors at the specimen under a 3-point bending test

5.3 Sensor arrangement and setup

As flexural loading is applied gradually to a concrete beam, tensile cracks typically developed first, and then shear and compression cracks develop later. The tensile cracks which develop from the bottom of concrete beams can be used for early damage assessment.

For characterisation of concrete, including crack detection and monitoring, Smart Aggregates were embedded in concrete members such as beams. However, externally mounted Smart Aggregate actuators and sensors have not received much attention in the literature. As demonstrated in Chapter 3, smart aggregates could be used as external actuators and sensors to transmit and receive signals propagated in concrete specimens. This experimental study extensively applies the proposed concept for the detection of cracks in concrete beams. For this purpose, three SA transducers were mounted in the mid-span of a concrete beam, as shown in Figure 5-6. Since in the concrete structures under bending, the cracks initiate from bottom of specimen, therefore one actuator (AC) and one sensor (S_T) mounted on the tension (bottom) side of the beam, and one sensor (S_C) mounted on the compression (top) side of the beam. It should be mentioned that the surface of concrete where the transducers were mounted were polished.

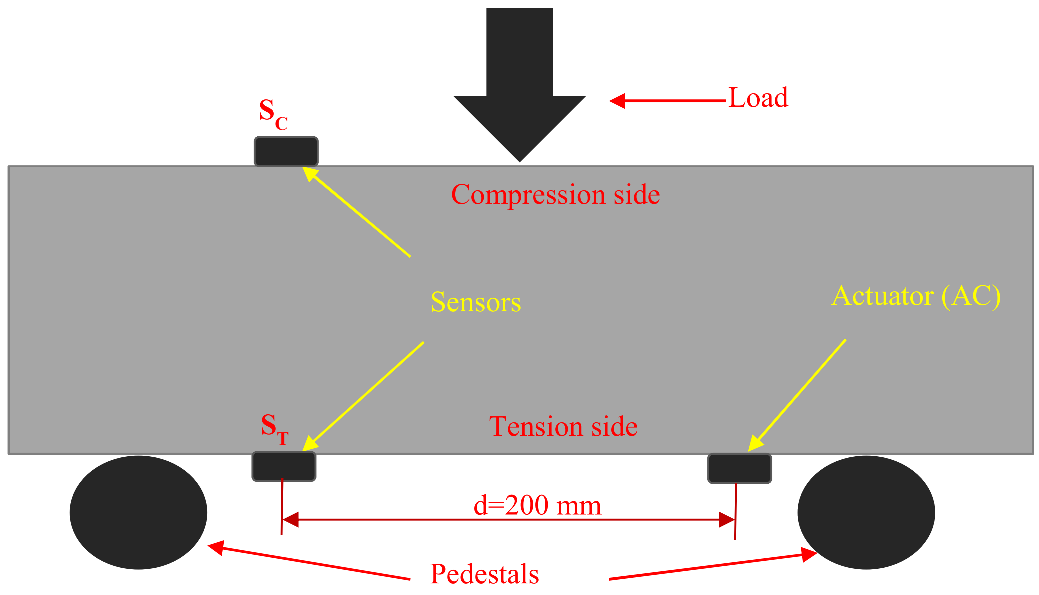

Figure 5-6: Schematic of SA transducers mounted on the concrete beam under test

The locations of the actuator and the sensors, plus the distance (d) between them, are important. In this study, the distance has been taken to be 200 mm to cover the mid-span area of each beam, as it was expected that cracks were concentrated in this area, especially for concrete beams that were not reinforced. For comparison, a wire strain gauge with resistance per meter 0.32 Ω was attached using glue in the mid-span area of a beam, as shown in Figure 5-7; this was done only for 4 out of 10 concrete beams. The strain gauge and transducer readings were continuously recorded at a rate of 10 channels per second using an automatic data-logger, which was calibrated before the start of each test. The strain gauges had a measurement sensitivity of strain and displacement for ±1 micro-strain and ±0.001 mm, respectively.

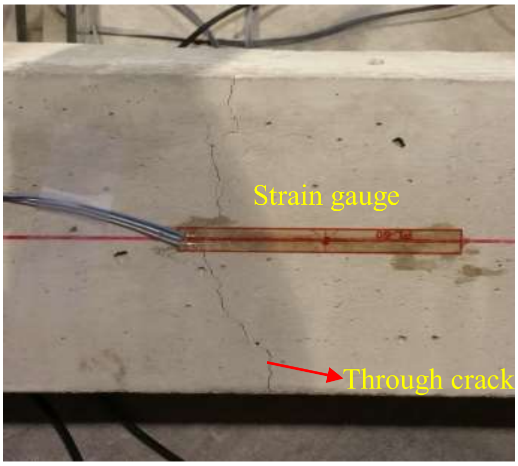

Figure 5-7: Strain gauge location at the bottom of a concrete beam

LabVIEW software was used to generate a swept sine-wave as an excitation and to process the signals received from the SA sensors. Frequency range, signal swept period, and the amplitude of the sine waves were set to be from 150 Hz-150 kHz, 1 s and 10 V, respectively. The software recorded the signal data in a time domain every minute from the beginning to the end of loading.

5.4 Results and discussions

In this study, a 28-day cylinder compressive strength of 40 MPa was chosen to be the design strength of the concrete. The cylinders were capped with a high strength sulfur compound and tested in an Instron machine at the Structural Laboratory with 5000 kN compression capacity (Figure 5-8). After 7, 14, 28, 56 and 92 days from the concrete casting, four cylinder specimens were tested each day. The measured compressive strength of the concrete cylinder specimens are provided in Table 5-2. The variation of the strength in the same day is due to the aleatoric concrete mixture variations, water content variations, and curing temperature changes. To avoid bias in these variations, the average value on each day was taken as the concrete compressive strength (Figure 5-9).

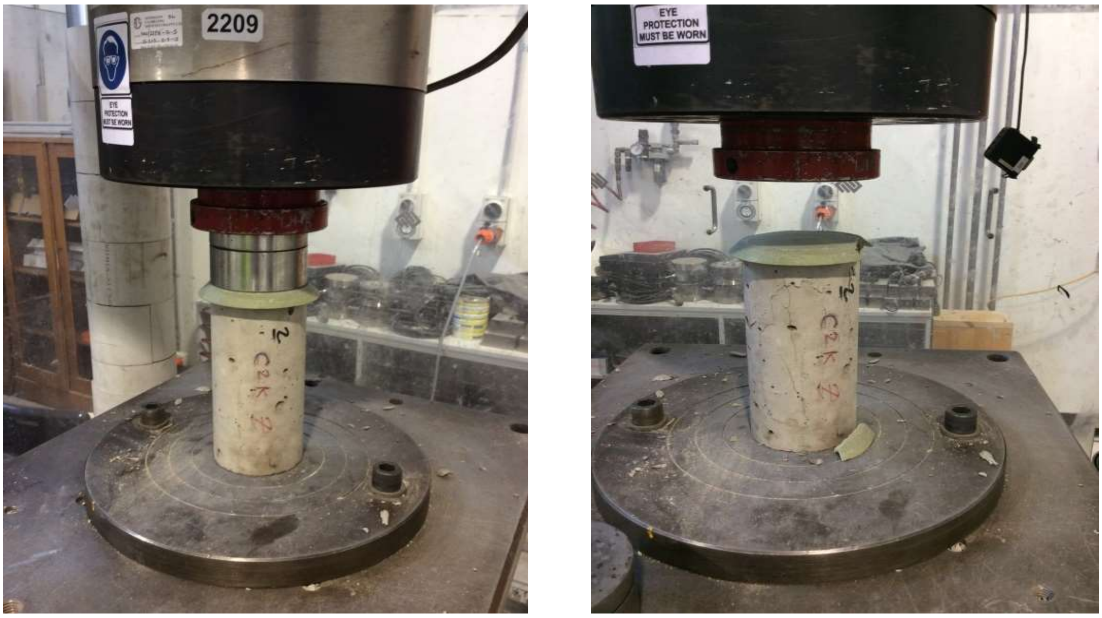

a) Before the test

b) After the test

Figure 5-8: Cylindrical concrete specimen: (a) before and (b) after the test

Table 5-2: Material compressive strength test results

Day / Specimen number	7	14	28	56	92
1	25.8	30.9	41.1	46	50.6
2	26.9	22	35.3	45.1	53.9
3	23.8	30.5	42.8	44.8	54.8
4	24.6	29	37.2	39.3	54.5

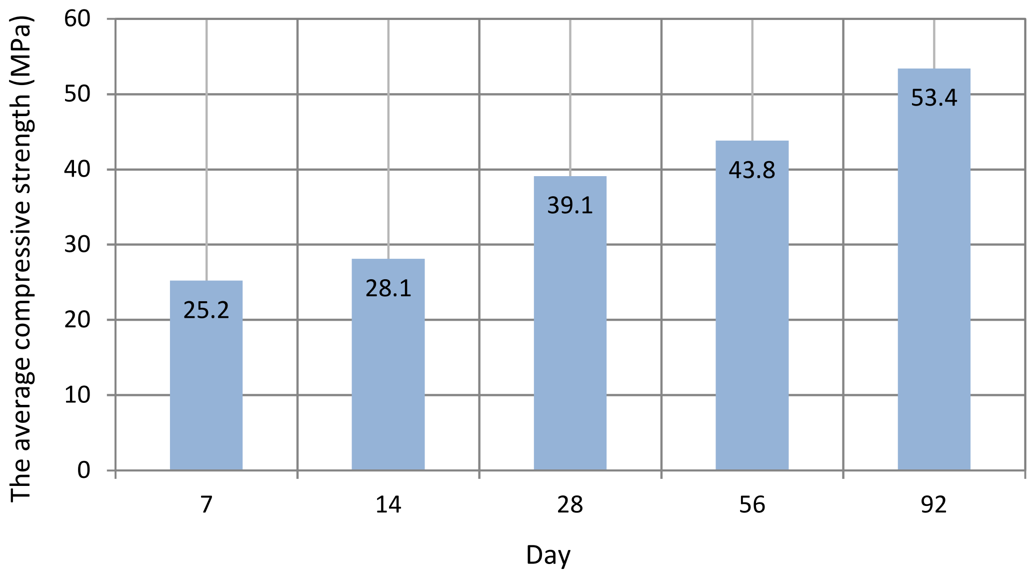

Figure 5-9: Average compressive strengths of the concrete cylinder specimens recorded 7, 14, 28, 56 and 92 days after casting

In this experiment, sweep sinusoidal signal waves were generated by the actuator. The sweep sinusoidal signal ranged from 100 Hz and ended at 150 KHz, with a magnitude of 10V. The sweep period was set as 1 second and the recording period was set as 4 seconds, and hence at least three complete sweep periods were recorded during each measurement.

During the loading procedure, the magnitude of the time-domain signals received by sensor was significantly decreased after the occurrence of cracking on the surface of concrete beams. This happened for both the tension sensor (S_T) and compression sensor (S_C). Figure 5-10 shows the time-domain signals received by the tension sensor (S_T) every 5 minutes after loading commenced. Each plot corresponds to only one cycle of the detected signal from repeated swept sine waves.

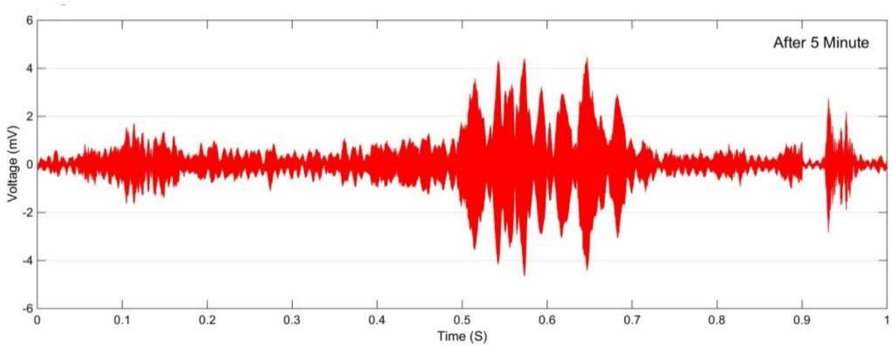
After 5 Minute
Voltage (mV)
Time (S)

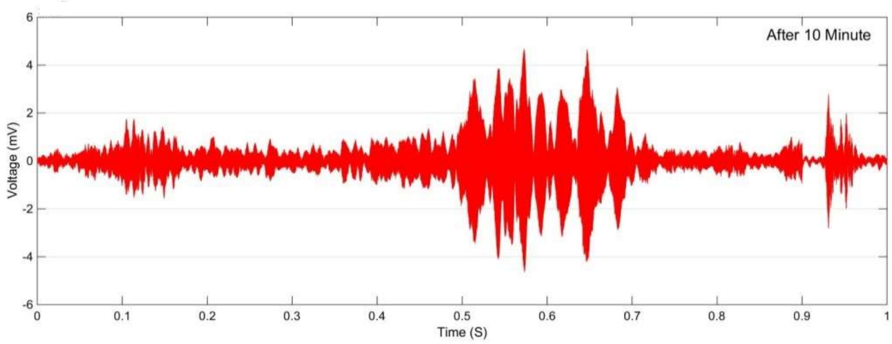
After 10 Minute
Voltage (mV)
Time (S)

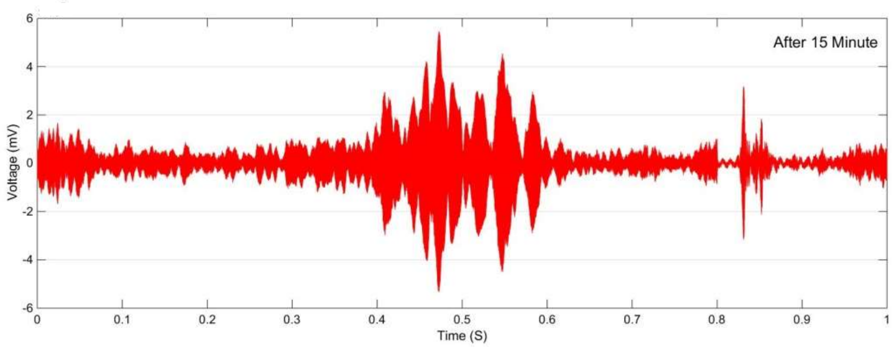
After 15 Minute
Voltage (mV)
Time (S)

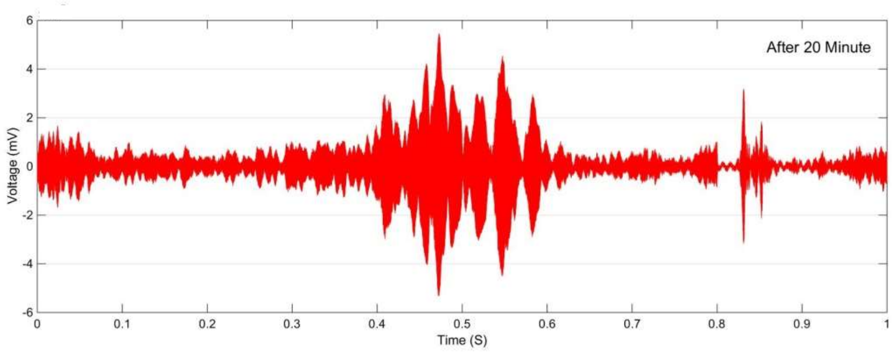
After 20 Minute
Voltage (mV)
Time (S)

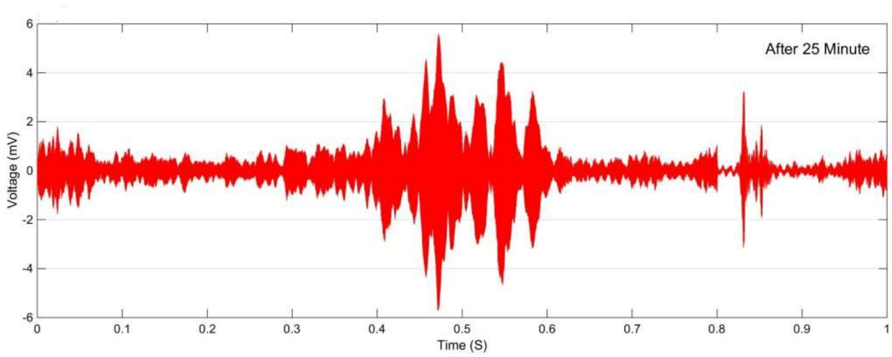
After 25 Minute
Voltage (mV)
Time (S)

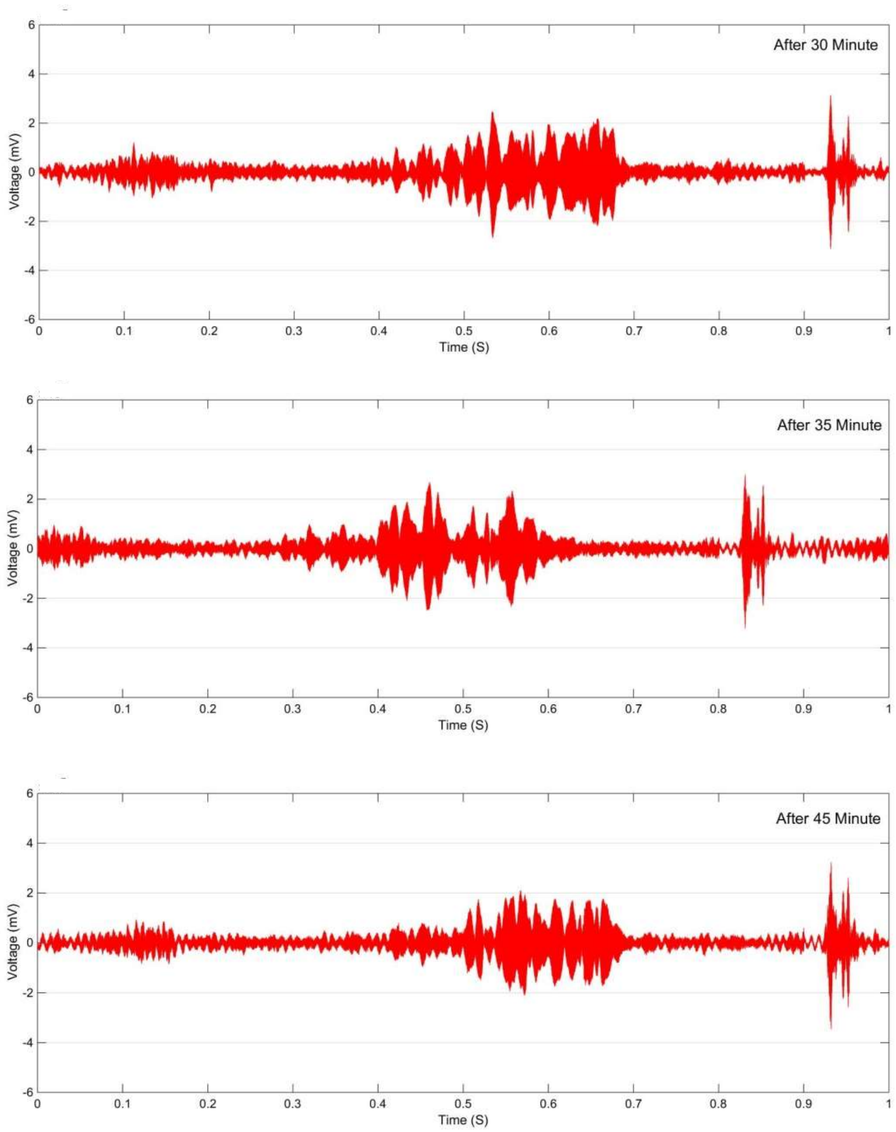

Figure 5-10: Time-domain signals received by the tension sensor (S_T) every 5 minutes after loading commenced

The recorded signals in Figure 5-10 show different shapes before and after cracking. Before cracking, the magnitude of the voltage gradually increases with loading. For example, the maximum sensor output value after 5 minutes is close to 4 mV, and after 25 minutes is close to 6 mV. However, after cracking occurs, the magnitude of the voltage significantly decreases. For example, the maximum voltage value after 25 minutes is close to 6 mV, while after 30 minutes it is close to 2 mV. This decrease is due to the blocked wave propagation by the cracking. We can infer that there was cracking between 25 and 30 minutes.

As mentioned in Chapter 3, the LabVIEW software is capable of calculating power spectral density (PSD), which is the Fourier transform of autocorrelation of the stationary time-domain signals. In this study, for the purpose of future investigation and analysis, the PSD results were exported from the LabVIEW program to the MATLAB program. Figure 5-11 shows the PSD plots in the frequency-domain transformed from the time-domain signals in Figure 5-10, which shows the PSD peaks at the corresponding resonant frequencies. All PSDs are calculated using 4 periods of swept sine-wave to ensure a sufficient accuracy.

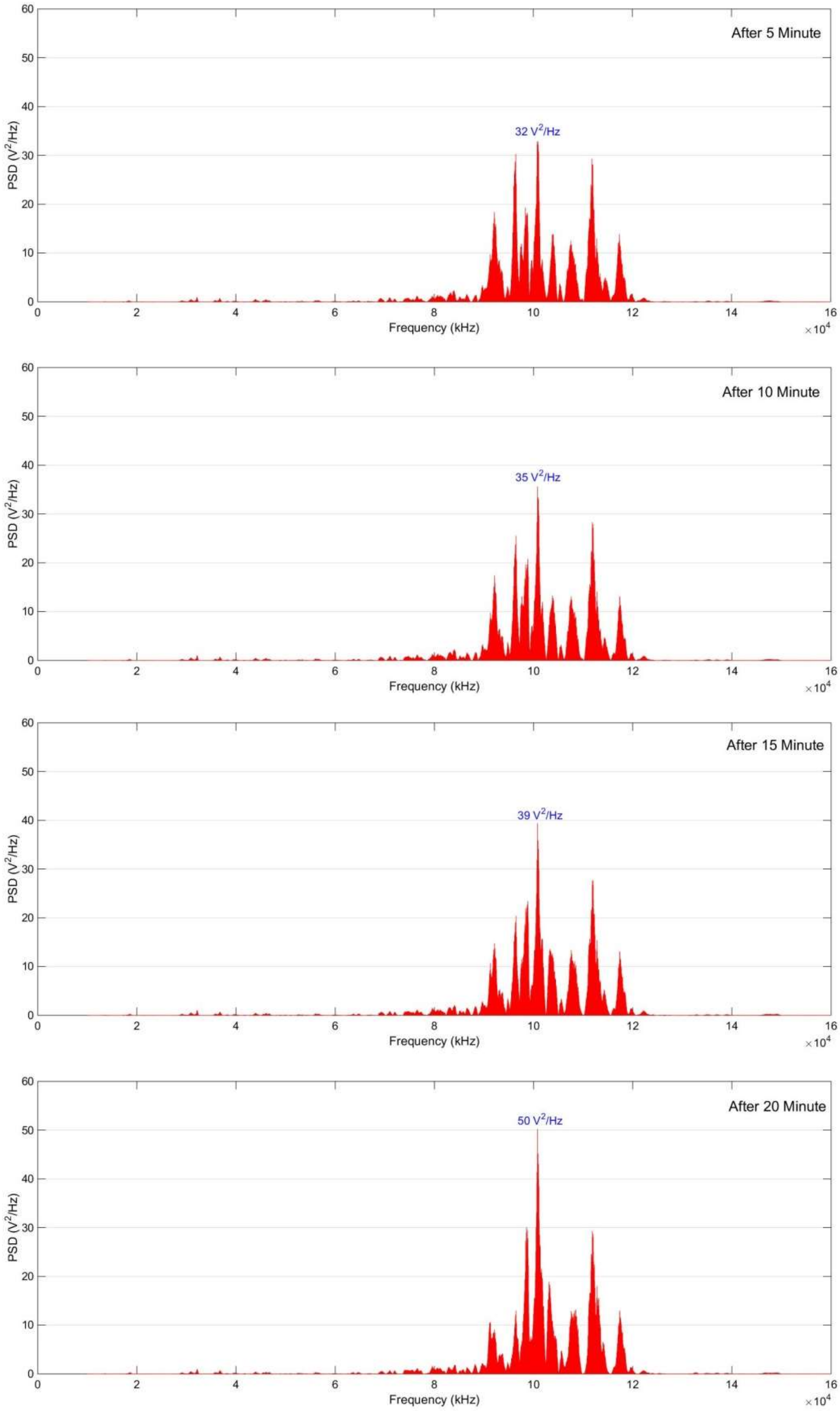
After 5 Minute
32 V²/Hz
After 10 Minute
35 V²/Hz
After 15 Minute
39 V²/Hz
After 20 Minute
50 V²/Hz
PSD (V²/Hz)
Frequency (kHz)
×10⁴

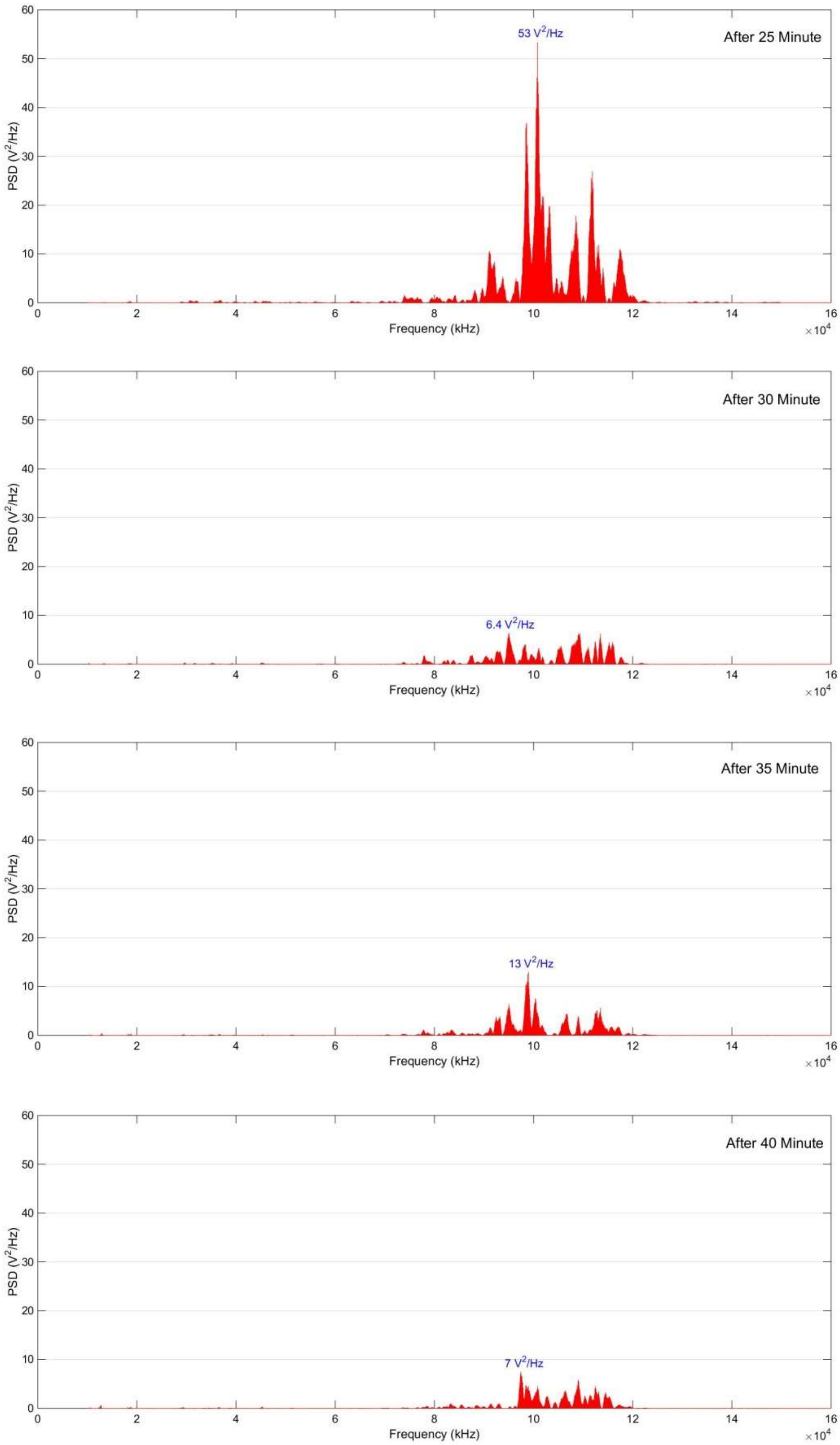

Figure 5-11: Power spectral density (PSD) for the tension sensor (S_T) every 5 minutes after loading commenced

The following observations can be made from these figures:

1) The frequency-domain results shown in Figure 5-11 demonstrate different trends before and after the cracking, such as the time-domain results. Before the cracking, the peak of PSD gradually increases with the increasing load value. The peak of PSD value after 5 minutes is close to 32 V^2/Hz, while after 25 minutes is close to 53 V^2/Hz. After the crack appears on the concrete beam, the peak of PSD significantly decreases with the increasing load value. The peak of PSD value after 30 minutes is close to 6.4 V^2/Hz. This means that the wave propagation was almost blocked by cracks.

2) Waves with lower frequencies attenuate much less than those with higher frequencies. For the time history response of sensors during the test, the magnitude decreases after a crack appears on the concrete beam in high frequency (80 kHz to 120 kHz).

3) A dramatic drop in the peak of PSD means an increase in crack width and length, and the wave propagation is prevented. It is noted that there is a dramatic reduction of the peak of PSD from between 25 and 30 minutes due to cracking. This shows useful information regarding the damaged or healthy status of the test specimen.

As seen in Figure 5-11, it is sometimes difficult to precisely pin-point the peak of PSD. In this study, as an alternative measure, the total received power is proposed to be used to monitor cracking. The total power received by the sensor within a frequency range from 100 Hz to 150 kHz is calculated as follows:

$$P_T = \sum_{i=150}^{150k} PSD(f_i) \times f_i \tag{5-1}$$

The MATLAB code was developed in this study to calculate the peak of PSD and total received power (Appendix A). The peak of PSD and the total received power for three concrete beams (SB22, SB16 and SB03) are shown in Figures 5-12 to 5-17, and the others are provided in Appendix B.

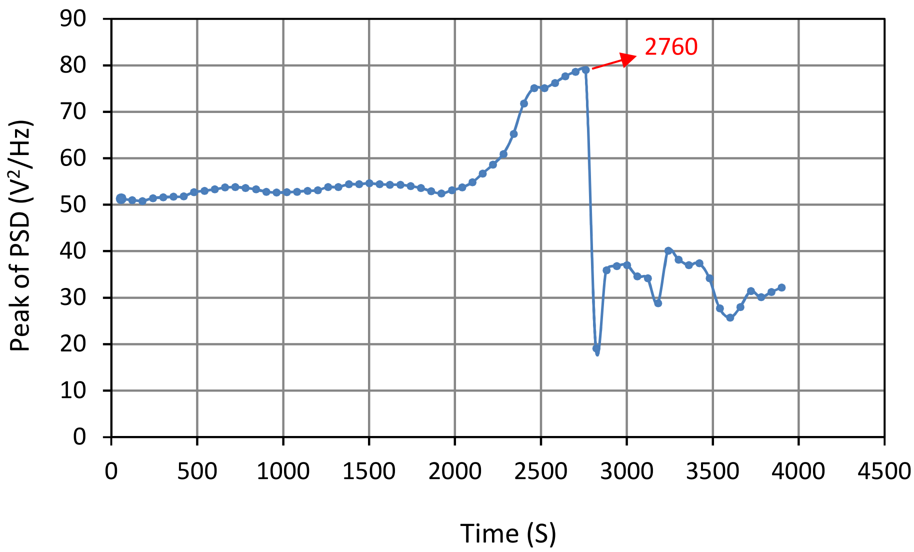

a) S_T sensor

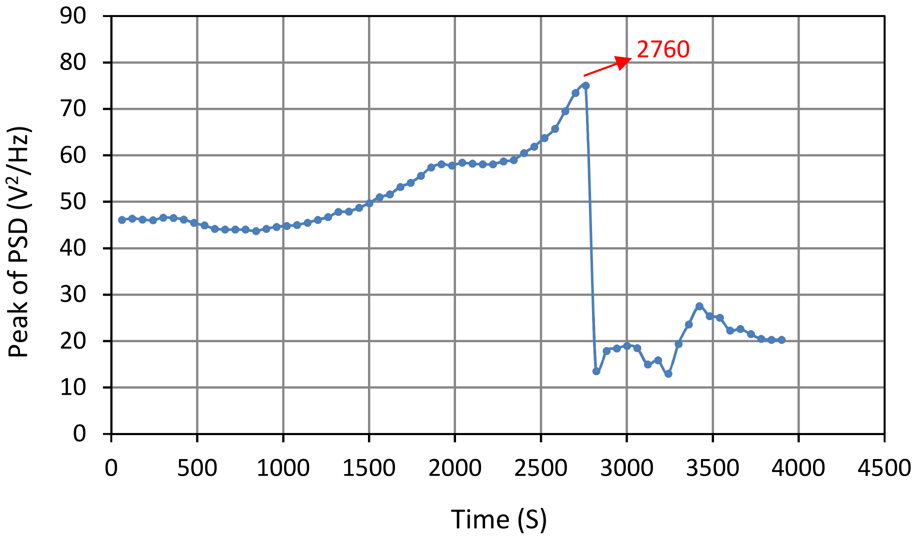

b) S_C sensor

Figure 5-12: Peak of PSD for (a) S_T sensor at the tension side and (b) S_C sensor at the compression side of concrete beam SB22

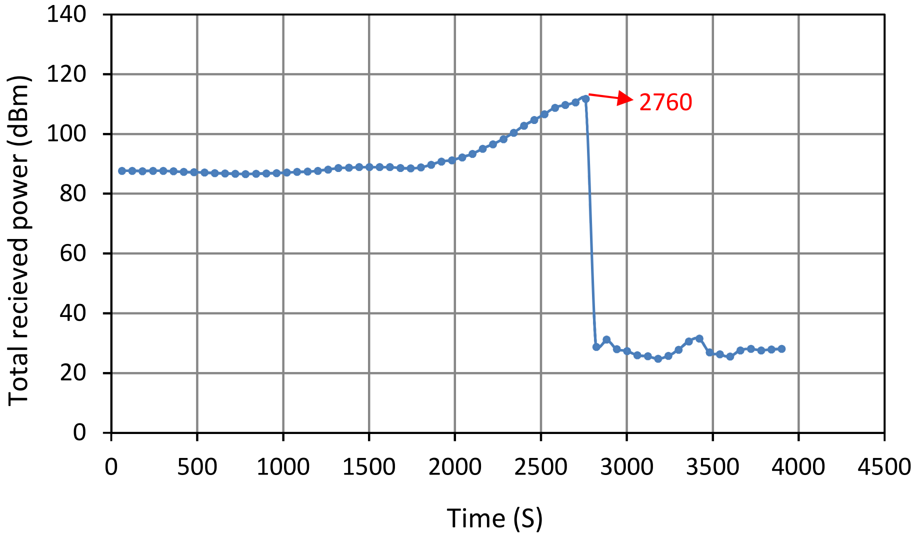

a) S_T sensor

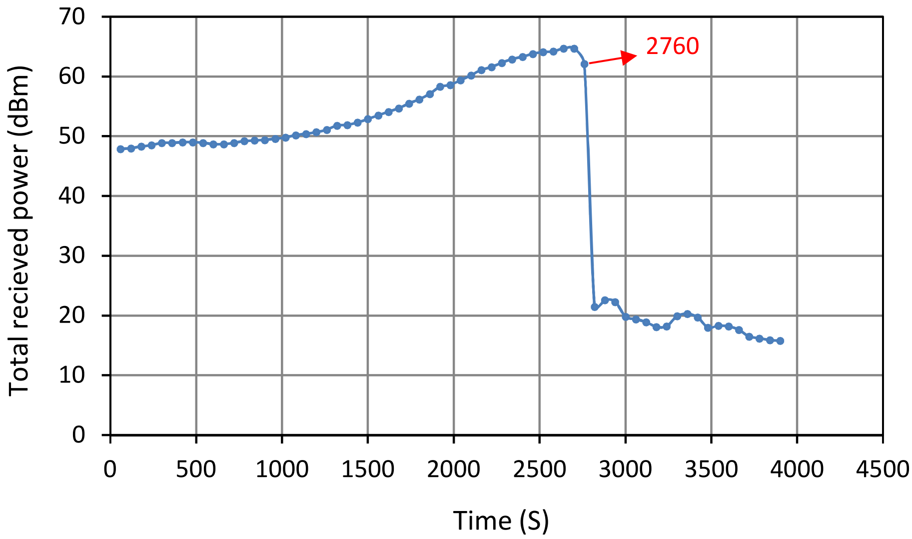

b) S_C sensor

Figure 5-13: Total received power for (a) S_T sensor at the tension side and (b) S_C sensor at the compression side of concrete beam SB22

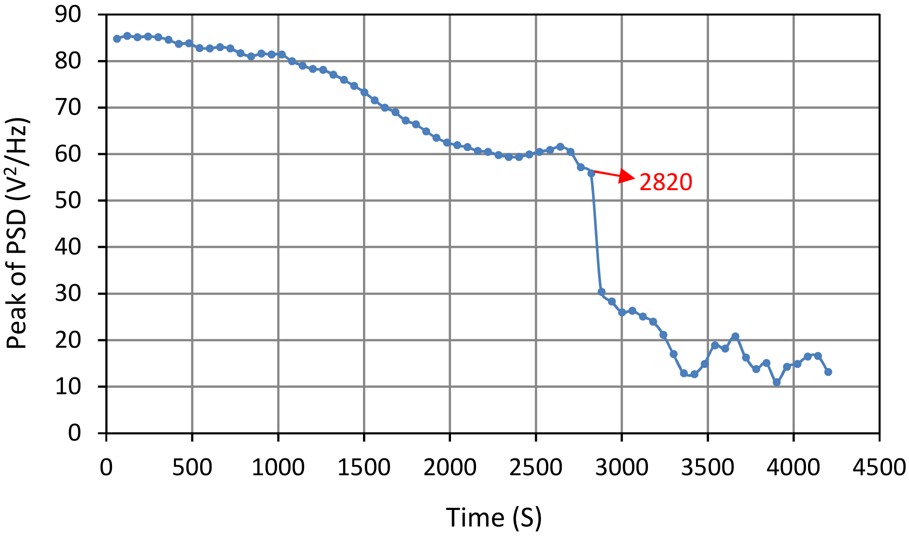

a) S_T sensor

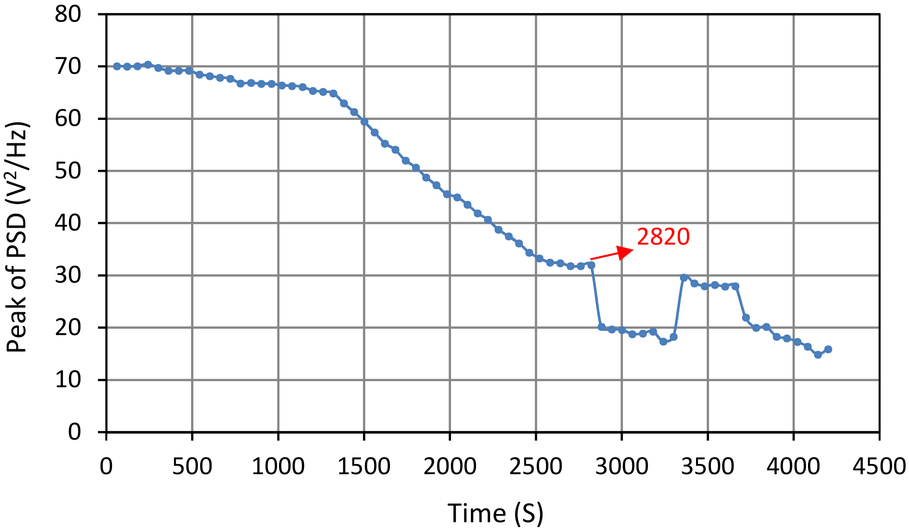

b) S_C sensor

Figure 5-14: Peak of PSD for (a) S_T sensor at the tension side and (b) S_C sensor at the compression side of concrete beam SB16

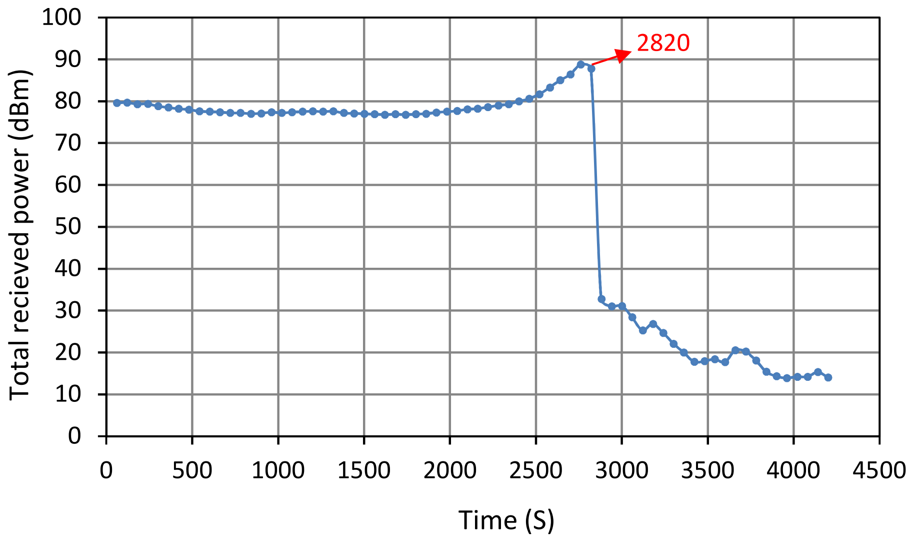

a) S_T sensor

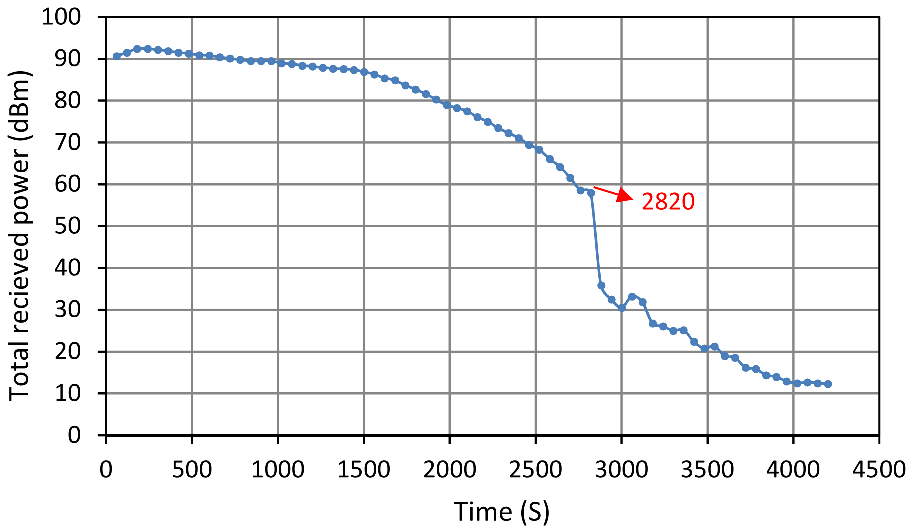

b) S_C sensor

Figure 5-15: Total received power for (a) S_T sensor at the tension side and (b) S_C sensor at the compression side of concrete beam SB16

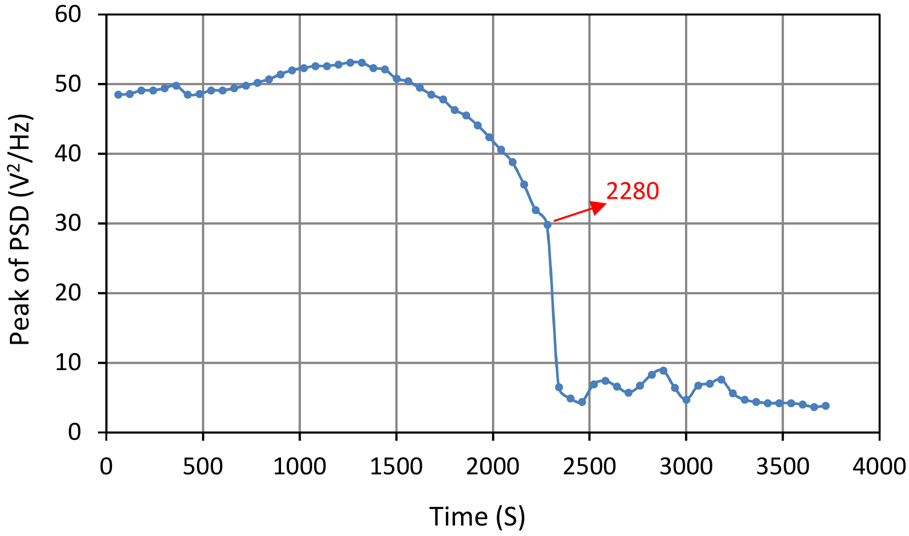

a) S_T sensor

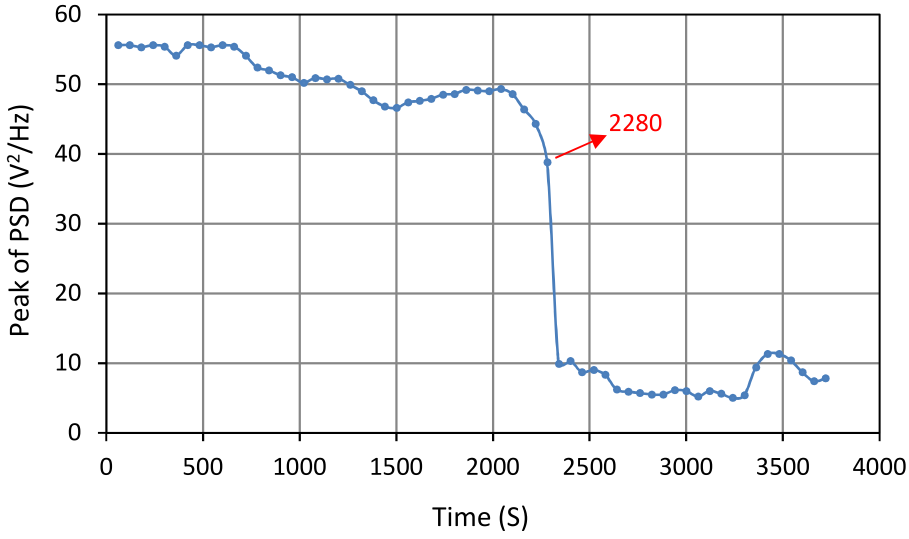

b) S_C sensor

Figure 5-16: Peak of PSD for (a) S_T sensor at the tension side and (b) S_C sensor at the compression side of concrete beam SB03

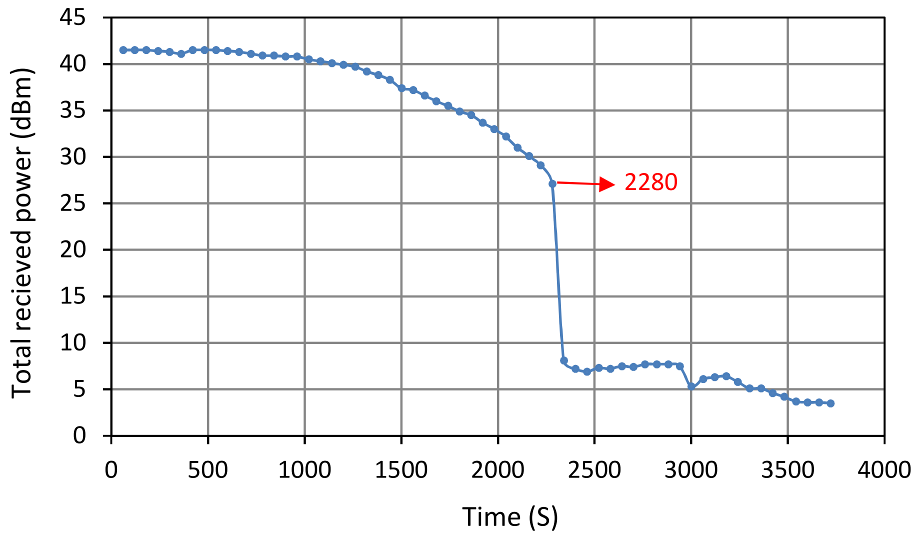

a) S_T sensor

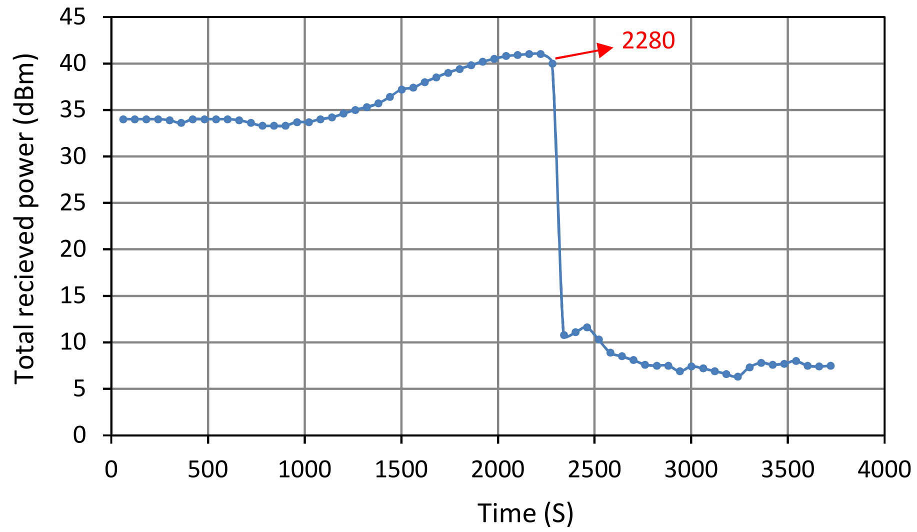

b) S_C sensor

Figure 5-17: Total received power for (a) S_T sensor at the tension side and (b) S_C sensor at the compression side of concrete beam SB03

The following observations can be drawn from these figures:

1) The test results for peak of PSD and total received power shown in Figure 5-12 are well distinguished before and after cracking. For example, specimen SB 22 shows the peak of PSD value dropped from 79 V^2/Hz to 19 V^2/Hz between 2500 and 3000 seconds, which is due to the cracking in the concrete beam. This means that the wave propagation was blocked by the cracking. These significant drops occur in both the peak of PSD and the total received for all concrete beam specimens.

2) The compression side sensor results of the peak of PSD and the total received power indicate that total received power shows smaller fluctuations. For instance, Figure 5-17 clearly shows a smoother curve in the total received power for specimen SB03, compared to that for the peak of PSD (Figure 5-16).

As mentioned in the signal processing section of Chapter 3, the standard deviation is a common measure to characterize the variation of signal measures. From the results of peak of PSD and total received power shown in Figure 5-12 to Figure 5-17, the variation for the values for different beams are obvious. To fairly compare and calculate the standard deviation of the signal measures, the peak of PSD and the total received power obtained from ten concrete beams were normalized and shown in Figure 5-18a and Figure 5-19a. The one standard deviation bounds of these results are plotted in Figure 5-18b and Figure 5-19b.

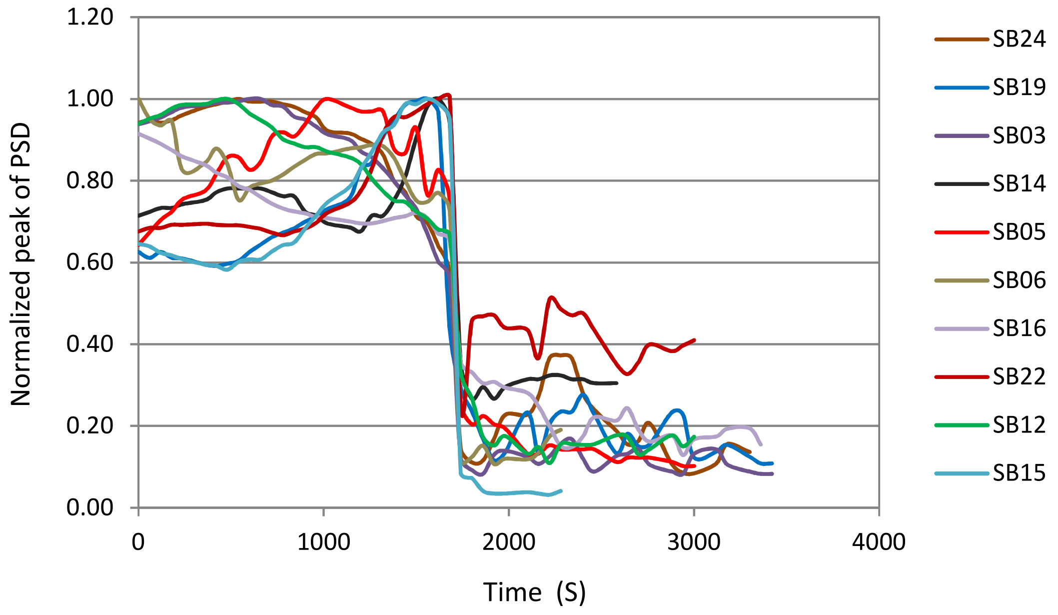

a) Normalised peak of PSD

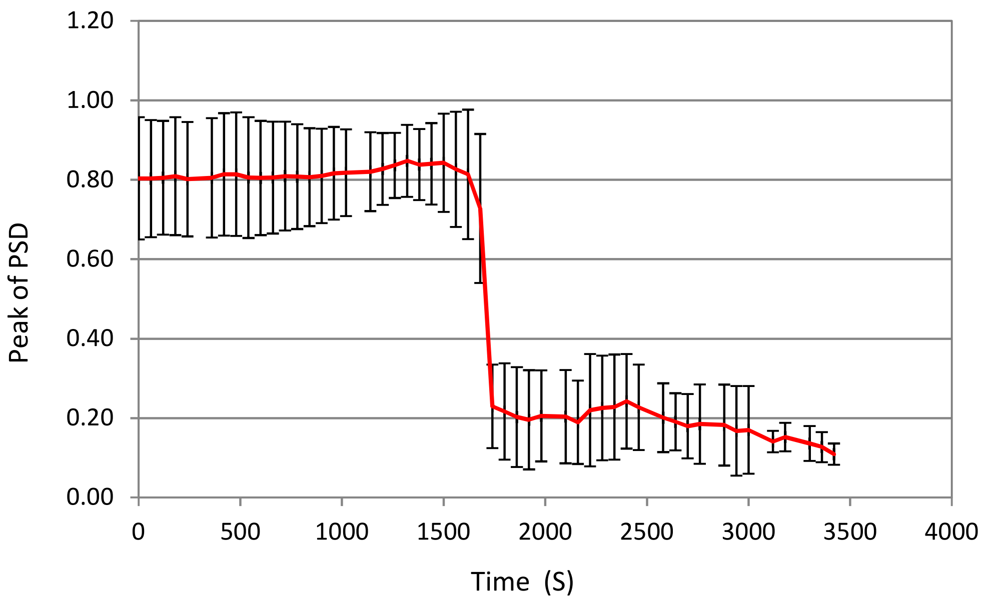

b) Standard deviation

Figure 5-18: a) Peak of PSD results obtained from ten concrete beams after normalization and b) their standard deviation

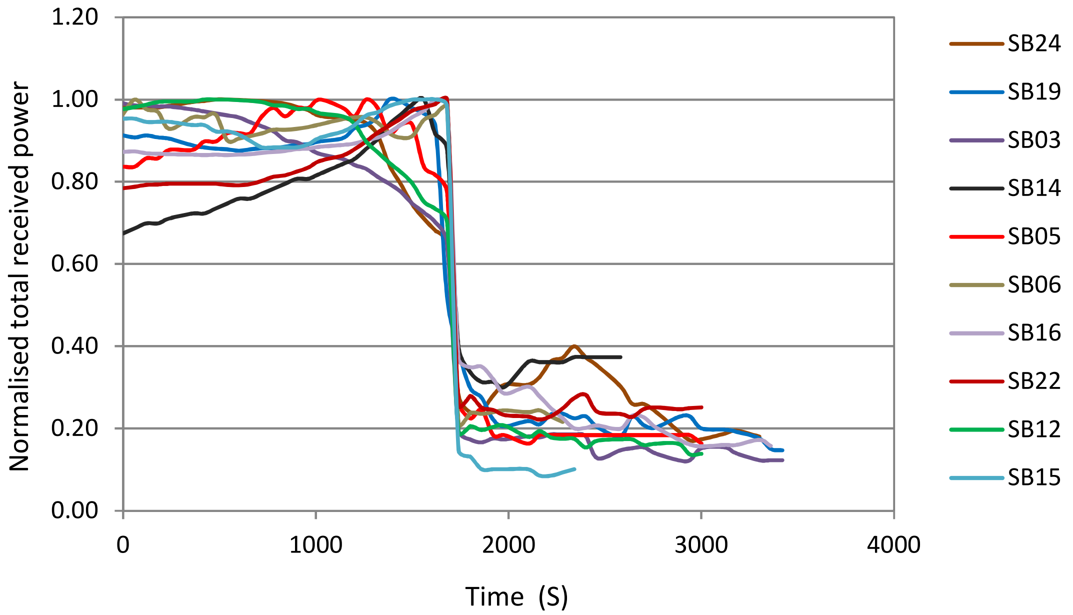

a) Normalised total received power

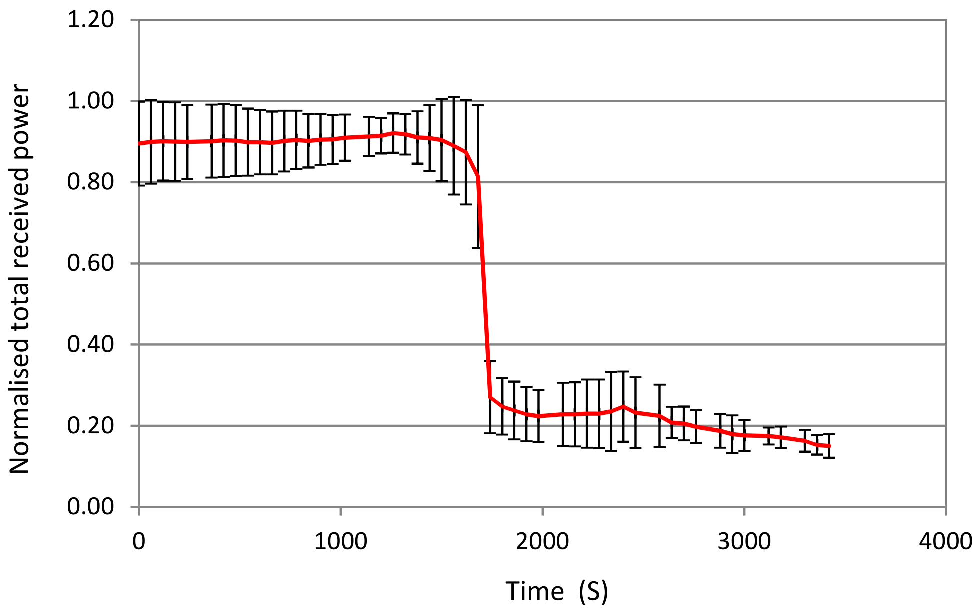

b) Standard deviation

Figure 5-19: a) Total received power results obtained from 10 concrete beams after normalisation and b) their standard deviation

Two important observations can be made from these figures as follows:

1) A dramatic drop in the received signal by the sensor suggests the occurrence of cracking in a concrete beam. This drop occurs to all 10 concrete beams tested in this study and gives information regarding the damaged or healthy status of the test specimens.

2) The fluctuations of the peak of PSD values in comparison to the total received power values are shown in the standard deviation curves. The overall standard deviation bounds are narrower in the total received power than in the peak of PSD.

As mentioned in the previous section, in this experimental study the load cell and strain gauges were also used for the purpose of comparison. The results of the peak of PSD and the total received power in the time domain were compared with those from the load cell and the strain gauge in the time domain. Figure 5-20 to Figure 5-22 show recorded load and strain by the load cell and the strain gauge, respectively.

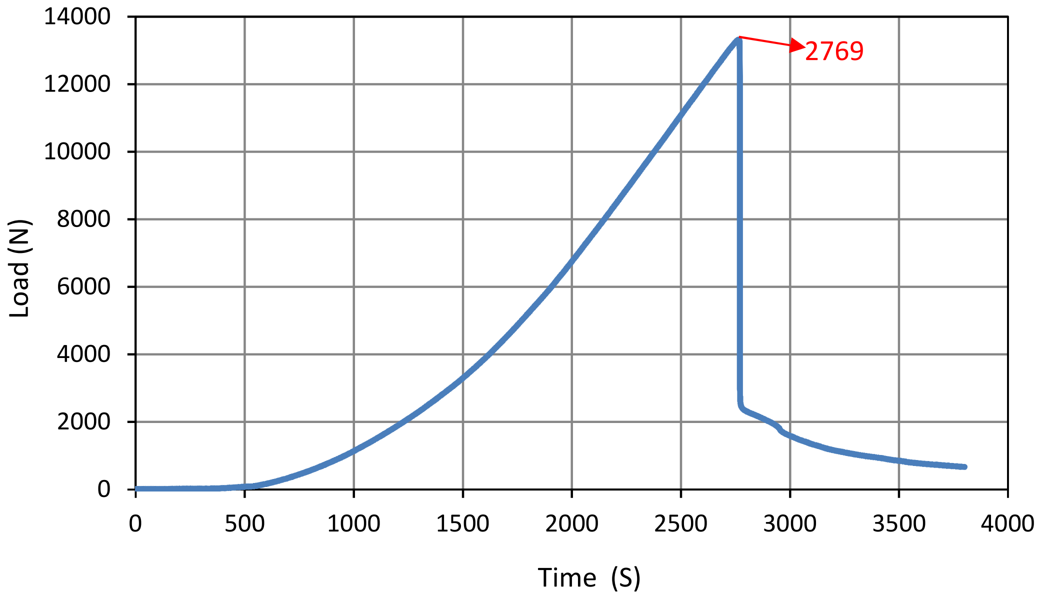

a) Loading history

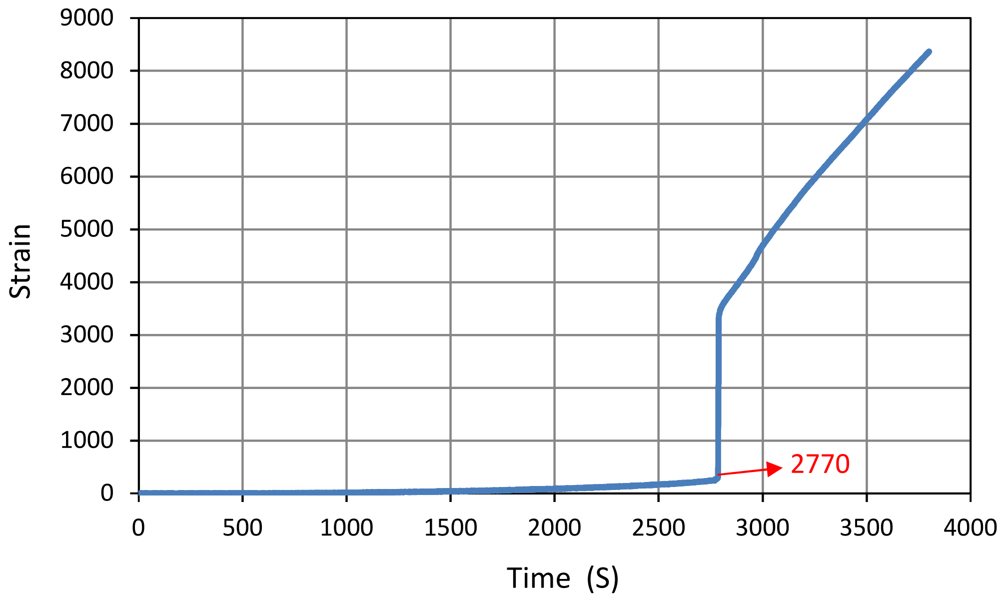

b) Strain gauge result

Figure 5-20: Results for (a) loading history recorded by a load cell and (b) a strain gauge result at mid-span of concrete beam SB22

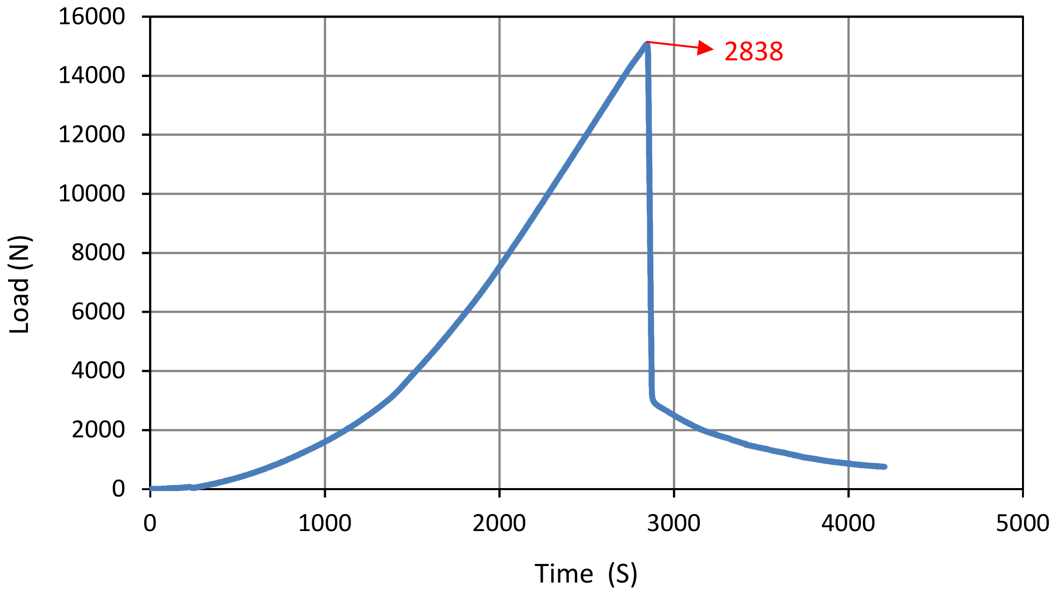

a) Loading history

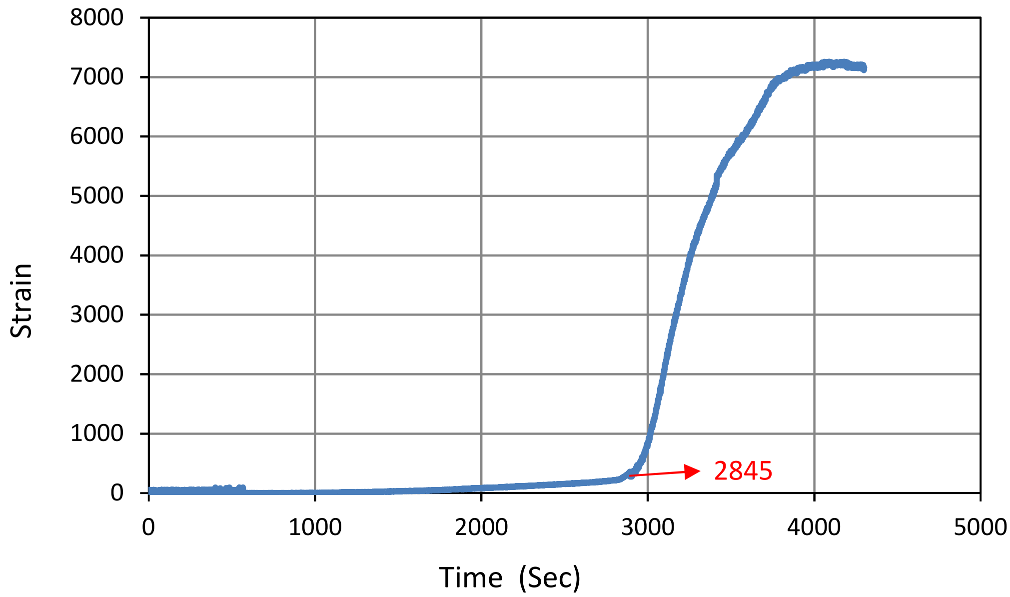

b) Strain gauge result

Figure 5-21: Results for (a) loading history recorded by a load cell and (b) a strain gauge result at mid-span of concrete beam SB16

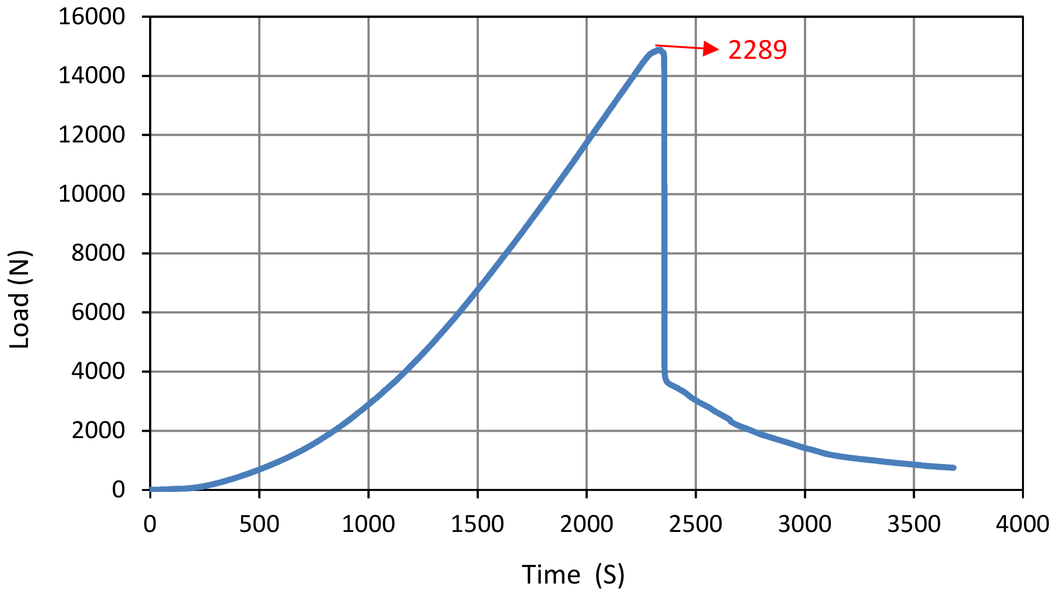

a) Loading history

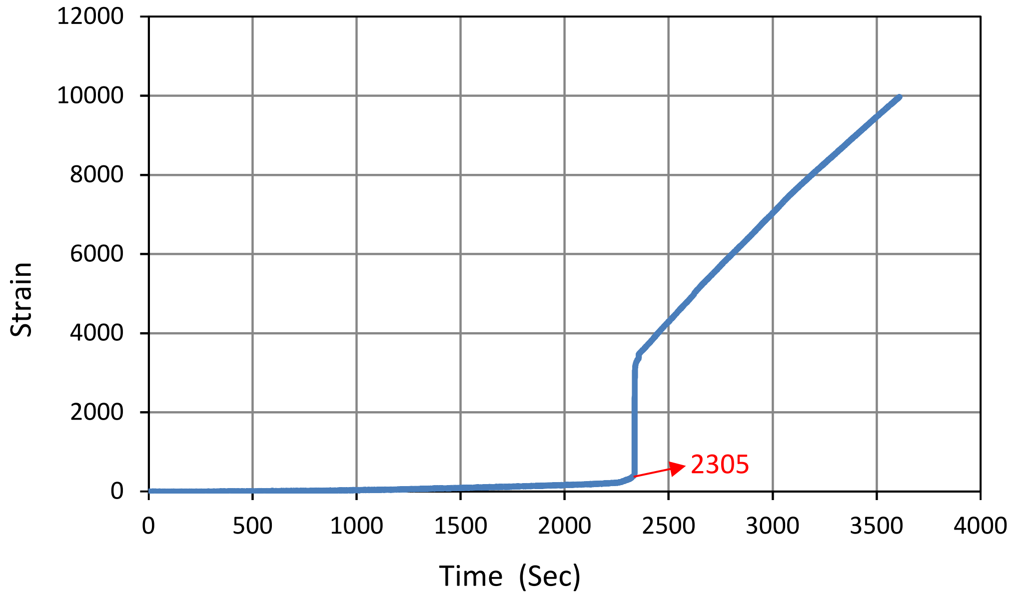

b) Strain gauge results

Figure 5-22: Results for (a) loading history recorded by a load cell and (b) a strain gauge result at mid-span of concrete beam SB03

As these figures show, significant drops in loading or significant increase in strain were observed when cracking occurred. The results of comparison between these loading and strain monitoring results and the results of the peak of PSD and the total received power obtained with the SA sensors can be summarise as follows.

The proposed SA sensory technique is sensitive to the detection of cracking. It is noted that the dramatic drop of specimen SB22 in the received signal happened at 2760 seconds, while the drop in loading history and increase in the strain were at 2769 and 2770 seconds, respectively. It means that the detection by the proposed SA sensory technique is faster than that by a load cell or a strain gauge; this is similar in the other specimens. It also means that the proposed technique captures the occurrence of internal micro cracks even before the major cracking, compared to the load cell and the strain gauge.

Table 5-3 and Figure 5-23 show the calculated damage indexes for 3 specimens, SB22, SB16 and SB03, until 3600 seconds after the start of the loading. The index is calculated using Equation 3-2, in which the total energy received by the tension sensor has been used. In Table 5-3, the values over the selected threshold value of 0.5 are highlighted. It is also observed that the damage index is increasing even before the cracking, and this can be considered as a warning of cracking. The selected threshold value of 0.5 is shown by red line at the figures. A dramatic jump in the value of the damage index in Figure 5-23 can be attributed to cracking.

Table 5-3: Damage index values vs. time for concrete beam SB22, SB16, and SB03

Time (S)	SB22	SB16	SB03	Time (S)	SB22	SB16	SB03
	Damage Index				Damage Index		
60	0	0	0	1860	0.02	0.03	0.17
120	0	0.00	0	1920	0.04	0.03	0.19
180	0.00	0.00	0	1980	0.04	0.03	0.20
240	0.00	0.00	0.00	2040	0.05	0.02	0.22
300	0.00	0.01	0.00	2100	0.06	0.02	0.25
360	0.00	0.01	0.01	2160	0.08	0.02	0.27
420	0.00	0.02	0.00	2220	0.10	0.01	0.30
480	0.01	0.02	0.00	2280	0.12	0.01	0.35
540	0.01	0.03	0.00	2340	0.14	0.00	0.80
600	0.01	0.03	0.00	2400	0.17	0.01	0.83
660	0.01	0.03	0.00	2460	0.19	0.01	0.83
720	0.01	0.03	0.01	2520	0.22	0.03	0.82
780	0.01	0.03	0.01	2580	0.24	0.05	0.83
840	0.01	0.03	0.01	2640	0.25	0.07	0.82
900	0.01	0.03	0.02	2700	0.26	0.09	0.82
960	0.01	0.03	0.02	2760	0.27	0.12	0.81
1020	0.01	0.03	0.02	2820	0.67	0.10	0.81
1080	0.00	0.03	0.03	2880	0.64	0.59	0.81
1140	0.00	0.03	0.03	2940	0.68	0.61	0.82
1200	0.00	0.03	0.04	3000	0.69	0.61	0.87
1260	0.00	0.03	0.04	3060	0.70	0.64	0.85
1320	0.01	0.03	0.06	3120	0.71	0.68	0.85
1380	0.01	0.03	0.07	3180	0.72	0.66	0.85
1440	0.01	0.03	0.08	3240	0.71	0.69	0.86
1500	0.01	0.03	0.10	3300	0.68	0.72	0.88
1560	0.01	0.03	0.10	3360	0.65	0.75	0.88
1620	0.01	0.04	0.12	3420	0.64	0.78	0.89
1680	0.01	0.03	0.13	3480	0.69	0.78	0.90
1740	0.01	0.04	0.14	3540	0.70	0.77	0.91
1800	0.01	0.03	0.16	3600	0.71	0.78	0.91

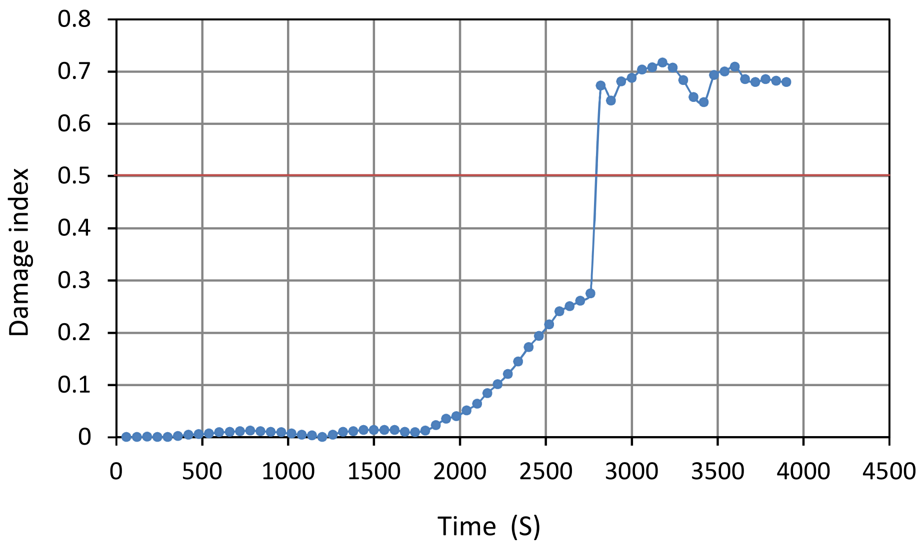

a) Concrete beam SB22

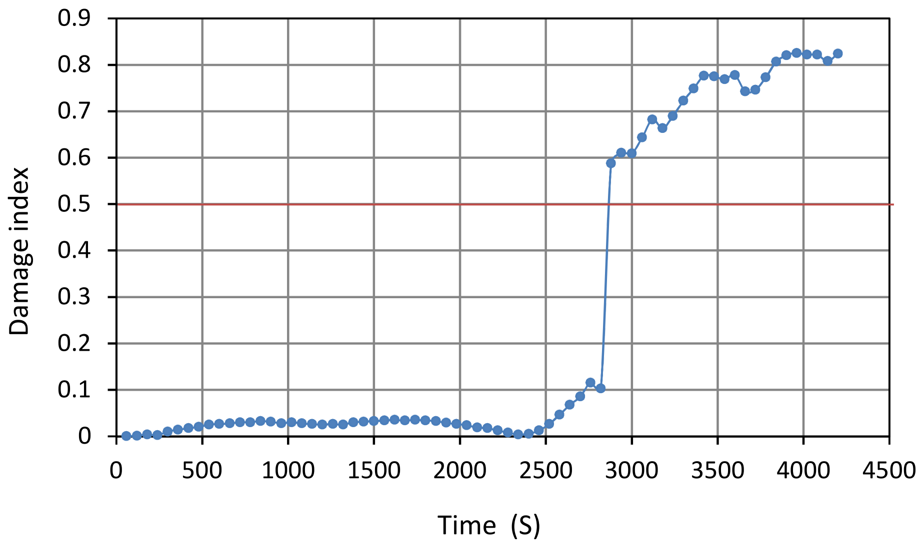

b) Concrete beam SB16

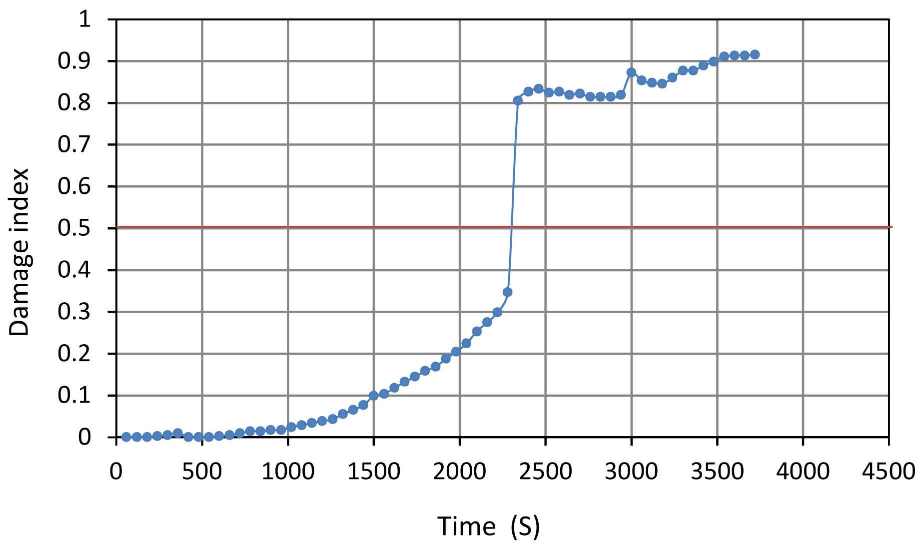

c) Concrete beam SB03

Figure 5-23: The damage index values for concrete beam a) SB22, b) SB16 and c) SB03

5.5 Summary

In this chapter, a mounted SA based approach for the first time was proposed and applied for structural health monitoring of unreinforced concrete beams under bending. This active sensory technique used SA transducers mounted on the specimen under test to detect load-induced cracking. Ten concrete beams were prepared and cracked under a 3-point bending machine, and these behaviours were monitored by the proposed sensory technique as well as by a load cell and strain gauge. In the concrete beams, one actuator and one sensor were mounted on the tension side, and one sensor was mounted on the compression side. Based on the experimental results, the following conclusions can be drawn:

1. The proposed mounted SA based active sensing approach provided a successful detection of the cracks in the mid-span area of concrete beams under bending.
2. The received signal analysis using the peak of PSD, the total received power and the damage index significantly enhanced indications of cracks.
3. Mounted SAs can be applied for existing concrete members at different places on their surface while embedded SAs should be located at certain places inside concrete using rebars or artificially embedded holders, and they may be broken during vibration procedure.
4. It was shown that the proposed method had an ability not only to detect the surface crack but also to detect the internal crack before it became visible.
5. The proposed SA based method was more sensitive to cracking than a conventional load cell and strain gauge. Due to its sensitivity, the proposed method could predict the beam failure earlier than load cells or strain gauges.
6. This method has the potential to be applied to the health monitoring of large-scale reinforced concrete elements.

Chapter 6 : Detection and Monitoring of Crack on RC Beams under 4-point Bending Load Using Mounted Smart Aggregates

6.1 Introduction

In this chapter, for further investigation on feasibility of the proposed mounted SA-based approach it is applied for health monitoring of existing large-scale RC beams which are the main parts of infrastructures. For this purpose, experiments are performed on four RC beams with mounted SAs to detect and monitor load-induced cracks which may occur in RC beams under flexural loading. SA transducers are mounted as an actuator and sensors on each of the RC beams. The load cell and strain gauge measurements of the RC beams are also performed for verification and comparison.

This chapter consists of three main sections. The first section presents RC beams design and fabrication, and loading setup which are used for this experimental investigation. The second section provides details of the proposed SA transducers arrangement and setup on RC beams. Finally, the results in time-domain and frequency-domain as well as those obtained after signal processing are presented and discussed.

6.2 Reinforced concrete beams and loading setup

Several RC beams were designed and fabricated for this experimental investigation. The mix proportion of the ready-mixed concrete was used to cast the specimens. The design was based on aggregates maximum size of 10 mm, 70 mm slump and 40MPa strength after 28 days. The water-cement ratio was 0.48. The Australian Portland cement type GB was used. Concrete and sand conformed to AS3600 (2009), while the coarse aggregate had a maximum size of 10 mm. The material properties used in this study are illustrated in Table 5-1. Twenty standard cylinders, measuring 102 x 203 mm, were cast along with concrete beams. The cylinders were cast and cured under the identical environmental condition as that of the specimens: 7 days under moist burlap cover and the remaining time in the air-conditioned laboratory until testing. The compressive strengths were measured of 7, 14, 28, 56, and 92 days after casting, respectively.

Four RC beam (1700×150×250 mm) specimens have been used in the experiment comprised of four deformed longitudinal reinforcements to allow an overall flexural failure. The RC beam specimens were rectangular in cross-section, with a width of 150 mm and a height of 250 mm. Deformed bar was a Class N (standard ductility with 500 MPa), manufactured by Australian Reinforcing Company (ARC) in Melbourne. The longitudinal and transverse reinforcement size used in this experiment were N16 steel bars, with a cross-sectional area of 201 mm^2, and the N10 stirrups with standard 90º cog (Table 6-1). The moulds have been fabricated in a laboratory using plywood material and steel mesh fabricated separately and installed inside the mould before casting (Figure 6-2a). After the beam was filled in three layers, the concrete was consolidated with an internal spud vibrator. The concrete adjacent to the perimeter of the casting form was more intensively vibrated so that the ultimate failure of the panels would occur away from the edges. Surfaced finishing was applied, using hand float a few minutes after casting (Figure 6-2b). The RC beams were wrapped in wet burlap, covered in plastic, and allowed to cure for 14 days at room temperature. After 14 days, the plastic and wet burlap were removed and the reinforced beams were allowed to cure in the ambient environment until testing.

Table 6-1: Longitudinal Rebar Arrangement

Designation	Compression side		Tension side	
	Number- size (mm)	Area As (mm^2)	Number-size (mm)	Area As (mm^2)
N1616	2-N16	402	2-N16	402

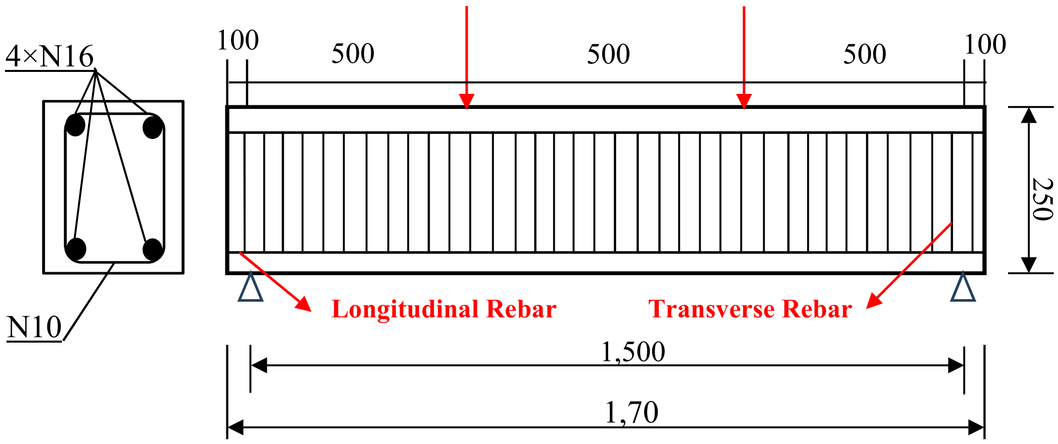

Figure 6-1: Schematic of rebar arrangement cross-sectional view

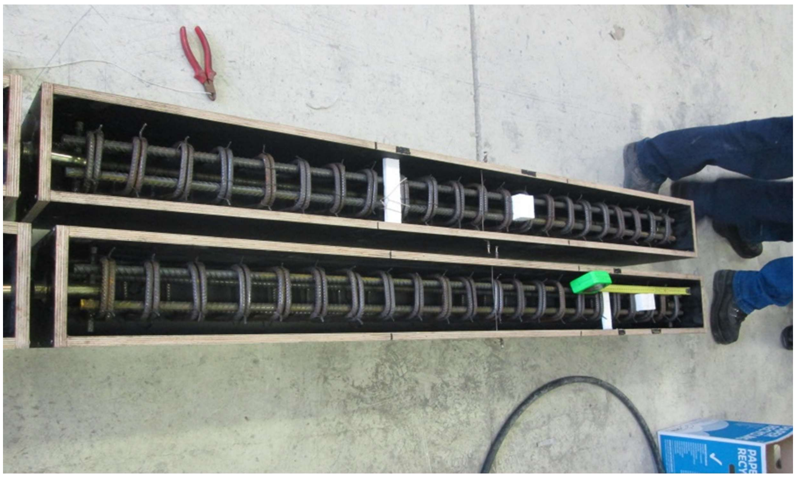

(a) Before casting

(b) After casting

Figure 6-2: RC beams specimens (a) before and (b) after casting

Each test specimen was installed in the test frame as shown in Figure 6-3. The test frame (INSTRON machine) was modified for 4-point bending with a working capacity of 45 kips (1000 kN), and was located in the Structural Engineering Laboratory at the Western Sydney University. The machine has high bandwidth Digital Signal Processing based electronics, and Bluehill modular applications software. The machine was equipped with loading cell to monitoring real time of loading on specimen, and software, designed to record loading variation.

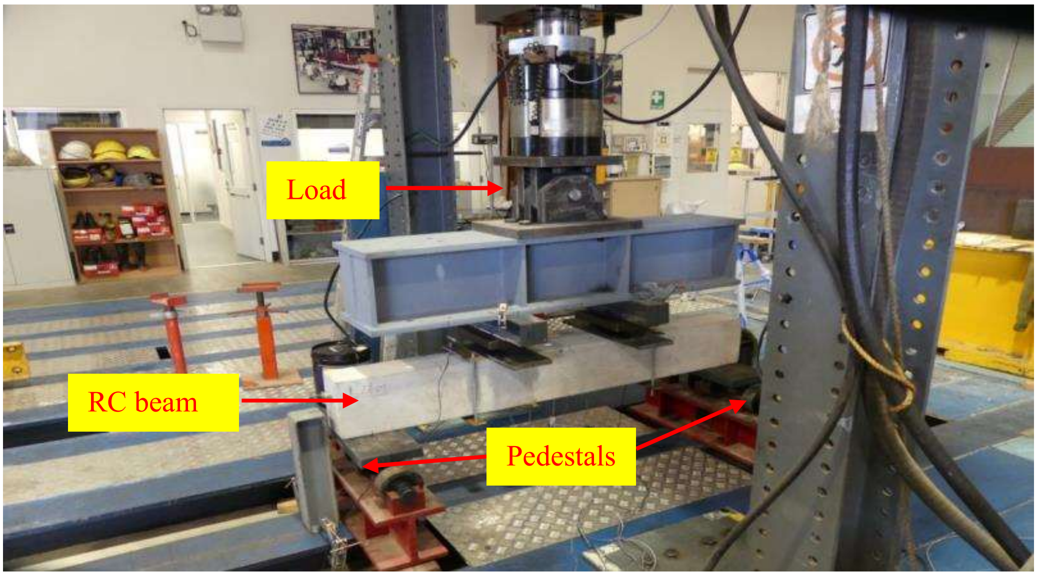

Figure 6-3: 4-Point test frame used in this study

The setup of the machine was based on specimen dimension, material properties, type of loading, and loading ratio. The loading cell must setup to zero force due to no pressure on specimen before loading. In this study speed of crack propagation was critical to obtain more accurate monitoring. Therefore, the loading of machine was in a quasi-static manner, with a constant testing machine crosshead displacement rate of (0.009 mm/sec) to allow accurate monitoring of the specimen cracking.

4-points flexural bending test was selected for this experimental study. The specimens in the test frame sit on the top of two roller pedestals to help to provide pure bending. The loading pin at the top of specimens moved with 0.009 mm/sec ratio which applied force to specimens. Due to a very slow loading ratio, each test took almost an hour from commencing loading to failure of the beam.

Two rolling plates impregnated by grease oil were used on top of the specimen for applied force. In addition, two rubber layer sheets were used to prevent vibration caused by the hydraulic pump (Figure 6-4).

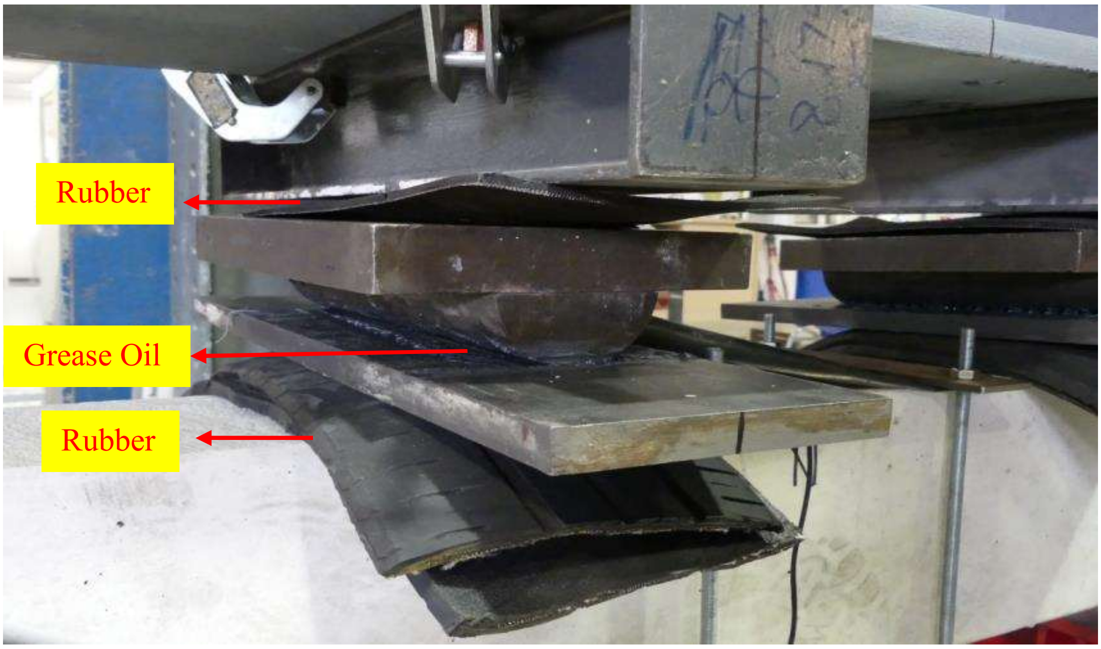

Figure 6-4: Rubber sheets used to prevent vibration

6.3 Sensor arrangement and setup

In most cases of material failure and loading until failure, tensile cracks develop at the initial stage of loading, while shear and compression cracks occur frequently in the latter stages of the process. This is typical for concrete beams and slabs that undergo bending. The initial cracking comes from the tensile load on the bottom of concrete, while the member ultimately fails with diagonal shear cracks. Therefore, it is beneficial to characterize the tension cracks as it can lead to early assessment of the material condition.

Chapter 5 demonstrated that the use of Smart Aggregate as external actuator and sensor investigated for concrete beams and the signal transmitted and received successfully by sensor. The results show the crack successfully detected by both sensor in tension and compression sides. These findings motivate the proposed approach for large RC beams under 4-point bending, which will provide more compliance to real structures condition.

As a shown on Figure 6-5, the arrangement of three SA transducers mounted on the specimen under test at the mild-span of specimen. Since in the concrete structures under bending, the cracks initiate from bottom of specimen, therefore one actuator (AC) and one sensor (S_T) mounted on the tension (bottom) side of the beam, and one sensor (S_C) mounted on the compression (top) side of the beam. In four-point concrete specimens testing, cracks started from the tension side (bottom of specimens) and spread to the neutral axis location. Cracks and delamination were expected at the top of specimen, due to increasing the comparison in this side. Therefore, unlike the results with the concrete beam in Chapter 5, expected different transmission properties were received by mounted SAs to RC beams.

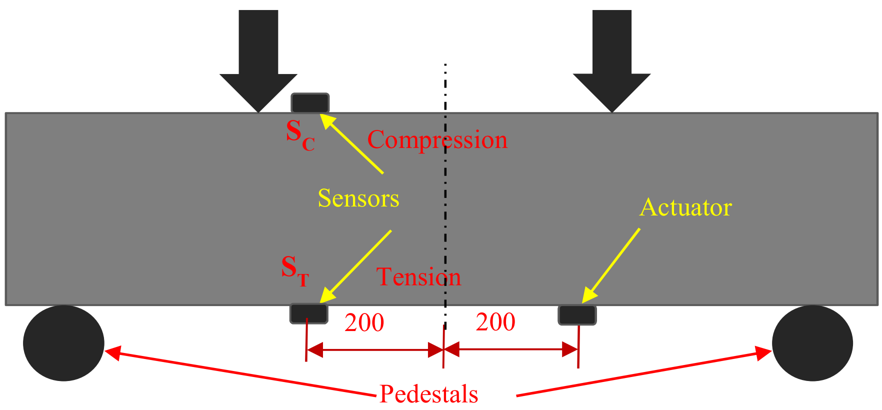

Figure 6-5: Schematic of SA transducers on the specimen under test

Due to the reinforcement of the concrete beam specimens, several anticipated cracks appeared in the mid-span area. As shown in Figure 6-5, d = 400 mm were selected to cover the mid-span area. For comparison, five strain gauges and linear LVTD traditional health monitoring approaches were implemented at the mid-spam of four concrete beams (Figure 6-6). The wire strain gauges with resistance per meter 0.32 Ω were attached using glue to bottom of concrete beam. The strain gauges were continuously recorded at a rate of 10 channels per second, using an automatic data-logger calibrated prior to each test and capable of measuring to a sensitivity of ±1 micro-strain and ±0.001 mm, respectively.

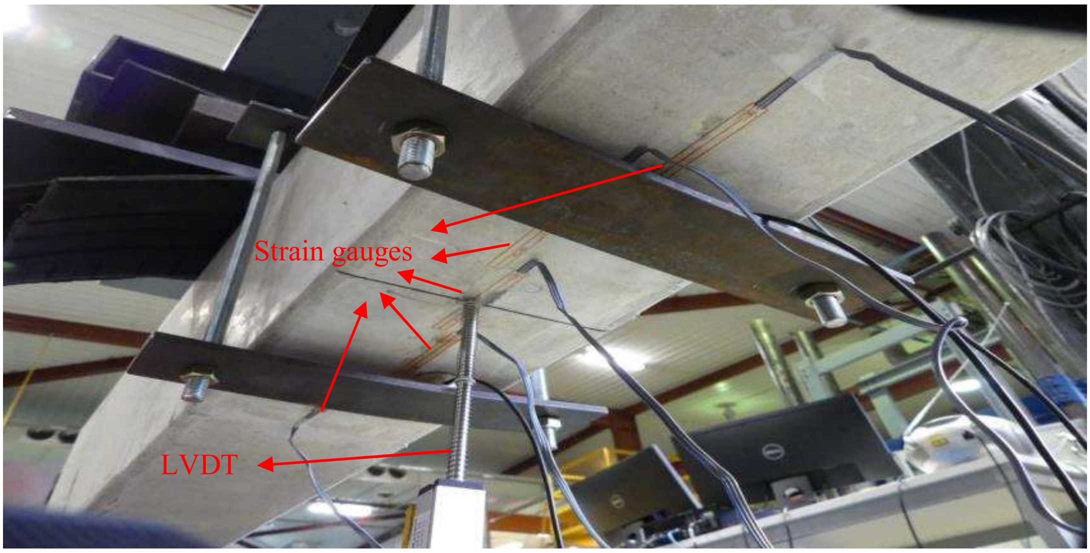

Figure 6-6: Strain gauges and LVDT location at the bottom of specimen

A LabVIEW program was used to generate the swept sine-wave as the excitation wave, and to provide signal processing of received signals, i.e., the output signals of the piezoceramic sensor. Unlike the minimum frequency range set in Chapter 5, the range was set for 500 Hz, to avoid low frequency noise caused by the hydraulic pump. The maximum frequency, signal swept period and amplitude of the sine waves were set to be 150 kHz, 1 s and 10 V, respectively. The program recorded every minute of test from beginning to end of loading, and saved the data in time-domain format. The received raw signal, using wavelet packet analysing, evaluated the health status of the tested concrete beams.

6.4 Results and discussions

For the purpose of this study, a cylinder compressive strength of 40MPa was chosen as the target test strength of the concrete after 28 days of casting, similar to the compressive strength selected for the study detailed in Chapter 5. The actual compressive strength of the concrete cylinder specimens are listed in Table 5-2. Four cylinder specimens were tested based on date plan and the average shown in Figure 5-9. The results obtained by sensors and attached LVDT and strain gauges are evaluated in the following two sections.

6.4.1 Signal processing data analysis

In this experiment, the sweep sinusoidal signal wave was generated by the actuator. The sweep sinusoidal signal started from 500 Hz and ended at 150 KHz, with a magnitude of 10V. The sweep period was set as 1 second and the recording period as 4 seconds, therefore a minimum of three complete sweep periods were recorded in each measurement. As mentioned in Chapter 3, the LabVIEW software can be setup based on the above assumptions and display the receive signal in time-domain format.

From the received signal, one record has been saved every second for future analysis. During the loading procedure, many noises appear in time-domain received signal which make it difficult to evaluate and compare time-domain signals. After recording the time-domain signal every few minutes throughout the test, the results were evaluated in frequency-domain to avoid noises which mostly happened in very low frequency.

Therefore, Fourier transform has been applied on recorded time-domain signal, by using LabVIEW program, and the results formatted in PSD (frequency-domain) were exported to MATLAB program for future investigation and analysis. A MATLAB code was used (Appendix A) for plotting and evaluation of frequency-domain signals. All PSDs were calculated using four periods of swept sine-wave in order to obtain a better accuracy.

Figure 6-7 depicts the received frequency-domain signals from the sensor (S_T) that were documented every 5 minutes after the loading commenced. Each plot corresponds to only one cycle of the detected signal, in the level of millivolts, from repeated swept sine wave.

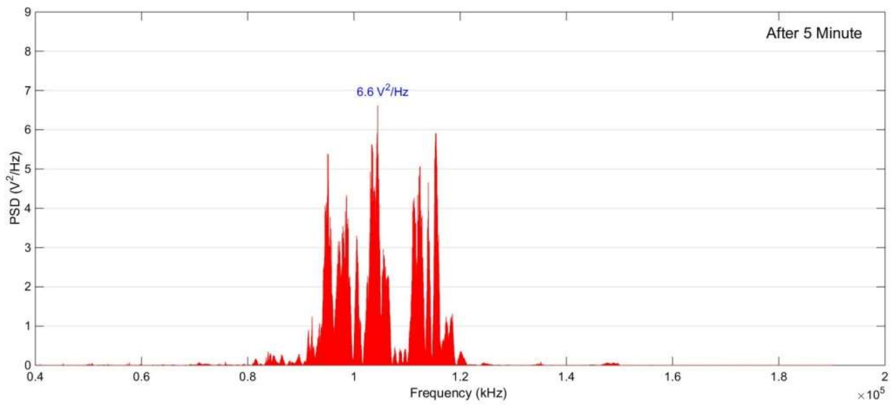
After 5 Minute
6.6 V^2/Hz
PSD (V^2/Hz)
Frequency (kHz)
×10^5

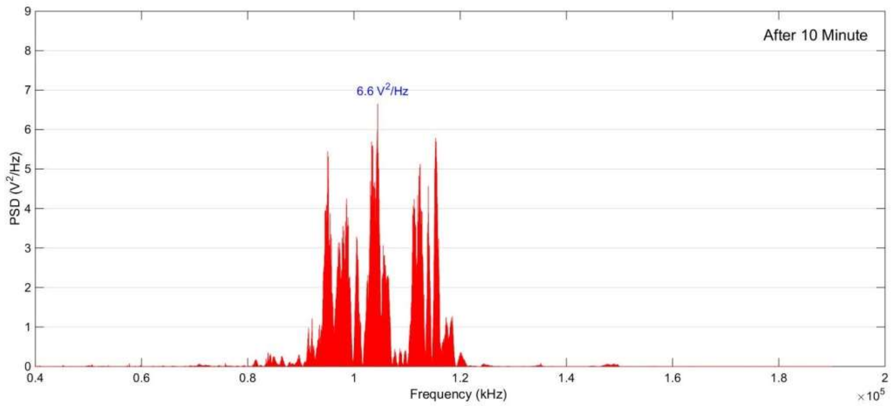
After 10 Minute
6.6 V^2/Hz
PSD (V^2/Hz)
Frequency (kHz)
×10^5

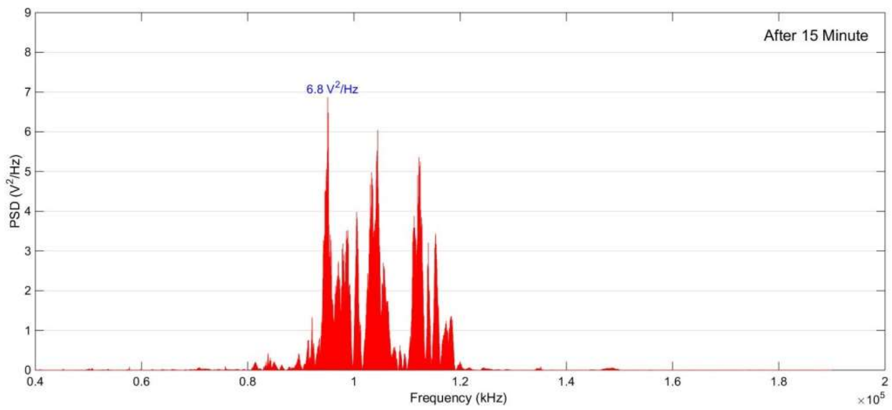
After 15 Minute
6.8 V^2/Hz
PSD (V^2/Hz)
Frequency (kHz)
×10^5

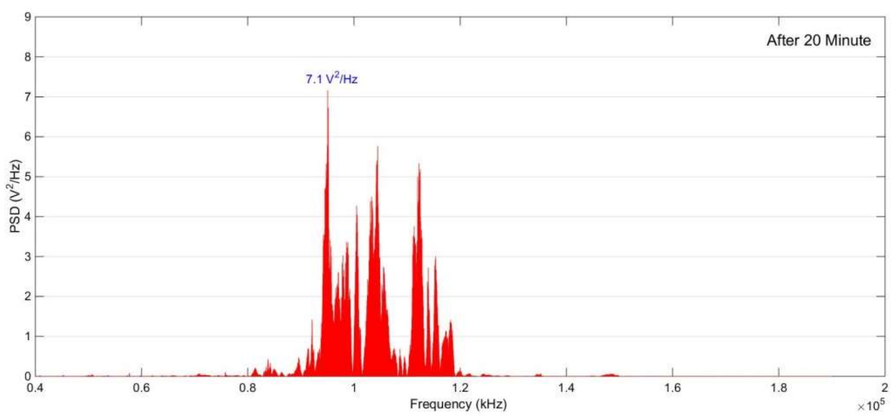
After 20 Minute
7.1 V^2/Hz
PSD (V^2/Hz)
Frequency (kHz)
×10^5

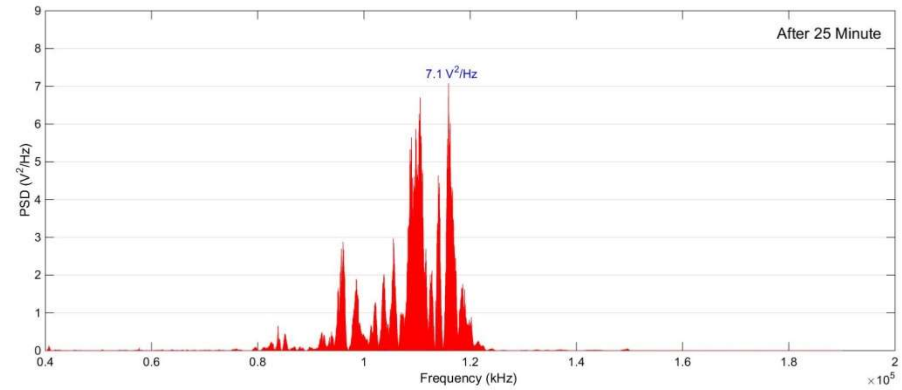
After 25 Minute
7.1 V^2/Hz
PSD (V^2/Hz)
Frequency (kHz)
$\times 10^5$

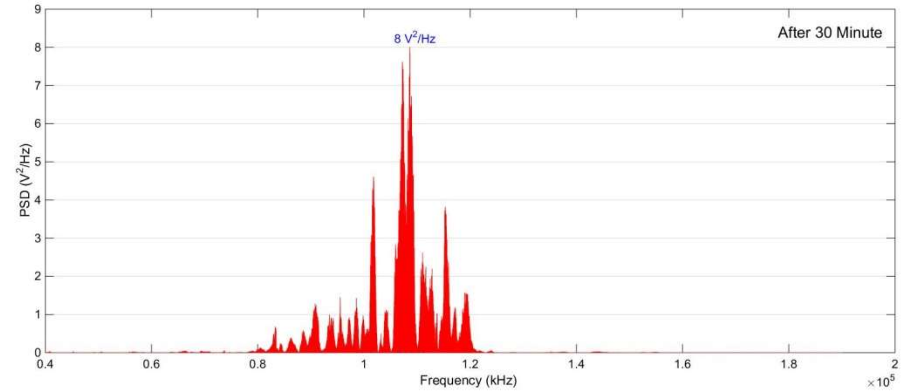
After 30 Minute
8 V^2/Hz
PSD (V^2/Hz)
Frequency (kHz)
$\times 10^5$

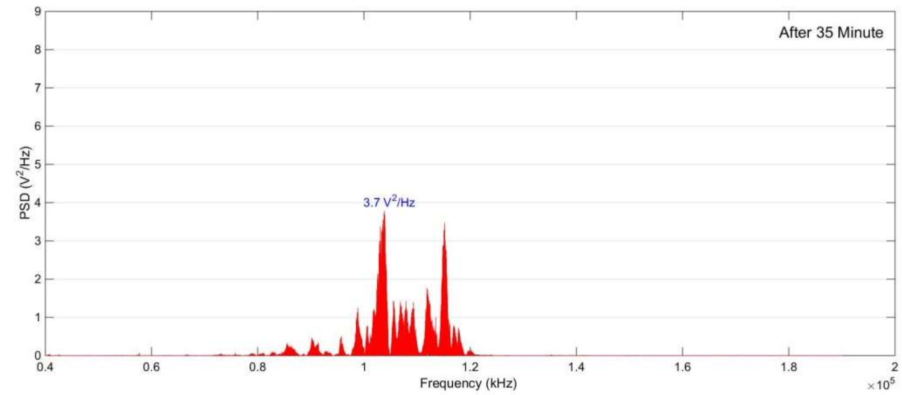
After 35 Minute
3.7 V^2/Hz
PSD (V^2/Hz)
Frequency (kHz)
$\times 10^5$

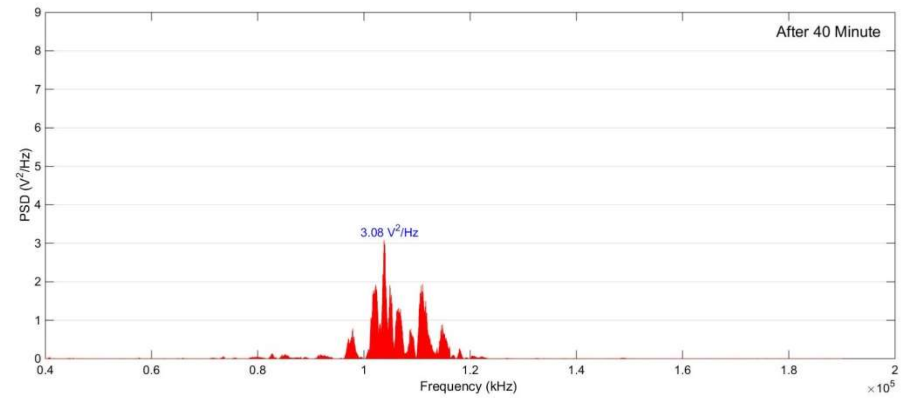
After 40 Minute
3.08 V^2/Hz
PSD (V^2/Hz)
Frequency (kHz)
$\times 10^5$

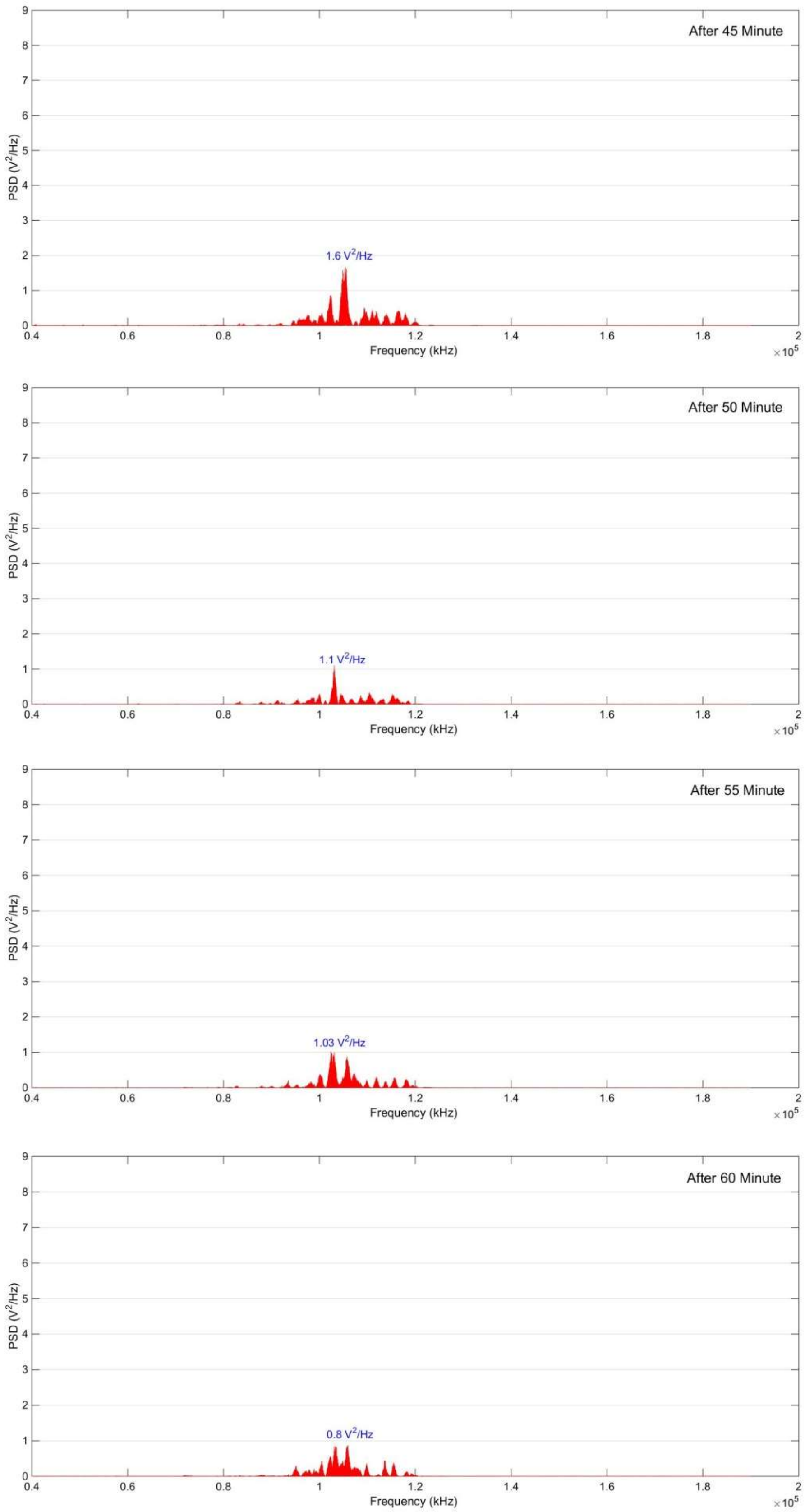

Figure 6-7: Power spectral density (PSD) for the sensor (S_T), measured every 5 minutes, after loading commenced, for the duration of 60 minutes

Several observations can be made from Figure 6-7 that show different properties of the transmission waves in the concrete beam. The test results in frequency-domain shows that there is deference between the before and after cracking moment. Before the cracking moment, the peak of PSD slightly increases with the increasing load value. The peak of PSD value after 5 minutes is close to 6.6 V^2/Hz, while after 30 minutes it is close to 8 V^2/Hz. After the cracking moment on RC beams, the peak of PSD dramatically dropped with the increasing load value. The peak of PSD value after 30 minutes is close to 8 V^2/Hz, while after 35 minutes it is close to 3.7 V^2/Hz. This dramatic drop can be correlated to the indication of a crack on the RC beam which is not visible (cracking moment). The reduction continues after the main drop, thus after 60 minutes of beginning the test, peak of PSD value rich to 0.8 V^2/Hz. This means that the wave propagation was almost totally blocked when the concrete beam failed by cracking.

Similar to the concrete beam results in Chapter 5, waves of lower frequencies attenuate much less than those of higher frequencies. In the frequency-domain response of sensors during tests, the magnitude variation was always in the range of 80 kHz to 120 kHz. Similar observations can be taken from the concrete beams results in Chapter 5. Therefore, it can be concluded that the sweep sine wave signal attenuated at a frequency range of 80 kHz to 120 kHz for concrete materials.

Shortly after a dramatic drop in peak of PSD, cracks become visible on the surface of RC beams, often causing RC beam failure. It is noteworthy that there is a dramatic reduction of the peak of PSD from 8 to 0.8 V^2/Hz after cracks appear in the RC beam; generally, cracks became so severe that they blocked most wave propagation. In summary, the raw frequency-domain data offers useful information regarding the damaged or healthy status of the RC beam and can be used for early assessment of RC beams.

For the damage and cracks induced in the mid-spam of the concrete beam, the bending moment is the major factor in generating damage and cracks. In flexural member like RC beam the crack always start from the tension side, which proved our approach in using a sensor in the bottom of specimens (Figure 6-5). Comparatively, by using additional sensors Figure 6-5 shows the detection of cracks in the tension side was investigated by using a sensor in the compression side (S_C). Figure 6-8 shows the received frequency-domain signals from the S_C every 5 minutes after commencing loading. Each plot corresponds to only one cycle of the detected signal, in the level of millivolts, from repeated sweep sine wave.

Similar to the results of S_T, the S_C results in frequency-domain shows the deference before and after the cracking moment. According to Figure 6-8, before the cracking moment, the peak of PSD slightly increases and then significantly decreases. The peak of PSD value before cracking moment is close to 3.8 V^2/Hz, while after cracking it is close to 2 V^2/Hz.

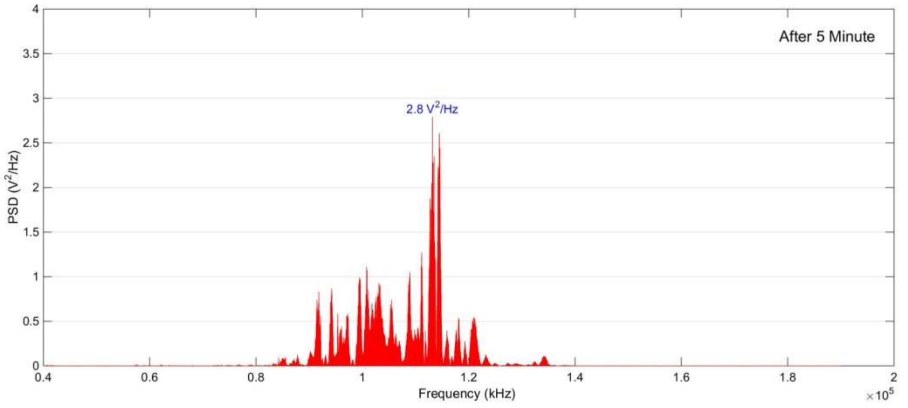
After 5 Minute
2.8 V^2/Hz
PSD (V^2/Hz)
Frequency (kHz)
$\times 10^5$

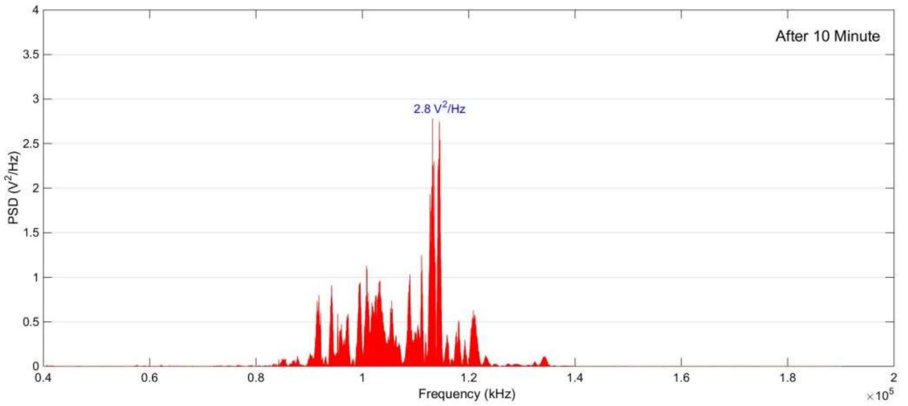
After 10 Minute
2.8 V^2/Hz
PSD (V^2/Hz)
Frequency (kHz)
$\times 10^5$

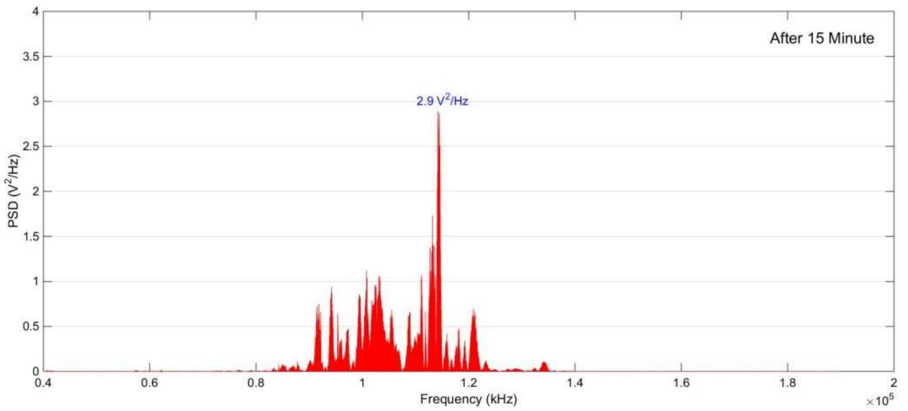
After 15 Minute
2.9 V^2/Hz
PSD (V^2/Hz)
Frequency (kHz)
$\times 10^5$

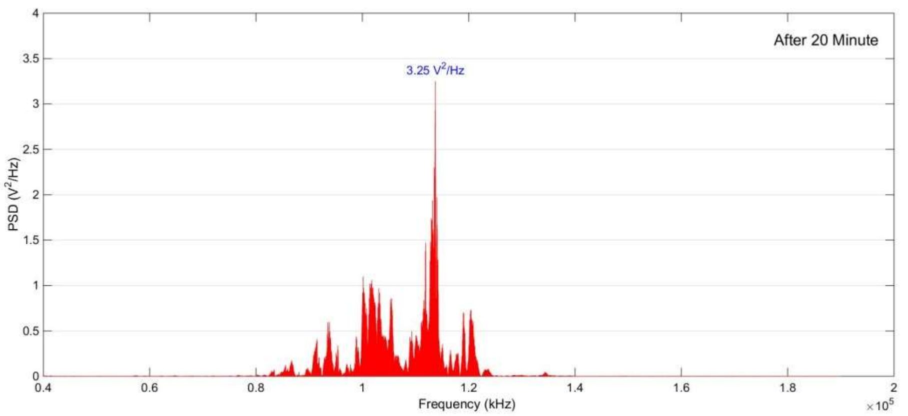
After 20 Minute
3.25 V^2/Hz
PSD (V^2/Hz)
Frequency (kHz)
$\times 10^5$

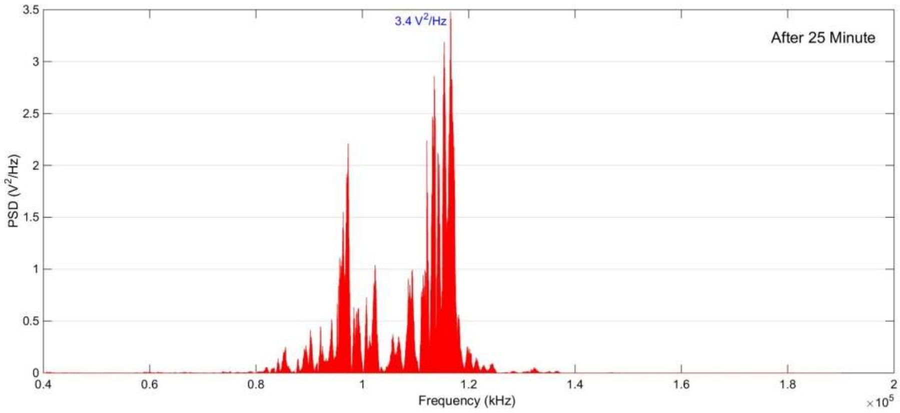
After 25 Minute
3.4 V²/Hz
PSD (V²/Hz)
Frequency (kHz)
×10⁵

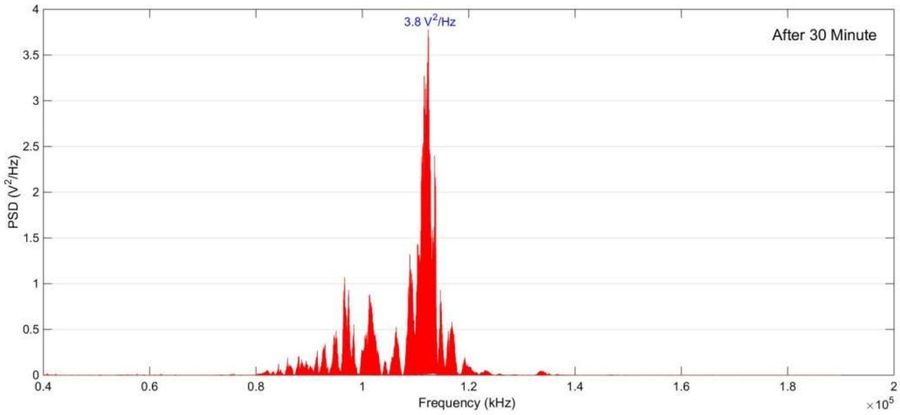
After 30 Minute
3.8 V²/Hz
PSD (V²/Hz)
Frequency (kHz)
×10⁵

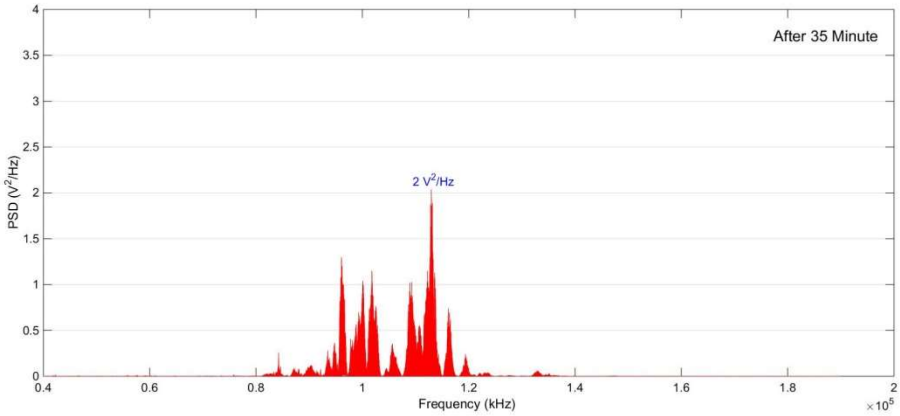
After 35 Minute
2 V²/Hz
PSD (V²/Hz)
Frequency (kHz)
×10⁵

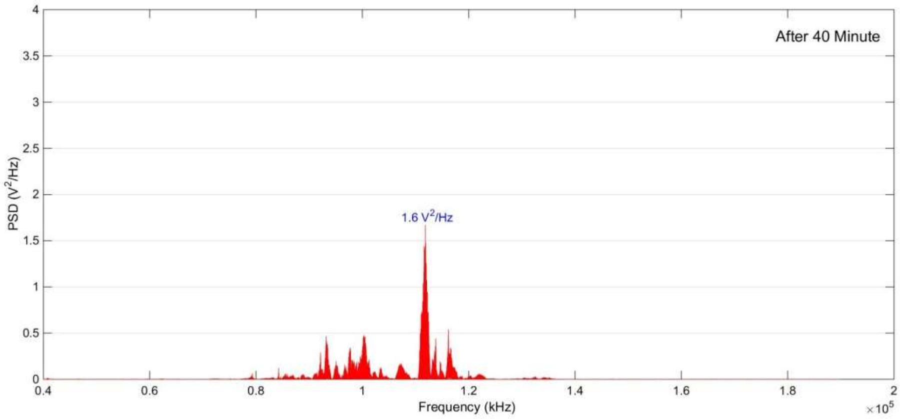
After 40 Minute
1.6 V²/Hz
PSD (V²/Hz)
Frequency (kHz)
×10⁵

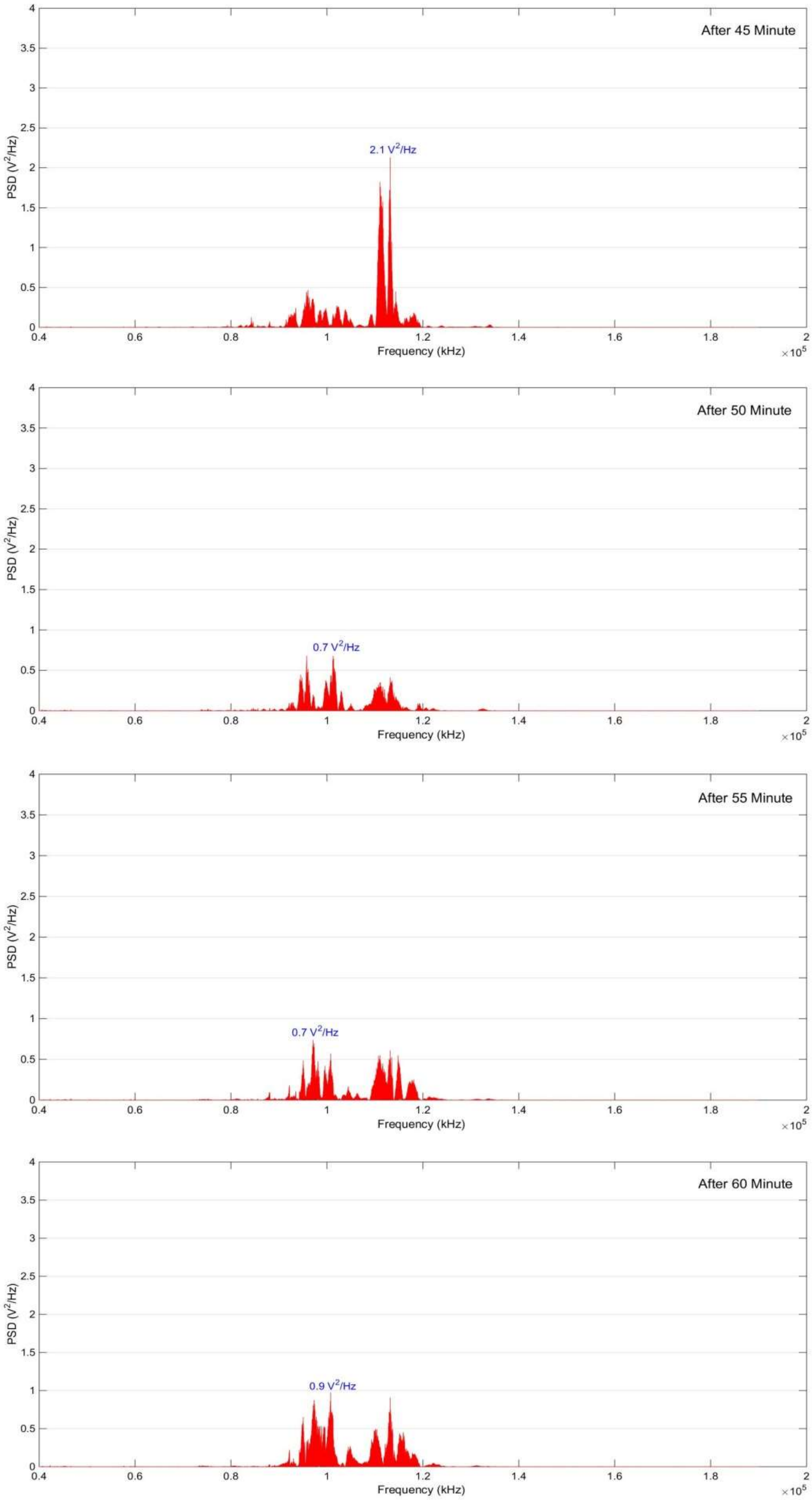

Figure 6-8: Power spectral density (PSD) for the sensor (S_C) measured every 5 minutes, after commencing loading, for the duration of 60 minutes

Although the variation in frequency-domain results of S_C at the cracking moment is very similar to S_T results, there is a difference after the cracking moment in the S_C results. The frequency-domain amplitude values after the cracking moment dramatically drop, while a few minutes after this drop it slightly increases then dropped again. The peak of PSD value after cracking appear to drop from 3.8 V^2/Hz, to 1.6 V^2/Hz and then slightly increases to 2.1 V^2/Hz, while after a further few minutes dropped to 0.7 V^2/Hz. This variation is related to RC beam behaviour under bending. The reason for the first drop was the indication of a crack in the tension side while the sensor was attached to the compression side (S_C). As shown in Figure 6-9a, after the cracking moment in the tension side, the compression in the top of the RC beam significantly increased, which is the prime reason for slightly increasing the amplitude of peak of PSD. As shown in Figure 6-9b, increasing the compression at the top of RC beam, cracks and delamination occurred which caused a second drop in amplitude of peak of PSD.

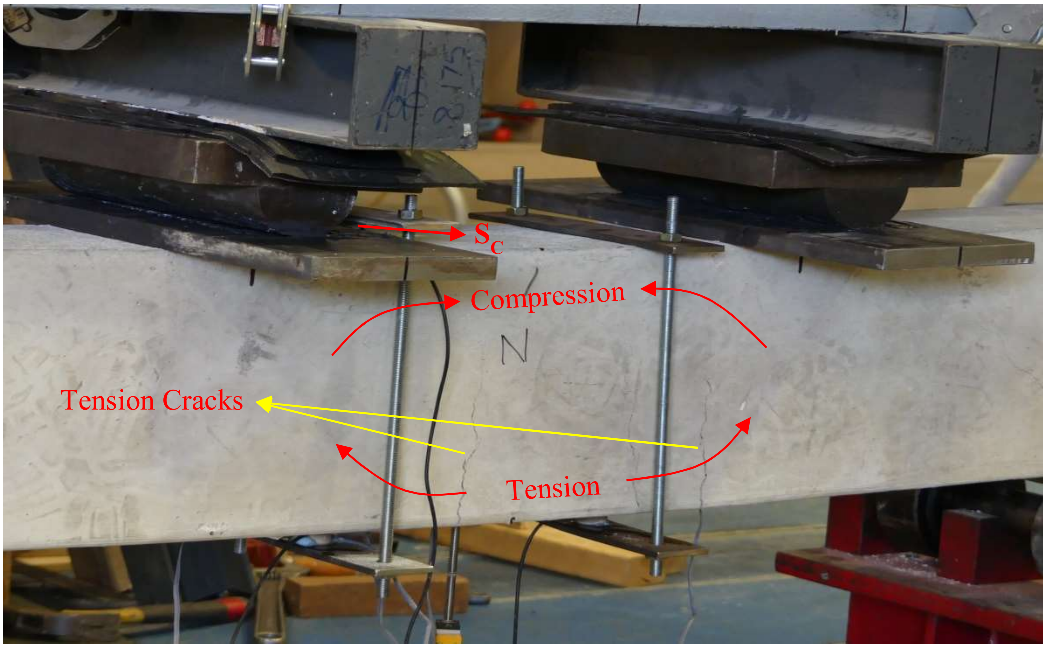

a) Tension cracks

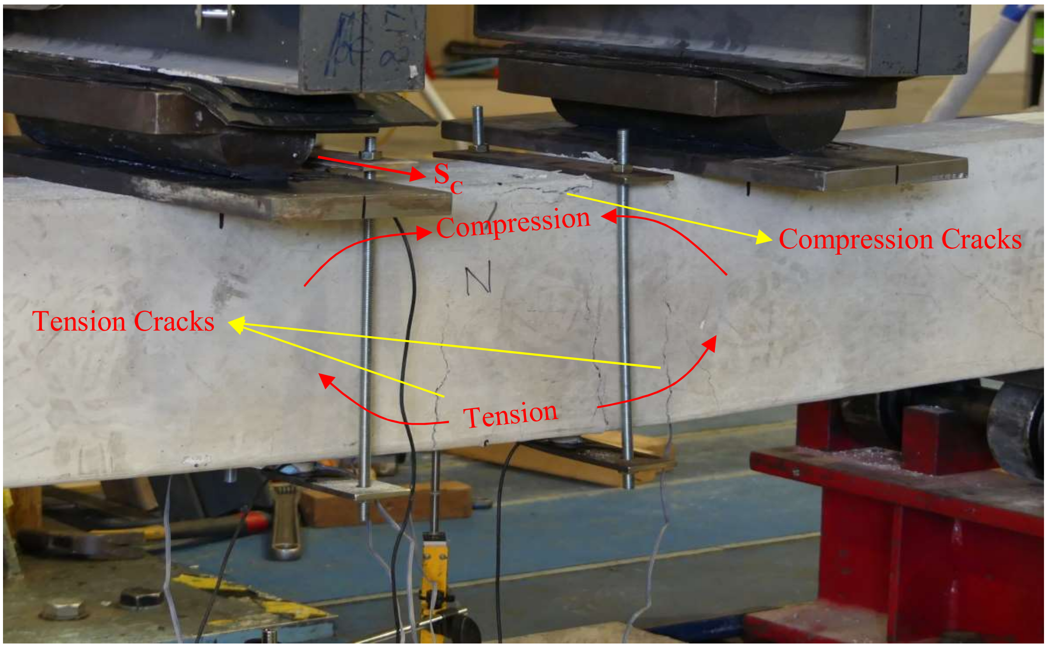

b) Tension and compression cracks

Figure 6-9: Different stage of loading which caused a) tension cracks and b) tension and compression cracks

For a more accurate comparison of the results, the value of peak of PSD and total received power for each record has been calculated using the MATLAB code (Appendix A). Figure 6-10 to Figure 6-17 shows the results of peak of PSD and total received power received by S_T and S_C for four RC beams (LB01, LB02, LB03, LB04) under 4-point loading.

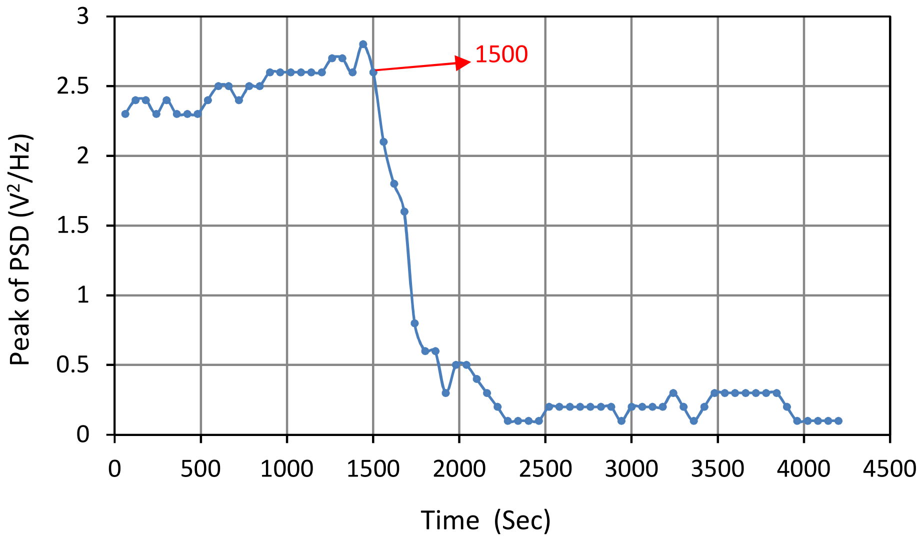

c) S_T sensor

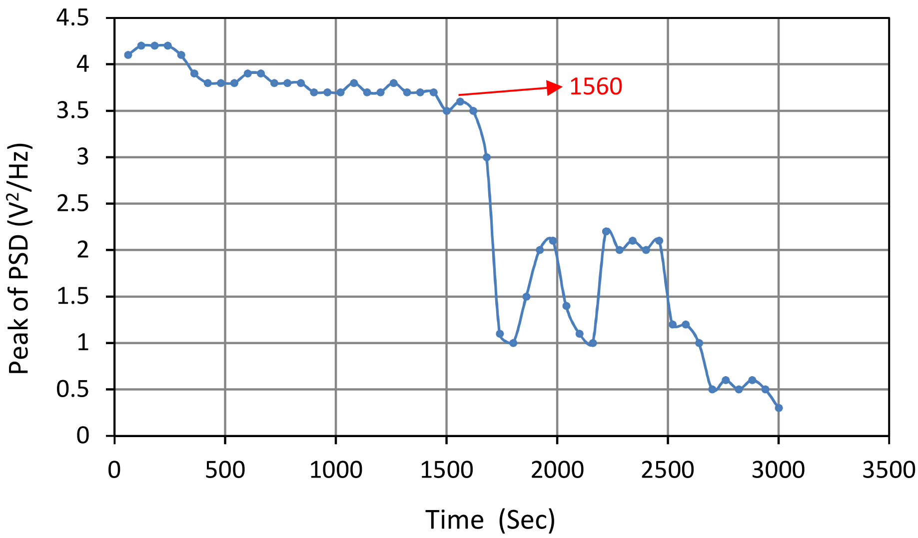

d) S_C sensor

Figure 6-10: Peak of PSD vs time for (a) S_T sensor at the tension side and (b) S_C sensor at the compression side of RC beam LB01

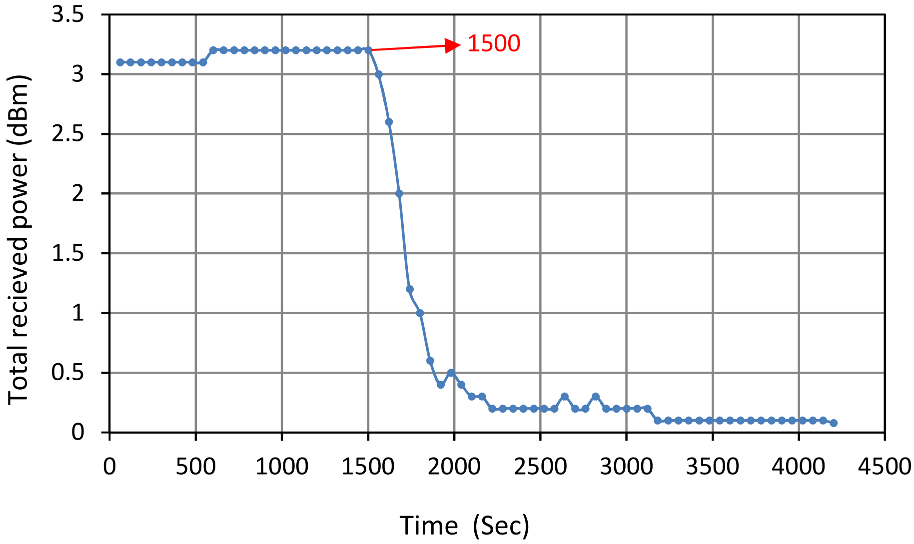

a) S_T sensor

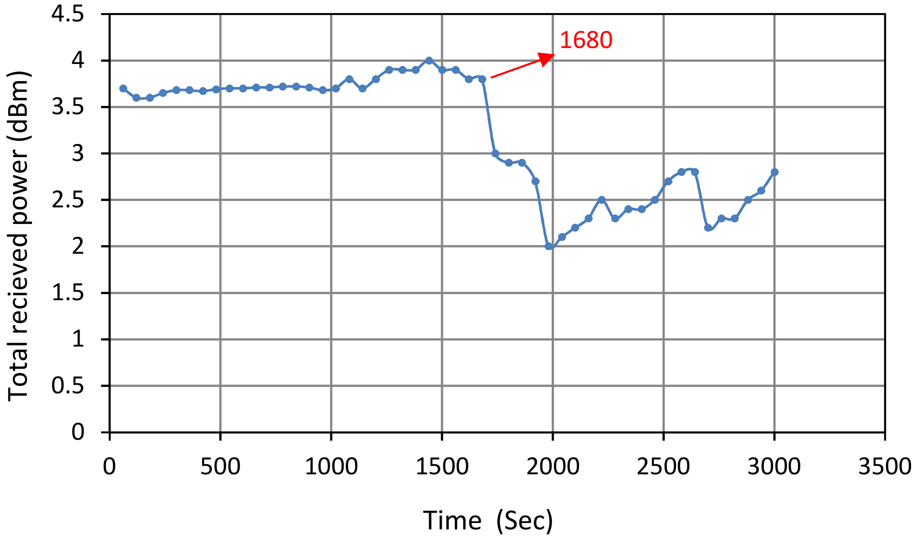

b) S_C sensor

Figure 6-11: Total received power vs time for (a) S_T sensor at the tension side and (b) S_C sensor at the compression side of RC beam LB01

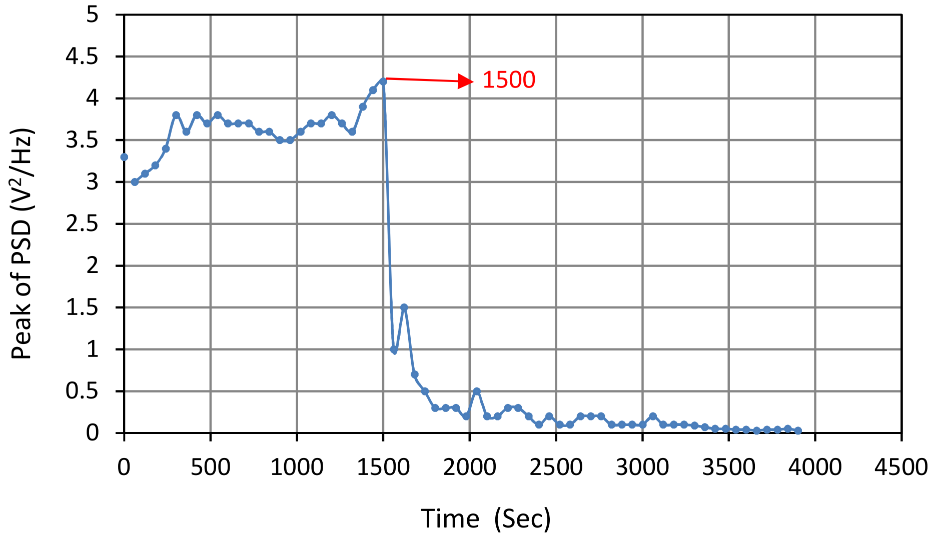

a) S_T sensor

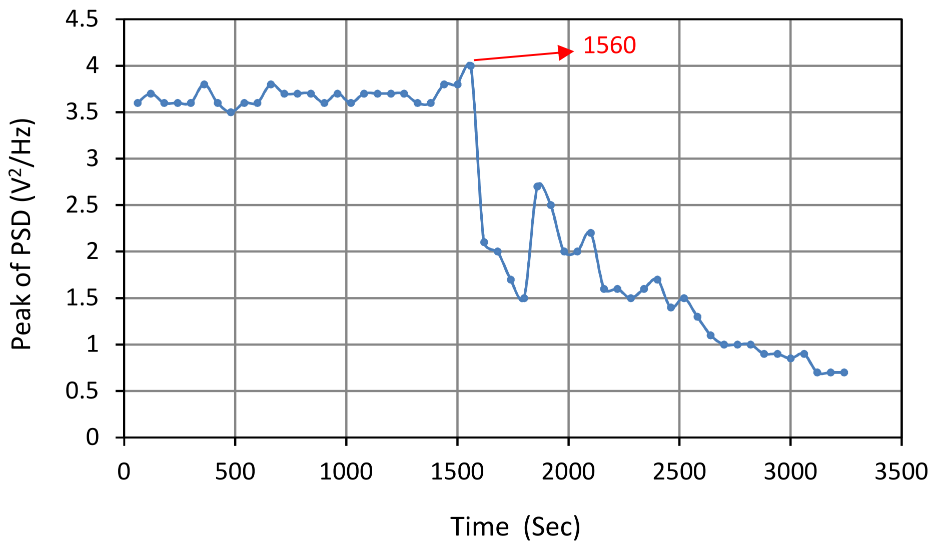

b) S_C sensor

Figure 6-12: Peak of PSD vs time for (a) S_T sensor at the tension side and (b) S_C sensor at the compression side of RC beam LB02

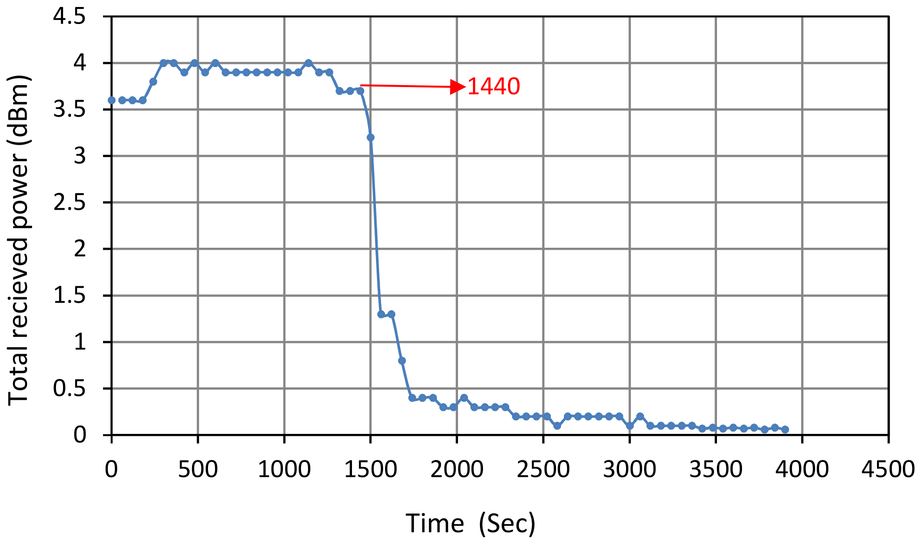

a) S_T sensor

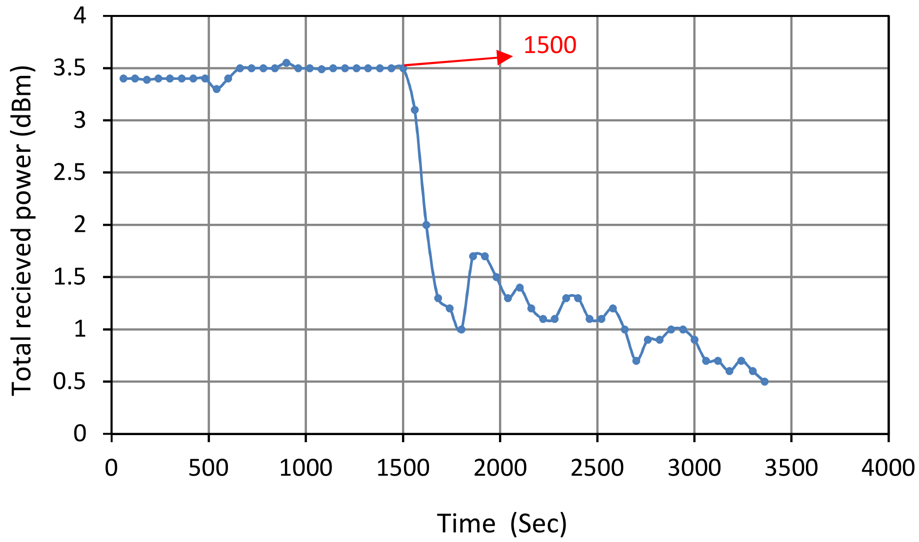

b) S_C sensor

Figure 6-13: Total received power vs time for (a) S_T sensor at the tension side and (b) S_C sensor at the compression side of RC beam LB02

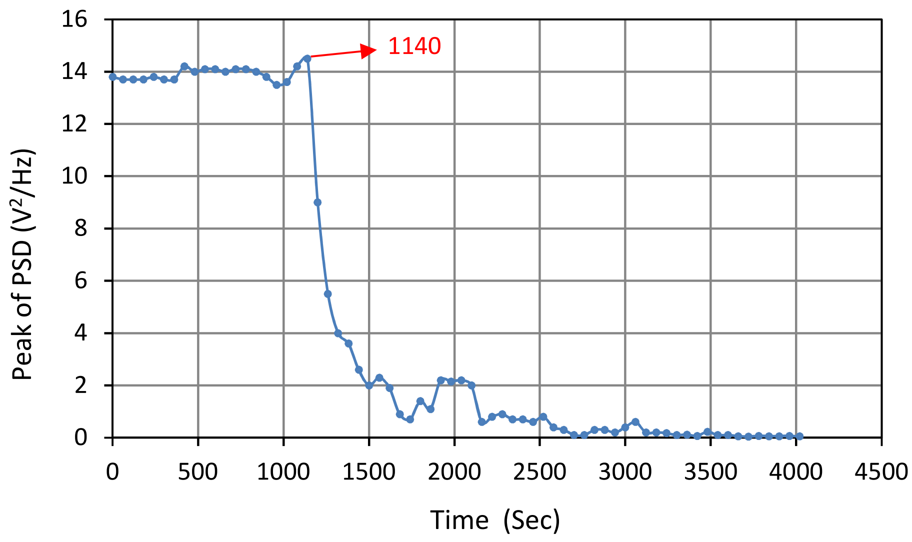

a) S_T sensor

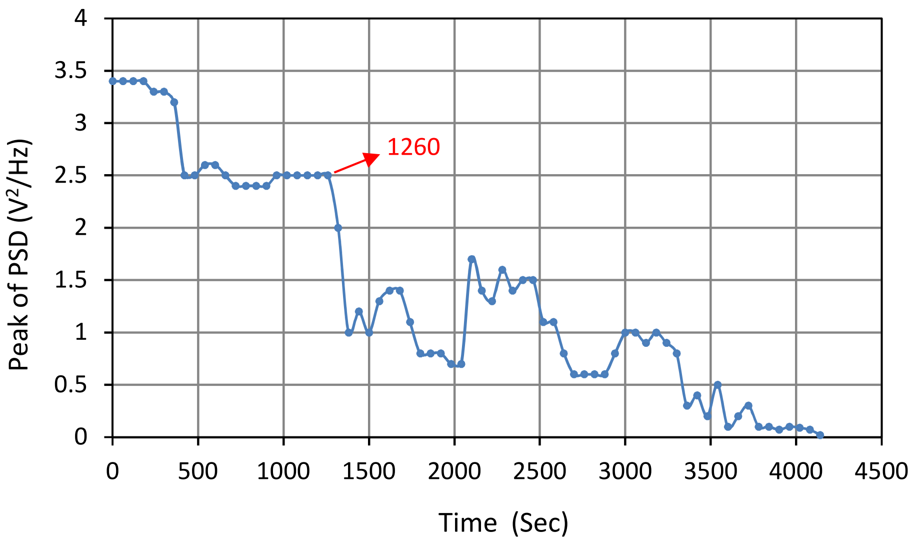

b) S_C sensor

Figure 6-14: Peak of PSD vs time for (a) S_T sensor at the tension side and (b) S_C sensor at the compression side of RC beam LB03

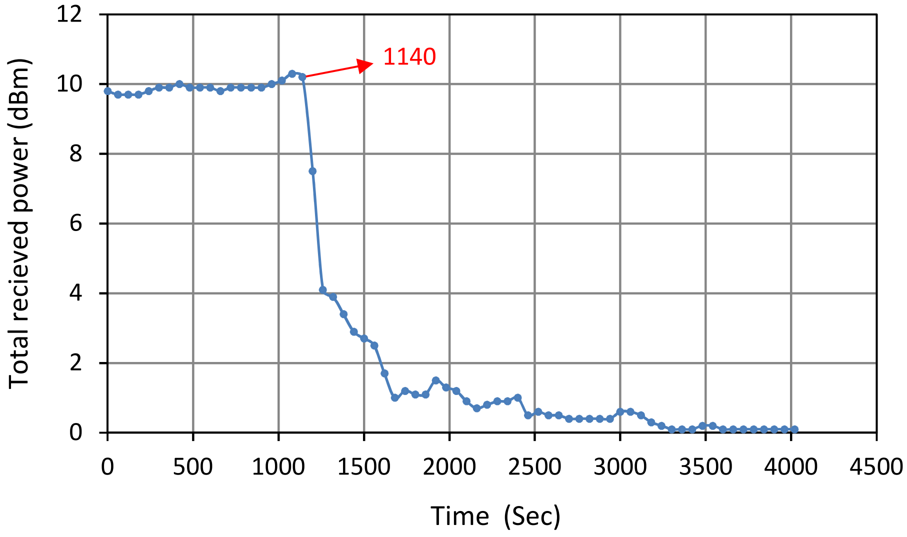

a) S_T sensor

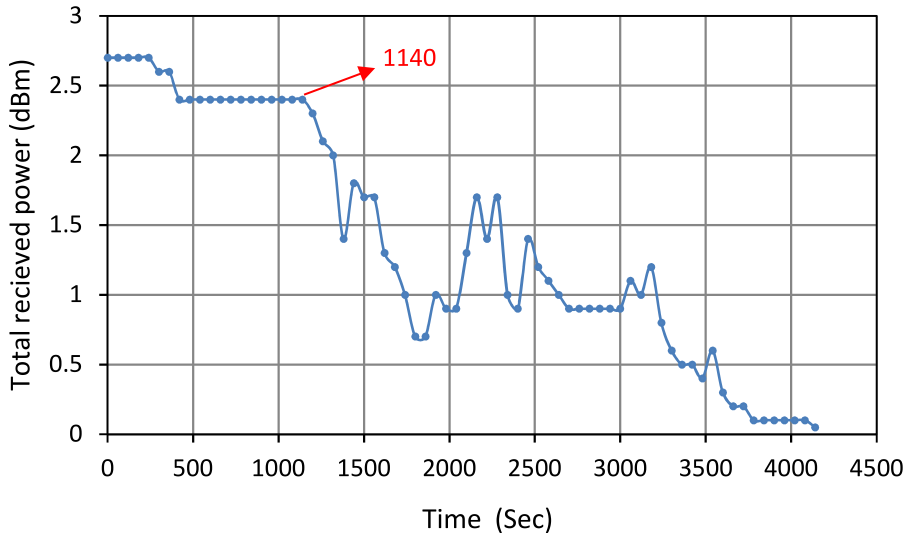

b) S_C sensor

Figure 6-15: Total received power vs time for (a) S_T sensor at the tension side and (b) S_C sensor at the compression side of RC beam LB03

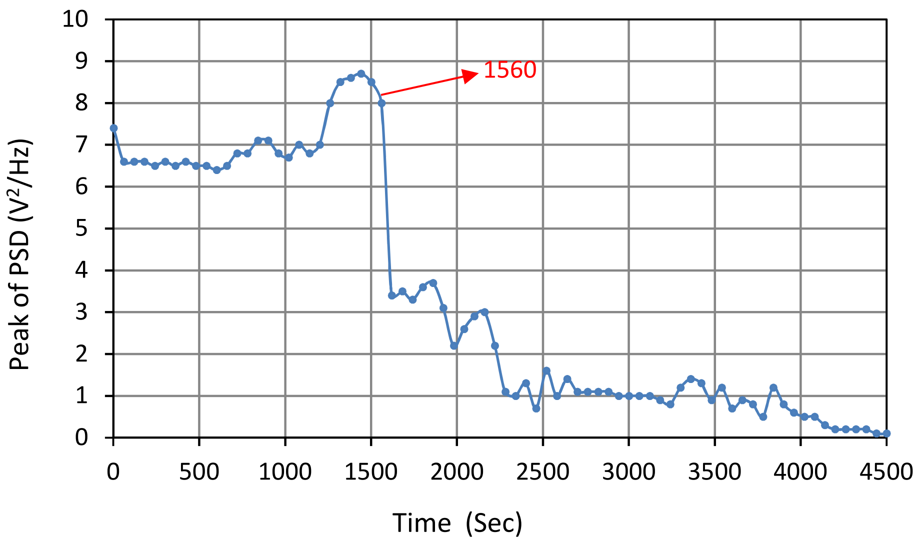

a) S_T sensor

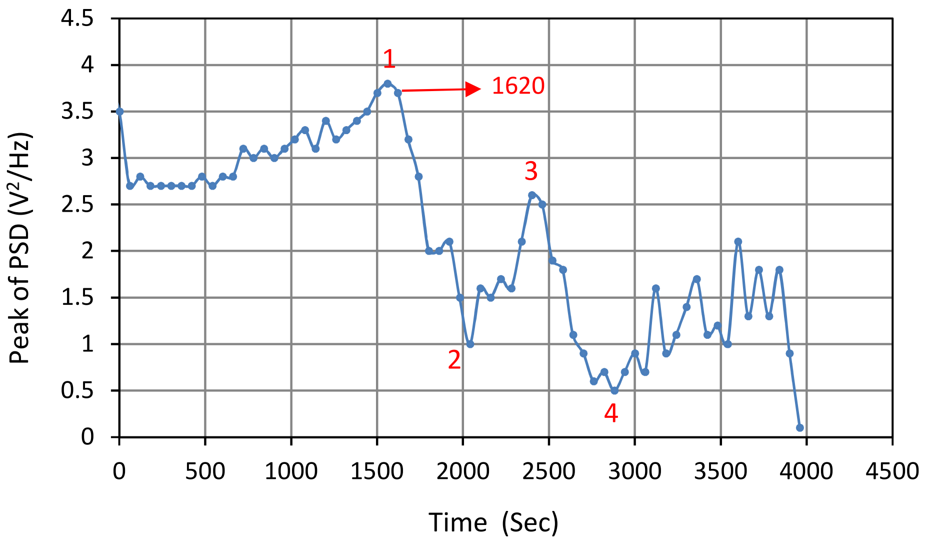

b) S_C sensor

Figure 6-16: Peak of PSD vs time for (a) S_T sensor at the tension side and (b) S_C sensor at the compression side of RC beam LB04

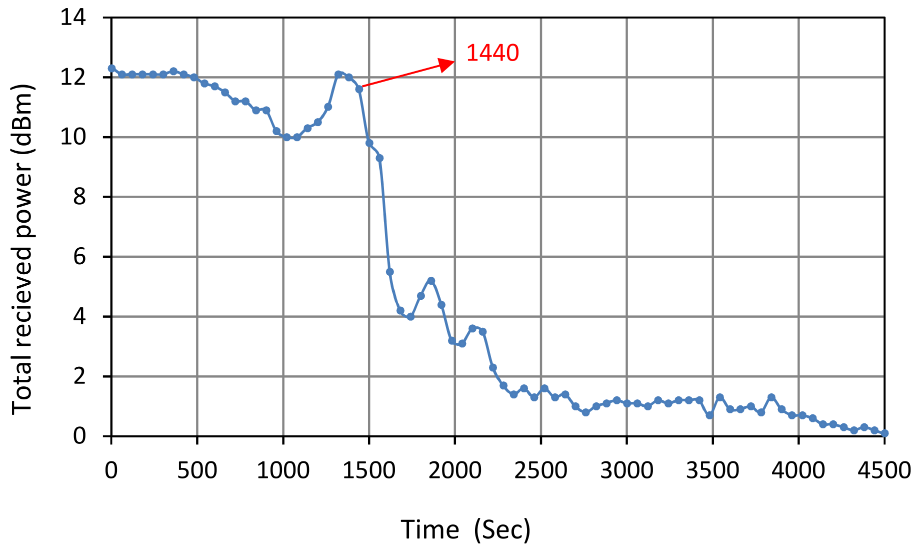

a) S_T sensor

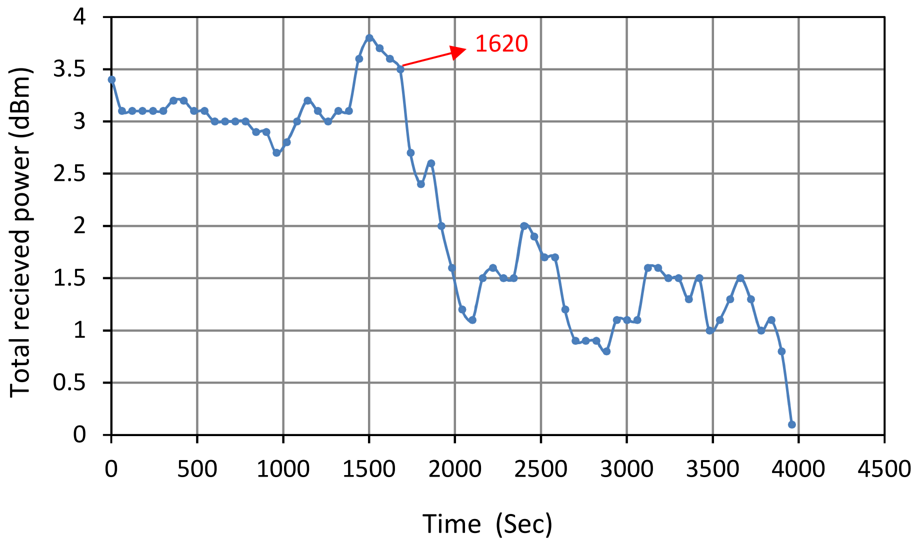

b) S_C sensor

Figure 6-17: Total received power vs time for (a) S_T sensor at the tension side and (b) S_C sensor at the compression side of RC beam LB04

Several observations can be made from Figure 6-10 to Figure 6-17 that shows variation of peak of PSD and total received power during loading:

1) The test results for peak of PSD and total received power shown in figures can be divided into the before and after cracking moment. For example, specimen LB02 shows peak of PSD value at the certain time from 4.2 V^2/Hz dramatically dropped to 1 V^2/Hz, which can be correlated to the beginning of a crack in the RC beam. This means that the wave propagation was almost totally blocked when the RC beam failed by cracking. This dramatic drop in value of peak of PSD and total received power happened in all RC beam specimens.

2) Similar to the results with concrete beams in Chapter 5, peak of PSD is not outstanding, rather a number of frequencies share the received power. So the compression results of peak of PSD and total received power indicate that total received power shows less variations in consecutive record before and after cracking. Figure 6-10a and Figure 6-11a, for specimen LB01, clearly shows how the variation of peak of PSD curves trended in total received power curves.

3) In the results of peak of PSD for all RC beam specimens, before indication of a crack, the value of peak of PSD slightly increased. For example, in specimen LB04 (Figure 6-16), the value of peak of PSD before the cracking moment increased from 7 V^2/Hz to 8.7 V^2/Hz and after dropped to 3.4 V^2/Hz. Similar observations were recorded from the other specimens with more or less variation. Therefore, the findings can be used for early assessment of RC beams before the cracking moment.

4) The results of peak of PSD for the sensor in the compression side (S_C) show that after indications of the cracks in the tension side the value of peak of PSD dropped.

With increased compression in the top of the specimen, the value of the peak of PSD slightly increased then dropped again due to cracks and delamination on the top of beams (Figure 6-9). For example, Figure 6-16b shows the peak of PSD after the cracking moment dramatically dropped from point 1 to 2 (marked on the figure) and then slightly increased to point 3, while dropping again to point 4 moments later. Therefore, the findings verify that it is not necessary that the actuator and sensor attach to the damaging zone of specimens which as mentioned in literature review was a challenging issue for researchers to take aware sensors from damage zone.

5) A comparison between the results of the sensor in the compression side (S_C) and sensor in (S_T) shows the dramatic drop in the value of peak of PSD and total received power occurred in the different time. For example, as shown in Figure 6-12, a dramatic drop in peak of PSD curves received by S_T and S_C were 1500 and 1560 seconds, respectively. This means the S_C detected the cracking moment 60 seconds later or the crack was closer to S_T sensor. Although 60 seconds in 0.009 mm/sec loading ratio is equal to a small amount of load, early assessment is the main priority for researchers. Therefore, the arrangement of sensors must be considered as another important aspect for early assessment of RC elements.

In the next step of data analysis, as mentioned in the signal processing section of Chapter 3, standard deviation is the most common way to characterise the spread of a data set. From the results of peak of PSD and total received power, shown in Figure 6-10 to Figure 6-17, the difference in level of received signal were obvious. These differences correlated to heterogeneity of concrete material structure which is effected by signal propagation in different specimens. Consequently, before applying the standard deviation, the results of peak of PSD and total received power obtained from four RC beams normalized, as shown in Figure 6-18a and Figure 6-19a; and then standard deviation was applied on normalized data, as illustrated in Figure 6-18b and Figure 6-19b.

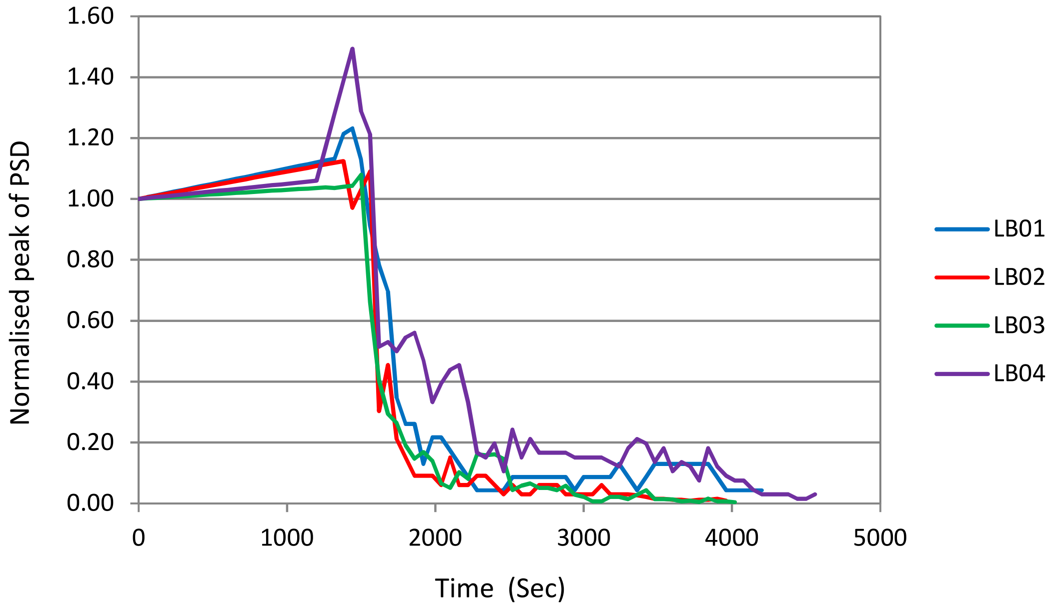

c) Normalised peak of PSD

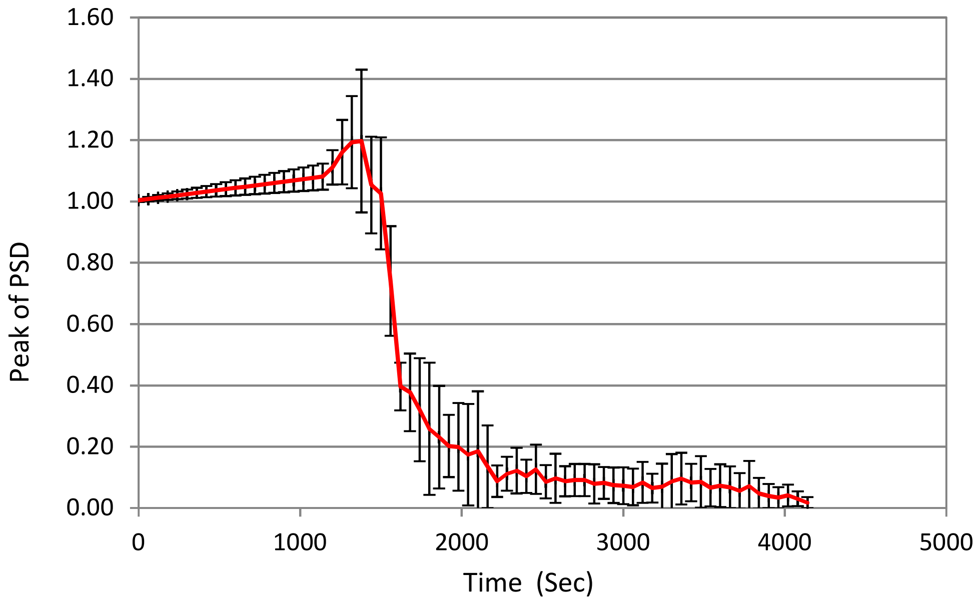

d) Standard deviation

Figure 6-18: Peak of PSD results obtained from four RC beams after a) normalisation and b) standard deviation

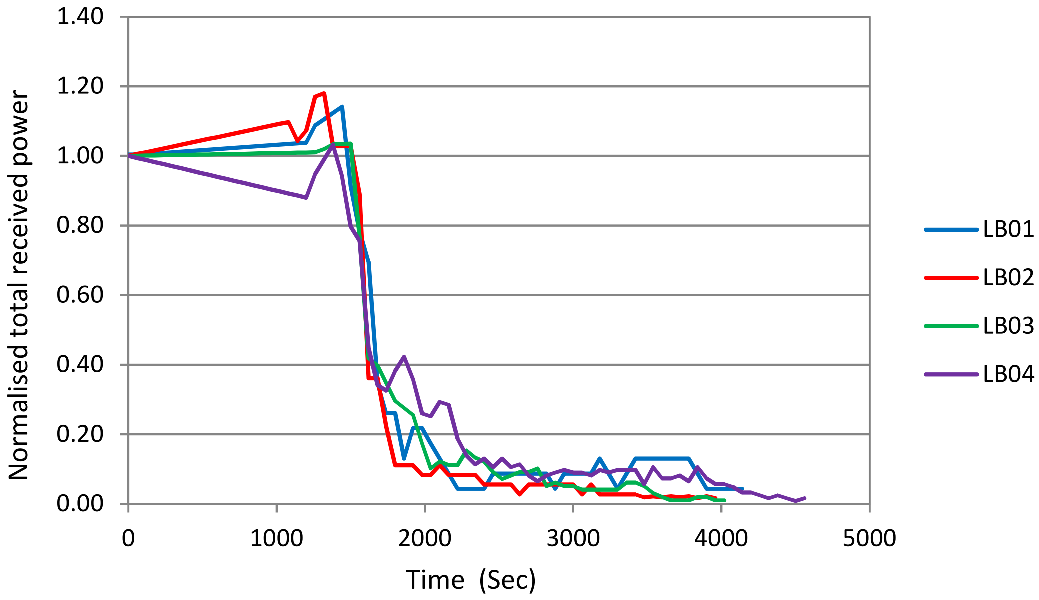

c) Normalised total received power

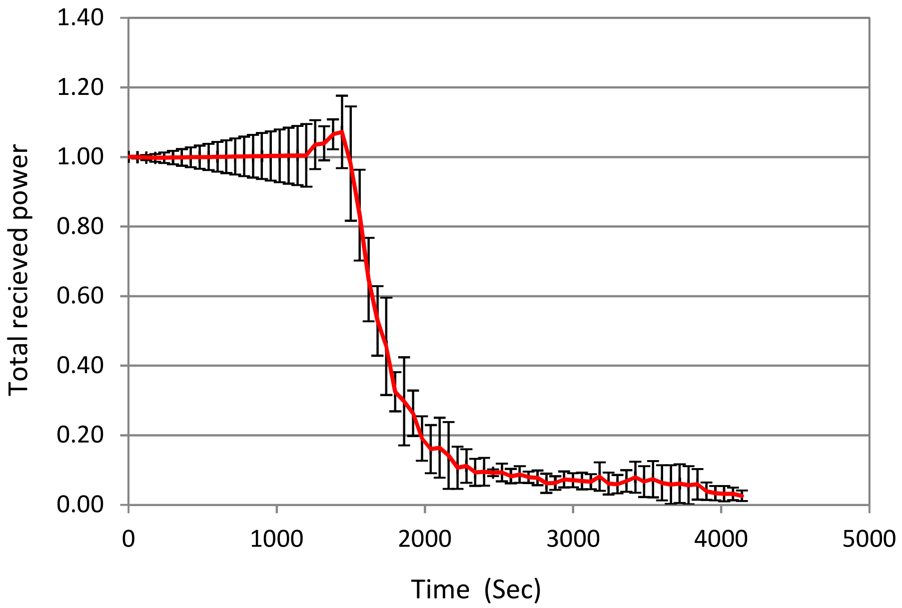

d) Standard Deviation

Figure 6-19: Total received power results obtained from four RC beams after a) normalisation and b) standard deviation

The normalised curves for peak of PSD and total received power shows the dramatic drop in signal that happened for all RC beams used in this study. The peak of PSD and total received power of specimen LB04 shows more variation in consecutive records in compression with other specimen results. This variation is clearly observable in standard deviation curves for LB04 specimen. However, the dramatic drop in the value of received signal before and after cracking promising all specimens clearly detected the cracking moment.

The proposed damage index in Chapter 3, using equation 3-2, represents the transmission energy loss caused by damage. When the damage index is close to 0, it means the structure is in a healthy state. When the damage index is greater than a certain threshold, it means damage has appeared. In this study, the index value more than 0.5 is categorised as serious damage. When the damage index is very close to 1 it means the concrete structure is near failure. Table 6-2 and consequently Figure 6-20 shows the calculated damage indexes for four RC beam specimens for a period of 4080 seconds after loading began. The highlighted damage index in the table shows the specimen cross the threshold to serious damage zone (highlighted by blue colour). The table also presents calculations of increasing the value of damage index before cracks occur (highlighted pink), which can be categorised as a warning before specimens cross the threshold into serious damage; this consequently predicts structure failure. The results in Table 6-2, shown on Figure 6-20, clearly show the jump in the value of damage index, which correlated to the cracking moment on RC beams and increase in number of cracks and width. The selected threshold value of 0.5 is shown by red line at the figures.

Table 6-2: Damage index values calculated at different time of loading

Time (S)	LB01	LB02	LB03	LB04	Time (S)	LB01	LB02	LB03	LB04
	Damage Index					Damage Index			
60	0	0	0	0	2100	0.83	0.83	0.85	0.56
120	0.04	0.06	0	0	2160	0.87	0.87	0.96	0.55
180	0.04	0.03	0	0	2220	0.91	0.91	0.94	0.67
240	0.00	0.03	0.01	0.02	2280	0.96	0.96	0.93	0.83
300	0.04	0.15	0	0	2340	0.96	0.96	0.95	0.85
360	0.00	0.09	0	0.02	2400	0.96	0.96	0.95	0.80
420	0.00	0.15	0.04	0	2460	0.96	0.96	0.96	0.89
480	0.00	0.12	0.02	0.02	2520	0.91	0.91	0.94	0.76
540	0.04	0.15	0.03	0.02	2580	0.91	0.91	0.97	0.85
600	0.09	0.12	0.03	0.03	2640	0.91	0.91	0.98	0.79
660	0.09	0.12	0.02	0.02	2700	0.91	0.91	0.99	0.83
720	0.04	0.12	0.03	0.03	2760	0.91	0.91	0.99	0.83
780	0.09	0.09	0.03	0.03	2820	0.91	0.91	0.98	0.83
840	0.09	0.09	0.02	0.08	2880	0.91	0.91	0.98	0.83
900	0.13	0.06	0.01	0.08	2940	0.96	0.96	0.99	0.85
960	0.13	0.06	0.01	0.03	3000	0.91	0.91	0.97	0.85
1020	0.13	0.09	0.01	0.02	3060	0.91	0.91	0.96	0.85
1080	0.13	0.12	0.04	0.06	3120	0.91	0.91	0.99	0.85
1140	0.13	0.12	0.26	0.03	3180	0.91	0.91	0.99	0.86
1200	0.13	0.15	0.34	0.06	3240	0.87	0.87	0.99	0.88
1260	0.17	0.12	0.60	0.21	3300	0.91	0.91	0.99	0.82
1320	0.17	0.09	0.71	0.29	3360	0.96	0.96	0.99	0.79
1380	0.13	0.18	0.74	0.30	3420	0.91	0.91	0.99	0.80
1440	0.22	0.24	0.81	0.32	3480	0.87	0.87	0.98	0.86
1500	0.13	0.27	0.85	0.29	3540	0.87	0.87	0.99	0.82
1560	0.09	0.70	0.83	0.21	3600	0.87	0.87	0.99	0.89
1620	0.22	0.55	0.86	0.50	3660	0.87	0.87	1.00	0.86
1680	0.30	0.79	0.93	0.51	3720	0.87	0.87	1.00	0.88
1740	0.65	0.85	0.95	0.50	3780	0.87	0.87	0.99	0.92
1800	0.74	0.91	0.90	0.45	3840	0.87	0.87	1.00	0.82
1860	0.74	0.91	0.92	0.44	3900	0.91	0.99	1.00	0.88
1920	0.87	0.91	0.84	0.53	3960	0.96	1.00	0.99	0.91
1980	0.78	0.94	0.84	0.67	4020	0.96	1.00	1.00	0.92
2040	0.78	0.85	0.84	0.61	4080	1.00			0.92

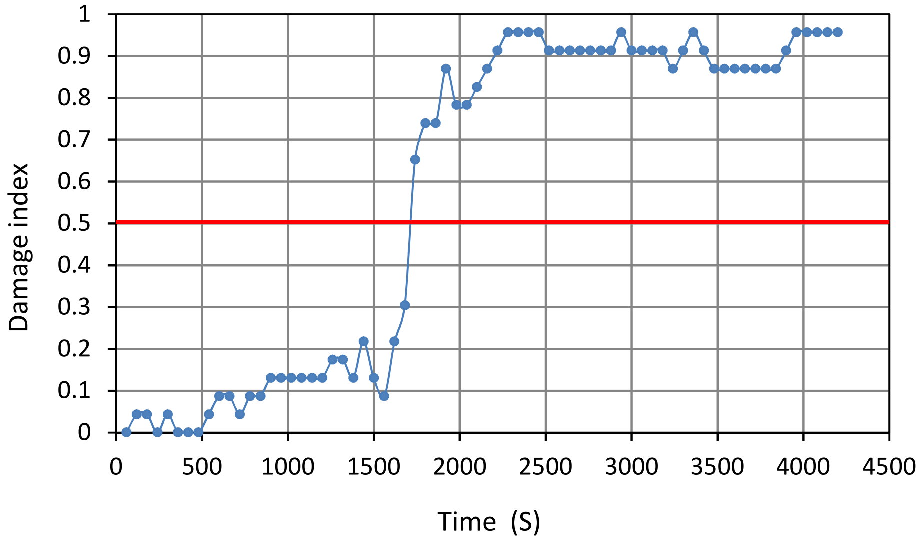

Damage index
Time (S)
0
0.1
0.2
0.3
0.4
0.5
0.6
0.7
0.8
0.9
1
0
500
1000
1500
2000
2500
3000
3500
4000
4500

a) LB01

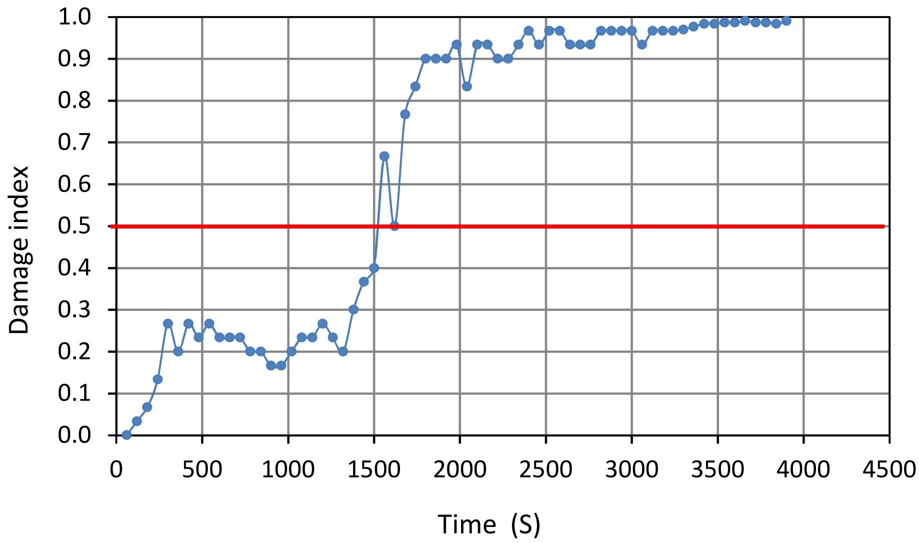

Damage index
Time (S)
0.0
0.1
0.2
0.3
0.4
0.5
0.6
0.7
0.8
0.9
1.0
0
500
1000
1500
2000
2500
3000
3500
4000
4500

b) LB02

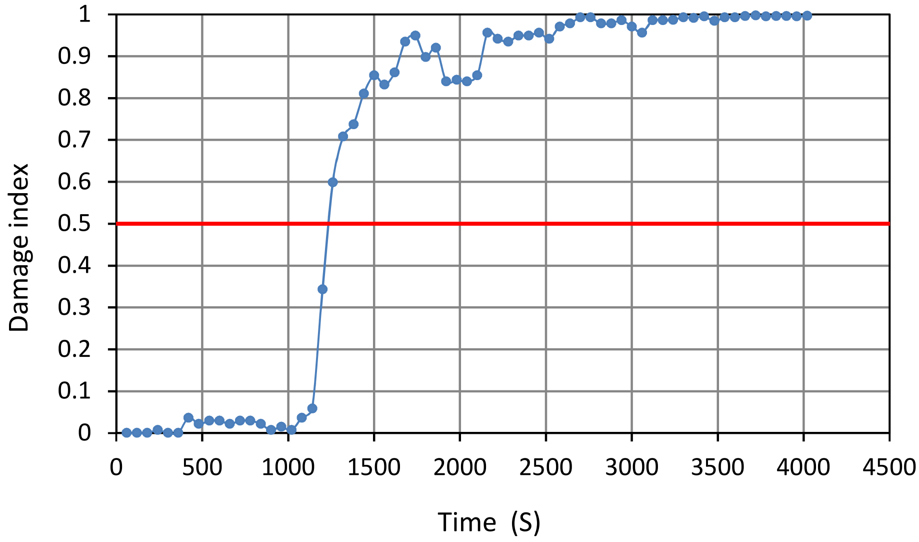

c) LB03

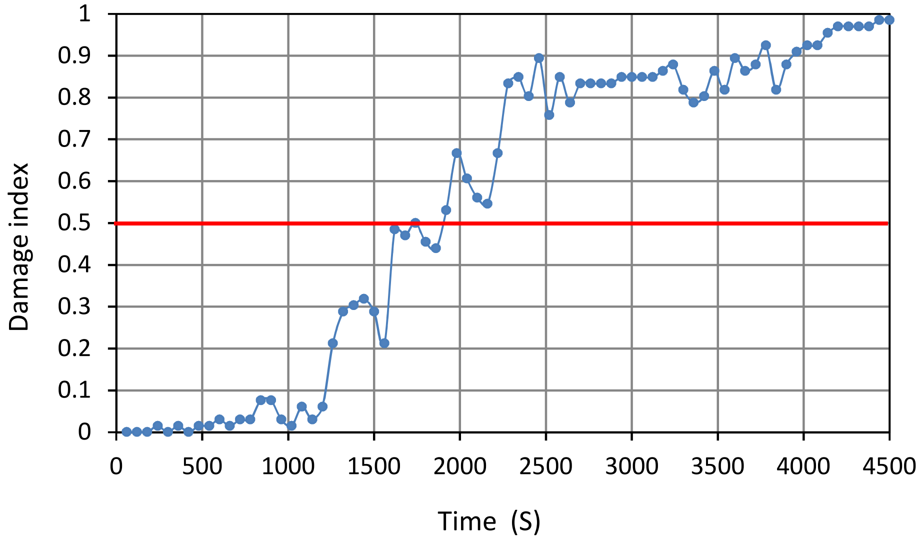

d) LB04

Figure 6-20: Damage index value for RC beam specimens a) LB01, b) LB02, c) LB03 and d) LB04

6.4.2 Verification of signal processing data

In this experimental study the load cell, strain gauges, and LVDT results are also implemented for comparison and verification purposes. Before investigation on these results, theoretical investigations are necessary to find the cracking moment and are used as a bridge between load cell results and sensor results. The theoretical investigations can show the sensor performance in detection, evaluation, and prediction of damage before RC beams failure. Initially, the beams are uncracked where they exhibited linear moment–deflection behaviour. This is attributed to the linear elastic characteristics of rebar and concrete. With additional loading, cracking occurs at the constant moment zone when the applied moment exceeds the cracking moment, causing a reduction in stiffness and resulting in beam failure. This is due to the wider crack openings in the RC beams, which is attributed to the modulus of elasticity of rebar. Therefore, early assessment of the cracking moment (M_{cr}) has been calculated using the following equations suggested by Australian standard (AS3600, 2009):

$$M_{cr} = Z\left(f'_{ct.f}\right) \geq 0.0 \tag{6-1}$$

where $f'_{ct.f}$ is the characteristic flexural tensile strength of concrete specified as $f'_{ct.f} = 0.6\sqrt{f'_c}$.

Z is the section modulus of the uncracked section obtained from dividing moment of inertia uncracked section to distance of neutral axis to top of the beam,

$$Z = I_{uncr}/y_b$$

$$Z = \frac{195.3\times10^6}{125} = 1.56 \times 10^6\ mm^3$$

and,

$$f'_{ct.f} = 0.6\sqrt{50}$$

$$f'_{ct.f} = 4.24\ MPa$$

Thus, the cracking moment can be found as following:

$$M_{cr} = 1.56 \times 10^{6} \times 10^{-9} \times (4240000)$$

$$M_{cr} = 6614.4 \text{ Nm}$$

and the applied load (F) at time of cracking moment can be calculated as following:

$$M_{cr} = \frac{FL}{4} \qquad (6\text{-}2)$$

$$F = (4 \times 6614.4)/1.5$$

$$F = 17638\ N \ \ or\ 17.638\ kN$$

The results of loading history for four RC beams have been shown in Figure 6-21. In addition, the cracking moment time has been shown using the intersection of load coordination obtained from Equation 6-2 and load history recorded by load cell.

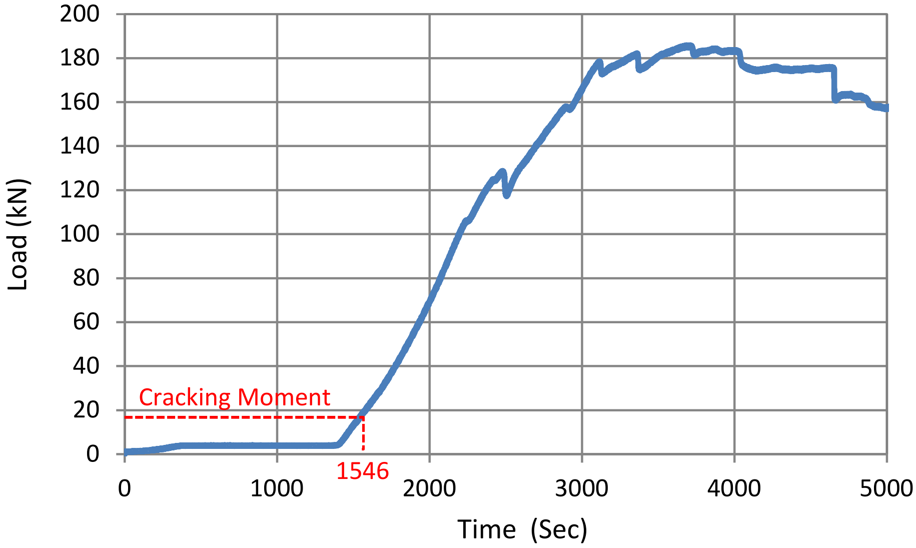
200
180
160
140
120
100
80
60
40
20
0
Load (kN)
Cracking Moment
1546
0
1000
2000
3000
4000
5000
Time (Sec)

a) LB01

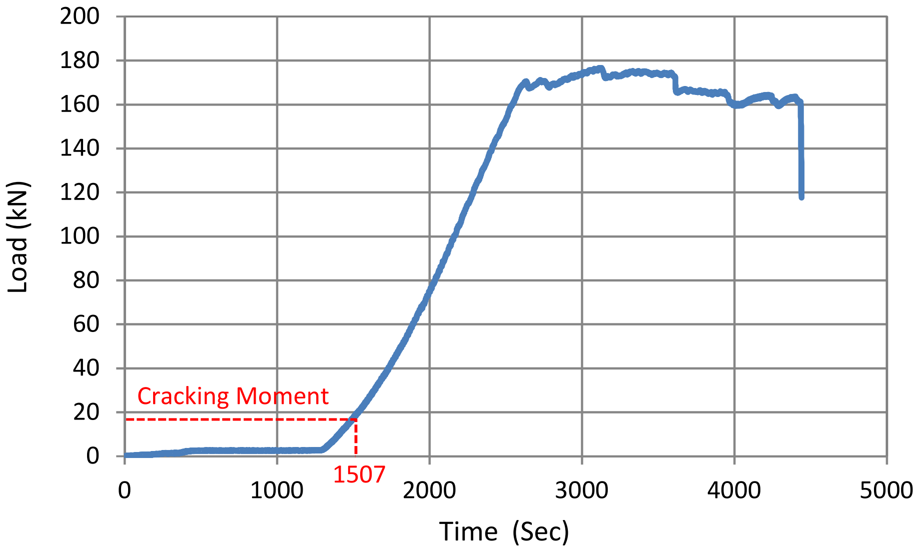
200
180
160
140
120
100
80
60
40
20
0
Load (kN)
Cracking Moment
1507
0
1000
2000
3000
4000
5000
Time (Sec)

b) LB02

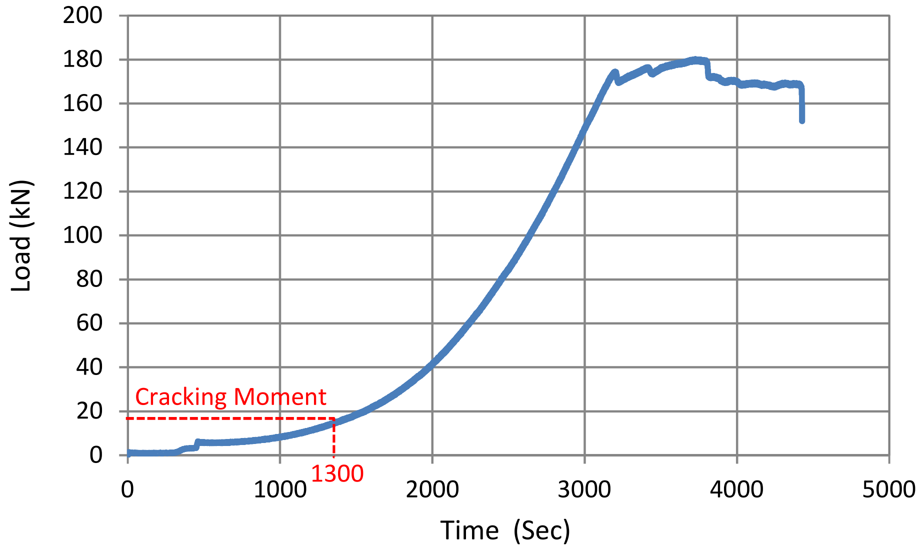

c) LB03

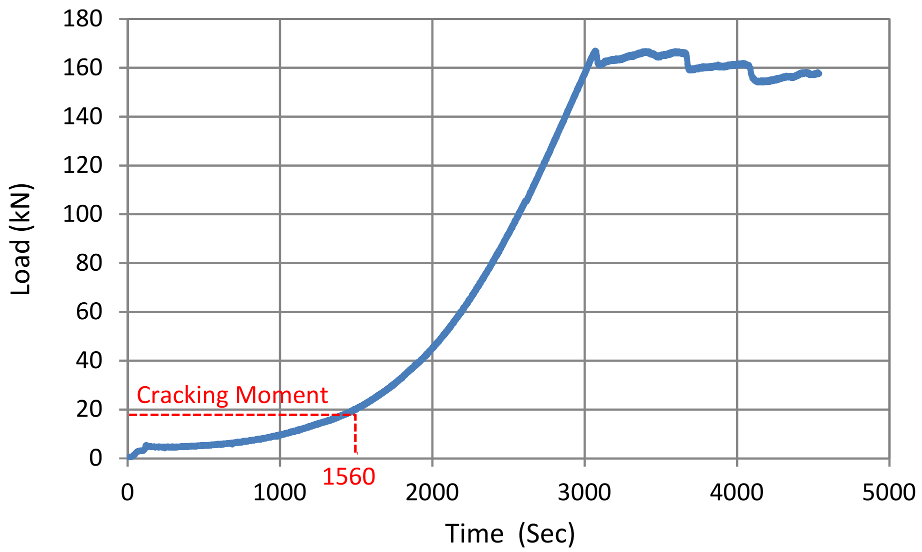

d) LB04

Figure 6-21: The loading history recorded by load cell for specimens a) LB01, b) LB02, c) LB03 and d) LB04

The comparison of loading history results (Figure 6-21) and sensor results (Figure 6-10 to Figure 6-17) reveals that the dramatic drop in peak of PSD and total received power were slightly before or equal to cracking moment in loading history results. The dramatic drop in peak of PSD results of four RC beams occurred 1500, 1500, 1140 and 1560 seconds after the tests began, while the cracking moment in time history results were 1546, 1507, 1300 and 1560, respectively. In summary, it seems that the attached sensors successfully detected the crack from the first sign (cracking moment) and before any failure in RC beam resistance. The above comparison may raise a question about verification not by theoretical calculation, but by the experimental test implemented during the RC beam test. Hence, the results of attached strain gauges and LVDT during the test were presented in time-history format as shown in Figure 6-22 and Figure 6-23. In both figures the marked red circle and consequent time has been marked as a sign of changes in deflection and strain value which can be correlated to the cracking moment.

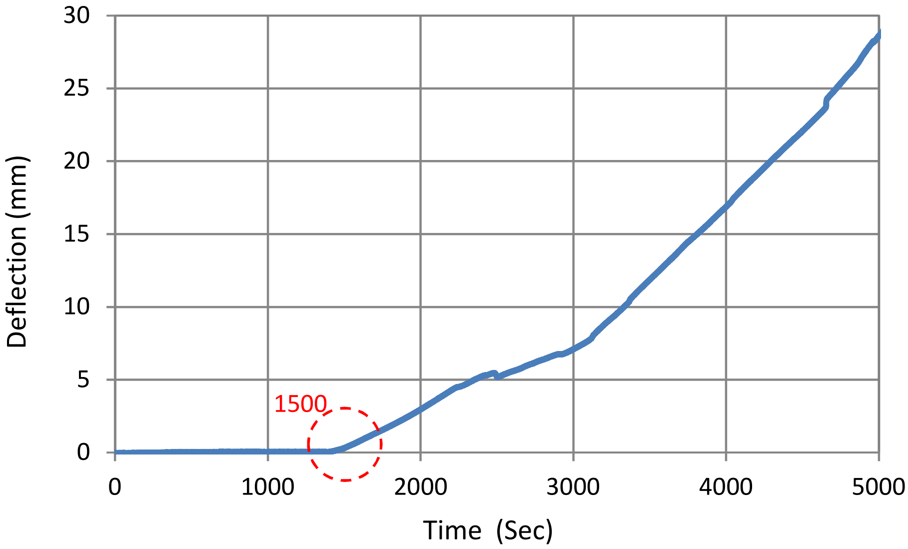

30
25
20
15
10
5
0
Deflection (mm)
1500
0
1000
2000
3000
4000
5000
Time (Sec)

a) LB01

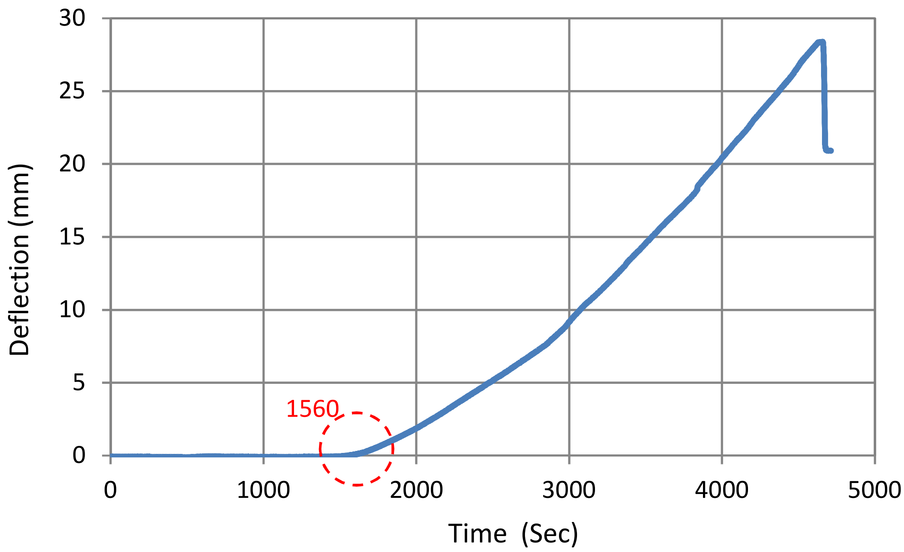

30
25
20
15
10
5
0
Deflection (mm)
1560
0
1000
2000
3000
4000
5000
Time (Sec)

b) LB02

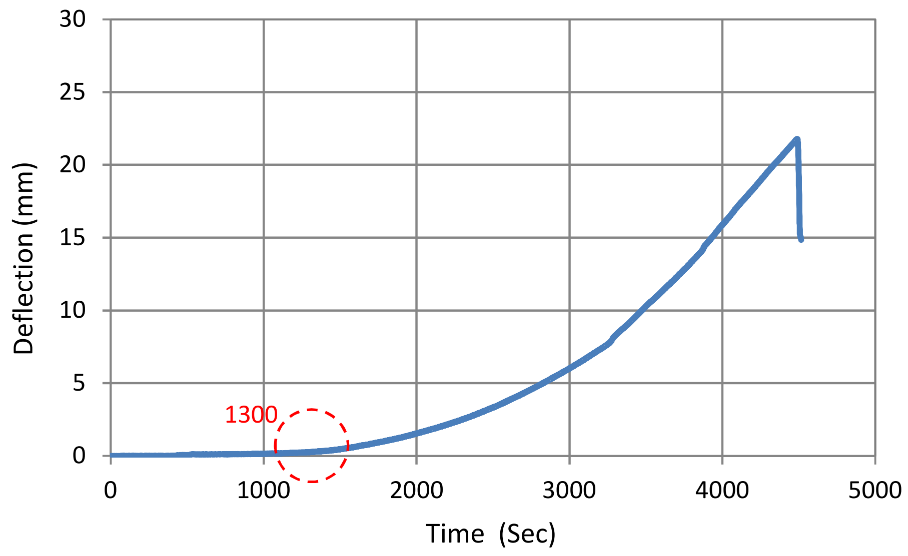

c) LB03

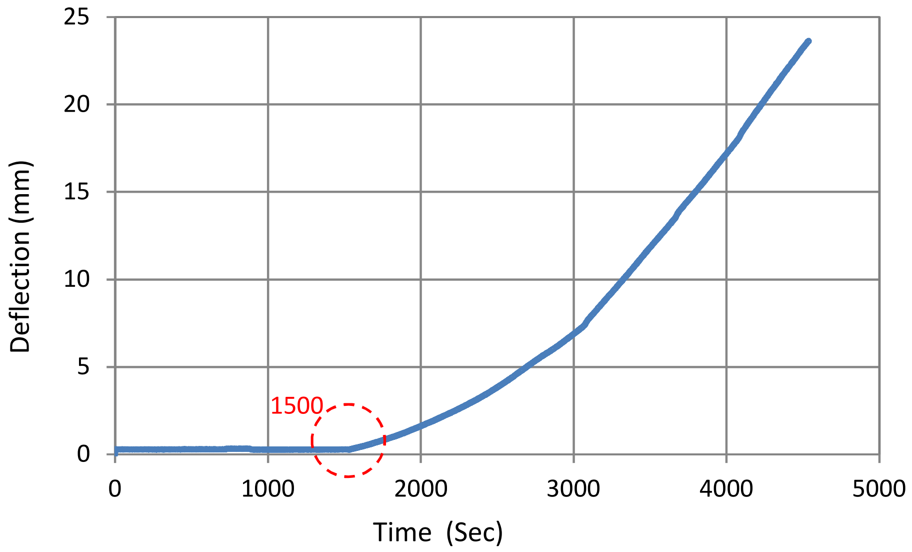

d) LB04

Figure 6-22: The LVTD data records at the bottom of specimens a) LB01, b) LB02, c) LB03 and d) LB04

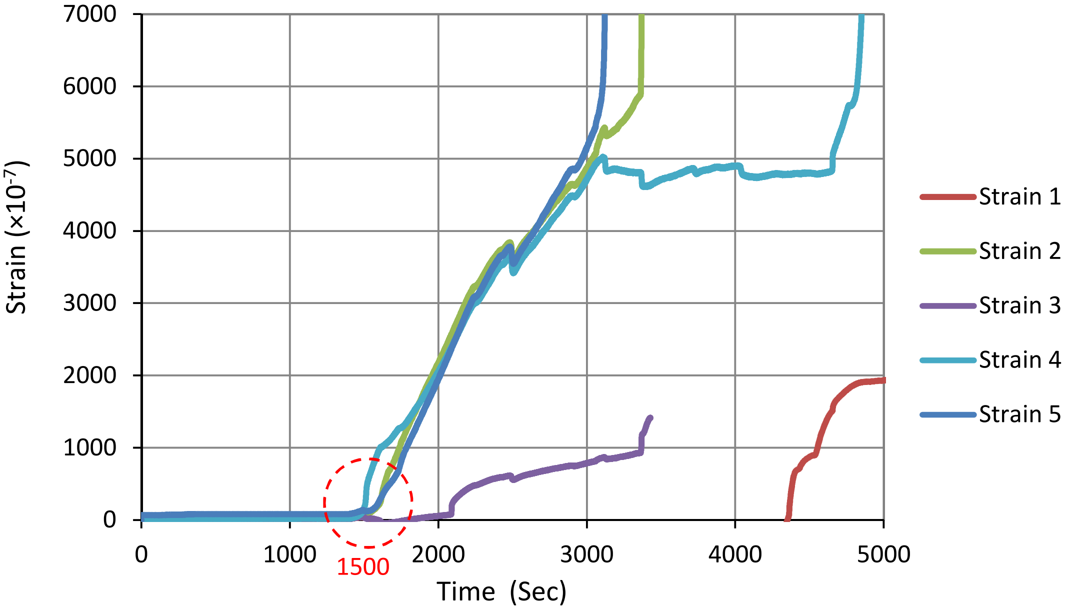

7000
6000
5000
4000
3000
2000
1000
0
Strain (×10-7)
0
1000
1500
2000
3000
4000
5000
Time (Sec)
Strain 1
Strain 2
Strain 3
Strain 4
Strain 5

a) LB01

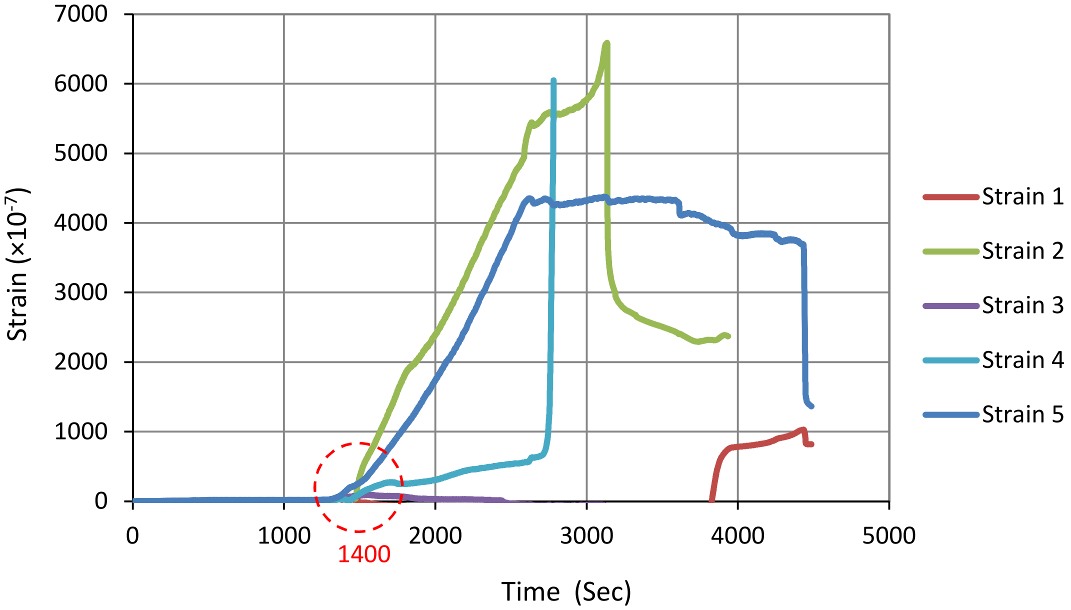

7000
6000
5000
4000
3000
2000
1000
0
Strain (×10-7)
0
1000
1400
2000
3000
4000
5000
Time (Sec)
Strain 1
Strain 2
Strain 3
Strain 4
Strain 5

b) LB02

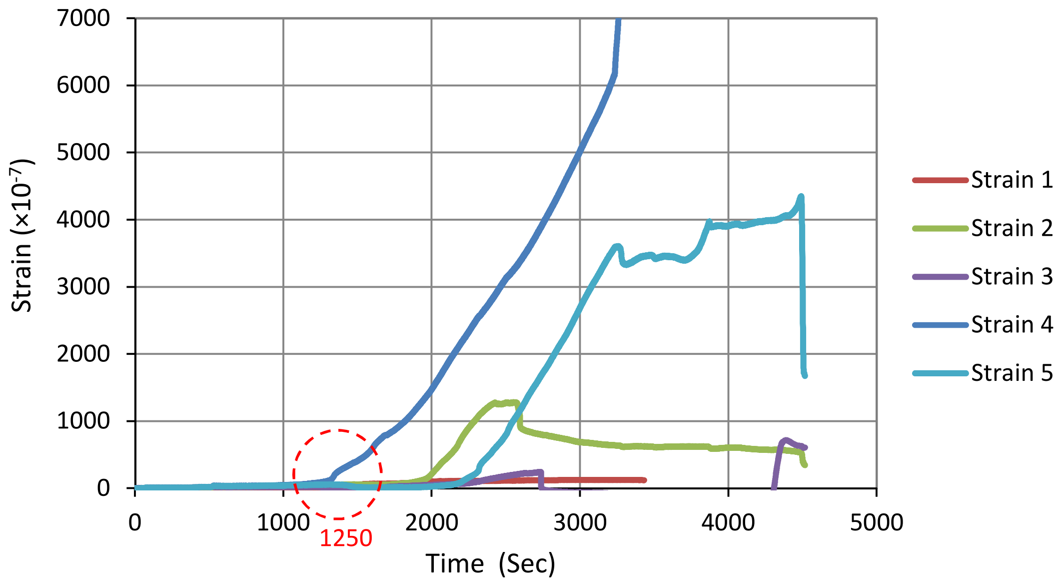

c) LB03

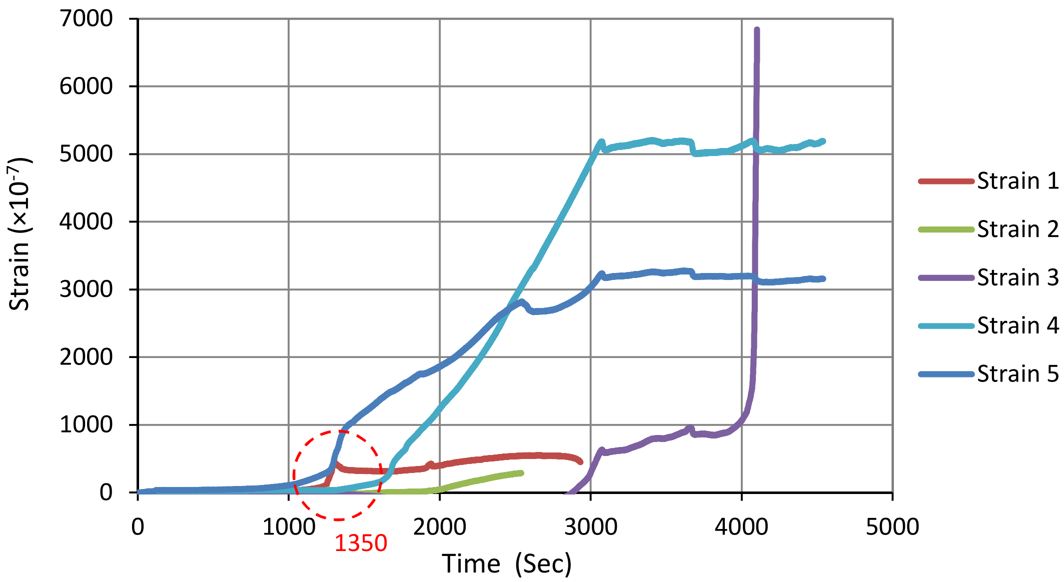

d) LB04

Figure 6-23: The strain gauges data records attached at the bottom of RC beam specimens a) LB01, b) LB02, c) LB03 and d) LB04

The above figures show the deflection on RC beams appears after strain increases in bottom of specimens; means strain gauges were changed earlier than LVDT. As Figure 6-23 shows, the first sign in increasing the value of externally bonded strain gauges happened in the certain time (marked with red circle) for each specimen and. The value of strain in this time was less than 0.001, while according to the ACI 318-08 (Committee et al., 2008) standard for RC beam design the maximum usable strain sets at 0.002 or 0.003. This means RC beams under a minimum 0.002 strain in the elastic zone without any cracking. Meanwhile, the results of peak of PSD were almost a coincidence, with appearance signs of strain occurring during the loading, and even more accurate in proposed damage index results. The signs of increasing strain for LB01, LB02, LB03 and LB04 appeared at 1500, 1400, 1250 and 1350 seconds, while damage index results were recorded at 1440, 1380, 1140 and 1260, respectively. Therefore the proposed damage index was more sensitive than the LVDTs and strain gauges, since the proposed damage index can detect internal strain and cracks before they appear on the structure's surface.

It is clear in Figure 6-23 some strain gauges did not change in terms of value, which is correlated to location of bonded strain gauge at the cracking zone. Figure 6-24 shows an LB01 specimen during the loading with five external bonded strain gauges located across the entire mid-spam to cover all the cracks. It is clear four of the strain gauges were in the cracking zone, while one strain gauge was out of the cracking zone. This is very common on RC beams under bending load, as cracks do not necessarily appear in the middle of the beam. Therefore, the ability of sensors to cover the entire area of the mid-spam is one of the advantages and points of excellence of the proposed approach.

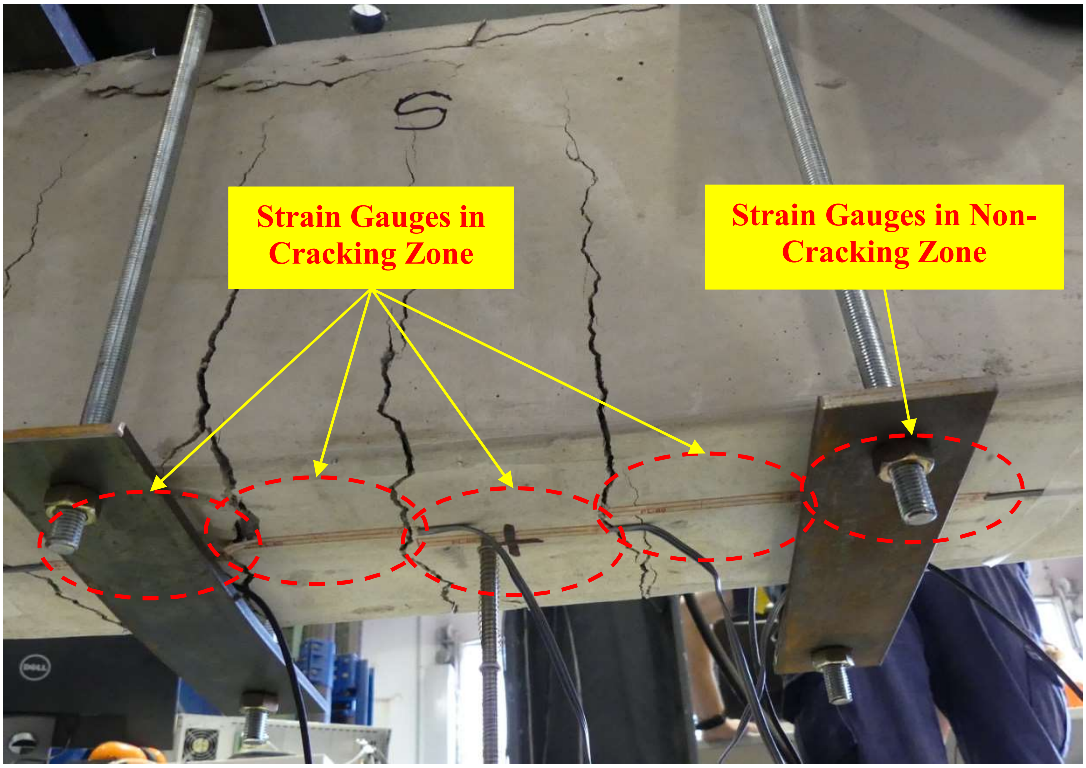

Figure 6-24: The location of cracks and bonded strain gauges in bottom of RC beam

6.5 Summary

This chapter presented application of the proposed mounted-SA based approach for health monitoring of RC beams. The SA transducers were used as both actuator and sensors to detect load-induced cracks. Four RC beams instrumented with SAs were gradually loaded under 4-point bending machines till failure. One actuator and one sensor were implemented in the tension side of the beam under test and one sensor was used in its compression side to cover the entire of the mid-spam area. The peak of PSD and the RMSD as a damage index were used for the detection and monitoring of cracking in RC beams under gradually increasing loading. The results were also verified and compare using the load cell and strain gauge measurements, and the design equation for predicting a cracking moment. Overall, the following conclusions can be made:

1. The proposed mounted-SA approach effectively evaluates the cracking status of RC beams under flexible loading using the peak of power spectral density, total received power and its standard deviation, and damage indexes.
2. It was shown for the first time that the proposed mounted-SA based sensory system could capture a precautionary signal for major cracking. The experimental results for peak of PSD and total received power showed that the transmission energy between the SA actuator and SA sensors in the RC beams dropped dramatically after the cracking moment.
3. The proposed mounted-SA sensory system is more sensitive to the cracking moment than the load cell and strain gauges.
4. When using the proposed approach the SA transducers should be located in critical parts (damage zones) of the RC members. Appropriate number of the SA sensors can provide the determination of location of cracks and their severity.
5. It was demonstrated that the mounted SAs are robust, reliable and easily implementable to concrete structures. They can be implemented to existing RC concrete members at different places.
6. The proposed mounted-SA based active sensing approach can be an effective method for structural health monitoring of practical-scale RC beams at an economical cost without using additional bulky equipment.

Chapter 7 : Detection and Monitoring of Crack on RC Composite Slab under Cyclic Load Using Mounted Smart Aggregates

7.1 Introduction

In practice, RC concrete slabs and beams are often connected with other members of infrastructures. For example, concrete-steel composite members, such as concrete-filled steel tubular (CFST) columns, have many structural and constructional benefits (Han et al., 2014). The CFST column, normally connected to the concrete beam, works as formwork for concrete pouring during construction, which reduces construction cost and time. The steel beams are also often connected to RC slabs using shear connectors which make a strong composite member. The use of these composite members in building construction has greatly increased in recent years. The well-known standards like FEMA-350 (2000) and Eurocode 8 Part 3 (2005) provide guidelines for the composite members, mainly based on studies of steel beams without floor slabs (Huang et al., 2014, Li et al., 2017). However, limited research has been performed on health monitoring of RC slab as a part of composite members.

This study is a part of a project which investigated the cyclic behaviour of composite members with joints and reduced beam sections (Li et al., 2017). Since SA transducers have the advantage of structural simplicity low cost, quick response and high reliability, feasibility of the developed mounted SA based approach for the health monitoring of RC slab with composite connections is investigated in this chapter. Experiments are performed on the composite member under cyclic load with

SAs transducers mounted on its RC slab to detect load-induced cracks. The measurements with a mechanical strain gauge are also conducted.

This chapter consists of three main sections, with the first section providing the information about the composite member preparation and the loading setup used in this study. The second section presents details of SA transducers arrangement and setup on the RC slab of the member. The third section focuses on the results and discussion of the investigation.

7.2 Specimen preparation and loading setup

A composite cruciform joint specimen was designed and constructed based on the provisions of EC3 (BS, 1993), EC4 (CEN), EC8 (Standard, 2005), AS 2327.1 standards (Mills, 2001), and a reduced beam section (RBS) was used for the specimen. The geometric details of the specimen with RBS beam are illustrated in Figure 7-1a, with the cut length of 80 mm and the cut depth of 31 mm.

The specimen was designed representing a joint at half scale. The profiles of circular steel tubes were 250 mm in diameter (D) and 6 mm in wall thickness (t_s), as shown in Figure 7-1b. Two types of universal steel beams (200UB25.4 and 250UB25.7) were used, with a length of 1500 mm from the centre of the column to the assumed inflection point of the beam. The width and depth of the RC slab were 800 mm and 60 mm, respectively. Through diaphragms, with a thickness of 10 mm, were used to connect the column to the steel beam. The outer diameter, inner diameter, and vent hole diameter of the through diaphragms were 300 mm, 120 mm, and 20 mm, respectively. Sixteen M19 headed shear studs, with a length of 50 mm and a diameter of 19.3 mm, were welded at a spacing of 200 mm along the steel beam to connect the steel beam to the floor slab, as shown in Figure 7-1a and c. A layer of reinforcement (10 mm) was placed in the RC slab, which were longitudinally and transversely distributed along the slab at a spacing of 100 mm. The clear cover to the reinforcement was 20 mm. Complete joint penetration (CJP) groove welds were used to connect the through diaphragm and the beam.

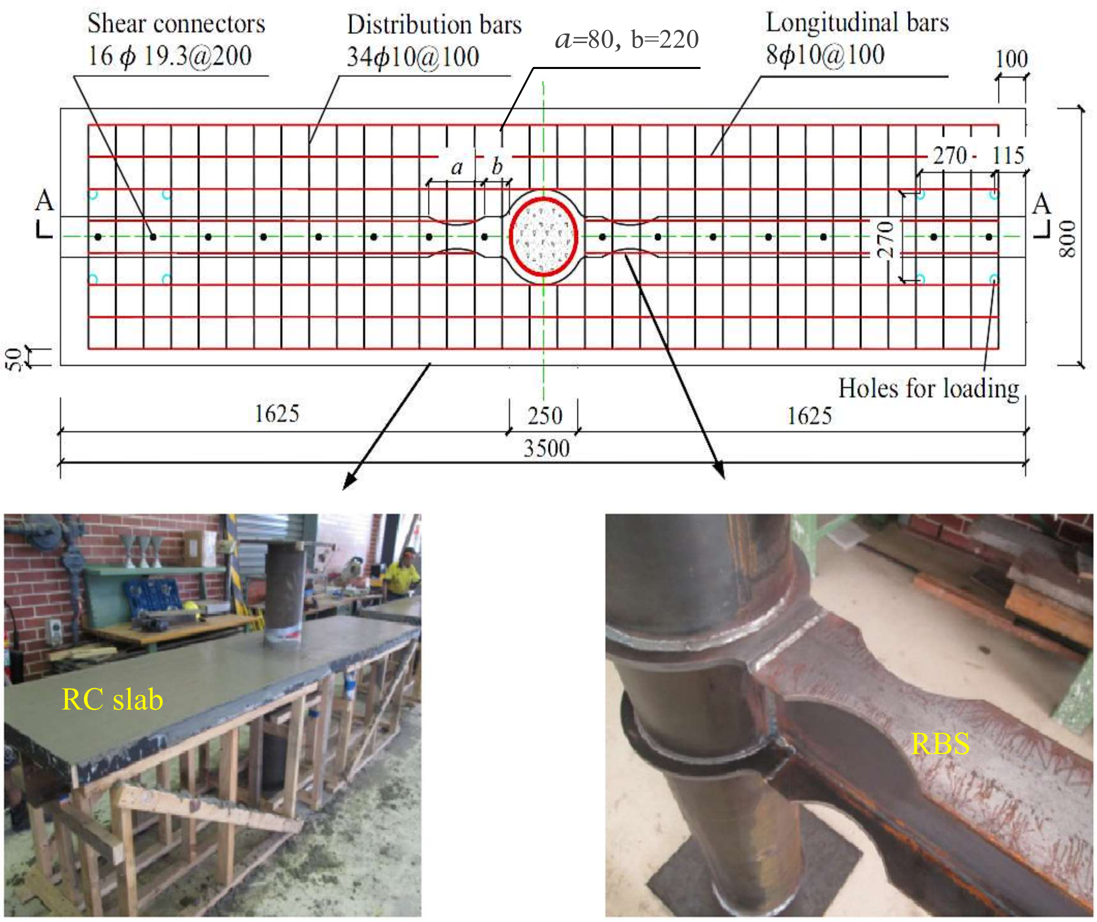

(a) Plan view of the RC slab and RBS with cross-section A-A

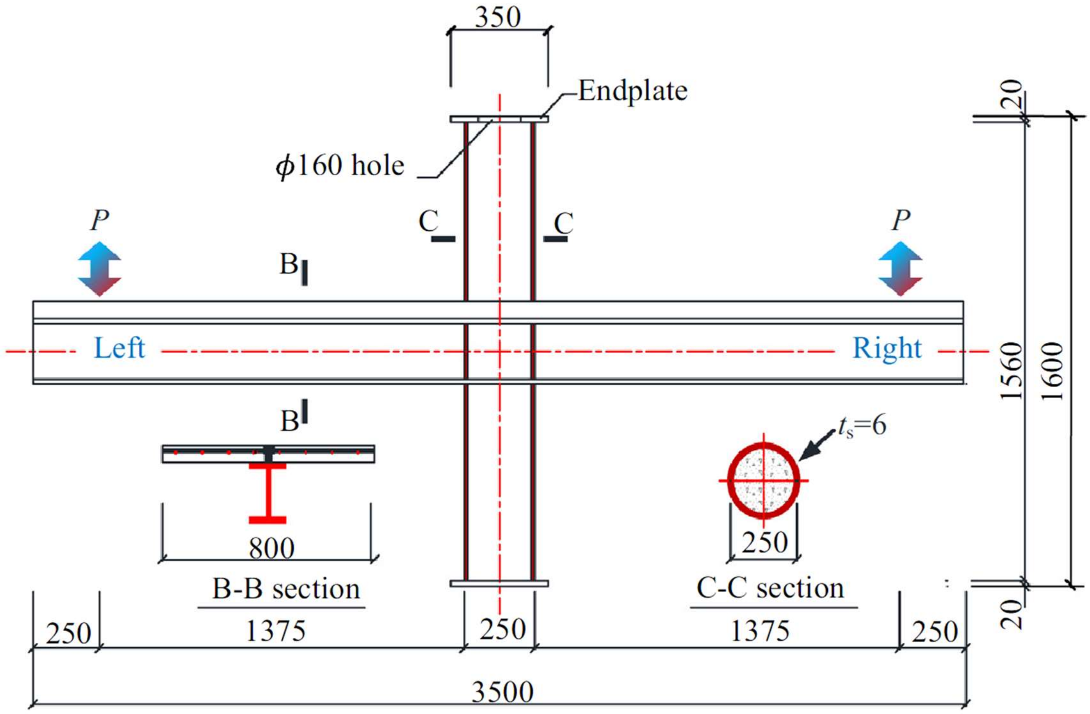

(b) Elevation of a typical test specimen with two cross-sections B-B and C-C

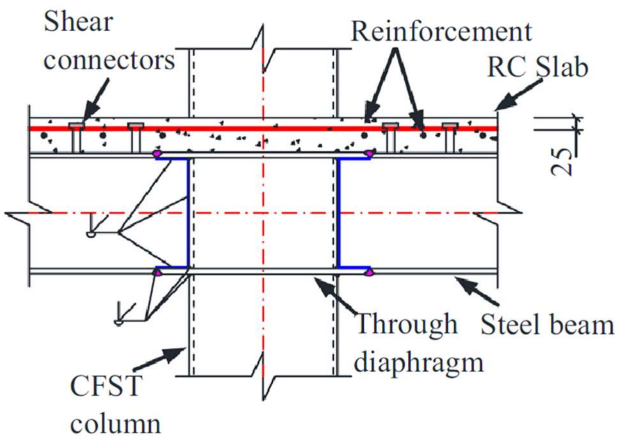

(c) Section A-A

Figure 7-1: Configuration of the specimen (units: mm) (Li et al., 2017)

Each CFST column, with two end plates measuring 1600 mm in length, was fabricated in three segments separated by two through diaphragms, as shown in Figure 7-2. The through diaphragms were welded to the steel tube by double-fillet welds. The beam flanges were welded to the through diaphragms, and the beam web was welded directly to the steel tube. The thicknesses of all weld seams measured approximately 6 mm. Each end of the steel tube was welded to a 350×350 mm^2 steel plate; the steel plate on the top end had a 160 mm diameter hole used for pouring concrete (Li et al., 2017).

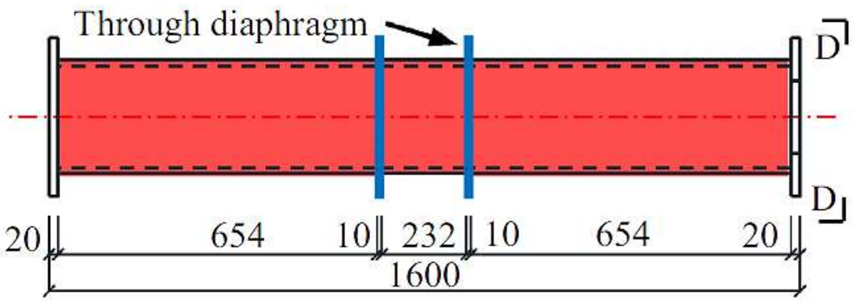

Figure 7-2: Details of the steel tube (units: mm) (Li et al., 2017)

Grade C32 concrete was used for the infilled concrete and RC slab. Concrete cylinder tests were conducted according to Australian standards to measure concrete properties. The measured concrete cylinder compressive strength and tensile strength were 36.5 and 4.7 MPa, respectively. The Young's modulus of concrete was 37,740 MPa at the time of testing.

A constant axial compressive load of 1116 kN was applied to the CFST column by a hydraulic jack during the testing (Tao et al., 2017). The axial load level (n) of the column was 0.4. Two hinges were attached to the top and bottom ends of the column to simulate a pin-pin boundary condition. The distance from the centre of a hinge to the nearest end of the specimen was 230 mm. The two ends of the beam were free where two actuators, with a loading capacity of 500 kN, were attached to apply cyclic loads. The distance from one loading point to the column centre was 1500 mm.

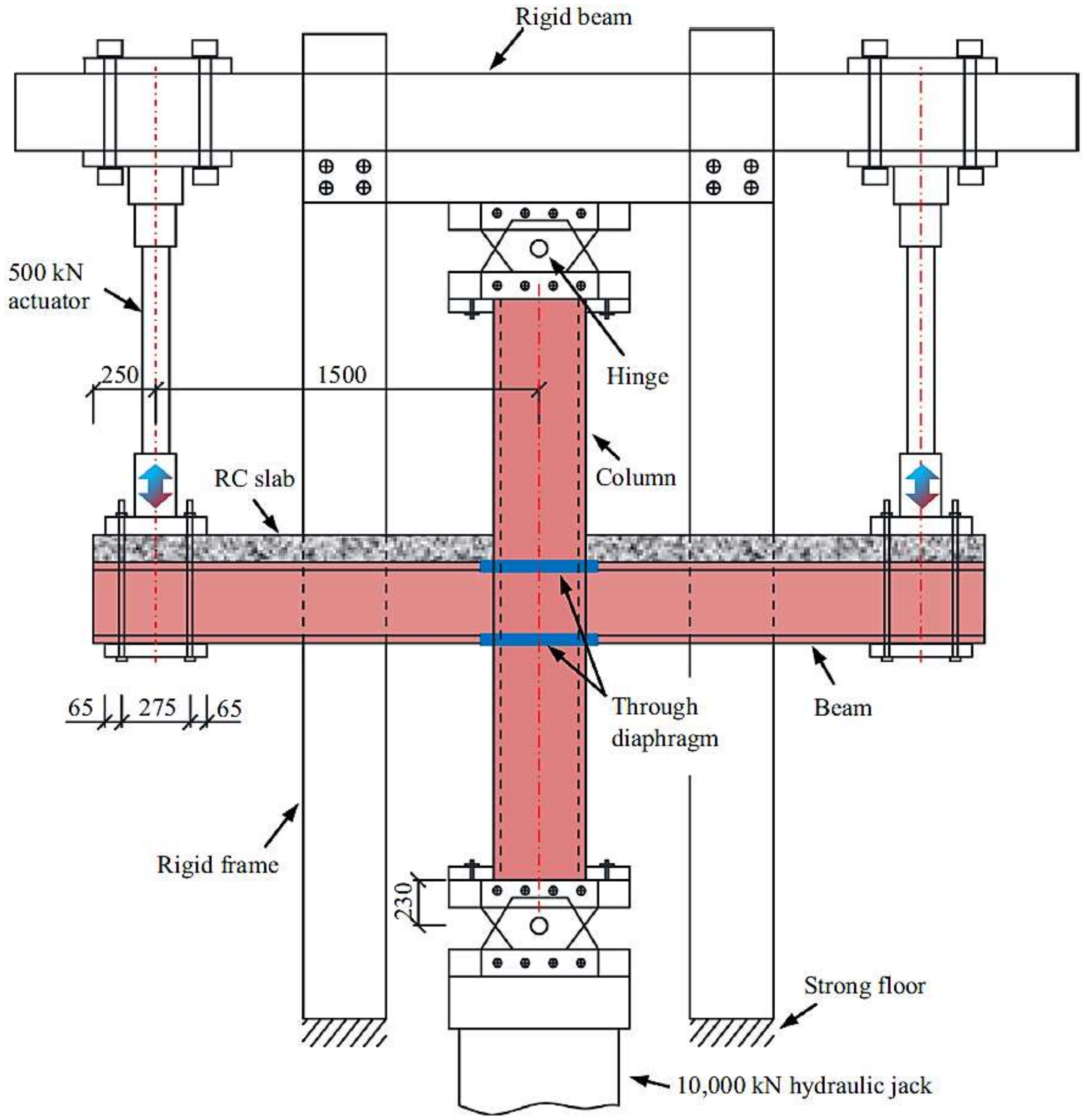

Figure 7-3: Schematic of test setup (units: mm)

The two actuators were arranged to apply equal but opposite displacements at the same time. The cyclic displacement amplitude followed the loading protocol in SAC (Venture, 1997). As shown in Figure 7-4, the Drift angle (θ) was used to control the loading history, which was defined as the beam deflection at the loading point divided by the beam span.

The loading history was divided into several steps. Firstly, the loading started with six cycles at each load step of 0.00375, 0.005 and 0.0075 rad rotation, respectively. The next four cycles in the 4th load step were at 0.01 rad rotation, followed by two cycles in the 5th load step of 0.015 rad rotation. The loading sequence completed two cycles at each rotation level, followed by increasing the rotation value to 0.02 rad, 0.03 rad, 0.04 rad…until the strength of the joint decreased to 85% of its ultimate flexural resistance. The cyclic loading speed was controlled at a rate of 0.5 mm/s.

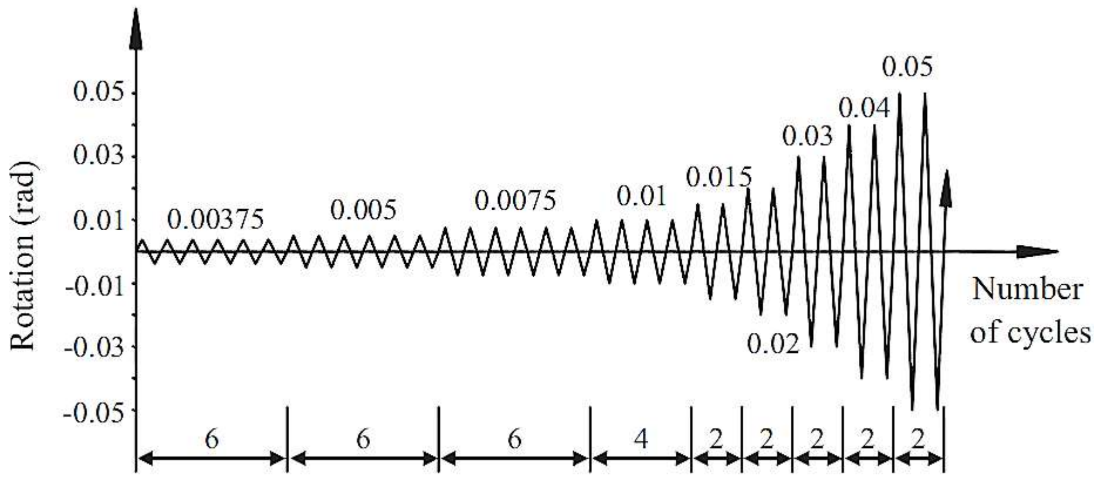

Figure 7-4: Cyclic loading protocol

7.3 Sensor arrangement and measurement setup

For early assessment of an RC element condition, it is important to promptly detect cracks. Chapter 6 successfully demonstrated the capability and reliability of the use of mounted SA transducers to health monitoring of RC beams under bending load. The SA arrangement provided useful information about cracks caused by tension and compression in two sides (top and bottom) of an RC slab. However, RC slab under cyclic loading for each loading cycle can experience tension and compression in each side (top and bottom). Therefore, unlike the arrangement of the transducers in the previous chapter, in this study SAs are mounted to only one side of a specimen. In this case one actuator (AC) and two sensors (SE1 and SE2) mounted on the top side of the slab with different distances.

In this experiment, a total of three SAs were mounted on each of the RC slabs around the beam-column joint, which consisted of one actuator and two sensors, as shown in Figure 7-5. In this RC slab, cracks were expected to be developed around the column area close to RBS zone; therefore, SAs were mounted to the surface of the slab around the column, close to the RBS zone. Sensors 1 and 2 were located at 300 mm and 400 mm distances from the actuator, respectively, as shown in Figure 7-5. In addition, a demountable mechanical strain gauge was bonded around RSB zone for the purpose of verification (Figure 7-6).

A LabVIEW software was used to generate a swept sine-wave as the excitation wave, and to process received signals. The minimum frequency range was set to 500 Hz to avoid noises in a very low frequency caused by a hydraulic pump. The maximum frequency, signal swept period, and amplitude of the sine waves were set to 150 kHz, 1 s, and 10 V, respectively. The test was recorded every 30 minutes during the loading, and the data were saved in a time-domain format. The received raw signals were analysed using the data analysis tools introduced in Chapter 3.

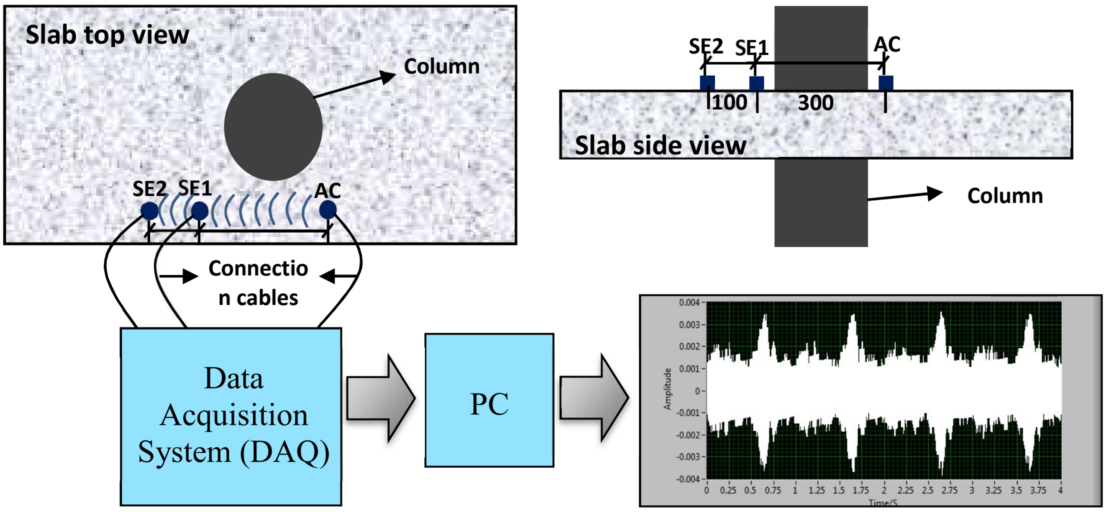

Figure 7-5: Schematic of the specimen, measurement setup, and its output signal in time-domain

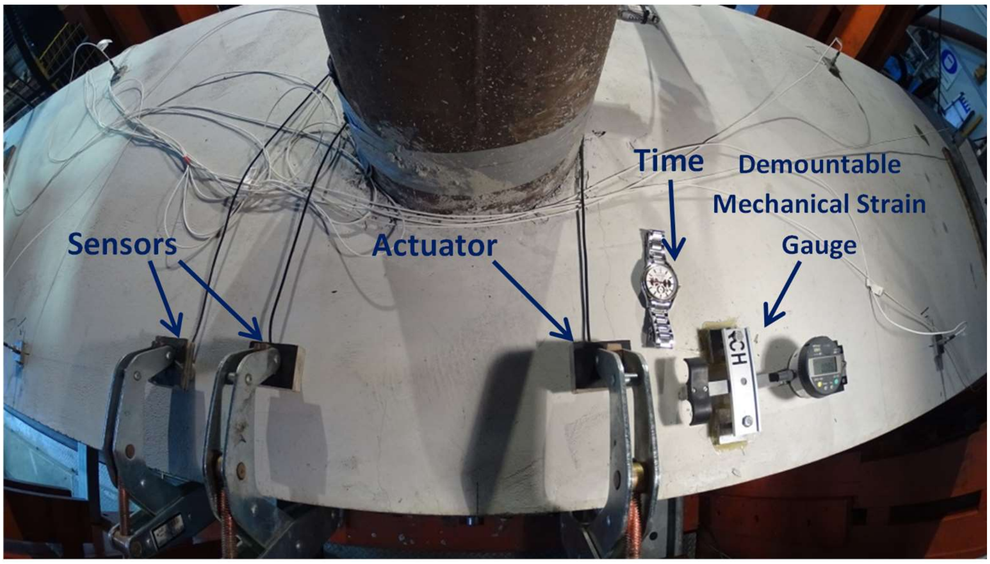

Figure 7-6: Top view of RC slab with SAs and demountable mechanical strain gauge

7.4 Results and discussion

Similar to Chapter 6, the results in this chapter will be presented in two sections for a signal processing and the verification of results.

7.4.1 Signal processing data analysis

In this experiment the sweep sinusoidal signal wave was generated by the actuator. The sweep sinusoidal signal started from 500 Hz and ended at 150 KHz, with a magnitude of 10V. The sweep period was set as 1 second and the recording period as 4 seconds; this means that at least three complete sweep periods were recorded in each measurement.

The received signal was saved every second for future processing and analysis. During the loading procedure, noises were found in the time-domain signals, and the signals were transformed to the frequency-domain to avoid noises which mostly happened in very low frequencies. For this purpose, a Fourier transform was applied to the recorded time-domain signal using LabVIEW software and the results were exported for further analysis to a MATLAB program, in the format of PSD (frequency-domain). All PSDs were calculated using four periods of swept sine-wave in order to obtain a better accuracy. Figure 7-7 depicts the received frequency-domain signals from sensor 1 every 30 minutes after loading commenced. Each plot corresponds to only one cycle of the detected signals, in the level of millivolts, from the repeated swept sine waves.

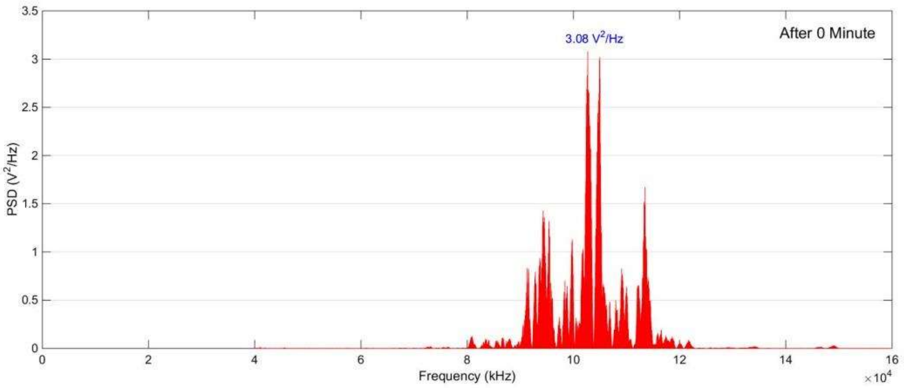
After 0 Minute
3.08 V²/Hz
PSD (V²/Hz)
Frequency (kHz)
×10⁴

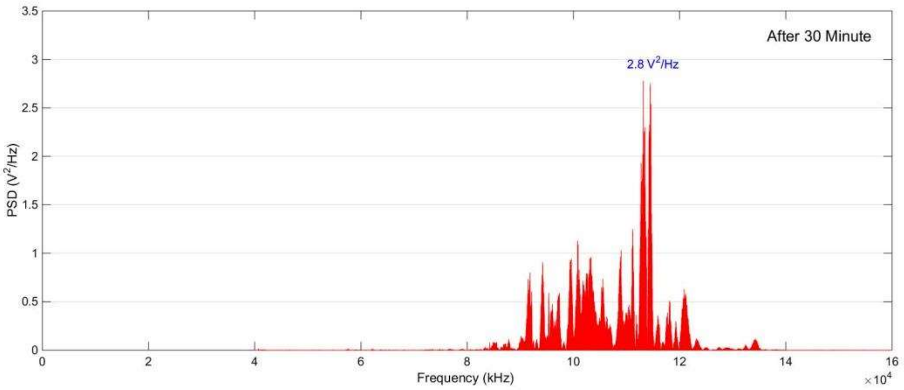
After 30 Minute
2.8 V²/Hz
PSD (V²/Hz)
Frequency (kHz)
×10⁴

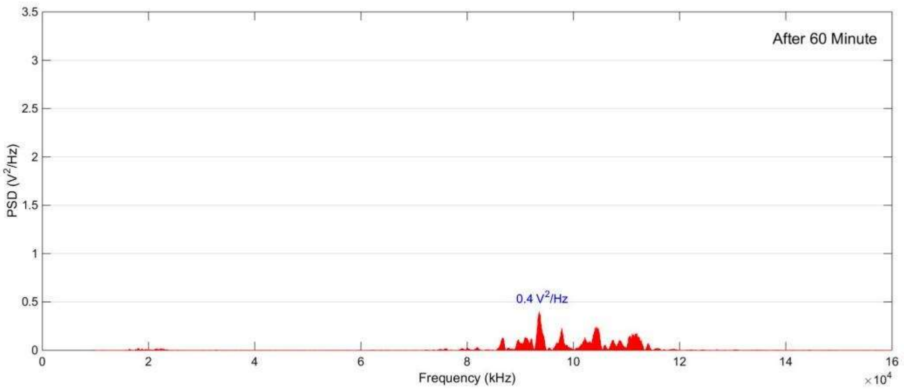
After 60 Minute
0.4 V²/Hz
PSD (V²/Hz)
Frequency (kHz)
×10⁴

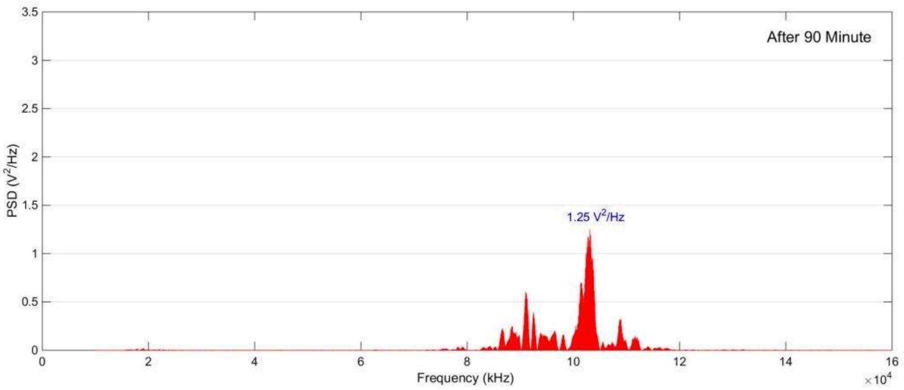
After 90 Minute
1.25 V²/Hz
PSD (V²/Hz)
Frequency (kHz)
×10⁴

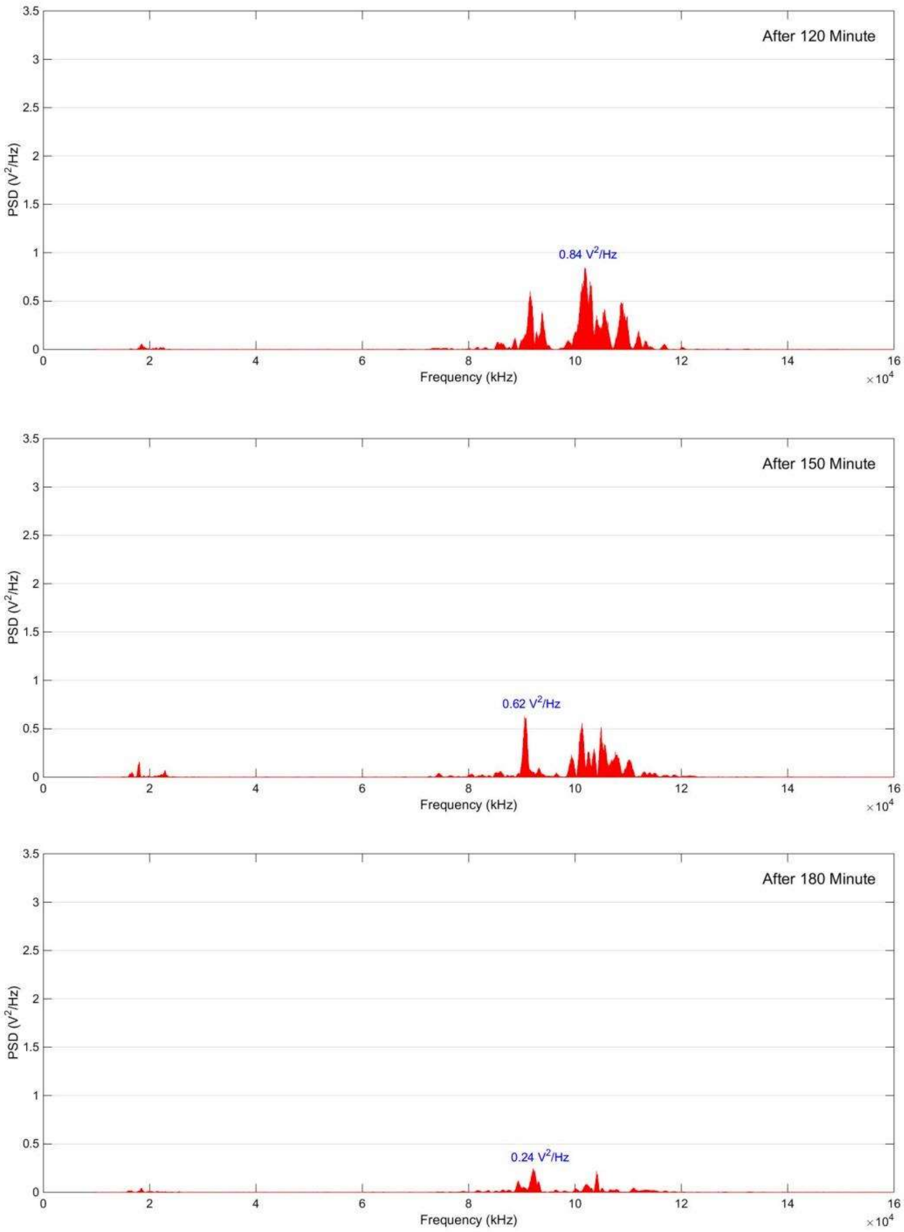

Figure 7-7: Power spectral density (PSD) for sensor 1 measured every 30 minutes after loading commenced

The test results in Figure 7-7 shows the difference between the signals before and after cracking. After the RC slab cracked, the peak of PSD dramatically drops with the increasing load. For example, the peak of PSD value after 30 minutes is close to 2.8 V^2/Hz, while after 60 minutes it is close to 0.4 V^2/Hz. This dramatic drop can be correlated to the cracks occurring on the RC beam, however they are not visible. The peak of PSD then slightly increases to 1.25 V^2/Hz, but after a few minutes, it drops again to 0.84 V^2/Hz. This variation is related to the RC slab behaviour under cyclic loading; the first cracking on the slab surface occurred when the slab was under tension, but by changing the loading cycle, the slab experienced compression, which prevented further development of cracks. In the next cycle of loading depth, cracks increased due to tension. Figure 7-8 shows the area of cracking under tension on top of an RC slab, but with the change of the loading cycle the crack almost disappears on the surface of the slab due to compression. The drop in the value of the peak of PSD means that the wave is not able to be propagated due to cracking.

Similar to the RC beam results in Chapter 6, waves of low frequencies attenuate much less than those of high frequencies. In the frequency-domain response of sensors during the test, the magnitude variation was always within the 80 kHz to 120 kHz range. Similar observations can be made from the RC beams results in Chapter 6. From these observations, a sweep sine wave signal is attenuated in the frequency range of 80 kHz to 120 kHz for concrete materials.

Shortly following a dramatic drop in the peak of PSD, cracks become visible on the surface of RC slab. Overall, the raw frequency-domain data offers useful information regarding the damaged or healthy status of the RC slab and can be used for early assessment of RC slabs.

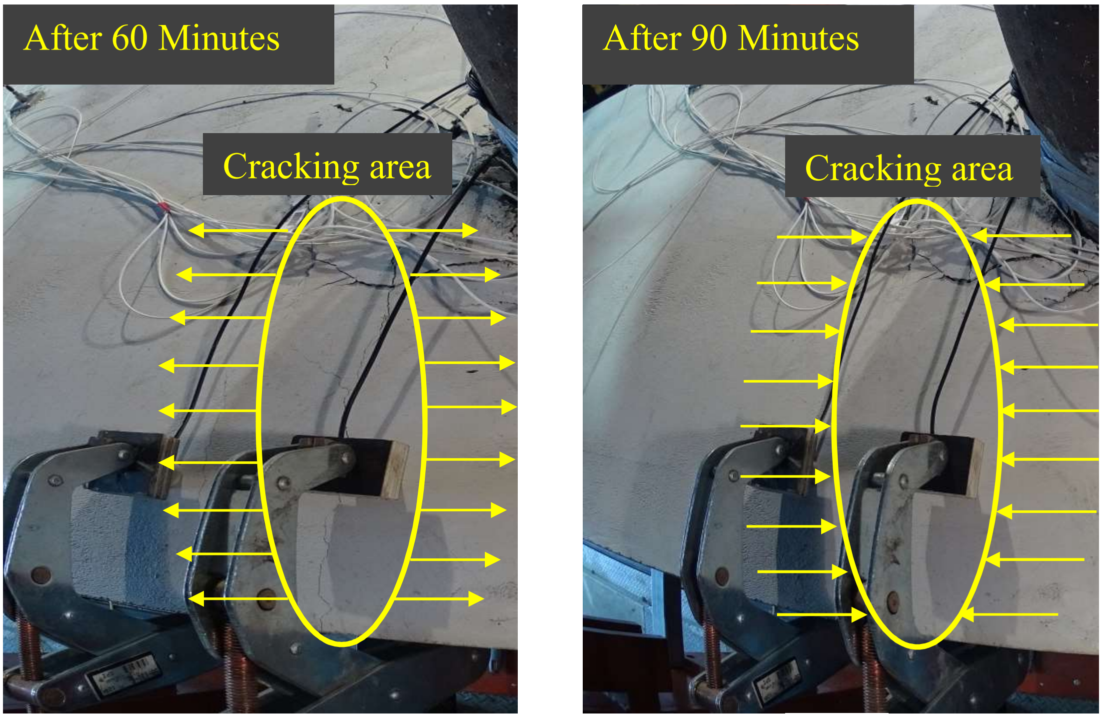

(a) (b)

Figure 7-8: Cracking area when the RC slab is under (a) tension and (b) compression

For further comparison of the results, the value of peak of PSD and total received power for each record has been calculated using the MATLAB code presented in Appendix A. Figure 7-9 and Figure 7-10 show the peak of PSD and total received power, received by sensor 1 and sensor 2 at the surface of RC slab under cyclic loading.

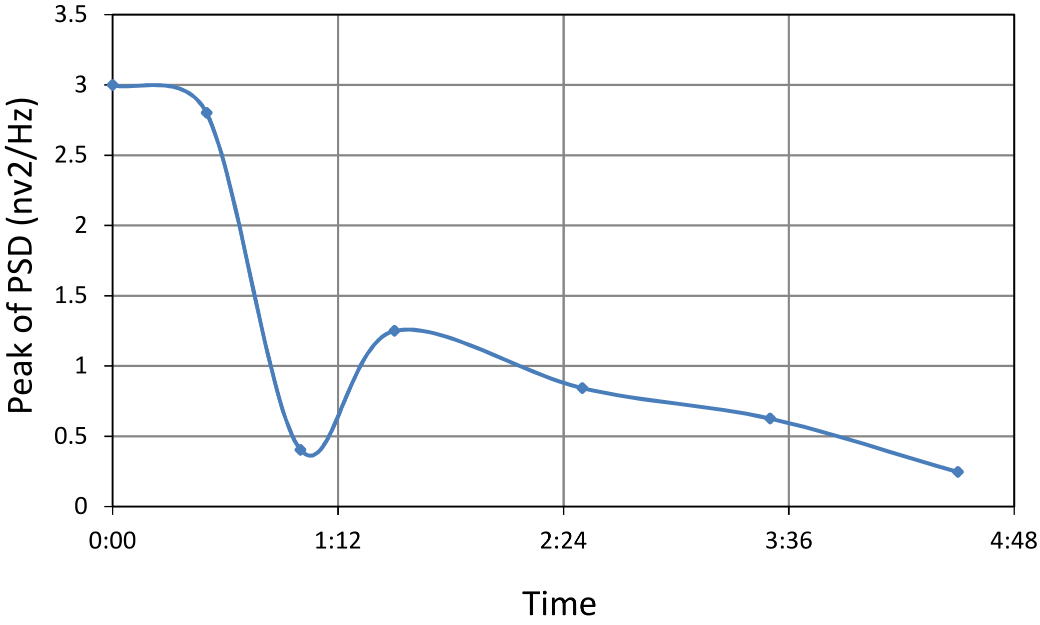

(a)

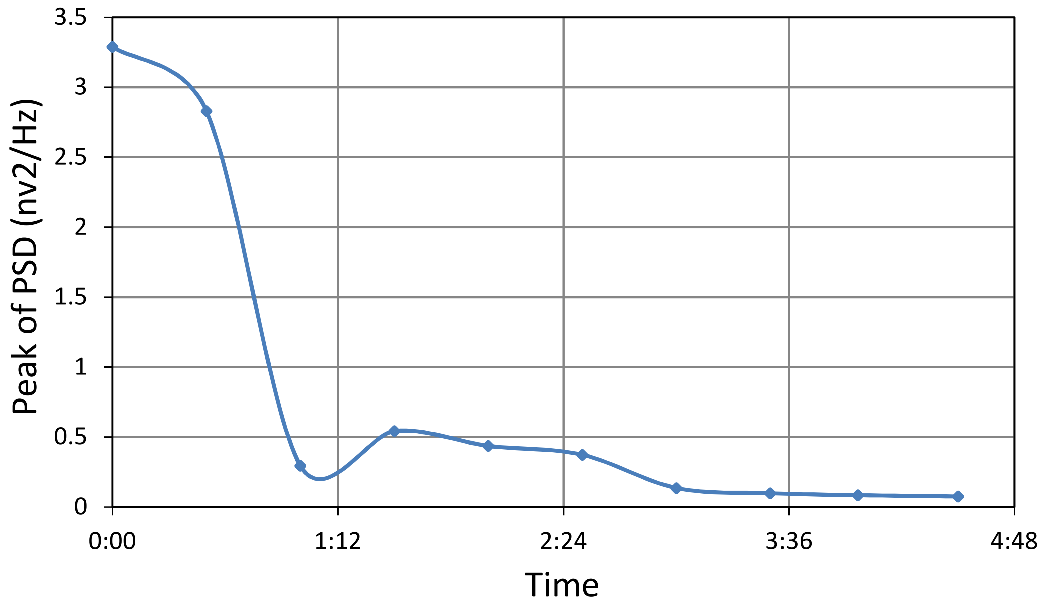

(b)

Figure 7-9: Peak of PSD vs time for (a) sensor 1 and (b) sensor 2

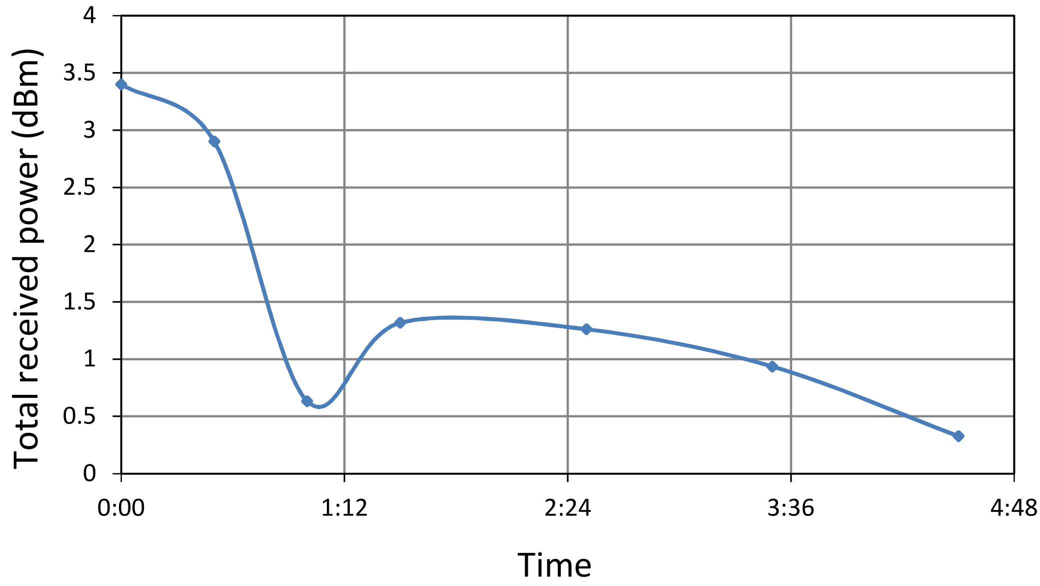

(a)

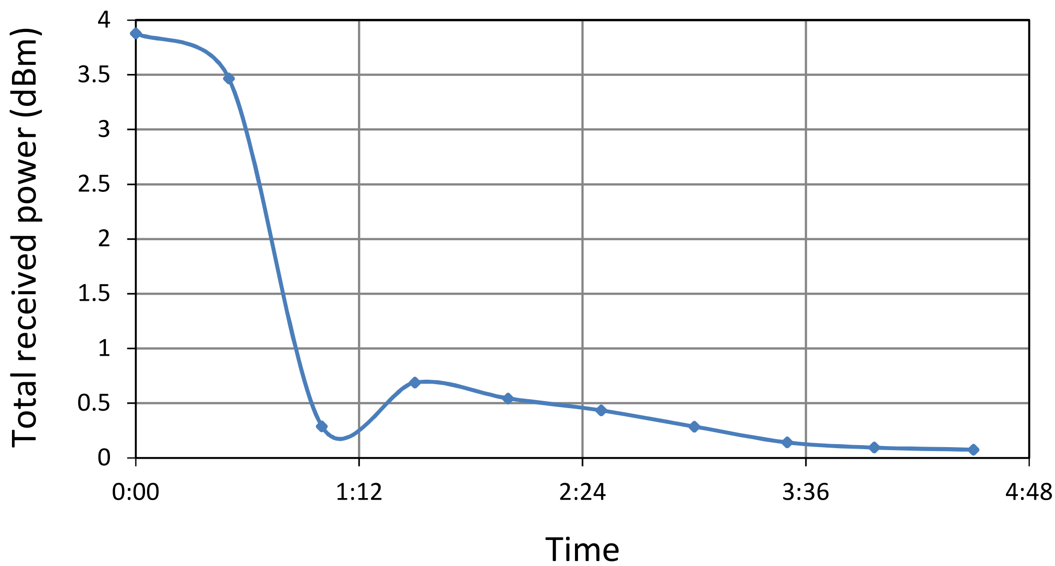

(b)

Figure 7-10: Total received power vs time for (a) sensor 1 and (b) sensor 2

These figures present the changes before and after cracking occurs. For example, for the sensor 2 peak of PSD value at the certain time from 2.82 V^2/Hz dramatically drops to 0.29 V^2/Hz, which can be correlated to the occurrence of a crack in the RC slab. This means that the wave propagation was almost blocked. This dramatic drop in the value of the peak of PSD and the total received power was observed in both sensors mounted to the RC slab specimens. Due to the loading cycle changing from tension to compression on top of the specimen, the signal values were slightly increased then dropped again due to increasing depths of the cracks.

7.4.1 Verification of signal processing data

Moment-rotation (M-θ) relations are widely used to illustrate the performance of joints. In this study, the applied moment (M) is calculated as the load P applied to the beam times the beam span ($M = P \times L$), where L is the distance from the loading point to the column centre, taken as 1500 mm. The rotation of the joint (θ) was calculated as the rotation of the slab (θ_b) minus the rotation of the column (θ_c). Two vertical differential transducers (VDT1 and VDT2) were used to measure the θ_b, where $\theta_b = (\Delta_1-\Delta_2)/ 2L$, and Δ_1 and Δ_2 are the vertical displacements measured by VDT 1 and VDT 2, respectively. Two horizontal differential transducers (HDT1 and HDT2) were used to monitor the θ_c, where $\theta_{c}= (\Delta_3-\Delta_4)/Ls$, and Δ_3 and Δ_4 are the horizontal displacements measured by HDT1 and HDT2, respectively. Ls is the distance between HDT1 and HDT2. The locations of the vertical and horizontal transducers are illustrated in Figure 7-11. Owing to the symmetry of the interior joints, hysteretic curves obtained from both sides of a specimen are almost identical, and hysteretic curves from one side are shown in Figure 7-12. In this figure, the marked points on the curves respectively denotes the crack initiation (Point 1), the yield point (Point 2), the maximum strength (Point 3), the local buckling of the web (Point 4) and the beam flange fracture (Point 5). It should be noted that the positive and negative moments in Figure 7-12 indicate the measurements under sagging and hogging conditions, respectively.

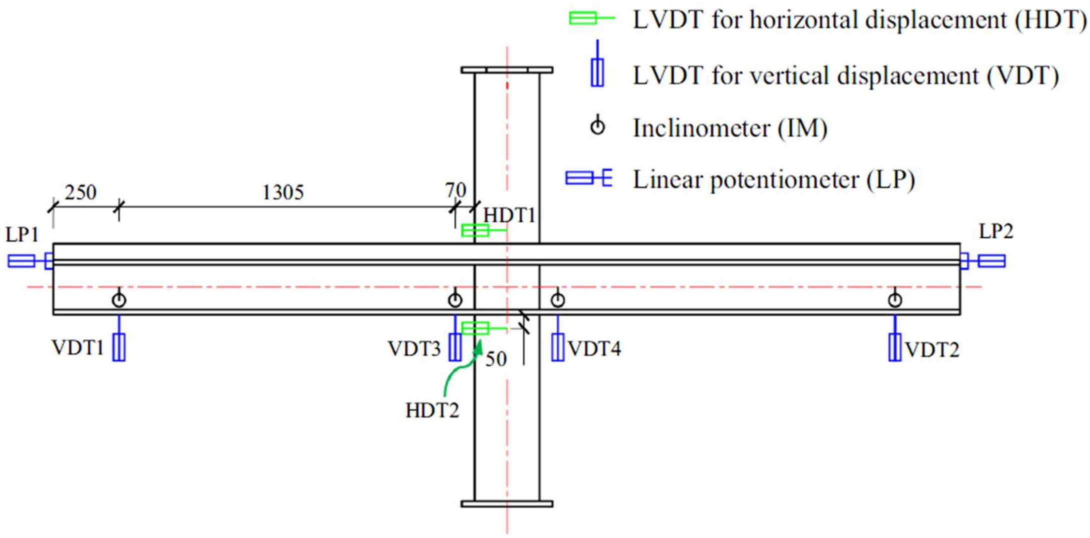

Figure 7-11: Setup of instrumentation LVDTs, LPs and inclinometers (units: mm) (Li et al., 2017).

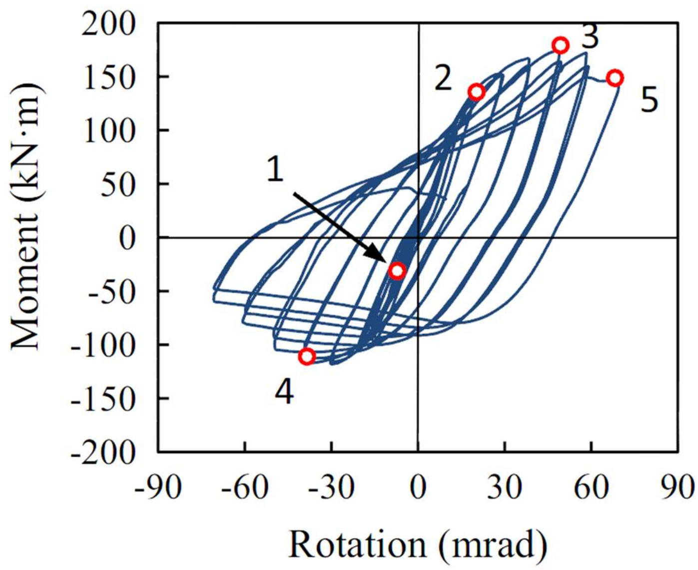

Figure 7-12: M-θ Hysteretic curves of specimen (Li et al., 2017)

As the Figure 7-12 shows, the joint's maximum strength was at point 3 in which specimen enters to large rotation. The first flexural crack developed on the slab's surface, close to the column, and grew with increasing cyclic loading. The progress of the test was as follows: initial elastic deformation, slab cracking, bottom beam flange and web yielding, beam local buckling in the RBS region, and concrete crushing in the slab and steel fracture of the beam bottom flange.

For a further verification, the demountable mechanical strain gauge results were also implemented. The demountable mechanical strain gauge regularly recorded displacements in the located position (Figure 7-6), and the results are illustrated in Figure 7-13. In Figure 7-13 the displacements are correlated to the cracking on an RC slab surface. A negative displacement means the slab is under tension and a positive displacement means the slab is under compression. Therefore the Sine diagram of the displacement and the cyclic loading are almost synchronized. Figure 7-13 shows a relatively large displacement at 57 minutes when the specimen was in tension and the cracking became visible. Interestingly, the results of the peak of PSD and the total received power by SAs in Figure 7-9 and Figure 7-10 showed a dramatic drop at the same time. This means that the mounted SAs were detected the crack at the same time when the demountable mechanical strain gauge detected.

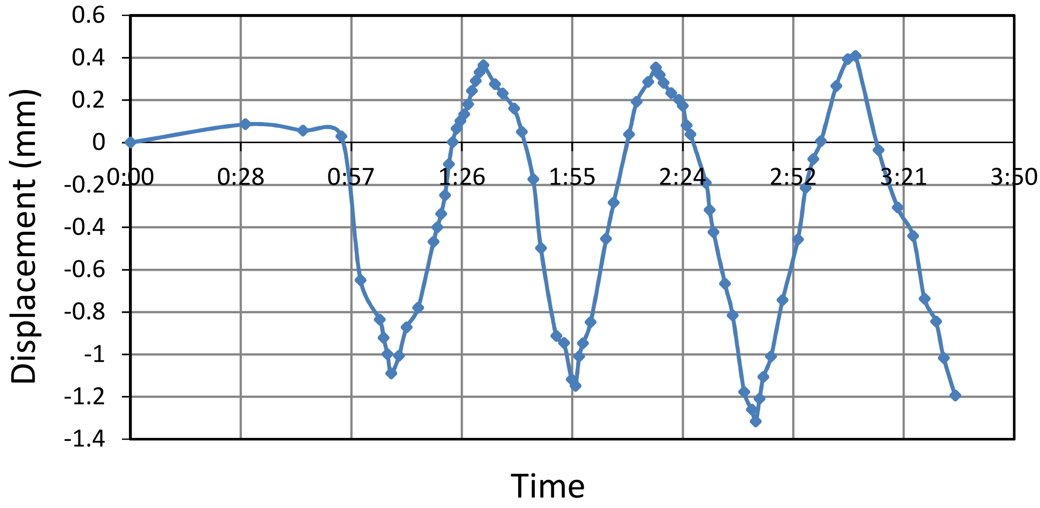

Figure 7-13: Displacement monitoring results using demountable mechanical strain gauge

7.5 Summary

This chapter presented the application of the proposed mounted SA based approach for health monitoring of the RC slab as a part of composite member with a composite joint and a reduced beam section. Three SA transducers as one actuator and two sensors were implemented on the RC slab to cover the expected damage zone. Two vertical and horizontal differential transducers were also used to monitor the development of cracks on the slab. The variations in the cracking behaviour of the RC slab were successfully monitored by both types of sensors. The proposed SA-based method showed the ability to detect the crack before it became visible on the surface of the RC slab. The proposed SA-based method predicted the failure moment earlier than the onset of the failure of the RC slab. Based on the experimental results, the following conclusions can be made:

1. The composite member under investigation in this chapter was more complex than ones in Chapters 5 and 6 of this thesis. It included a concrete-filled tubular steel tube, a reduced beam section, a RC slab and connectors. In addition, it was under relatively complex cyclic loading; therefore, the RC slab had no separated tension and compression sides.
2. The proposed mounted SA based approach could be successfully applied for the health monitoring of RC slab in this composite member under cyclic loading. It was shown that the energy of the received power dramatically decreased when cracking occurred and then slightly increased due to compression force (i.e., decreasing crack width) when the direction of loading changes.
3. There was a good correlation between the results obtained with two SA sensors located at different distances from the SA actuator.
4. Overall, the results show that the proposed mounted SA based approach could be successfully applied for the detection and monitoring cracking in of RC slab of composite members.

Chapter 8 : Conclusion and Future Work

8.1 Conclusion

Piezoceramic-based transducers have been used in a wide range of non-destructive testing systems due to the advantages of low cost, quick response, light weight, and solid-state actuation. In this thesis SA based approaches were developed and applied for characterisation of concrete members at different stages of their life. They used stress wave propagation characteristics, appropriate arrangement of SAs in and on concrete members, and analysis of the received signal using the power spectral density, total received power and damage indexes. These techniques were applied for monitoring of early-age concrete, and detection and monitoring of cracking in concrete members of different complicity under bending or cyclic loading.

The most significant findings of this research are the following:

1. The received signals in time-domain and frequency-domain may not provide sufficient information about a status of concrete member with respect to quality of concrete and/or integrity of the member. Therefore, power spectral density (PSD), total received power and damage indexes were presented as useful data analysis tool for health monitoring of concrete members.
2. The embedded SA based approach provided monitoring of a very early-age concrete hydration process monitoring. The peak of PSD and total received power increased with the development of hydration process. The received signal

gradually decreased when the separation distance between SA actuator and sensor increased.

3. The proposed embedded SA based approach can be used for the determination of initial w/c ratio and compressive strength of concrete at its early-age stage.
4. The investigation of SAs embedded in water showed that the received signal was measurable and its amplitude could be controlled by changing amount of water in moulds. In general, the preliminary measurement in water can be used for selection and calibration of SAs before concrete casting.
5. The proposed mounted SA based approach has demonstrated ability to detect cracks in concrete members. In this case location of SA transducers on the surface of concrete members can be changed and optimized. This approach is very suitable for detection and monitoring of cracks in concrete and reinforced concrete members under loading.
6. It was shown that the proposed method had an ability not only to detect the surface crack but also to detect the internal crack before it became visible. It was more sensitive to cracking than a conventional load cell and strain gauge. Due to its sensitivity, the proposed method could predict the beam failure earlier than load cells or strain gauges.
7. It was shown that the proposed mounted SA based sensory system could capture a precautionary signal for major cracking in large-scale reinforced concrete beams. The experimental results for peak of PSD and total received power showed that the transmission energy between the SA actuator and SA sensors in the RC beams dropped dramatically after the cracking moment. The proposed mounted SA sensory system is more sensitive to the cracking moment than the load cell and strain gauges.

8. The proposed mounted SA based approach has demonstrated capability of NDT of a relatively complex composite member such is one consisted of a concrete-filled tubular steel tube, a reduced beam section, a RC slab and connectors under relatively complex cyclic loading. It was shown that the energy of the received power dramatically decreased when cracking occurred and then slightly increased due to compression force (i.e., decreasing crack width) when the direction of loading changes. It means the stages of crack opening and closing during the cycle can be detected that may increase probability of crack detection and monitoring.

8.2 Future work

This study focused on application of SAs for concrete material characterisation and detection and evaluation of cracks on concrete structures. However, much research is still needed to be done in order to deliver this system to the industry. Future study suggestions are as following:

1. Concrete properties are diverse in the sense of material. In order to design multifunctional sensing system for determination of w/c ration and compressive strength of different types of concrete more concrete specimens with different compositions should be tested.
2. Future research should focus on very early-age concrete characterization for the prediction of the concrete strength development data at first 24 hours.
3. NDT of RC members should be extended to experiments with these members under dynamic load.
4. The optimization of the installation and location of the mounted SAs should be studied for more accurate localisation of defects.

5. Artificial intelligence techniques should be developed and applied for the received signal to enhance the developed SA based approaches for NDT of concrete based members. This work is in progress (please see [3] in 1.3 Publications).

References

ABO-QUDAIS, S. A. 2005. Effect of concrete mixing parameters on propagation of ultrasonic waves. *Construction and building materials,* 19**,** 257-263.

ABRAMS, D. P. 1979. Experimental study of frame-wall interaction in reinforced concrete structures subjected to strong earthquake motions.

ACI201.2R-08 2008. Guide to Durable Concrete. American Concrete Institute.

ACI209 2008. Guide for modeling and calculating shrinkage and creep in hardened concrete (ACI 209.2R-8). Farmington Hills, Michigan: American Concrete Institute.

ACI, A. 1991. 211.1-Standard Practice for Selecting Proportions for Normal. *Heavyweight, and Mass Concrete,* 2002.

ACI, H. 2001. 308R-Guide to Curing Concrete. *American Concrete Institute International*.

ADRIAN, P. Static Modulus of Elasticity of Concrete as Affected by Density. *Journal Proceedings,* 57.

AGGELIS, D. G. 2011. Classification of cracking mode in concrete by acoustic emission parameters. *Mechanics Research Communications,* 38**,** 153-157.

ANDRÉ, P., VARUM, H., ANTUNES, P., FERREIRA, L. & SOUSA, M. 2012. Monitoring of the concrete curing process using plastic optical fibers. *Measurement,* 45**,** 556-560.

AS3600 2009. Australian Standard for Concrete Structures. Sydney.

ASTM, C. 617 (2009). Standard Practice for Capping Cylindrical Concrete Specimens. American Society for Testing and Materials, 2009.

AYOTTE, E., MASSICOTTE, B., HOUDE, J. & GOCEVSKI, V. 1997. Modeling the thermal stresses at early ages in a concrete monolith. *ACI Materials Journal,* 94.

AZENHA, M., FARIA, R. & FIGUEIRAS, H. 2011. Thermography as a technique for monitoring early age temperatures of hardening concrete. *Construction and Building Materials,* 25**,** 4232-4240.

BAZANT, Z. P. & BAWEJA, S. 2000. Creep and shrinkage prediction model for analysis and design of concrete structures: Model B3. *ACI Special Publications,* 194**,** 1-84.

BAŽANT, Z. P. & LI, G.-H. 2008. Unbiased statistical comparison of creep and shrinkage prediction models. *ACI materials Journal,* 105**,** 610-621.

BEEBY, A. 1978. Corrosion of reinforcing steel in concrete and its relation to cracking. *Structural Engineer,* 56.

BEHNIA, A., CHAI, H. K. & SHIOTANI, T. 2014. Advanced structural health monitoring of concrete structures with the aid of acoustic emission. *Construction and Building Materials,* 65**,** 282-302.

BENT, A. A. & PIZZOCHERO, A. E. Recent advances in active fiber composites for structural control. SPIE's 7th Annual International Symposium on Smart Structures and Materials, 2000. International Society for Optics and Photonics, 244-254.

BENTZ, E. C., VECCHIO, F. J. & COLLINS, M. P. 2006. Simplified modified compression field theory for calculating shear strength of reinforced concrete elements. *ACI Structural Journal,* 103**,** 614.

BHALLA, A., CROSS, L. & WHATMORE, R. 1985. Pyroelectric and piezoelectric properties of lithium tetraborate single crystal. *Japanese Journal of Applied Physics,* 24**,** 727.

BOROSNYÓI, A. & BALÁZS, G. 2005. Models for flexural cracking in concrete: the state of the art. *Structural Concrete,* 6**,** 53-62.

BOUCHILLOUX, P., CLAEYSSEN, F. & LE LETTY, R. Amplified piezoelectric actuators: from aerospace to underwater applications. Smart Structures and Materials, 2004. International Society for Optics and Photonics, 143-154.

BRANCO, F. A., MENDES, P. & MIRAMBELL, E. 1992. Heat of hydration effects in concrete structures. *ACI Materials Journal,* 89.

BS, B. S. 1993. Code of practice for fatigue design and assessment of steel structures. *British Standards Institution*.

BUNGEY, J. H., GRANTHAM, M. G. & MILLARD, S. 2006. *Testing of concrete in structures*, Crc Press.

C143, A. 2004. Standard Test Method for Slump of Hydraulic Cement Concrete. ASTM International West Conshohocken, PA.

CABRERA, J. 1996. Deterioration of concrete due to reinforcement steel corrosion. *Cement and concrete composites,* 18**,** 47-59.

CARPINTERI, A., LACIDOGNA, G. & PUGNO, N. 2007. Structural damage diagnosis and life-time assessment by acoustic emission monitoring. *Engineering Fracture Mechanics,* 74**,** 273-289.

CASTEL, A. & FRANÇOIS, R. 2011. Modeling of steel and concrete strains between primary cracks for the prediction of cover-controlled cracking in RC-beams. *Engineering Structures,* 33**,** 3668-3675.

CEN, E. Design of Composite Steel and Concrete Structures. Part.

CHAIX, J.-F., GARNIER, V. & CORNELOUP, G. 2003. Concrete damage evolution analysis by backscattered ultrasonic waves. *NDT & E International,* 36**,** 461-469.

CHANG, F.-K. 1998. Structural Health Monitoring: A Summary Report on the First Stanford Workshop on Structural Health Monitoring, September 18-20, 1997. DTIC Document.

CHEN, X. & ANSARI, F. 1999. Fiber optic stress wave sensor for detection of internal flaws in concrete structures. *Journal of intelligent material systems and structures,* 10**,** 274-279.

CHENG, X., XU, D., LU, L., HUANG, S. & JIANG, M. 2010. Performance investigation of 1-3 piezoelectric ceramic–cement composite. *Materials Chemistry and Physics,* 121**,** 63-69.

CHUNG, K., KHARKOVSKY, S., KONG, Q. & SONG, G. 2014. Cure-State Monitoring of Concrete and Mortar Specimens using Smart Aggregates. *IEEE International Instrumentation and Measurement Technology Conference (I2MTC 2014).*

COLLINS, F. & SANJAYAN, J. 2000. Cracking tendency of alkali-activated slag concrete subjected to restrained shrinkage. *Cement and Concrete Research,* 30**,** 791-798.

COMMITTEE, A., INSTITUTE, A. C. & STANDARDIZATION, I. O. F. Building code requirements for structural concrete (ACI 318-08) and commentary. 2008. American Concrete Institute.

CURIE, J. & CURIE, P. 1880. Développement, par pression, de l'électricité polaire dans les cristaux hémièdres à faces inclinées. *Comptes Rendus,* 91**,** 294-295.

DEMIRBOĞA, R., TÜRKMEN, İ. & KARAKOC, M. B. 2004. Relationship between ultrasonic velocity and compressive strength for high-volume mineral-admixtured concrete. *Cement and Concrete Research,* 34**,** 2329-2336.

DERAEMAEKER, A. & WORDEN, K. 2012. *New trends in vibration based structural health monitoring*, Springer Science & Business Media.

DEROO, F., KIM, J.-Y., QU, J., SABRA, K. & JACOBS, L. J. 2010. Detection of damage in concrete using diffuse ultrasound. *The Journal of the Acoustical Society of America,* 127**,** 3315-3318.

DESMET, B., ATITUNG, K. C., SANCHEZ, M. A. A., VANTOMME, J., FEYS, D., ROBEYST, N., AUDENAERT, K., DE SCHUTTER, G., BOEL, V. & HEIRMAN, G. 2011. Monitoring the early-age hydration of self-compacting concrete using ultrasonic p-wave transmission and isothermal calorimetry. *Materials and structures,* 44**,** 1537-1558.

DIVSHOLI, B. S. & YANG, Y. 2012. Health monitoring of steel structures using sub-frequency electromechanical impedance technique. *Journal of Nondestructive Evaluation,* 31**,** 197-207.

DONG, B. & LI, Z. 2005. Cement-based piezoelectric ceramic smart composites. *Composites Science and Technology,* 65**,** 1363-1371.

DU BÉTON, F. 1993. *CEB-FIP Model Code 1990: Design Code*, T. Telford.

DUMOULIN, C., KARAISKOS, G., CARETTE, J., STAQUET, S. & DERAEMAEKER, A. 2012. Monitoring of the ultrasonic P-wave velocity in early-age concrete with embedded piezoelectric transducers. *Smart materials and structures,* 21**,** 047001.

DUMOULIN, C., KARAISKOS, G. & DERAEMAEKER, A. 2015. Monitoring of crack propagation in reinforced concrete beams using embedded piezoelectric transducers. *Acoustic Emission and Related Non-destructive Evaluation Techniques in the Fracture Mechanics of Concrete: Fundamentals and Applications***,** 161.

DUMOULIN, C., KARAISKOS, G., SENER, J.-Y. & DERAEMAEKER, A. 2014. Online monitoring of cracking in concrete structures using embedded piezoelectric transducers. *Smart materials and structures,* 23**,** 115016.

EBRAHIMPOUR, A. & SACK, R. L. 2005. A review of vibration serviceability criteria for floor structures. *Computers & Structures,* 83**,** 2488-2494.

FENG, Q., KONG, Q., HUO, L. & SONG, G. 2015. Crack detection and leakage monitoring on reinforced concrete pipe. *Smart Materials and Structures,* 24**,** 115020.

FENG, Q., KONG, Q. & SONG, G. 2016. Damage detection of concrete piles subject to typical damage types based on stress wave measurement using embedded smart aggregates transducers. *Measurement,* 88**,** 345-352.

GILBERT, R. I. 1988. *Time effects in concrete structures*, Elsevier.

GILBERT, R. I. & RANZI, G. 2010. *Time-Dependent Behaviour of Concrete Structures*, Taylor & Francis.

GOOCH, J. W. 2011. Acoustic Emission Testing. *Encyclopedic Dictionary of Polymers***,** 14-14.

GOTO, Y. Cracks formed in concrete around deformed tension bars. Journal Proceedings, 1971. 244-251.

GROSSE, C. U. 2002. About the improvement of US measurement techniques for the quality control of fresh concrete. *Otto-Graf-Journal,* 13**,** 93.

GROSSE, C. U. & OHTSU, M. 2008. *Acoustic emission testing*, Springer.

GU, H. 2007. *Innovative application of smart piezoelectric material to vibration control and health monitoring*.

GU, H., SONG, G., DHONDE, H., MO, Y. & YAN, S. 2006. Concrete early-age strength monitoring using embedded piezoelectric transducers. *Smart materials and structures,* 15**,** 1837.

HAMRAT, M., BOULEKBACHE, B., CHEMROUK, M. & AMZIANE, S. 2016. Flexural cracking behavior of normal strength, high strength and high strength fiber concrete beams, using digital image correlation technique. *Construction and Building Materials,* 106**,** 678-692.

HAN, B., WANG, Y., DONG, S., ZHANG, L., DING, S., YU, X. & OU, J. 2015. Smart concretes and structures: A review. *Journal of intelligent material systems and structures,* 26**,** 1303-1345.

HAN, L.-H., LI, W. & BJORHOVDE, R. 2014. Developments and advanced applications of concrete-filled steel tubular (CFST) structures: Members. *Journal of Constructional Steel Research,* 100**,** 211-228.

HASSAN, A. F. & SOZEN, M. A. 1997. Seismic vulnerability assessment of low-rise buildings in regions with infrequent earthquakes. *ACI Structural Journal,* 94**,** 31-39.

HORNER, G., TETER, J. & ROBBINS, E. Flex Patch, a highly flexible piezoceramic composite with attached electrical leads. Proc SPIE, 2001. 259-268.

HUANG, Y., YI, W., ZHANG, R. & XU, M. 2014. Behavior and design modification of RBS moment connections with composite beams. *Engineering Structures,* 59**,** 39-48.

HUSAIN, S. I. & FERGUSON, P. M. 1968. Flexural crack width at the bars in reinforced concrete beams.

INSTITUTION, B. S. & STANDARDIZATION, E. C. F. 2004. *Eurocode 2: Design of Concrete Structures : Part 1-1: General Rules and Rules for Buildings*, British Standards Institution.

JAFFE, B., COOK, W. R. & JAFFE, H. L. 1971. *Piezoelectric ceramics*, Academic Press.

KEATING, J., HANNANT, D. J. & HIBBERT, A. P. 1989. Correlation between cube strength, ultrasonic pulse velocity and volume change for oil well cement slurries. *Cement and Concrete Research,* 19**,** 715-726.

KIM, W. & WHITE, R. N. 1999. Shear-critical cracking in slender reinforced concrete beams. *ACI Structural Journal,* 96.

KONG, Q., HOU, S., JI, Q., MO, Y. & SONG, G. 2013. Very early age concrete hydration characterization monitoring using piezoceramic based smart aggregates. *Smart Materials and Structures,* 22**,** 085025.

KRAUSS, M. & HARIRI, K. Assessment of concrete's stiffness development by means of ultrasonics ISA TECH/EXPO Technology Update Conf. Proc, 2001. 7-15.

KRAUTKRÄMER, J. & KRAUTKRÄMER, H. 1977. *Ultrasonic testing of materials*, Springer-Verlag.

KREGER, M. E. & SOZEN, M. A. 1983. A study of the causes of column failures in the Imperial County Services Building during the 15 October 1979 Imperial Valley earthquake. University of Illinois Engineering Experiment Station. College of Engineering. University of Illinois at Urbana-Champaign.

LAROSE, E. & HALL, S. 2009. Monitoring stress related velocity variation in concrete with a 2× 10− 5 relative resolution using diffuse ultrasound. *The Journal of the Acoustical Society of America,* 125**,** 1853-1856.

LI, R., SAMALI, B., TAO, Z. & HASSAN, M. K. 2017. Cyclic behaviour of composite joints with reduced beam sections. *Engineering Structures,* 136**,** 329-344.

LI, Z., QIN, L. & HUANG, S. 2009. Embedded piezo-transducer in concrete for property diagnosis. *Journal of materials in civil engineering,* 21**,** 643-647.

LI, Z., WEI, X. & LI, W. 2003. Preliminary interpretation of Portland cement hydration process using resistivity measurements. *ACI Materials Journal,* 100.

LI, Z., ZHANG, D. & WU, K. 2002. Cement-Based 0-3 Piezoelectric Composites. *Journal of the American Ceramic Society,* 85**,** 305-313.

LIANG, Y., LI, D., PARVASI, S. M., KONG, Q. & SONG, G. 2016. Bond-slip detection of concrete-encased composite structure using electro-mechanical impedance technique. *Smart Materials and Structures,* 25**,** 095003.

LIAO, W.-I., WANG, J., SONG, G., GU, H., OLMI, C., MO, Y., CHANG, K. & LOH, C. 2011. Structural health monitoring of concrete columns subjected to seismic excitations using piezoceramic-based sensors. *Smart Materials and Structures,* 20**,** 125015.

LIPPMANN, R. P. 1987. An introduction to computing with neural nets. *ASSP Magazine, IEEE,* 4**,** 4-22.

LIU, Z., ZHANG, Y., JIANG, Q., SUN, G. & ZHANG, W. 2011. In situ continuously monitoring the early age microstructure evolution of cementitious materials using ultrasonic measurement. *Construction and Building Materials,* 25**,** 3998-4005.

LU, S. W. & XIE, H. Q. 2006. Real-time Monitoring and Simulating the Load Effects of Smart" CFRP-Strengthened RC Beams. *Key Engineering Materials,* 324**,** 129-132.

LU, Y. 2010. *Non-destructive Evaluation on Concrete Materials and Structures using Cement-based Piezoelectric Sensor*, HONG KONG UNIV. OF SCI. AND TECH.(HONG KONG).

LU, Y., LI, Z. & LIAO, W.-I. 2011. Damage monitoring of reinforced concrete frames under seismic loading using cement-based piezoelectric sensor. *Materials and structures,* 44**,** 1273-1285.

LU, Y., ZHANG, J. & LI, Z. 2013. Study on hydration process of early-age concrete using embedded active acoustic and non-contact complex resistivity methods. *Construction and Building Materials,* 46**,** 183-192.

MAIERHOFER, C. 2010. Planning a non-destructive test programme for reinforced concrete structures.

MALHOTRA, V. M. & CARINO, N. J. 2003. *Handbook on Nondestructive Testing of Concrete Second Edition*, CRC press.

MASON, W. P., MCSKIMIN, H. J. & SHOCKLEY, W. 1948. Ultrasonic Observation of Twinning in Tin. *Physical Review,* 73**,** 1213-1214.

MCCANN, D. & FORDE, M. 2001. Review of NDT methods in the assessment of concrete and masonry structures. *NDT & E International,* 34**,** 71-84.

MIKULIĆ, D., MILOVANOVIĆ, B. & GABRIJEL, I. 2013. Analysis of thermal properties of cement paste during setting and hardening. *Nondestructive Testing of Materials and Structures.* Springer.

MILLS, O. M. 2001. Composite Structures Design Manual-Design Booklet 1.2, Design of the Shear Connection of Simply-Supported Composite Beams (to Australian Standard AS 2327.1-1996). February.

MOSLEHY, Y., GU, H., BELARBI, A., MO, Y. & SONG, G. 2010. Smart aggregate based damage detection of circular RC columns under cyclic combined loading. *Smart Materials and Structures,* 19**,** 065021.

NAIK, T. R., MALHOTRA, V. M. & POPOVICS, J. S. 2004. The ultrasonic pulse velocity method. *Handbook on nondestructive testing of concrete***,** 169-188.

NEWNHAM, R. E., BOWEN, L., KLICKER, K. & CROSS, L. 1980. Composite piezoelectric transducers. *Materials & Design,* 2**,** 93-106.

NI, X., RIZZO, P., YANG, J., KATRI, D. & DARAIO, C. 2012. Monitoring the hydration of cement using highly nonlinear solitary waves. *NDT & E International,* 52**,** 76-85.

NOJAVAN, S. & YUAN, F.-G. 2006. Damage imaging of reinforced concrete structures using electromagnetic migration algorithm. *International Journal of solids and structures,* 43**,** 5886-5908.

NORRIS, A., SAAFI, M. & ROMINE, P. 2008. Temperature and moisture monitoring in concrete structures using embedded nanotechnology/microelectromechanical systems (MEMS) sensors. *Construction and building materials,* 22**,** 111-120.

OHTSU, M. 1996. The history and development of acoustic emission in concrete engineering. *Magazine of concrete research,* 48**,** 321-330.

OHTSU, M., SHIGEISHI, M., IWASE, H. & KOYANAGIT, W. 1991. Determination of crack location, type and orientation ina concrete structures by acoustic emission. *Magazine of Concrete Research,* 43**,** 127-134.

OTANI, S. & SOZEN, M. A. 1972. Behavior of multistory reinforced concrete frames during earthquakes. University of Illinois Engineering Experiment Station. College of Engineering. University of Illinois at Urbana-Champaign.

PACHECO, C. & SNIEDER, R. 2005. Time-lapse travel time change of multiply scattered acoustic waves. *The Journal of the Acoustical Society of America,* 118**,** 1300-1310.

PADMARAJAIAH, S. & RAMASWAMY, A. 2002. A finite element assessment of flexural strength of prestressed concrete beams with fiber reinforcement. *Cement and Concrete Composites,* 24**,** 229-241.

PARK, G., SOHN, H., FARRAR, C. R. & INMAN, D. J. 2003. Overview of piezoelectric impedance-based health monitoring and path forward. *Shock and Vibration Digest,* 35**,** 451-464.

PARK, S., AHMAD, S., YUN, C.-B. & ROH, Y. 2006. Multiple crack detection of concrete structures using impedance-based structural health monitoring techniques. *Experimental Mechanics,* 46**,** 609-618.

PARK, S., YUN, C.-B. & ROH, Y. 2007. Damage diagnostics on a welded zone of a steel truss member using an active sensing network system. *NDT & E International,* 40**,** 71-76.

PARK, Y.-J., ANG, A. H.-S. & WEN, Y. K. 1985. Seismic damage analysis of reinforced concrete buildings. *Journal of Structural Engineering,* 111**,** 740-757.

PLANÈS, T. & LAROSE, E. 2013. A review of ultrasonic Coda Wave Interferometry in concrete. *Cement and Concrete Research,* 53**,** 248-255.

PLEVRIS, N. & TRIANTAFILLOU, T. C. 1994. Time-dependent behavior of RC members strengthened with FRP laminates. *Journal of Structural Engineering,* 120**,** 1016-1042.

POZOS-ESTRADA, A., HONG, H. & GALSWORTHY, J. 2010. Serviceability design factors for wind-sensitive structures. *Canadian Journal of Civil Engineering,* 37**,** 728-738.

QIN, L. & LI, Z. 2008. Monitoring of cement hydration using embedded piezoelectric transducers. *Smart Materials and Structures,* 17**,** 055005.

QIN, L., PENG, Y., REN, H. & LI, Z. Application of cement-based piezoelectric composites in acoustic emission detection for concrete. Second International Conference on Smart Materials and Nanotechnology in Engineering, 2009. International Society for Optics and Photonics, 74930G-74930G-9.

QUIVIGER, A., PAYAN, C., CHAIX, J.-F., GARNIER, V. & SALIN, J. 2012. Effect of the presence and size of a real macro-crack on diffuse ultrasound in concrete. *NDT & E International,* 45**,** 128-132.

REBIBOU, S., DUX, P. & NOORU-MOHAMED, M. 2003. Shrinkage in concrete pavements. *Australian Journal of Civil Engineering,* 1**,** 23-28.

REINHARDT, H. & GROSSE, C. 2004. Continuous monitoring of setting and hardening of mortar and concrete. *Construction and building materials,* 18**,** 145-154.

REN, L., LI SR, H.-N., LI, X., ZHOU, J. & XIANG, L. Application of FBG sensors in rolled concrete dam model. Smart Structures and Materials, 2006. International Society for Optics and Photonics, 617436-617436-7.

RITTENMYER, K., SHROUT, T., SCHULZE, W. & NEWNHAM, R. 1982. Piezoelectric 3–3 composites. *Ferroelectrics,* 41**,** 189-195.

SAFARI, H. R., FASSETT, M. J., SOUTER, I. C., ALSULYMAN, O. M. & GOODWIN, T. M. 1998. The efficacy of methylprednisolone in the treatment of hyperemesis gravidarum: a randomized, double-blind, controlled study. *American journal of obstetrics and gynecology,* 179**,** 921-924.

SAIIDI, M. & SOZEN, M. A. 1981. Simple nonlinear seismic analysis of R/C structures. *Journal of the Structural Division,* 107**,** 937-953.

SCHURR, D. P., KIM, J.-Y., SABRA, K. G. & JACOBS, L. J. 2011. Damage detection in concrete using coda wave interferometry. *NDT & E International,* 44**,** 728-735.

SHAH, A. & RIBAKOV, Y. 2010. Effectiveness of nonlinear ultrasonic and acoustic emission evaluation of concrete with distributed damages. *Materials & Design,* 31**,** 3777-3784.

SHAH, A. A., RIBAKOV, Y. & HIROSE, S. 2009. Nondestructive evaluation of damaged concrete using nonlinear ultrasonics. *Materials & Design,* 30**,** 775-782.

SHIOTANI, T. & AGGELIS, D. G. 2009. Wave propagation in cementitious material containing artificial distributed damage. *Materials and structures,* 42**,** 377-384.

SHOKOUHI, P., ZOËGA, A. & WIGGENHAUSER, H. 2010. Nondestructive investigation of stress-induced damage in concrete. *Advances in Civil Engineering,* 2010.

SNIEDER, R. 2006. The theory of coda wave interferometry. *Pure and Applied Geophysics,* 163**,** 455-473.

SOH, C., TSENG, K. K., BHALLA, S. & GUPTA, A. 2000. Performance of smart piezoceramic patches in health monitoring of a RC bridge. *Smart materials and Structures,* 9**,** 533.

SOHN, H., PARK, G., WAIT, J. R., LIMBACK, N. P. & FARRAR, C. R. 2003. Wavelet-based active sensing for delamination detection in composite structures. *Smart Materials and structures,* 13**,** 153.

SONG, G., GU, H. & MO, Y.-L. 2008. Smart aggregates: multi-functional sensors for concrete structures—a tutorial and a review. *Smart Materials and Structures,* 17**,** 033001.

SONG, G., GU, H., MO, Y., HSU, T. & DHONDE, H. 2007. Concrete structural health monitoring using embedded piezoceramic transducers. *Smart Materials and Structures,* 16**,** 959.

SONG, G., GU, H., MO, Y., HSU, T., DHONDE, H. & ZHU, R. Health monitoring of a concrete structure using piezoceramic materials. Smart Structures and Materials, 2005. International Society for Optics and Photonics, 108-119.

SONG, G., SETHI, V. & LI, H.-N. 2006. Vibration control of civil structures using piezoceramic smart materials: A review. *Engineering Structures,* 28**,** 1513-1524.

STANDARD, A. 2003. C31/C31M (2010),“. *Standard Practice for Making and Curing Concrete Test Specimens in the Field,” ASTM International, West Conshohocken, PA*.

STANDARD, B. 2005. Eurocode 8: Design of structures for earthquake resistance—.

SU, H., ZHANG, N., WEN, Z. & LI, H. 2016. Experimental study on obtaining hydraulic concrete strength by use of concrete piezoelectric ceramic smart module pairs. *Journal of Intelligent Material Systems and Structures,* 27**,** 666-678.

SUBRAMANIAN, N. 2014. *Design of Reinforced Concrete Structures*, Oxford University Press.

TAO, Z., HASSAN, M. K., SONG, T.-Y. & HAN, L.-H. 2017. Experimental study on blind bolted connections to concrete-filled stainless steel columns. *Journal of Constructional Steel Research,* 128**,** 825-838.

TAWIE, R. & LEE, H. 2010. Monitoring the strength development in concrete by EMI sensing technique. *Construction and Building Materials,* 24**,** 1746-1753.

TAYLOR, H., FAMY, C. & SCRIVENER, K. 2001. Delayed ettringite formation. *Cement and concrete research,* 31**,** 683-693.

TAYLOR, J. R. 1997. *An Introduction to Error Analysis: The Study of Uncertainties in Physical Measurements*, University Science Books.

TORRES, L., LOPEZ-ALMANSA, F. & BOZZO, L. 2004. Tension-stiffening model for cracked flexural concrete members. *Journal of Structural Engineering,* 130**,** 1242-1251.

TOURIN, A., FINK, M. & DERODE, A. 2000. Multiple scattering of sound. *Waves in random media,* 10**,** R31-R60.

VENTURE, S. J. 1997. Protocol for fabrication, inspection, testing, and documentation of beam-column connection tests and other experimental specimens. *Rep. No. SAC/BD-97,* 2.

VENTURE, S. J. & COMMITTEE, G. D. 2000. *Recommended seismic design criteria for new steel moment-frame buildings*, Federal Emergency Management Agency.

VOIGT, T., GROSSE, C. U., SUN, Z., SHAH, S. & REINHARDT, H.-W. 2005a. Comparison of ultrasonic wave transmission and reflection measurements with P-and S-waves on early age mortar and concrete. *Materials and Structures,* 38**,** 729-738.

VOIGT, T., YE, G., SUN, Z., SHAH, S. P. & VAN BREUGEL, K. 2005b. Early age microstructure of Portland cement mortar investigated by ultrasonic shear waves and numerical simulation. *Cement and concrete research,* 35**,** 858-866.

WANG, C.-H. & WEN, Y.-K. 2000. Evaluation of pre-Northridge low-rise steel buildings. I: Modeling. *Journal of Structural Engineering,* 126**,** 1160-1168.

WANG, C. S., WU, F. & CHANG, F.-K. 2001. Structural health monitoring from fiber-reinforced composites to steel-reinforced concrete. *Smart Materials and Structures,* 10**,** 548.

WEISS, W. J., YANG, W. & SHAH, S. P. 1998. Shrinkage cracking of restrained concrete slabs. *Journal of Engineering Mechanics,* 124**,** 765-774.

WHITTLE, R. 2012. *Failures in Concrete Structures: Case Studies in Reinforced and Prestressed Concrete*, Taylor & Francis.

WILKIE, W. K., BRYANT, R. G., HIGH, J. W., FOX, R. L., HELLBAUM, R. F., JALINK JR, A., LITTLE, B. D. & MIRICK, P. H. Low-cost piezocomposite actuator for structural control applications. SPIE's 7th Annual International Symposium on Smart Structures and Materials, 2000. International Society for Optics and Photonics, 323-334.

WILLIAMS, A. 2003. *Design of reinforced concrete structures*, Dearborn Trade Publishing.

WOLANSKI, A. J. 2004. *Flexural behavior of reinforced and prestressed concrete beams using finite element analysis.* Citeseer.

XIAO, L. 2007. Interpretation of hydration process of concrete based on electrical resistivity measurement.

XIAO, L. & LI, Z. 2008. Early-age hydration of fresh concrete monitored by non-contact electrical resistivity measurement. *Cement and Concrete Research,* 38**,** 312-319.

XU, B., ZHANG, T., SONG, G. & GU, H. 2013. Active interface debonding detection of a concrete-filled steel tube with piezoelectric technologies using wavelet packet analysis. *Mechanical Systems and Signal Processing,* 36**,** 7-17.

YAN, S., SUN, W., SONG, G., GU, H., HUO, L.-S., LIU, B. & ZHANG, Y.-G. 2009. Health monitoring of reinforced concrete shear walls using smart aggregates. *Smart Materials and Structures,* 18**,** 047001.

YANG, Y., DIVSHOLI, B. S. & SOH, C. K. 2010. A reusable PZT transducer for monitoring initial hydration and structural health of concrete. *Sensors,* 10**,** 5193-5208.

YANG, Y., HU, Y. & LU, Y. 2008. Sensitivity of PZT impedance sensors for damage detection of concrete structures. *Sensors,* 8**,** 327-346.

YE, G., LURA, P., VAN BREUGEL, K. & FRAAIJ, A. 2004. Study on the development of the microstructure in cement-based materials by means of numerical simulation and ultrasonic pulse velocity measurement. *Cement and Concrete Composites,* 26**,** 491-497.

ZENG, L., PARVASI, S. M., KONG, Q., HUO, L., LI, M. & SONG, G. 2015. Bond slip detection of concrete-encased composite structure using shear wave based active sensing approach. *Smart Materials and Structures,* 24**,** 125026.

ZHANG, C., YU, X., ALEXANDER, L., ZHANG, Y., RAJAMANI, R. & GARG, N. 2016. Piezoelectric active sensing system for crack detection in concrete structure. *Journal of Civil Structural Health Monitoring,* 6**,** 129-139.

ZHANG, J., QIN, L. & LI, Z. 2009. Hydration monitoring of cement-based materials with resistivity and ultrasonic methods. *Materials and Structures,* 42**,** 15-24.

ZHANG, W., GAO, J., SHI, B., CUI, H. & ZHU, H. 2006. Health monitoring of rehabilitated concrete bridges using distributed optical fiber sensing. *Computer-Aided Civil and Infrastructure Engineering,* 21**,** 411-424.

ZHANG, Y., ABRAHAM, O., GRONDIN, F., LOUKILI, A., TOURNAT, V., LE DUFF, A., LASCOUP, B. & DURAND, O. 2012. Study of stress-induced velocity variation in concrete under direct tensile force and monitoring of the damage level by using thermally-compensated coda wave interferometry. *Ultrasonics,* 52**,** 1038-1045.

ZHAO, J., BAO, T., CHEN, S. & KUNDU, T. 2016. Smart aggregate-piezoceramic patch combination for health monitoring of concrete structures. *Journal of Sensors,* 2016.

ZHOU, F. P. 1992. Time-dependent crack growth and fracture in concrete. *Report TVBM 1011*.

ZOU, D., LIU, T., LIANG, C., HUANG, Y., ZHANG, F. & DU, C. 2015. An experimental investigation on the health monitoring of concrete structures using piezoelectric

transducers at various environmental temperatures. *Journal of Intelligent Material Systems and Structures*, 1045389X14566525.
ZOU, X., CHAO, A., TIAN, Y., WU, N., ZHANG, H., YU, T.-Y. & WANG, X. 2012. An experimental study on the concrete hydration process using Fabry–Perot fiber optic temperature sensors. *Measurement,* 45, 1077-1082.

Appendix A

The MATLAB code developed to calculate the peak of PSD and total received power

```
X1(1:160000,:)=[];
X1(600000:end,:)=[];

X1(:,2)=X1(:,2).*1e9;
figure(1)
plot(X1(:,1),X1(:,2));
grid on
AreaX1=trapz(X1(:,1),X1(:,2));
AreaX1=AreaX1/1000;
maxX1=max(X1(:,2));
[maxYValue, indexAtMaxY] = max(X1(:,2));
    Y1=X1(indexAtMaxY,1) %frequency

X2(1:160000,:)=[];
X2(600000:end,:)=[];

X2(:,2)=X2(:,2).*1e9;
figure(2)
plot(X2(:,1),X2(:,2));
grid on
AreaX2=trapz(X2(:,1),X2(:,2));
AreaX2=AreaX2/1000;
maxX2=max(X2(:,2));
[maxYValue, indexAtMaxY] = max(X2(:,2));
    Y2=X2(indexAtMaxY,1) %frequency

X3(1:160000,:)=[];
X3(600000:end,:)=[];

X3(:,2)=X3(:,2).*1e9;
figure(3)
plot(X3(:,1),X3(:,2));
grid on
AreaX3=trapz(X3(:,1),X3(:,2));
AreaX3=AreaX3/1000;
maxX3=max(X3(:,2));
[maxYValue, indexAtMaxY] = max(X3(:,2));
    Y3=X3(indexAtMaxY,1) %frequency

X4(1:160000,:)=[];
X4(600000:end,:)=[];

X4(:,2)=X4(:,2).*1e9;
figure(4)
plot(X4(:,1),X4(:,2));
grid on
AreaX4=trapz(X4(:,1),X4(:,2));
AreaX4=AreaX4/1000;
maxX4=max(X4(:,2));
[maxYValue, indexAtMaxY] = max(X4(:,2));
```

```
    Y4=X4(indexAtMaxY,1) %frequency


X5(1:160000,:)=[];
X5(600000:end,:)=[];

X5(:,2)=X5(:,2).*1e9;
figure(5)
plot(X5(:,1),X5(:,2));
grid on
AreaX5=trapz(X5(:,1),X5(:,2));
AreaX5=AreaX5/1000;
maxX5=max(X5(:,2));
[maxYValue, indexAtMaxY] = max(X5(:,2));
    Y5=X5(indexAtMaxY,1) %frequency


X6(1:160000,:)=[];
X6(600000:end,:)=[];

X6(:,2)=X6(:,2).*1e9;
figure(6)
plot(X6(:,1),X6(:,2));
grid on
AreaX6=trapz(X6(:,1),X6(:,2));
AreaX6=AreaX6/1000;
maxX6=max(X6(:,2));
[maxYValue, indexAtMaxY] = max(X6(:,2));
    Y6=X6(indexAtMaxY,1) %frequency


X7(1:160000,:)=[];
X7(600000:end,:)=[];

X7(:,2)=X7(:,2).*1e9;
figure(7)
plot(X7(:,1),X7(:,2));
grid on
AreaX7=trapz(X7(:,1),X7(:,2));
AreaX7=AreaX7/1000;
maxX7=max(X7(:,2));
[maxYValue, indexAtMaxY] = max(X7(:,2));
    Y7=X7(indexAtMaxY,1) %frequency


X8(1:160000,:)=[];
X8(600000:end,:)=[];

X8(:,2)=X8(:,2).*1e9;
figure(8)
plot(X8(:,1),X8(:,2));
grid on
AreaX8=trapz(X8(:,1),X8(:,2));
AreaX8=AreaX8/1000;
maxX8=max(X8(:,2));
[maxYValue, indexAtMaxY] = max(X8(:,2));
    Y8=X8(indexAtMaxY,1) %frequency
```

```
X9(1:160000,:)=[];
X9(600000:end,:)=[];

X9(:,2)=X9(:,2).*1e9;
figure(9)
plot(X9(:,1),X9(:,2));
grid on
AreaX9=trapz(X9(:,1),X9(:,2));
AreaX9=AreaX9/1000;
maxX9=max(X9(:,2));
[maxYValue, indexAtMaxY] = max(X9(:,2));
    Y9=X9(indexAtMaxY,1) %frequency


X10(1:160000,:)=[];
X10(600000:end,:)=[];

X10(:,2)=X10(:,2).*1e9;
figure(10)
plot(X10(:,1),X10(:,2));
grid on
AreaX10=trapz(X10(:,1),X10(:,2));
AreaX10=AreaX10/1000;
maxX10=max(X10(:,2));
[maxYValue, indexAtMaxY] = max(X10(:,2));
    Y10=X10(indexAtMaxY,1) %frequency
```

Appendix B

The peak of PSD and the total received power for concrete beam specimens

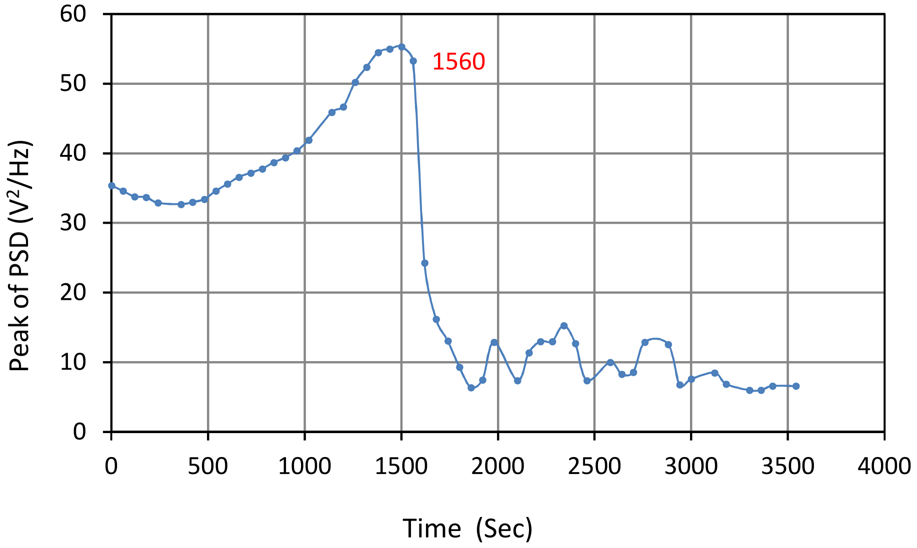

a) S_T sensor

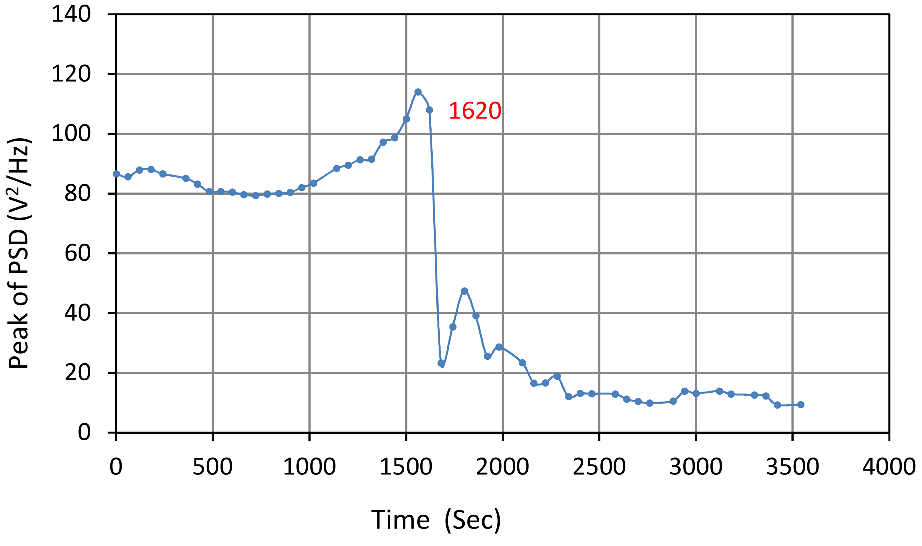

b) S_C sensor

Figure B 1: Peak of PSD for (a) S_T sensor at the tension side and (b) S_C sensor at the compression side of concrete beam SB19

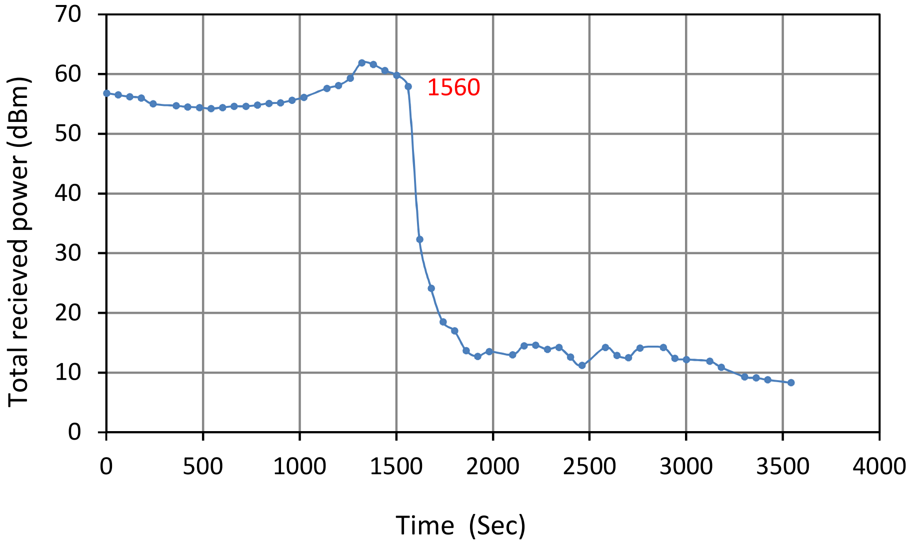

a) S_T sensor

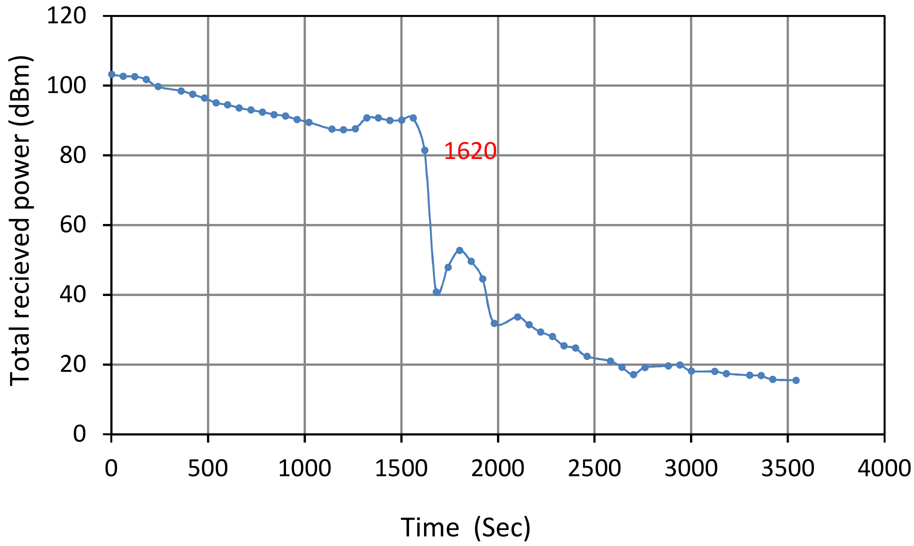

b) S_C sensor

Figure B 2: Total received power for (a) S_T sensor at the tension side and (b) S_C sensor at the compression side of concrete beam SB19

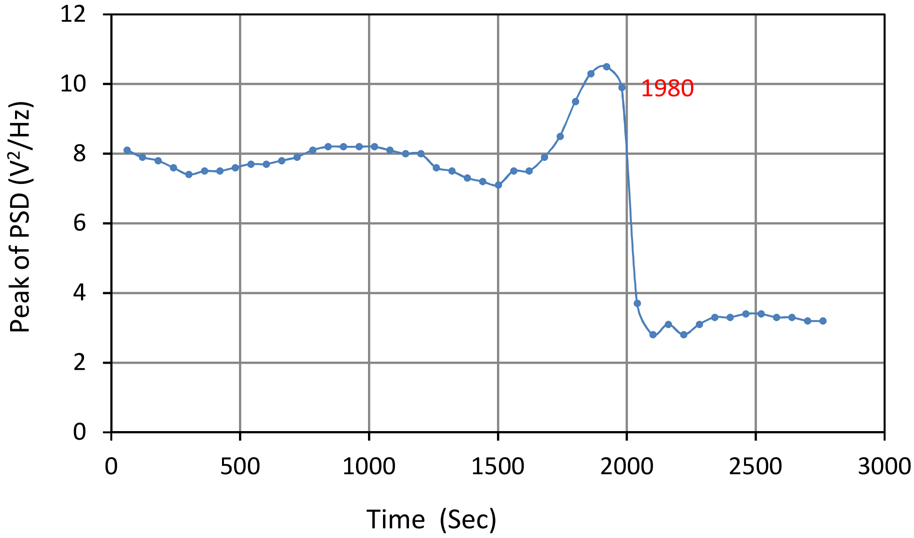

a) S_T sensor

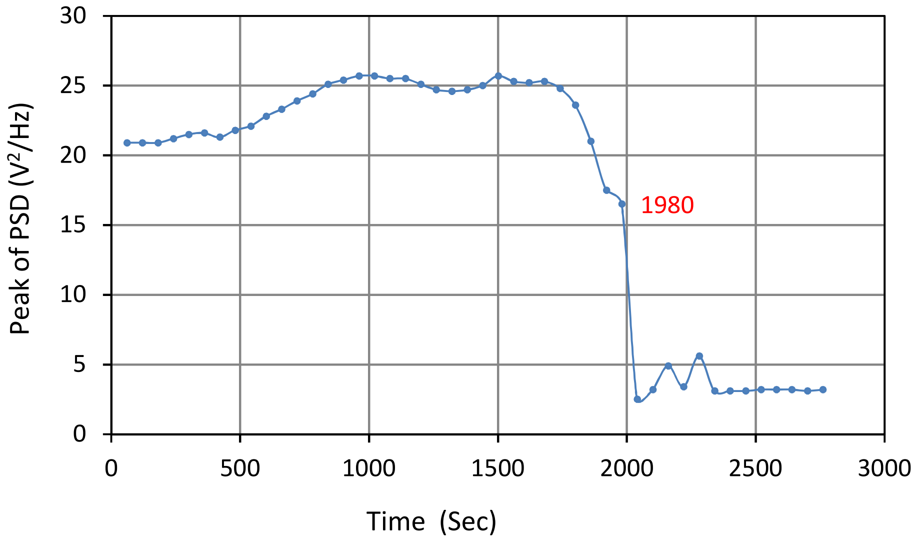

b) S_C sensor

Figure B 3: Peak of PSD for (a) S_T sensor at the tension side and (b) S_C sensor at the compression side of concrete beam SB14

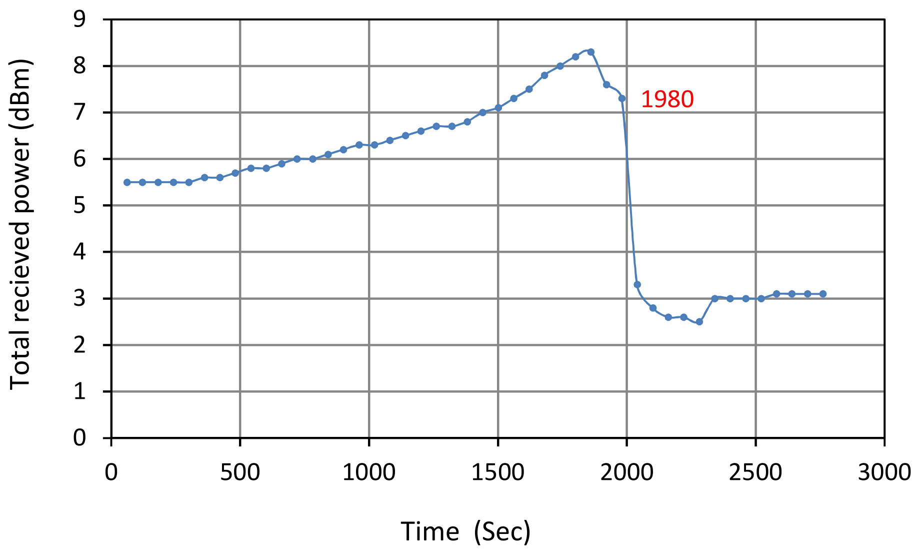

a) S_T sensor

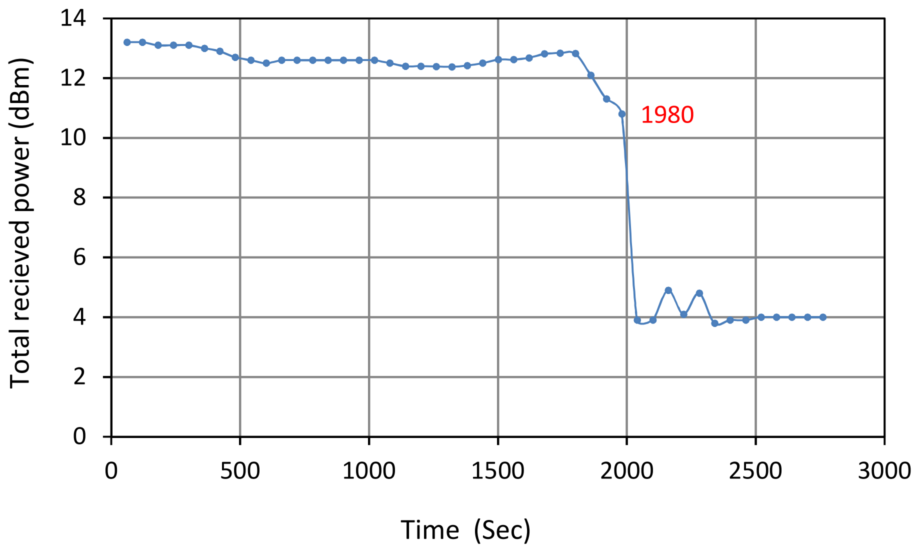

b) S_C sensor

Figure B 4: Total received power for (a) S_T sensor at the tension side and (b) S_C sensor at the compression side of concrete beam SB14

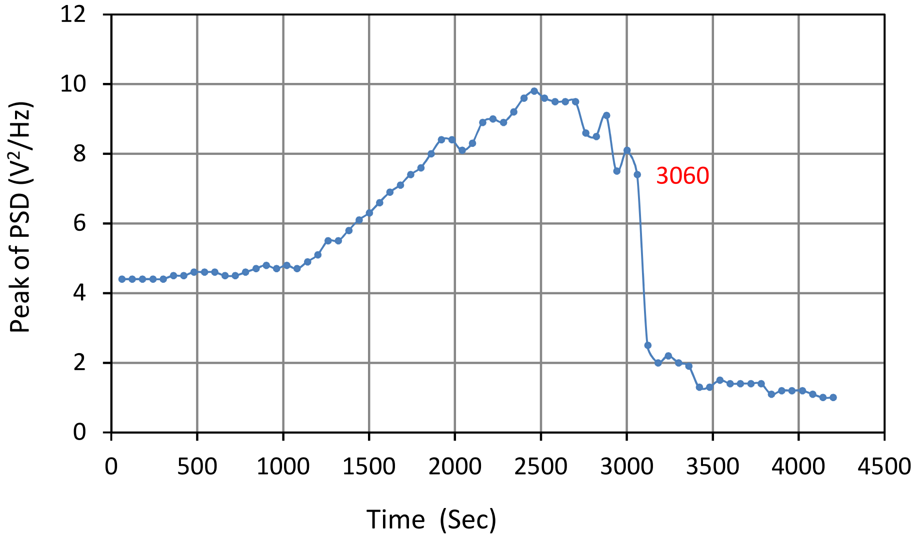

a) S_T sensor

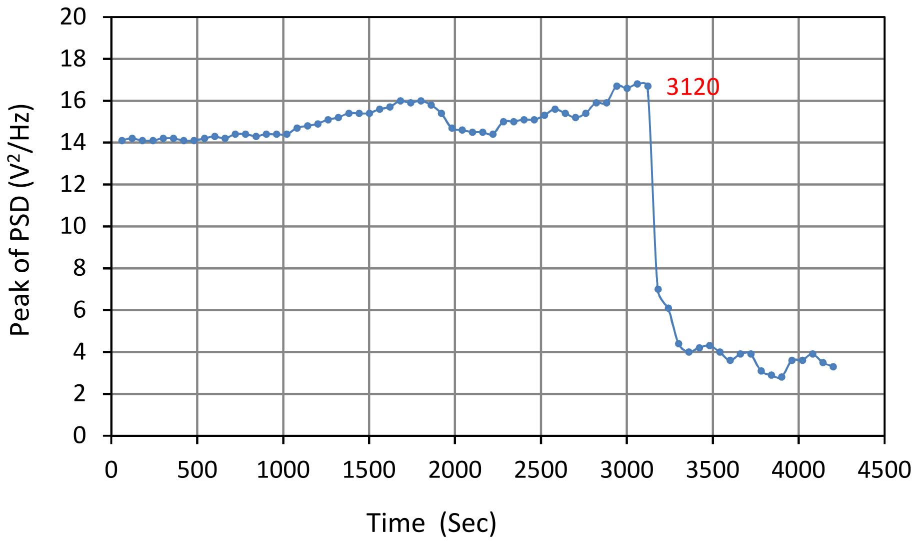

b) S_C sensor

Figure B 5: Peak of PSD for (a) S_T sensor at the tension side and (b) S_C sensor at the compression side of concrete beam SB05

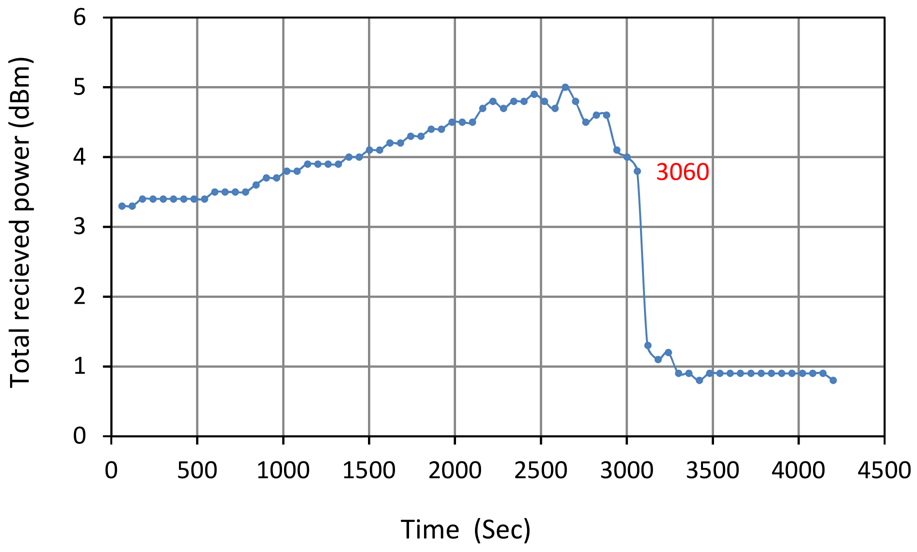

a) S_T sensor

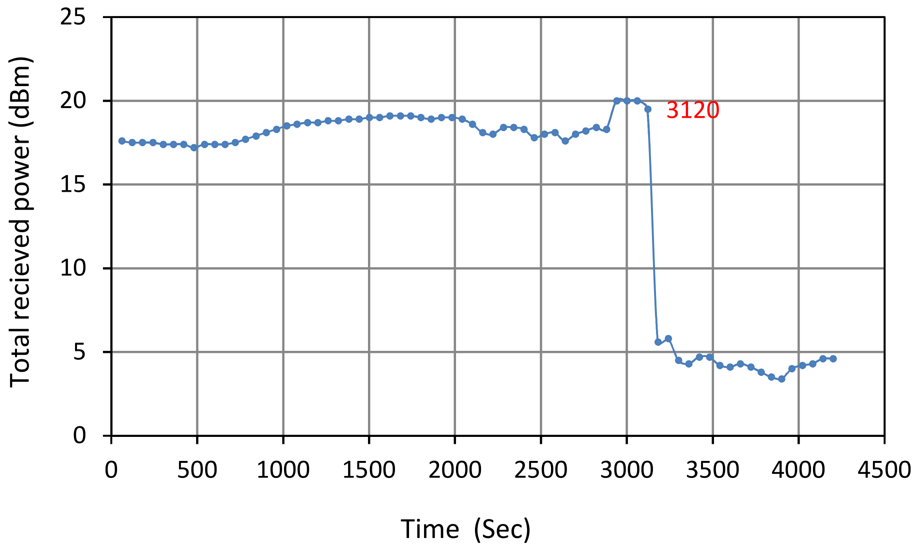

b) S_C sensor

Figure B 6: Total received power for (a) S_T sensor at the tension side and (b) S_C sensor at the compression side of concrete beam SB05

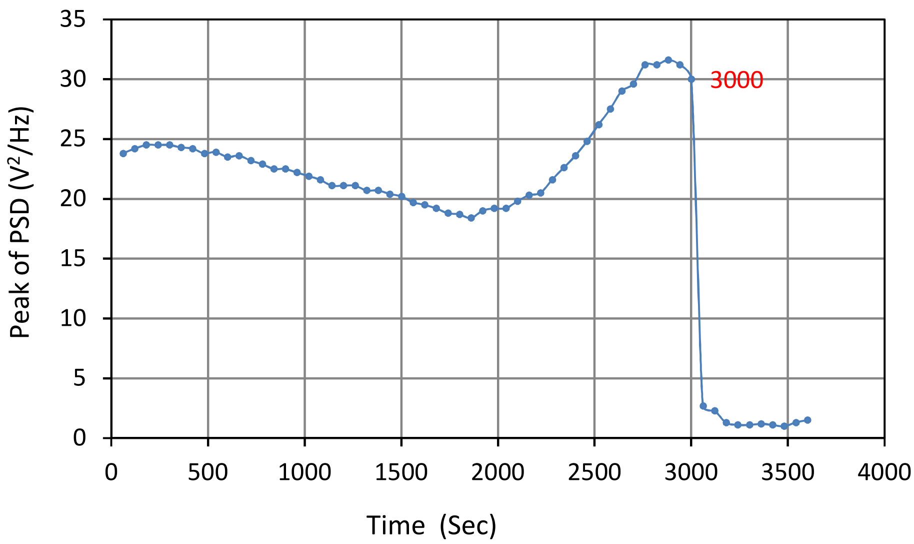

a) S_T sensor

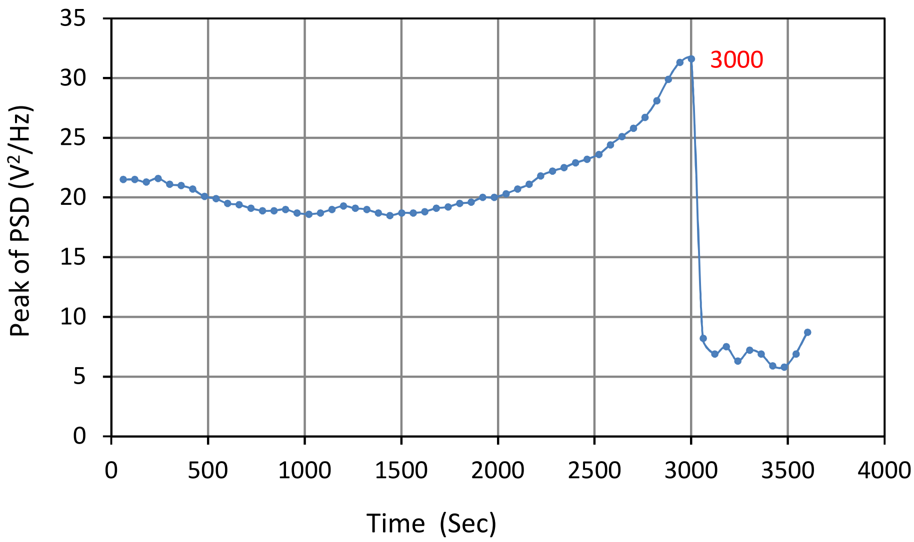

b) S_C sensor

Figure B 7: Peak of PSD for (a) S_T sensor at the tension side and (b) S_C sensor at the compression side of concrete beam SB15

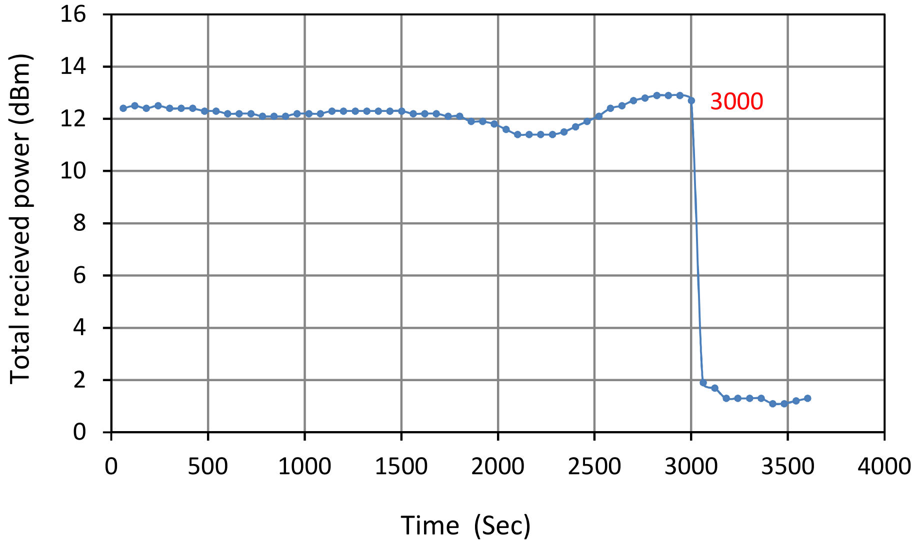

a) S_T sensor

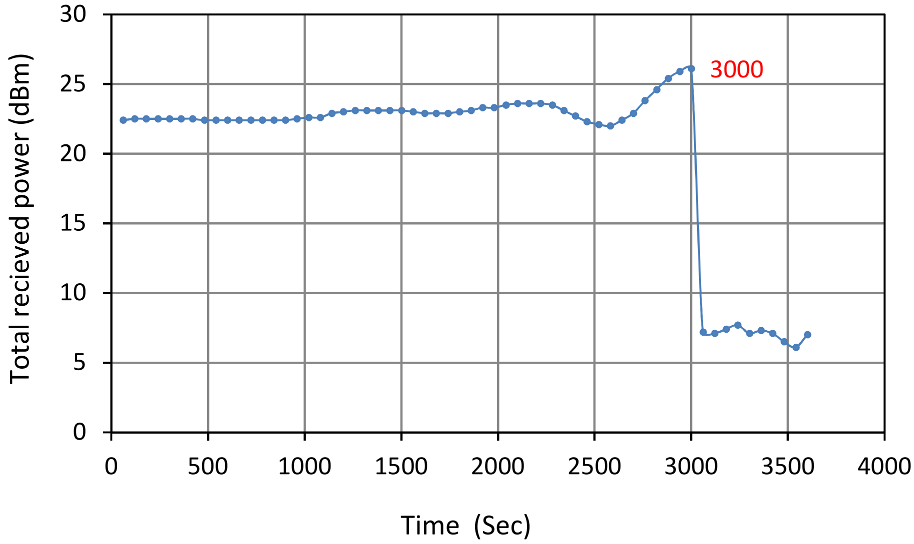

b) S_C sensor

Figure B 8: Total received power for (a) S_T sensor at the tension side and (b) S_C sensor at the compression side of concrete beam SB15